



THE UNIVERSITY OF
WAIKATO
Te Whare Wānanga o Waikato

Research Commons

<http://researchcommons.waikato.ac.nz/>

Research Commons at the University of Waikato

Copyright Statement:

The digital copy of this thesis is protected by the Copyright Act 1994 (New Zealand).

The thesis may be consulted by you, provided you comply with the provisions of the Act and the following conditions of use:

- Any use you make of these documents or images must be for research or private study purposes only, and you may not make them available to any other person.
- Authors control the copyright of their thesis. You will recognise the author's right to be identified as the author of the thesis, and due acknowledgement will be made to the author where appropriate.
- You will obtain the author's permission before publishing any material from the thesis.

Modelling the Spatial Effects of the Anaesthetic-Induced Phase-Transition in the Cerebral Cortex

A thesis submitted in partial fulfilment
of the requirements for the degree of

Master of Science

in Physics

University of Waikato

by

David Robin Whiting



The
University
of Waikato
*Te Whare Wānanga
o Waikato*

2003

To my mother Jenny
father Robin
sisters Amelia and Karen,
and my partner Helen.

Acknowledgements

I would like to give a special thanks to Alistair and Moira Steyn-Ross, along with Jamie Sleigh, for involving me in their reasearch and for much guidance and advice. Thankyou Alistair for always having time for my queries no matter how small. Michael Cree your valued assistance with Unix and \LaTeX was much appreciated. I would also like to thank Fisher and Paykel Healthcare and Wel Energy for the funding they supplied me. Thankyou to my friends and family for much encouragement, and fun times.

Abstract

In this thesis I investigate the theoretical stochastic behaviour of a one-dimensional model of the cerebral cortex, exposed to varying concentrations of a general anaesthetic agent. The model is that of Steyn-Ross *et al.* (2003). There is a continuum theory based on the electrical response of a neural mass known as the macrocolumn. The model predicts that as anaesthetic concentration is increased the cortex will undergo a sudden electrical phase transition corresponding to loss of consciousness (LOC). Similarly, at return of consciousness (ROC) a second distinct phase transition is predicted. Spatial variability is incorporated into the original homogeneous cortical model of Steyn-Ross *et al.* (1999). This is done by including the possibility of spatial variation in distant excitatory and inhibitory inputs. By modelling the cortex in this way, we hope to gain an understanding of how the cortex functions, and how anaesthetic agents “shut-down” the brain.

I simulate the one-dimensional system numerically in order to verify analytical predictions. Both analytical and numerical results show an increase in the coherence (spatial-correlation) of the electrical activity along the one-dimensional rod on approach to both LOC and ROC. Theory and simulations also show that the electrical fluctuations in the unconscious cortex should have a *larger* correlation length than for the cortex in the conscious state, suggesting that the unconscious state is the more ordered. I derive the theoretical power spectrum and discuss some of its properties.

By expanding the model to include spatial variability, we discover the possibility of self-organized structures forming spontaneously in the one-dimensional cortex. These “Turing” or dissipative structures are stationary in time, showing giant DC voltage variations along the cortical rod. Although the dissipative structures can form a rich variety of pseudo-periodic patterns, the physiological significance of such stationary neural structures is not yet clear.

Contents

Abstract	i
List of Figures	vi
List of Tables	viii
Acronyms and Abbreviations	ix
Chapter 1 Introduction	1
1.1 Thesis Overview	2
1.2 Thesis Structure	2
1.3 Original Work	3
Chapter 2 Neurophysiology	5
2.1 The Cerebral Cortex	5
2.2 Resting and Nernst Potential	7
2.3 The Cerebral Cortex and Anaesthetics	9
Chapter 3 Cortical Modelling	11
3.1 The Macrocolumn	11
3.2 The Cerebral Cortex and the EEG	11
3.3 Neural Circuits	13
3.4 The Liley Equations	20
3.5 The Steyn-Ross Model	25
3.6 Stationary States	28
3.7 Adiabatic Elimination of Fast Variables	30
3.8 Linearizing and Stability Analysis	34
Chapter 4 Spatial Variation	37
4.1 Nonequilibrium Phase Transitions	37
4.2 The Brusselator	39
4.3 Linear Stability Analysis	41
4.3.1 Linear Stability Analysis for Diffusive Systems	43
4.4 Linear Stability Analysis of the Brusselator	45
4.5 Spatial Correlation Functions	49

4.6	Linearization of the 1-D Cortex	49
4.7	Infinite Brain	54
4.8	Stability of the Spatio-Adiabatic system	57
4.9	Spatial Covariance of \hat{h}_e	60
4.10	Previous Models and Clinical Evidence	62
Chapter 5 Diffusion		65
5.1	The Diffusion Equation	65
5.2	Numerical Approximation for Derivatives	65
5.3	Numerical Solution of the Diffusion Equation	66
5.4	Simulations of the Diffusion Equation	68
5.5	Noise and the Diffusion Equation	75
5.6	Correlations and the Diffusion Equation	78
5.7	Disagreement with Stochastic Theory	81
Chapter 6 Numerical Simulations		83
6.1	Numerical Method for Discretizing White-Noise	83
6.2	Difference Equations	86
6.2.1	Linearized “Spatio-Adiabatic” Equations	86
6.2.2	“Spatio-Adiabatic” Equations	87
6.3	Avoiding Negative Subcortical Inputs	93
6.4	von Neumann Stability Analysis	94
6.5	Boundary Conditions	99
6.6	Examples of h_e time-series	100
Chapter 7 Properties of the “Spatio-Adiabatic” Macrocolumn		101
7.1	Altering the Strength of the $e-e$ Diffusivity Relative to the $e-i$ Diffusivity	101
7.2	Correlation Length	102
7.2.1	Theoretical Predictions of Correlation Length for $c_3 > 0$	104
7.2.2	Zero-lag Covariance	105
7.3	Covariance Agreement with Numerical Simulations	111
7.3.1	Nonlinear Spatio-Adiabatic Simulations Near Equilibrium	111
7.3.2	Linearized Spatio-Adiabatic Simulations Near Equilibrium	113
7.4	Theoretical Predictions of Covariance and Numerical Agreement for $c_3 < 0$	114
7.5	Stability of the Homogeneous Steady-State	116
7.6	Formation of Nonequilibrium Steady-States	118
Chapter 8 Power Spectra of Linearized Spatio-Adiabatic Equations		127
8.1	Theoretical Power Spectrum of Stationary Stochastic Processes	127
8.2	General Power Spectrum $S(q, \omega)$	128
8.3	Power spectrum for $q = 0$	131
8.4	Power Spectrum including Spatial Variation	131
8.5	Power Spectrum Predictions and Numerical Agreement	136

Chapter 9	Conclusions and Future Work	145
9.1	Overview	145
9.1.1	Diffusion Equation	145
9.1.2	Numerical Simulation of the “Spatio-Adiabatic” Equations	146
9.1.3	Theoretical Predictions	146
9.1.4	Formation of Nonequilibrium States	147
9.2	Further Work	147
Appendix A	Summary of MATLAB Code Used	149
References		151

List of Figures

2.1	Schematic view of a typical neuron	6
2.2	Release of neurotransmitters at a chemical synapse	8
3.1	Schematic representation of a macrocolumn	12
3.2	Excitatory and inhibitory neurons viewed via Golgi stain	13
3.3	Golgi stain showing parallel alignment of excitatory dendrites	14
3.4	Hodgkin and Huxley equivalent circuit of a neuron	15
3.5	Equivalent circuit for excitatory and inhibitory average neurons	16
3.6	Equivalent circuit of a macrocolumn showing local feedbacks	17
3.7	Lumped equivalent circuit for the full Liley equations	19
3.8	Sigmoid functions relating average firing rate to soma potential	24
3.9	Time-evolution of an inhibitory post-synaptic potential	25
3.10	Isocline intersections used to locate the macrocolumn steady-state	30
3.11	Model prediction for stationary states	31
3.12	Post-synaptic potentials for the Liley and adiabatic equations	32
3.13	Stationary states of the macrocolumn separated into three regions	35
4.1	Turing structures produced with the CIMA chemical reaction	38
4.2	Schematic diagram of the 10/20 EEG electrode positioning system	62
5.1	Discretized representation of a delta spike	69
5.2	Plot of a temperature spike diffusing along a rod	70
5.3	Diffusion of a delta spike for different grid spacings	71
5.4	Error profile for diffusion simulations using grid spacings 1 and 2 cm	72
5.5	Decay of peak of delta spikes illustrating effect of truncation error	74
5.6	Discretized (triangle) representation of spatial white noise	75
5.7	Effect of changing the grid spacing for an initial-condition spike constant	77
5.8	Diffusion process with noise for grid spacings of 1 cm and 4 cm	79
5.9	Spatial correlations for two diffusion simulations	80
6.1	Stability of linearized difference equations for $\lambda_{\text{GABA}} = 0.3$ top-branch	98
6.2	Stability of linearized difference equations for $\lambda_{\text{GABA}} = 1.31$ top-branch	98
6.3	Simulated EEG times-series	100
7.1	Theoretical predictions for correlation lengths	103
7.2	Theoretical covariance curves at an anaesthetic effect of $\lambda_{\text{GABA}} = 1$	103

7.3	Theoretical covariance predictions along the top-branch	104
7.4	Theoretical covariance predictions along the bottom-branch	106
7.5	Top-branch theoretical zero-lag covariance	107
7.6	$\lambda_{\text{GABA}} \rightarrow 0$ region of top-branch theoretical zero-lag covariance	108
7.7	Bottom-branch theoretical zero-lag covariance	109
7.8	$\lambda_{\text{GABA}} \rightarrow 20$ region of the bottom-branch theoretical zero-lag covariance	110
7.9	Covariance predictions and stochastic results for nonlinear equations	112
7.10	Covariance curve showing “hump”, indicating cortical-rod is too short	113
7.11	Covariance predictions and simulation results for linear equations	114
7.12	Unstable covariance curve for formation of steady-states	115
7.13	Eigenvalue stability analysis	116
7.14	Example of long-lived eigenmode	120
7.15	Example of long-lived out-of-phase modes	121
7.16	System moving from unstable top-branch to stable bottom-branch	122
7.17	Simulation showing the emergence of nonequilibrium steady-states	123
7.18	Emergence of nonequilibrium steady-states for factor $f = 1.2$ at $\lambda_{\text{GABA}} = 4$	124
7.19	Distribution of nonequilibrium steady-states for factor $f = 1.2$ at $\lambda_{\text{GABA}} = 4$	125
8.1	Contour of integration (circling the two poles p_{c1} and p_{c2}) in the complex plane. Adapted from Spiegel (1974)	133
8.2	Theoretical and numerical power spectra	137
8.3	Top-branch analytic spectra for the linearized spatio-adiabatic equations	138
8.4	Bottom-branch analytic spectra of the linearized spatio-adiabatic equations	139
8.5	Top-branch analytical spectra in the region $\lambda_{\text{GABA}} = 0.3 \rightarrow 0$	139
8.6	Top-branch analytical spatial spectra $S(q)$	140
8.7	Bottom-branch analytical temporal spectra $S(\omega)$ in region $\lambda_{\text{GABA}} \rightarrow 20$	142
8.8	Bottom-branch analytical spatial spectra $S(q)$ for the region $0 < \lambda_{\text{GABA}} < 20$ using log scale	142
8.9	Bottom-branch analytical spatial spectra $S(q)$ in the region $\lambda = 20$	143

List of Tables

3.1	Definitions and constants for Liley model	21
-----	---	----

Acronyms and Abbreviations

1-D	one-dimensional
CIMA	chlorite iodide malonic acid-starch (a type of chemical reaction)
DE	differential equation
EEG	electroencephalogram (brain activity recorded via scalp electrodes)
EPSP	excitatory postsynaptic potential
DFT	discrete Fourier transform
FTCS	forward-time centered-space scheme
GABA	γ -aminobutyric acid (an inhibitory neurotransmitter)
IPSP	inhibitory postsynaptic potential
LOC	loss of consciousness
ODE	ordinary differential equation
OU	Ornstein–Uhlenbeck (random process describing the velocity of a Brownian particle)
PDE	partial differential equation
PSP	postsynaptic potential
SWS	slow-wave sleep
REM	rapid eye movement (used to specify a type of sleep)
RMS	root-mean square
ROC	return of consciousness

Introduction

In 1997 the Waikato cortical modelling group (Dr Moira Steyn-Ross, Dr Alistair Steyn-Ross and Prof Jamie Sleight) began developing a mean-field model for anaesthesia in the human cerebral cortex. Their ambition was to craft a theory that describes the changes in electrical activity that occur in the cortex as a person is rendered anaesthetically unconscious. Their model predicts that the cortex can only exist in either a highly disordered conscious state, or a more ordered unconscious state. For an initially conscious patient, the model predicts that as anaesthetic concentration is increased, a critical concentration will be reached at which the cortex undergoes a sudden phase transition, from the conscious state to the unconscious state. The loss of consciousness is *sudden* and not a gradual descent.

This predicted change in state is analogous to water freezing. When water is sufficiently cooled it forms ice. The transition from liquid water to solid ice happens abruptly and, in general, there is no well-defined intermediate state.

How anaesthetics “shut down” the brain is not well understood. To our knowledge the Waikato model is the only theoretical physics-based theory of the cortex to include the effect of anaesthetics.

A rigorous model that could be used to accurately determine when a patient is unconscious would be very beneficial to public health and well-being, for any procedures requiring general anaesthetics.

Present-generation consciousness-monitoring devices can be inaccurate, reporting an awake patient as unconscious. However, the drugs used to induce unconsciousness are often complemented by muscle relaxant drugs designed to stop muscles “flinching” during surgery and have the effect of paralyzing the body. Due to this paralyzing effect, an awake patient thought to be unconscious cannot communicate the fact to the surgeon. Such a situation would undoubtedly be very traumatic. Furthermore, anaesthetics are known to cause loss of memory for the period

surrounding an operation. So, even if a person was aware during an operation they most likely would “forget” the experience before being able to report it.

1.1 Thesis Overview

When the initial Waikato cortical model was developed, in order to simplify the equations, Steyn-Ross *et al.* (1999) deliberately neglected the possibility of spatial variability among populations of connected neurons by assuming a spatially homogeneous cortex. More recently Steyn-Ross *et al.* have generalized their model to allow for spatial fluctuations within the cortex. The aim of this thesis is to investigate the simplest case of spatial variability, corresponding to a one-dimensional “line” of *continuous* macrocolumn “mass”. Initially I was given the task of numerically simulating the one-dimensional system, in order to compare the analytical and numerical spatial covariance curves. However, in doing so I discovered that the inclusion of space could lead to the possibility of nonequilibrium structures forming. I also determined analytically the power spectrum for the linearized one-dimensional system.

1.2 Thesis Structure

In Chapter 2 a brief review of the neurophysiology relevant to the model is given. The cerebral cortex, which consists of billions of neurons is introduced. I discuss the electrical activity generated by a typical neuron, as well as how a neuron maintains a potential difference across its membrane. How anaesthetics effect neurons is also reviewed.

Chapter 3 discusses how the physiological processes in the cortex can be mapped to mathematical formulas. The neural structure known as the macrocolumn is introduced, as well as the cortical models of Liley *et al.* (1998, 1999, 2002) and Steyn-Ross *et al.* (1999). Some detail of the construction of these models is given, and the identification of different states of the cortex by Steyn-Ross *et al.* is shown.

In Chapter 4 the model of Steyn-Ross *et al.* (2003), which includes the possibility of spatial variation in the cortex, is introduced. A chemical model named the Brusselator, which displays similar behaviour to the cortical model is reviewed. The Brusselator predicts that a system forced far from thermodynamic equilibrium can undergo a phase-change such that far-from-equilibrium dissipative structures or patterns can form spontaneously. Such patterns have been observed in a number of chemical reactions.

Theoretical spatial covariance functions for the cortex are derived. These Predict an increase in correlation length just prior to loss of consciousness, and ageing just prior to return of consciousness. The covariance function also predicts a general increase in spatial coherence for the unconscious state relative to the conscious state. The stability of the cortical system is investigated, leading to the prediction that spatial dissipative structures (Turing patterns) could form.

Chapter 5 reviews the classic heat diffusion equation. This was done in order to investigate how to discretize continuous spatial and temporal noise, and to serve as an intermediate step towards stochastic simulation of the one-dimensional cortex.

In Chapter 6 I examine how to simulate numerically the continuous one-dimensional model of the cortex. Three sets of difference equations are derived. These are used respectively to simulate (i) the linearized system, (ii) the nonlinear system near thermodynamic equilibrium and, (iii) the nonlinear system far from thermodynamic equilibrium.

In Chapter 7 I investigate the theoretical predictions for the covariance function and test the theory against numerical simulations. The stability of the linearised system is looked at and the formation of dissipative structures (nonequilibrium steady-states) is demonstrated.

In chapter 8 I calculate the analytic spectra for the linearised one-dimensional equations. I compare the simulation results with the analytic predictions, and explore a few peculiarities that arise in the cortical power spectrum.

1.3 Original Work

Chapter 1 is a summary of well-documented cortical processes. Chapter 2 is a summary of the work of Liley *et al.* (1998, 1999, 2002) and Steyn-Ross *et al.* (1999), containing one piece of original work showing that the area of the adiabatic PSP is identical to that for the full-equations. Chapter 4 is a review of the work done by Chaturvedi *et al.* (1977) and Steyn-Ross *et al.* (2003), with a small original contribution: I developed a method for linearizing systems with a Laplacian term, and apply this analysis to the Brusselator (for which I derived the spatial homogeneous steady-state) and also to the cortical model. I also approach the stability analysis differently to Steyn-Ross *et al.* (2003). Chapter 5 is a summary of the features of the diffusion equation. I wrote the code used, and also investigated driving the system with noise.

Via personal communication with Alistair Steyn-Ross and Lara Wilcocks, I determined how to accurately model spatio-temporal white-noise. The numerical schemes derived in Chapter 6 are original with me, although motivated by the methods of Wilcocks (2001). The MATLAB codes used here are a combination of original code plus code written by Steyn-Ross (2002) and Wilcocks (2001). The root-finding algorithms of Steyn-Ross were used to calculate the homogeneous steady-states of the cortex, while Wilcocks' code was almost completely rewritten to include spatial variability. The sections showing how to avoid negative subcortical inputs and how to discretely approximate spatio-temporal white-noise is a generalization, to include space, of the work done by Steyn-Ross (2002). The comparisons between numerical data and theoretical predictions in Chapter 7 is completely original with me. Likewise, the analysis of the analytical predictions is original work. Chapter 8 is completely original, while being based on similar work done by Wilcocks (2001).

Neurophysiology

2.1 The Cerebral Cortex

The human brain is one of the largest organs in the body (Tortora and Grabowski (1996)). It consists of four principal parts: the brain stem, cerebellum, diencephalon, and the cerebrum (the largest part). A 1–4 mm layer of grey matter known as the *cerebral cortex* makes up the external layer of the cerebrum. The cerebral cortex contains billions of neurons and is thought to be involved in many of the brain’s complicated processes such as memory, awareness, judgement, vision and consciousness.

A typical neuron (see Fig. 2.1) consists of a cell body (the soma), dendrites and an axon. The dendrites are usually short, highly branched structures that probe outwards from the cell body. The primary role of a dendrite is to sample its environment, receiving inputs from surrounding neurons. Axons are long, thin cylindrical structures that extend out from the cell body and end in a branched configuration. Each neuron has a single axon that sends out information (nerve pulses) from the cell body into the surrounding neural mass.

Neurons interact with each other via electrical and chemical signals. The fluid contained within a neuron’s soma (intracellular fluid) has different concentrations of ionic species compared to the extracellular fluid surrounding the neuron. This ionic concentration difference causes a potential difference to be generated across a neuron’s membrane. When measuring the transmembrane voltage, it is common practice to use the extracellular ionic “sea” as the reference point defining zero potential. When the voltage difference across a neuron’s membrane rises above (becomes more positive than) a threshold value (approximately -60 mV), the neuron generates a pulse of voltage (it fires) called an *action potential*. After the neuron fires, it quickly returns to its resting potential (~ -70 mV). The action potential travels along the neuron’s axon, which connects to other neurons within the cerebral cortex. These connections, known

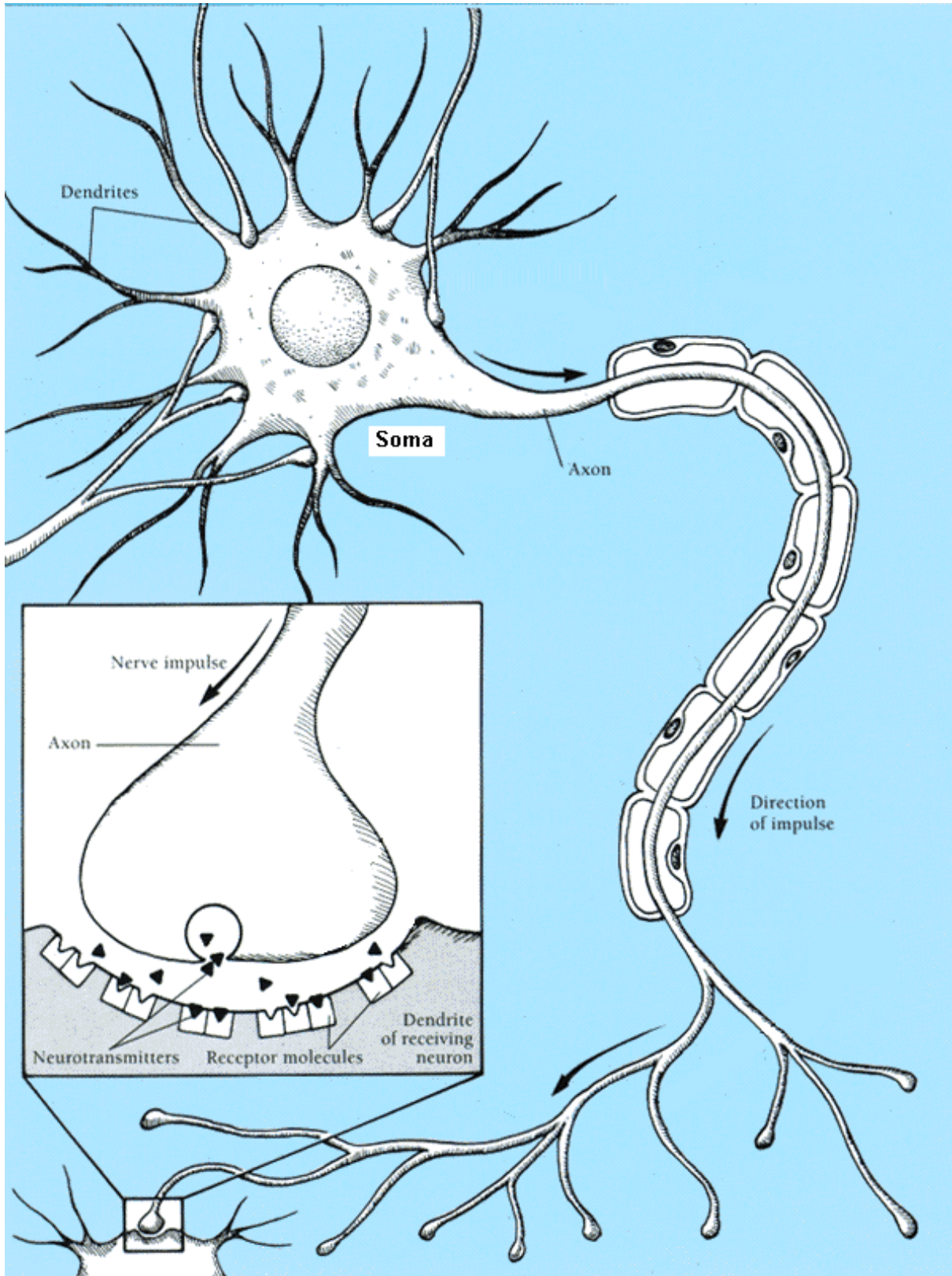


Figure 2.1: Diagram showing a “white matter” neuron, consisting of a soma with dendrite and axon extensions. An action potential, generated in the presynaptic neuron, propagates down the axon until it reaches the end of one of the axon’s branches. At this point neurotransmitters are released into the synaptic gap, causing ion gates to be opened in the postsynaptic neuron. Note, the “white matter” neuron shown here has a fatty coat (myelin) surrounding the axon, while a cerebral cortex or “grey matter” neuron lacks this feature. [Source: <http://www.pfizer.com/brain/dlgame.html>]

as *synapses*, are located at the junctions between axon and dendrite, axon and soma, and axon and axon (Tortora and Grabowski (1996)).

Depending on the type of presynaptic neuron, its firing can have the effect of either *hyperpolarising* or *depolarising* the postsynaptic neuron. Hyperpolarisation occurs when an input potential makes the membrane more negative (less likely to fire), and depolarisation occurs when a potential input makes the membrane less negative (more likely to fire). It is believed the cerebral cortex consists of 85% depolarising (excitatory) neurons and 15% hyperpolarising (inhibitory) neurons (Braitenberg and Schüz (1991)). A typical neuron receives inputs from hundreds of neurons throughout the cortex. The summation of all of these synaptic inputs at a given instant determines whether or not a given neuron will fire.

Neurons in the cerebral cortex communicate with each other by electrochemical impulses passed from one neuron to another at a chemical synapse. At a chemical synapse the two membranes are very close together but do not touch. This gap is known as a synaptic cleft. The action potential cannot jump this gap but somehow needs to be relayed to the postsynaptic neuron. This is achieved by chemicals known as neurotransmitters. When the electrical pulse from the presynaptic neuron reaches the synaptic cleft, the signalling neuron releases a neurotransmitter that diffuses across the gap and acts on the receptors of the postsynaptic neuron (see Fig. 2.1). The received neurotransmitters cause a postsynaptic potential that depolarises (produces an excitatory postsynaptic potential at) or hyperpolarises (produces an inhibitory postsynaptic potential at) the receiving neuron. The type of potential generated depends on the type of presynaptic neuron. The neurotransmitters act by opening specific gated ion channels, allowing selected ions to diffuse across the membrane.

2.2 Resting and Nernst Potential

The four most important ionic species in a neuron's intracellular and extracellular fluid are: sodium (Na^+), potassium (K^+), chloride (Cl^-) and calcium (Ca^{2+}). Neurons are said to be at *rest* if they are not receiving any stimuli from other neurons. A neuron at *rest* has a non-zero membrane potential due to the intracellular and extracellular fluid containing different concentrations of ions.

The cell membrane is permeable to ions. Of importance here is that the permeability is different for different ions. The permeability of K^+ is 50 to 100 times greater than that of Na^+ , for example. Relative to the extracellular fluid, the intracellular fluid has an excess of K^+ and a

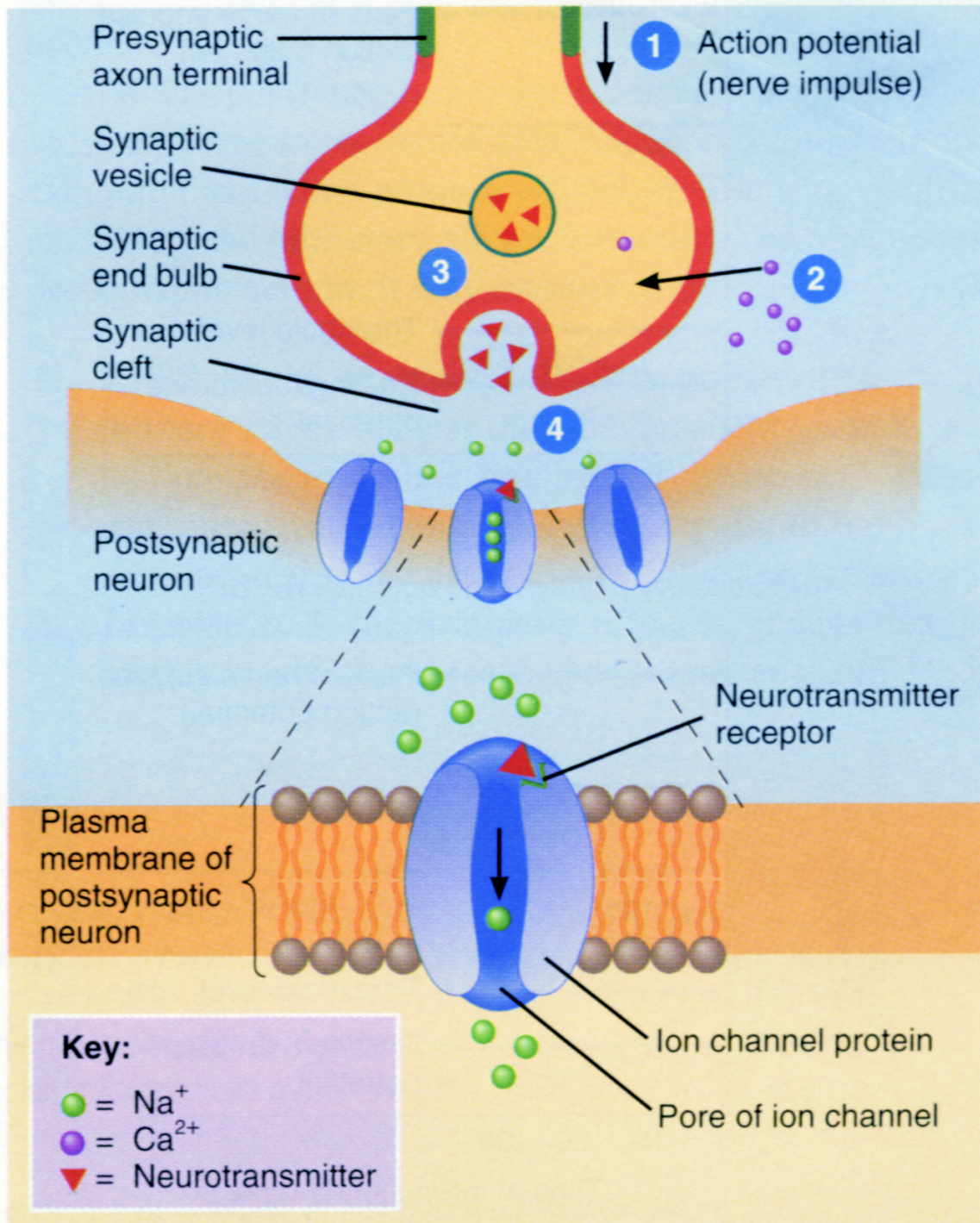


Figure 2.2: At a chemical synapse an action potential causes the release of neurotransmitters that bind to the receptors of the postsynaptic neuron [From Tortora and Grabowski (1996)]

deficit of Na^+ . If potassium ions diffuse out of the cell due to the chemical gradient, the interior of the cell will become more negative, eventually causing K^+ to be drawn back into the cell. If the membrane was only permeable to potassium, an internal membrane potential of -90 mV (relative to the extracellular ionic sea) would just balance the concentration difference. This is known as the *potassium equilibrium potential* (or *potassium Nernst potential*).

As a neuron's membrane is permeable to Na^+ , K^+ and Cl^- ions, if the ionic concentration difference between the extra- and intra-cellular fluid were not maintained, the electrochemical gradients would eventually run down. In order to maintain the ionic concentration imbalance, *sodium-potassium pumps* remove sodium as fast as it enters the intracellular fluid and at the same time brings in potassium (for every three Na^+ ions expelled, two K^+ ions are brought in). Using the ionic concentration differences, the relative Nernst potentials, and correct permeability factor, the resting potential can be calculated to be approximately -70 mV (Stein-Ross (2002)). This value describes the “average” neuron, whereas in reality the resting membrane potential for an individual neuron could lie anywhere in the range -40 to -90 mV .

2.3 The Cerebral Cortex and Anaesthetics

As well as the membrane being permeable to certain ions, it contains *gated channels* which open and close in response to neurotransmitters. An inhibitory neurotransmitter, known as GABA (gamma aminobutyric acid), has the effect of opening chloride channels, allowing an influx of Cl^- ions thereby hyperpolarising the postsynaptic neuron. It is thought that anaesthetics work by *increasing* the duration of the chloride gate opening (Franks and Lieb (1997)). This means that postsynaptic neurons will be hyperpolarised for longer, and hence less likely to fire. Evidently, by reducing the number of neurons firing in the cerebral cortex, an anaesthetist is able to induce a state of unconsciousness in the patient.

Cortical Modelling

3.1 The Macrocolumn

The cerebral cortex contains billions of neurons that control consciousness and other vital functions of the human brain. Modelling the electrical processes of every neuron in the cortex would be an impossible task. It is believed that neurons in the cortex operate with a certain degree of cooperation: groups of closely-spaced neurons (neural masses) act in a cooperative and organized fashion. Using this assumption the brain is often modelled using *mean-field* theories. Mean-field theories model neural masses as single entities whose properties are determined from the spatial average of all the neurons within the mass.

The mean-field approach has been used for the past 50 years to model the electrical behaviour of the cerebral cortex: Beurle (1956); Wilson and Cowan (1972, 1973); Freeman (1975); Nunez (1974, 1981); Rotterdam *et al.* (1982); Wright and Liley (1996); Robinson *et al.* (1997, 1998); Jirsa and Haken (1996, 1997); Steyn-Ross *et al.* (1999).

Throughout this thesis we make use of a mean-field theory that refers to the electrical activity of a neural mass known as a *macrocolumn*. A macrocolumn is a cylindrical column of organized excitatory and inhibitory neural cells acting cooperatively inside the cortex. A macrocolumn has a diameter of $\sim 0.3\text{--}1$ mm and contains 40,000–100,000 neurons. Excitatory (pyramidal) cells make up $\sim 85\%$ of the total number of neurons (Braitenberg and Schüz (1991)). A schematic representation of a macrocolumn is shown in Fig. 3.1.

3.2 The Cerebral Cortex and the EEG

The electrical activity in the cerebral cortex can be indirectly measured by electrodes placed on the scalp. The data recording is called an *electroencephalogram* (EEG). This EEG signal originates from electrical activity generated from the longitudinal flow of current that arises due to the particular structure of the excitatory neurons within macrocolumns of the cerebral cortex.

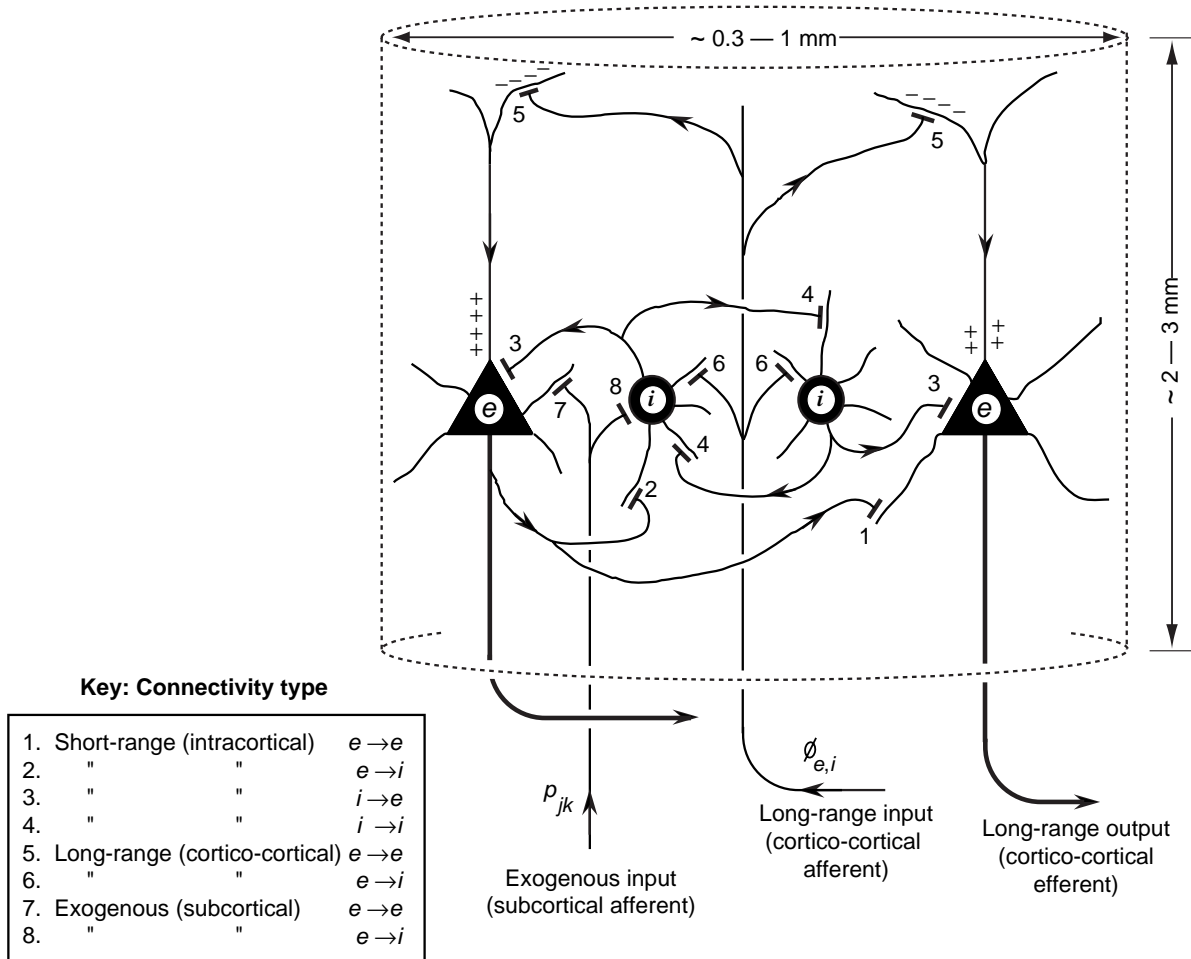


Figure 3.1: Schematic representation of a macrocolumn. Triangles are excitatory neural cells, while circles represent inhibitory neural cells. [From Steyn-Ross *et al.* (1999)]

The structure of the excitatory and the inhibitory neurons is fundamentally different (see Fig. 3.2; an inter-neuron is a type of inhibitory neuron). Excitatory neurons have long parallel dendrites (see Fig. 3.3) that align perpendicular to the surface of the cortex and co-axial with the macrocolumn, so the potential that arises at the cortical surface, due to the excitatory synaptic activity, can be approximated by a current dipole term.

In contrast, inhibitory neurons are smaller and have their dendrites extending out with an approximately spherical distribution. This spherical symmetry leads to a much smaller dipole term, and hence the inhibitory neuron's field at the cortical surface is vanishingly small. Because of these factors, the local field potential at the cortical surface, and hence the scalp EEG, is proportional to the spatially-averaged soma membrane potential of the excitatory neurons in the cortex (Liley *et al.* (2002)).

By modelling the fluctuations of the excitatory membrane potential, we can make comparisons between theory and the experimentally acquired EEG. In order to understand how a model

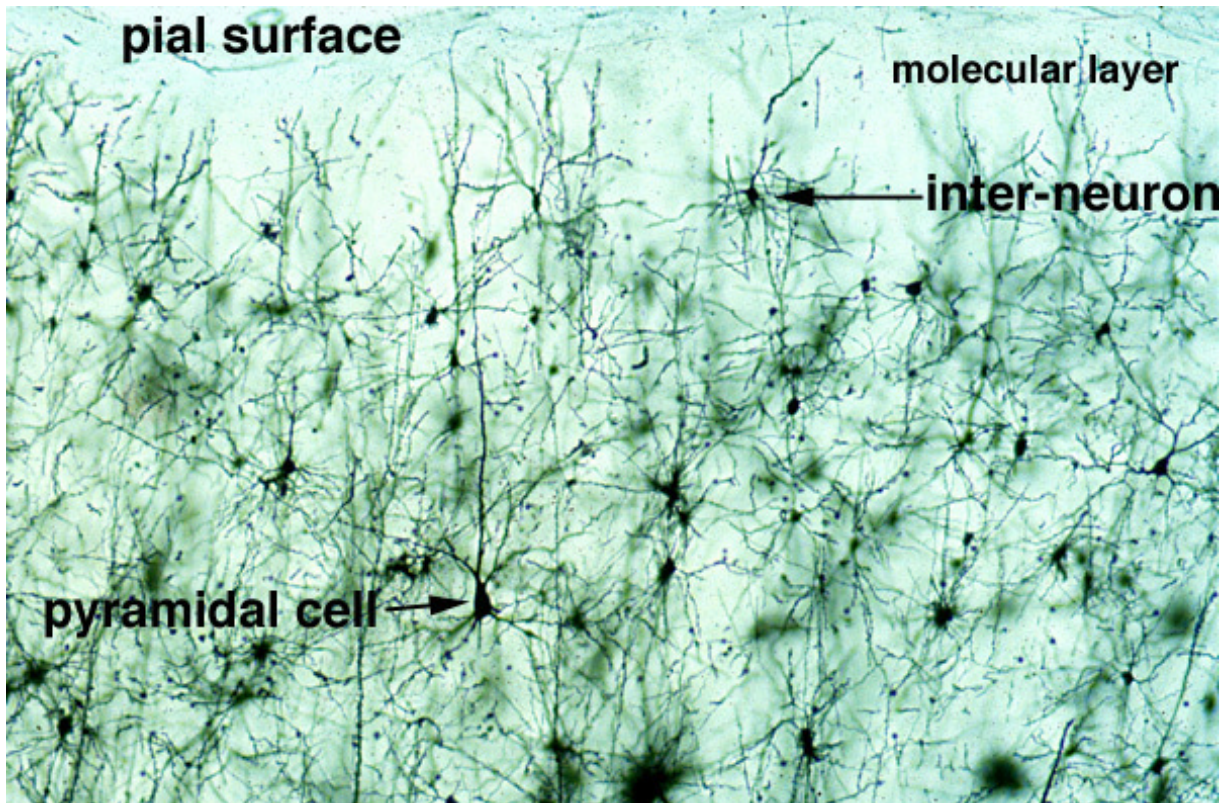


Figure 3.2: Photomicrograph of a *Golgi stained* slice of a cat's cerebral cortex. The Golgi preparation randomly stains 1 – 2 percent of the neurons in a slice of neural mass. If all the neurons were stained it would be impossible to make out individual neurons. This photomicrograph shows the structural difference between a pyramidal (excitatory) and an inter- (inhibitory) neuron. Pyramidal nerve cells have long dendrites that are aligned axial to the cortical surface while the inter-neuronal cell's dendrites are randomly distributed with approximate spherical symmetry. [Source: <http://www.medinfo.ufl.edu/year1/neurosci/histo/>]

for the cortex is derived, I will follow Steyn-Ross (2002) in reviewing how the modelling of a single neuron can be scaled up to give a mean-field theory describing populations of cooperating neurons.

3.3 Neural Circuits

A neuron can be modelled by an equivalent circuit as follows: The constant flow of ions between a neuron's extracellular and intracellular fluid can be modelled as a battery; the membrane can be modelled via variable conductances and a capacitor. These variable conductances take into account the stimulated opening and closing of gated ion channels. Hodgkin and Huxley (1952) used the equivalent circuit of Fig. 3.4 to model the ion channels within a single neuron (Tuckwell (1988a)). Because their equations accurately described the formation of a neuron's action potential, Hodgkin and Huxley were awarded a Nobel prize in 1963 for their work.

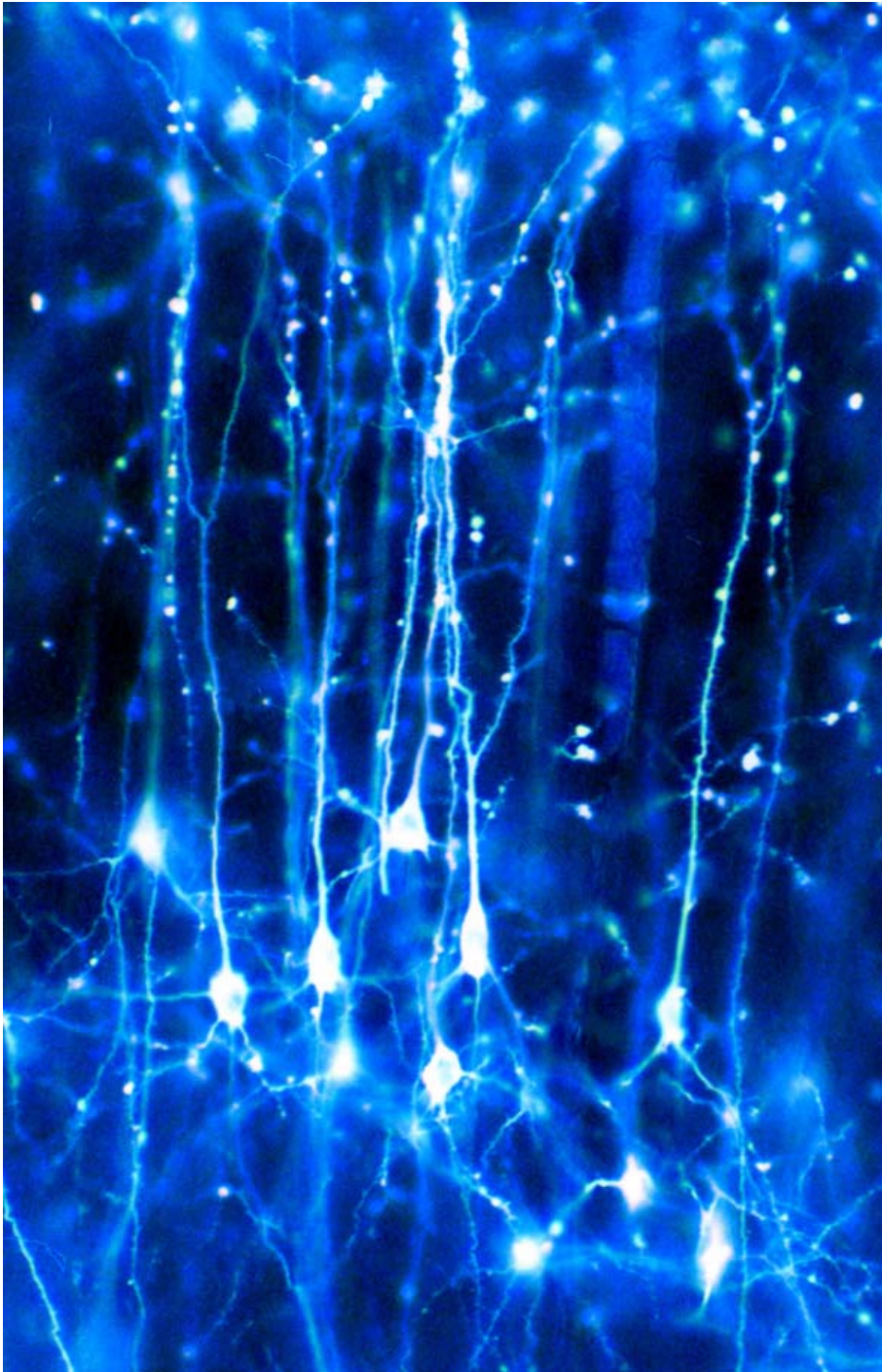


Figure 3.3: A Golgi stained slice of cortex showing how dendrites of excitatory neurons are aligned parallel to each other. [From: <http://www.anat.ucl.ac.uk/research/clarke-group/gallery.html>]

Hogkin and Huxely modelled the electrical dynamics of a single neuron. In contrast, the model investigated in this thesis uses a mean-field approach. The starting point is the mean-field theory developed by Liley *et al.* (1998, 1999, 2002) that attempts to model the EEG generated by millions of neurons contained within the cerebral cortex. Liley *et al.* use a mean-field picture that describes the fluctuating potential of *populations* of excitatory and inhibitory neurons contained within a macrocolumn. Because the Liley “neurons” are spatial averages, it would not be sensible

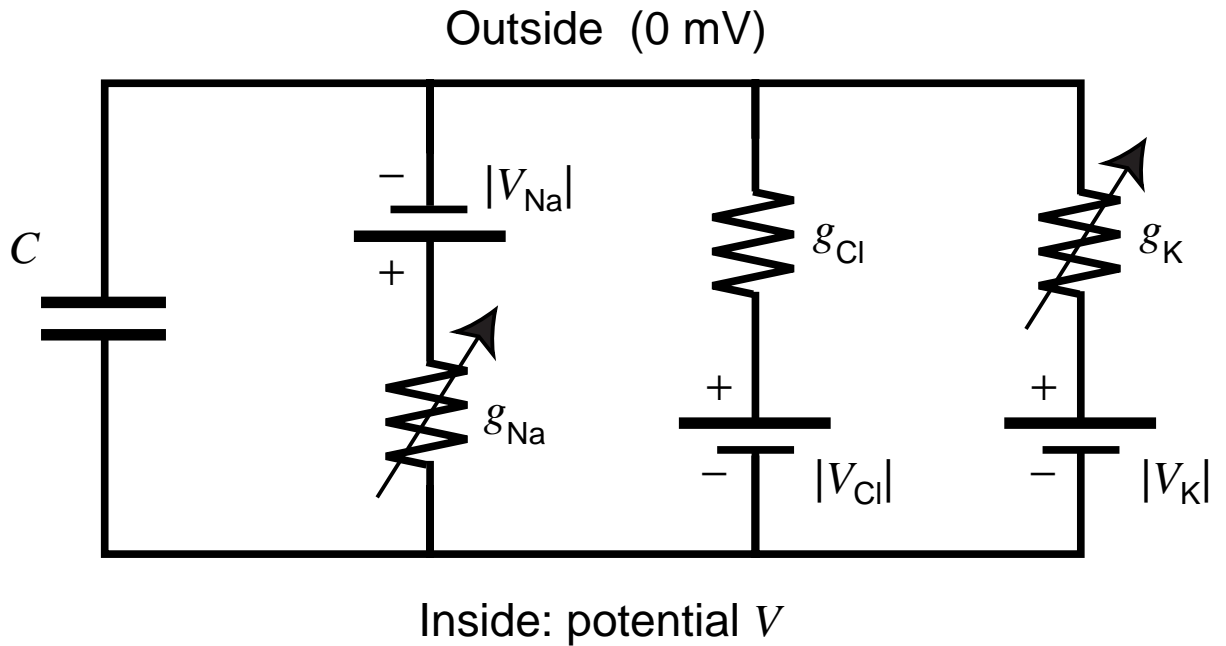


Figure 3.4: Hodgkin and Huxley equivalent circuit of a neuron, used to model the formation of an action potential. The g_{Na} and g_K variable conductances are voltage- and time-dependent, while the g_{Cl} conductance is fixed. When a neuron fires, voltage-gated sodium channels open, increasing sodium conductance and inward sodium current, which depolarizes the membrane. After a delay, potassium channels begin to open, and, at the same time, sodium channels close. The outwards flow of potassium ions restores the membrane to its resting potential and the potassium channels close. [Source of graphic: Steyn-Ross (2002)]

for these “neurons” to fire (produce a grossly-coordinated action potential). Of note here is that action potentials are never seen in scalp-measured EEGs. This is because action potentials have very fast rise and fall times that are strongly low-passed filtered by cerebrospinal fluid, skull, and scalp tissue that lies between the brain surface and the scalp electrode (Steyn-Ross (2002)). As the Liley “neurons” never fire, we can approach them as generalizations of the Tuckwell subthreshold neuron (Tuckwell (1988b)).

Tuckwell produces an equivalent circuit of a *subthreshold* neuron by modelling a *resting* neuron coupled with synaptic inputs. For the *resting* neuron, its sodium, chloride, and potassium batteries, and their associated conductances, are replaced by a single battery V_{rest} in series with a constant resting conductance g_{rest} (not variable as the neuron never fires). For simplicity it is assumed that there are only two ion species involved in mediating the synaptic inputs, one for the excitatory inputs, and another for the inhibitory inputs. Each synaptic input is then modelled by a synaptic *reversal potential* (set equal to the Nernst potential of the relevant ion), and a variable conductance. The circuit for the two Tuckwell neurons, representing Liley’s population average excitatory and inhibitory neurons appears in Fig. (3.5).

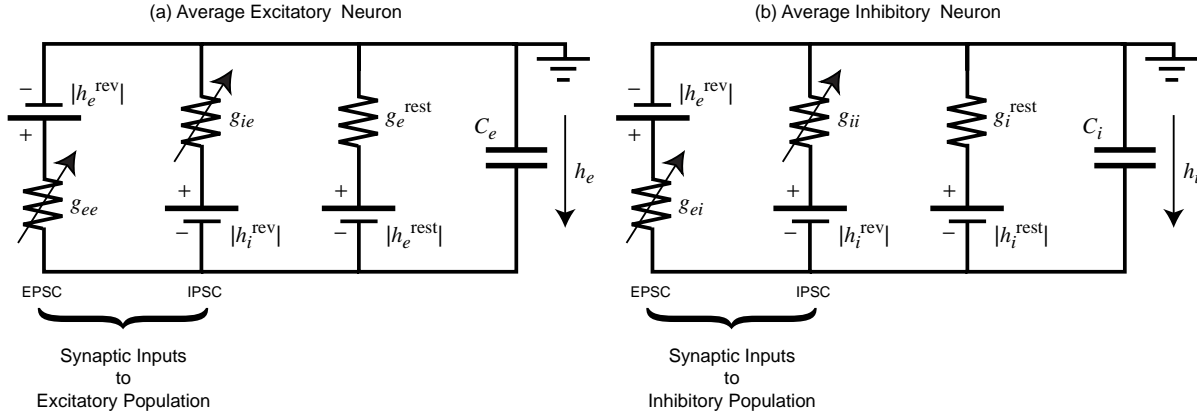


Figure 3.5: Equivalent circuit for the (a) excitatory and (b) inhibitory neural populations modelling the macrocolumn of Fig. 3.1. This is the Liley generalization of the Tuckwell subthreshold neuron. [Source: Steyn-Ross (2002)].

The equations of motion for $h_{e,i}$ in Fig. 3.5 are,

$$C_e \frac{dh_e}{dt} = (h_e^{\text{rev}} - h_e)g_{ee} + (h_i^{\text{rev}} - h_e)g_{ie} + (h_e^{\text{rest}} - h_e)g_e^{\text{rest}} \quad (3.1)$$

$$C_i \frac{dh_i}{dt} = (h_e^{\text{rev}} - h_i)g_{ei} + (h_i^{\text{rev}} - h_i)g_{ii} + (h_i^{\text{rest}} - h_i)g_i^{\text{rest}} \quad (3.2)$$

where the variables are defined as,

h_e, h_i	excitatory and inhibitory membrane voltages
h_e^{rev}	excitatory reversal potential = +45 mV
h_i^{rev}	inhibitory reversal potential = -90 mV
$h_e^{\text{rest}}, h_i^{\text{rest}}$	resting potential = -70 mV
C_e, C_i	membrane capacitance
g_{ee}, g_{ie}	conductance for excitatory-reversal battery
g_{ei}, g_{ii}	conductance for inhibitory-reversal battery
$g_e^{\text{rest}}, g_i^{\text{rest}}$	conductance for resting-potential battery

In the *absence* of synaptic inputs, a pair of membrane time-constants can be defined,

$$\tau_e = C_e / g_e^{\text{rest}} \quad (3.3)$$

$$\tau_i = C_i / g_i^{\text{rest}} \quad (3.4)$$

The time-constants defined in Eqs. (3.3–3.4) give the time for a perturbation in $h_{e,i}$ to decay back to the resting potential $h_{e,i}^{\text{rest}}$. With synaptic inputs coupled in, these time-“constants” will be approximately constant or will become membrane-voltage dependent, depending on the frequency of the synaptic events.

Following Liley, τ_e and τ_i are assumed to be constant. If we divide Eqs. (3.1–3.2) through by g_e^{rest} , g_i^{rest} and rearrange, we obtain,

$$\tau_e \frac{dh_e}{dt} = (h_e^{\text{rest}} - h_e) + (h_e^{\text{rev}} - h_e) \frac{g_{ee}}{g_e^{\text{rest}}} + (h_i^{\text{rev}} - h_e) \frac{g_{ie}}{g_e^{\text{rest}}} \quad (3.5)$$

$$\tau_i \frac{dh_i}{dt} = (h_i^{\text{rest}} - h_i) + (h_e^{\text{rev}} - h_i) \frac{g_{ei}}{g_i^{\text{rest}}} + (h_i^{\text{rev}} - h_i) \frac{g_{ii}}{g_i^{\text{rest}}} \quad (3.6)$$

These equations of motion are essentially the same as the first two equations in the Liley set

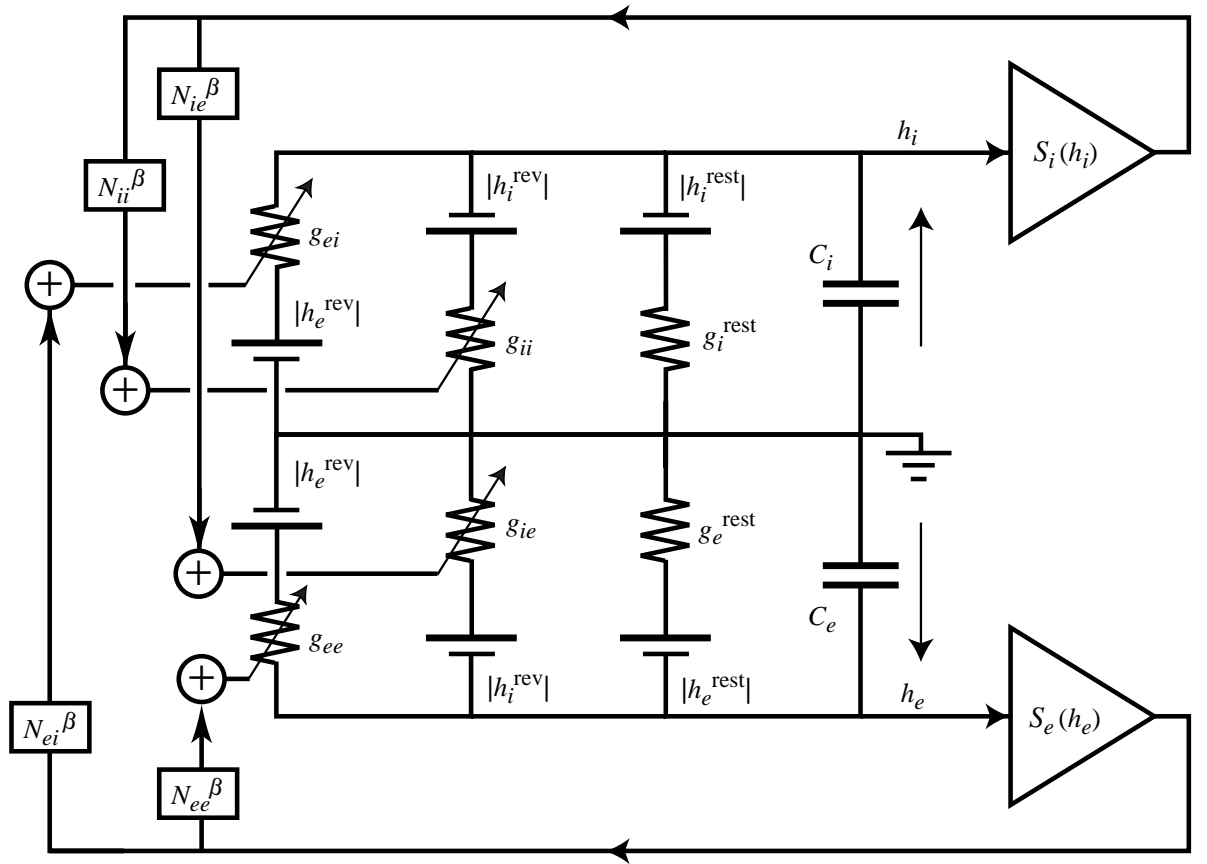


Figure 3.6: Equivalent circuit for the Liley macrocolumn with local feedbacks explicitly shown. The excitatory and inhibitory output voltages $h_{e,i}$ are coupled back to the four g_{jk} synaptic input conductances via a pair of nonlinear voltage-to-spike-rate converters by the $S_e(h_e)$ (lower) and $S_i(h_i)$ (upper) triangles. The four N_{jk}^β boxes are constant multiplicative scale-factors that represent the number of *local* interconnections between the excitatory and inhibitory populations within the macrocolumn. All possible local feedbacks are allowed: $e \rightarrow e$, $e \rightarrow i$, $i \rightarrow e$, $i \rightarrow i$. [Source: Steyn-Ross (2002)]

Eq. (3.7) (introduced shortly). For example, Liley uses the product $\psi_{ee}(h_e)I_{ee}(h_e)$ to represent the excitatory synaptic input to an excitatory “neuron”. Here, $\psi_{ee}(h_e)$ is a weighting factor and $I_{ee}(h_e)$ is the synaptic input voltage. Writing $\psi_{ee}(h_e)I_{ee}(h_e)$ out in full, we have,

$$\begin{aligned}\psi_{ee}(h_e)I_{ee}(h_e) &= \frac{h_e^{\text{rev}} - h_e}{|h_e^{\text{rev}} - h_e^{\text{rest}}|} I_{ee}(h_e) \\ &= (h_e^{\text{rev}} - h_e) \frac{I_{ee}(h_e)}{|h_e^{\text{rev}} - h_e^{\text{rest}}|} \\ &= (h_e^{\text{rev}} - h_e) \frac{g_{ee}(h_e)}{g_e^{\text{rest}}}\end{aligned}$$

Liley has used the fact that an incremental change in a synaptic conductance g_{jk} is directly proportional to the resulting change in the soma voltage, where the change in soma voltage is determined by the relevant synaptic input.

The two circuits in Fig. 3.5 are strongly coupled. In the Liley model there are only two “neurons” per macrocolumn. A macrocolumn consists of 40000-100000 neurons and has various neural connections, as shown in Fig. 3.1. In order to include the short-range connections, Liley includes feedback terms in the equivalent neural circuits. The feedback term models the spatially-averaged effect of short-range neural activity arriving at the synaptic input receptors. This term is calculated using an idea from Wilson and Cowan (1972): that there exists a nonlinear sigmoidal (Eq. 3.23) mapping from soma voltage (input) to average firing rate (output). Figure 3.6 shows how the excitatory and inhibitory “neurons” are coupled together via feedback terms.

Liley adds subcortical spike inputs, then links macrocolumns together via long-range (cortico-cortical) connections. A lumped equivalent circuit for the full Liley equations is shown in Fig. 3.7. The equations of motion for the Liley model are described in the following section.

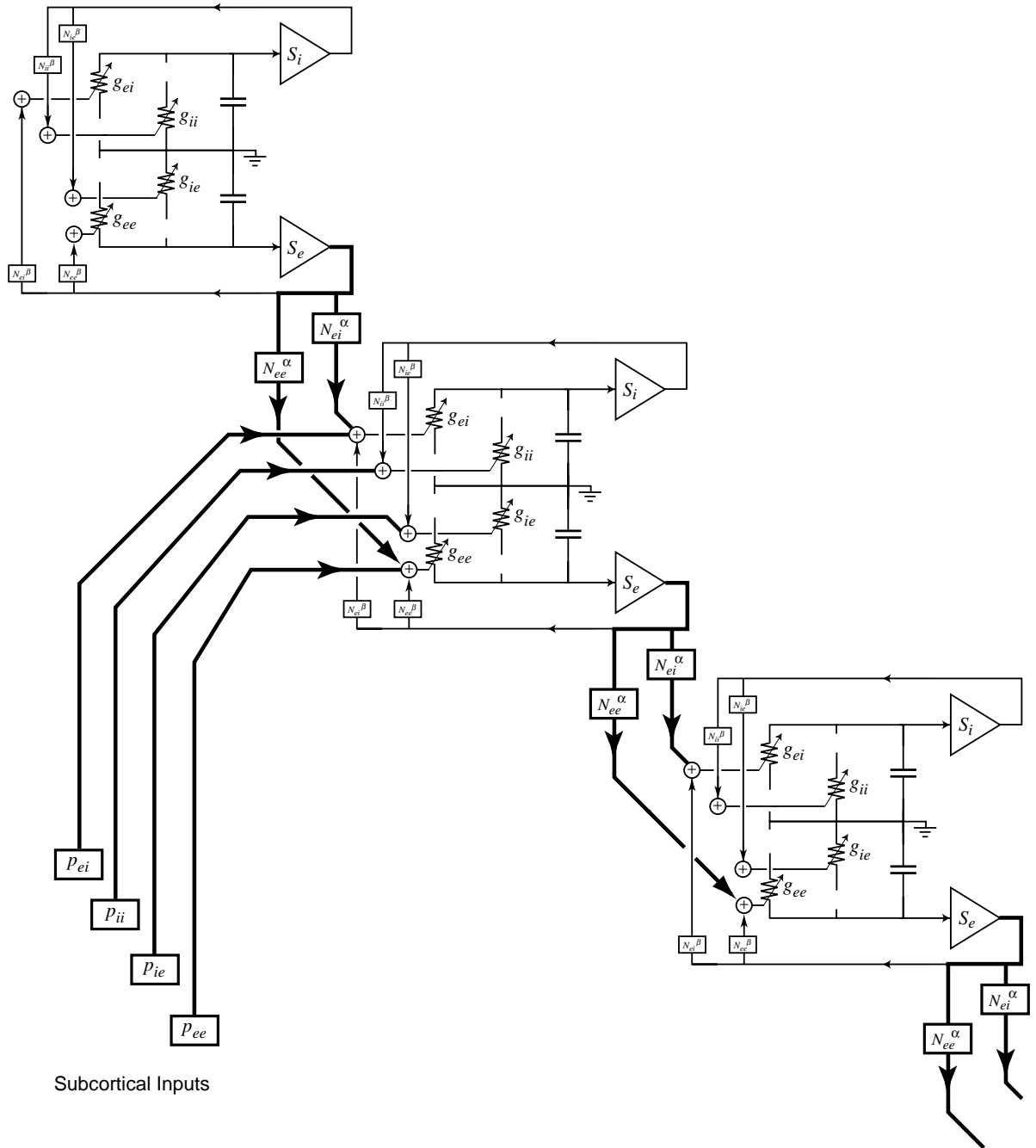


Figure 3.7: Lumped equivalent circuit for the full Liley equations. The cerebral cortex is pictured as a 1-D chain of discrete macrocolumns. Each macrocolumn is connected to its neighbour via their excitatory sigmoid outputs. The Liley model is the continuum limit of this picture, which forms a 1-D line of macrocolumn “mass”. The dynamics of the inter-macrocolumn connections is governed by a pair of 1-D wave equations. In addition, every macrocolumn receives excitatory and inhibitory p_{jk} exogenous inputs coming up from the subcortex. All inputs (local, distant, and external), are combined at the \oplus summing points to determine the g_{jk} synaptic conductances. The resulting synaptic currents are integrated at the soma capacitor to give a soma voltage h_k ($k = e, i$). To aid clarity, the “batteries” (reversal and resting) have not being included. The complete schematic would also show independent p_{jk} subcortical inputs entering *every* macrocolumn, rather than just the middle one. [Source: Steyn-Ross (2002)]

3.4 The Liley Equations

The model studied in this thesis is the Steyn-Ross *et al.* (1999) adaption of the Liley *et al.* (1999) cortical equations. The Liley equations are one-dimensional and use mean-field theory in order to describe the fluctuations of the excitatory and inhibitory soma voltage. They model the time evolution of the soma voltages and synaptic inputs illustrated in Fig. 3.7, and will be referred to as the Liley equations throughout the rest of this thesis. The Liley equations consist of the following eight coupled differential equations:

$$\tau_e \frac{\partial h_e}{\partial t} = (h_e^{\text{rest}} - h_e) + \psi_{ee}(h_e)I_{ee}(h_e) + \psi_{ie}(h_e)I_{ie}(h_i) \quad (3.7)$$

$$\tau_i \frac{\partial h_i}{\partial t} = (h_i^{\text{rest}} - h_i) + \psi_{ei}(h_i)I_{ei}(h_e) + \psi_{ii}(h_i)I_{ii}(h_i) \quad (3.8)$$

$$\left(\frac{\partial}{\partial t} + \gamma_e\right)^2 I_{ee}(h_e) = [N_{ee}^\beta \mathcal{S}_e(h_e) + \phi_e(h_e) + p_{ee}]G_e \gamma_e e \quad (3.9)$$

$$\left(\frac{\partial}{\partial t} + \gamma_e\right)^2 I_{ei}(h_e) = [N_{ei}^\beta \mathcal{S}_e(h_e) + \phi_i(h_e) + p_{ei}]G_e \gamma_e e \quad (3.10)$$

$$\left(\frac{\partial}{\partial t} + \gamma_i\right)^2 I_{ie}(h_i) = [N_{ie}^\beta \mathcal{S}_i(h_i) + p_{ie}]G_i \gamma_i e \quad (3.11)$$

$$\left(\frac{\partial}{\partial t} + \gamma_i\right)^2 I_{ii}(h_i) = [N_{ii}^\beta \mathcal{S}_i(h_i) + p_{ii}]G_i \gamma_i e \quad (3.12)$$

$$\left[\left(\frac{\partial}{\partial t} + \bar{v}\Lambda_{ee}\right)^2 - \bar{v}^2 \frac{\partial^2}{\partial x^2}\right] \phi_e(h_e) = \bar{v}\Lambda_{ee}N_{ee}^\alpha \left(\frac{\partial}{\partial t} + \bar{v}\Lambda_{ee}\right) \mathcal{S}_e(h_e) \quad (3.13)$$

$$\left[\left(\frac{\partial}{\partial t} + \bar{v}\Lambda_{ei}\right)^2 - \bar{v}^2 \frac{\partial^2}{\partial x^2}\right] \phi_i(h_e) = \bar{v}\Lambda_{ei}N_{ei}^\alpha \left(\frac{\partial}{\partial t} + \bar{v}\Lambda_{ei}\right) \mathcal{S}_e(h_e) \quad (3.14)$$

The values and definitions of the parameters of the Liley equations are listed in Table 3.1. The aim of the Liley equations is to reproduce the scalp-measured EEG generated by macrocolumns within the cerebral cortex. Each Liley macrocolumn consists of two “neurons” whose properties represent the spatial average of the inhibitory and excitatory neurons within the macrocolumn.

Table 3.1: Symbol definitions and model constants for the Liley equations (Steyn-Ross *et al.* (2001)). Here, the maximum spike rate $\mathcal{S}_{e,i}^{\max}$ has been lowered from 1000 (ms)^{-1} to 100 (ms)^{-1} , to better represent the cortical physiology.

Symbol	Description	Value	Unit
e, i	(as subscript) excitatory, inhibitory cell populations		
$h_{e,i}$	population mean soma voltage		mV
$\tau_{e,i}$	membrane time constant	0.040, 0.040	s
$h_{e,i}^{\text{rest}}$	cell resting potential	-70, -70	mV
$h_{e,i}^{\text{rev}}$	cell reversal potential (Nernst potential)	45, -90	mV
$I_{ee,ie}$	total $e \rightarrow e, i \rightarrow e$ “current” input to excitatory synapses		mV
$I_{ei,ii}$	total $e \rightarrow i, i \rightarrow i$ “current” input to inhibitory synapses		mV
$\psi_{jk} \text{ (} j,k \in \{e,i\} \text{)}$	weighting factors for the I_{jk} inputs		
$p_{ee,ie}$	exogenous (subcortical) spike input to e population	1100, 1600	s^{-1}
$p_{ei,ii}$	exogenous (subcortical) spike input to i population	1600, 1100	s^{-1}
$\phi_{e,i}$	long-range (cortico-cortical) spike input to e, i populations		s^{-1}
$\Lambda_{ee,ei}$	characteristic cortico-cortical inverse-length scale	0.40, 0.65	$(\text{cm})^{-1}$
EPSP, IPSP	excitatory, inhibitory post-synaptic potential		mV
$\gamma_{e,i}$	neurotransmitter rate constant for EPSP, IPSP	300, 65	s^{-1}
$G_{e,i}$	peak amplitude of EPSP, IPSP	0.18, 0.37	mV
e	(e.g., Eqs (3.9–3.12)) base of natural logarithms	2.71828...	
$N_{ee,ei}^{\beta}$	total number of local $e \rightarrow e, e \rightarrow i$ synaptic connections	3034, 3034	
$N_{ie,ii}^{\beta}$	total number of local $i \rightarrow e, i \rightarrow i$ synaptic connections	536, 536	
$N_{ee,ei}^{\alpha}$	total number of synaptic connections from distant e -populations	4000, 2000	
\bar{v}	mean axonal conduction speed	700	cm s^{-1}
$\mathcal{S}_e(h_e), \mathcal{S}_i(h_i)$	sigmoid function mapping soma voltage to firing rate		s^{-1}
$\mathcal{S}_e^{\max}, \mathcal{S}_i^{\max}$	maximum value for sigmoid function	100, 100	s^{-1}
$\theta_{e,i}$	inflexion-point voltage for sigmoid function	-60, -60	mV
$g_{e,i}$	sigmoid slope at inflexion point	0.28, 0.14	$(\text{mV})^{-1}$

The first two equations of the Liley set,

$$\tau_e \frac{\partial h_e}{\partial t} = (h_e^{\text{rest}} - h_e) + \psi_{ee}(h_e)I_{ee}(h_e) + \psi_{ie}(h_e)I_{ie}(h_i) \quad (3.15)$$

$$\tau_i \frac{\partial h_i}{\partial t} = (h_i^{\text{rest}} - h_i) + \psi_{ei}(h_i)I_{ei}(h_e) + \psi_{ii}(h_i)I_{ii}(h_i) \quad (3.16)$$

describe the time-course of the excitatory (h_e) and inhibitory (h_i) soma voltages. Liley uses a double indexing scheme to indicate the sense of “flow” or influence. For example, $I_{ie}(h_i)$ is read as the voltage contribution, from the mass-averaged inhibitory neuron to the mass-averaged excitatory neuron. $\psi_{ie}(h_e)$ is a factor, dependent on the voltage at the receiving neuron, which moderates this $i \rightarrow e$ input (shortly to be explained). On the right-hand side of Eqs. (3.15–3.16), the first two terms represent an exponential decay back to the resting potential of the

soma membrane (-70 mV). The time-constant for this decay is given by $\tau_{e,i}$. The next two terms model perturbations away from the resting potential due to synaptic activity.

Depending on the potential or “state” of the membrane, the effect of synaptic inputs will vary. $I_{jk}(j, k \in \{e, i\})$ represents the total input to the relative synapse (which is always positive) and the corresponding ψ_{jk} term modulates its effectiveness and determines its sign. The ψ_{jk} terms are dimensionless scale factors defined as,

$$\psi_{ee}(h_e) = \frac{h_e^{\text{rev}} - h_e}{|h_e^{\text{rev}} - h_e^{\text{rest}}|}, \quad \psi_{ei}(h_i) = \frac{h_e^{\text{rev}} - h_i}{|h_e^{\text{rev}} - h_i^{\text{rest}}|} \quad (3.17)$$

$$\psi_{ie}(h_e) = \frac{h_i^{\text{rev}} - h_e}{|h_i^{\text{rev}} - h_e^{\text{rest}}|}, \quad \psi_{ii}(h_i) = \frac{h_i^{\text{rev}} - h_i}{|h_i^{\text{rev}} - h_i^{\text{rest}}|} \quad (3.18)$$

These definitions take into account the fact that the magnitude of the post-synaptic potential depends on the present voltage state of the neuron, and also the fact that inhibition and excitation are mediated by different ionic species and hence have different reversal potentials ($h_e^{\text{rev}} = +45$ mV, the sodium reversal potential; $h_i^{\text{rev}} = -90$ mV, the potassium reversal potential). The weighting factors are arranged such that if a neuron is highly *depolarized* it is easier to *hyperpolarize* and vice-versa. If a neuron’s soma potential exceeds h_e^{rev} then all four weights have an inhibitory or hyperpolarising effect. On the other hand, if a neuron’s soma potential falls below h_i^{rev} all the weights have an excitatory, depolarising effect (Steyn-Ross (2002)).

The time-evolution of the four synaptic voltage inputs I_{jk} are given by

$$\left(\frac{\partial}{\partial t} + \gamma_e\right)^2 I_{ee}(h_e) = [N_{ee}^\beta \mathcal{S}_e(h_e) + \phi_e(h_e) + p_{ee}] G_e \gamma_e e \quad (3.19)$$

$$\left(\frac{\partial}{\partial t} + \gamma_e\right)^2 I_{ei}(h_e) = [N_{ei}^\beta \mathcal{S}_e(h_e) + \phi_i(h_e) + p_{ei}] G_e \gamma_e e \quad (3.20)$$

$$\left(\frac{\partial}{\partial t} + \gamma_i\right)^2 I_{ie}(h_i) = [N_{ie}^\beta \mathcal{S}_i(h_i) + p_{ie}] G_i \gamma_i e \quad (3.21)$$

$$\left(\frac{\partial}{\partial t} + \gamma_i\right)^2 I_{ii}(h_i) = [N_{ii}^\beta \mathcal{S}_i(h_i) + p_{ii}] G_i \gamma_i e \quad (3.22)$$

The first pair of equations model the time-evolution of the *excitatory* postsynaptic potentials (EPSP) induced by synaptic flux into the excitatory and inhibitory postsynaptic neurons respectively; the second pair model the time-evolution of the *inhibitory* postsynaptic potentials (IPSP)

induced in the excitatory and inhibitory receiving neuron. The terms on the right sum to give the total presynaptic input. Sources of the presynaptic potential are: local excitatory feedback within the macrocolumn ($N_{ee}^\beta \mathcal{S}_e(h_e)$ in Eq. (3.19)), excitatory input from *distant* macrocolumns ($\phi_e(h_e)$), and *exogenous* (subcortical) spike inputs (p_{ee}). As all *distant* macrocolumn input is believed to be excitatory, the time evolution of the postsynaptic potential within inhibitory neurons (Eq. (3.21 and 3.22)) do not contain this term. Local feedback within the macrocolumn is modelled via a $N_{jk}^\beta S_j(h_j)$ term. N_{jk}^β is the total number of local connections, and $S_j(h_j)$ are *sigmoids* which model the output pulse rate of a homogeneous neural mass in response to a mean field of h_e, h_i ,

$$\mathcal{S}_e(h_e) = \frac{\mathcal{S}_e^{\max}}{1 + \exp(-g_e(h_e - \theta_e))}, \quad \mathcal{S}_i(h_i) = \frac{\mathcal{S}_i^{\max}}{1 + \exp(-g_i(h_i - \theta_i))} \quad (3.23)$$

This sigmoid definition comes about by considering a single neuron's firing dependence. As stated earlier, neurons have a threshold voltage, above which they fire action potentials. For an "ideal" neuron, one could write the firing rate in terms of a Heaviside function,

$$H(\theta_j) = \begin{cases} 0 & \text{for } \theta_j < -60 \text{ mV} \\ 1 & \text{for } \theta_j > -60 \text{ mV} \end{cases} \quad (3.24)$$

The mean-field approach has the effect of "smearing" this pure step function so that the threshold voltage is mapped to the sigmoid inflection point $\theta_j = -60$ mV. For small values of average soma potential, the number of active neurons will be low (low firing rate). As the soma potential becomes less negative, firing rate increases rapidly, eventually levelling off at a maximum value (this is shown in Fig. 3.8).

Liley selected the form of Eq. (3.19), in order that the Green's function (impulse response) for the DE is,

$$I(t) = \gamma t e^{1-\gamma t} \quad (3.25)$$

This models the postsynaptic potential which has a rapid rise to a maximum value followed by a slow decay back to zero (Fig. 3.9). Eq. (3.25) gives a good approximation of the experimentally-observed form of the postsynaptic potential (Tuckwell (1988a)).

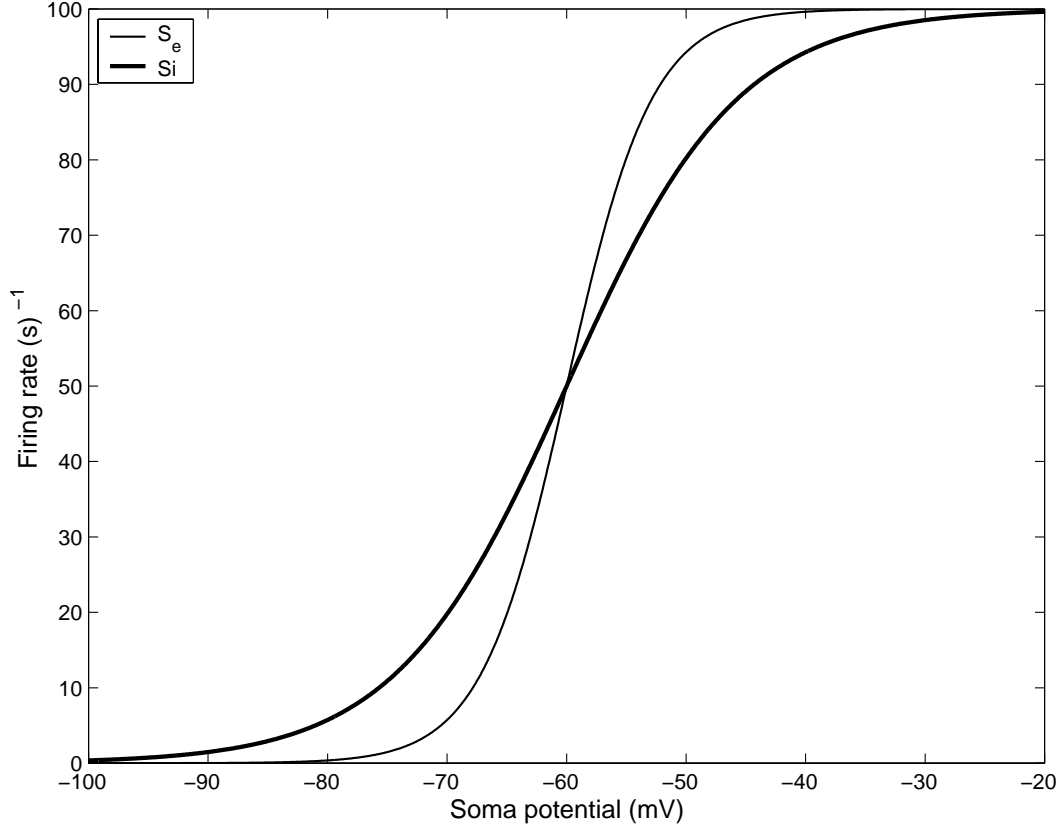


Figure 3.8: Sigmoid functions relating average firing rate to soma potential. See Eq. (3.23)

The last two equations of the Liley set,

$$\left[\left(\frac{\partial}{\partial t} + \bar{v}\Lambda_{ee} \right) - \bar{v}^2 \frac{\partial^2}{\partial x^2} \right] \phi_e(h_e) = \bar{v}\Lambda_{ee}N_{ee}^\alpha \left(\frac{\partial}{\partial t} + \bar{v}\Lambda_{ee} \right) \mathcal{S}_e(h_e) \quad (3.26)$$

$$\left[\left(\frac{\partial}{\partial t} + \bar{v}\Lambda_{ei} \right)^2 - \bar{v}^2 \frac{\partial^2}{\partial x^2} \right] \phi_i(h_e) = \bar{v}\Lambda_{ei}N_{ei}^\alpha \left(\frac{\partial}{\partial t} + \bar{v}\Lambda_{ei} \right) \mathcal{S}_e(h_e) \quad (3.27)$$

are a form of one-dimensional wave equation that describe the long-distance macrocolumn contributions to the population EPSP and IPSP events. The number of long-range $e \rightarrow e$ cortico-cortical connections is given by N_{ee}^α , and the $e \rightarrow i$ connections by N_{ei}^α . These connections are assumed to drop-off exponentially in space, with the characteristic cortico-cortical inverse-length scales given by Λ_{ee} and Λ_{ei} (see Table 3.1). Voltage impulses travel along the cortico-cortical axons with an average conduction speed of \bar{v} .

Figure 3.7 illustrates how the Liley equations model the connections and feedbacks of a one-dimensional chain of macrocolumns. The bulk of this thesis looks at a one-dimensional stochastic cortical model of the cerebral cortex. Before this 1-D model is examined, the Steyn-Ross spatially homogeneous model (Steyn-Ross *et al.* (1999)) will be reviewed in order to show

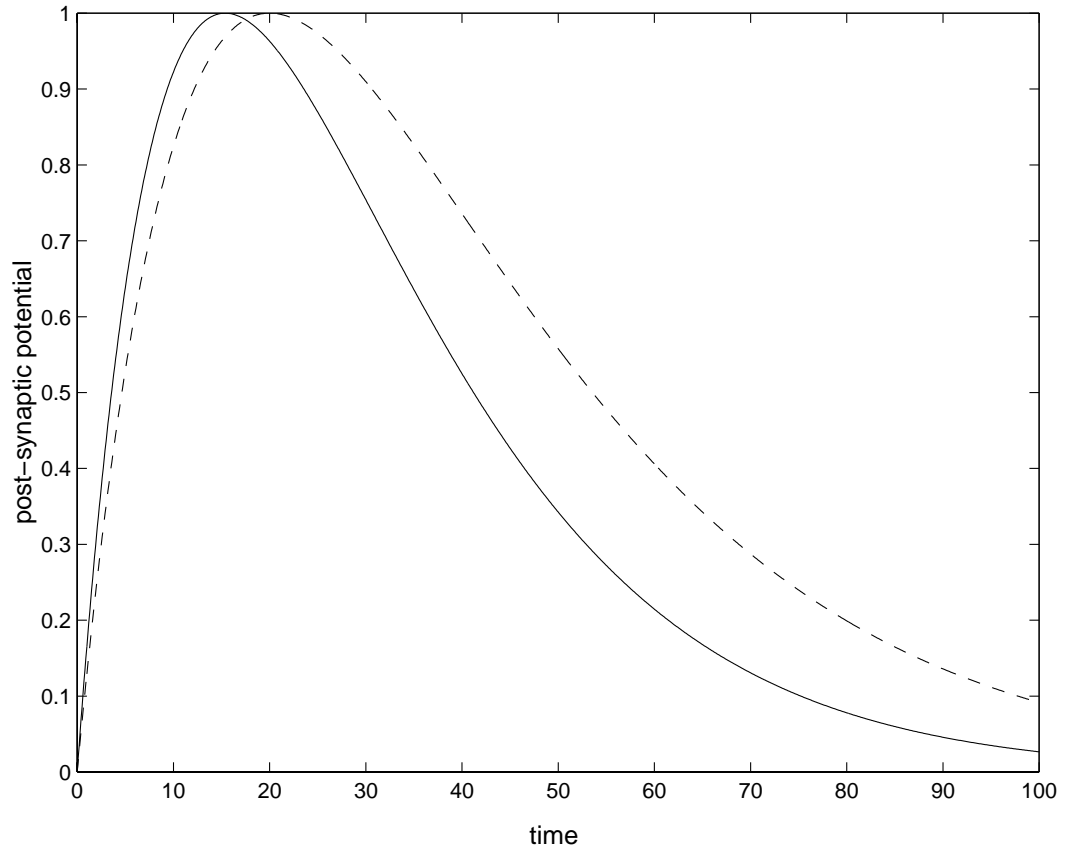


Figure 3.9: The time-evolution of a IPSP post-synaptic potential as described by Eq. (3.25). For the solid line the default value for the IPSP rate-constant γ_i (refer to Table 3.1) was used, while for the dashed line γ_i was altered to include an anaesthetic effect of $\lambda_{\text{GABA}} = 1.3$ (see Eq. (3.28)).

how different states of consciousness can arise. The 1-D model is the next step, in which spatial homogeneity is *not* assumed.

3.5 The Steyn-Ross Model

The aim of the Steyn-Ross *et al.* (1999) theory was to create a model that predicts how the brain reacts to general anaesthetic. Their starting point was the spatially homogeneous form of the Liley equations. After including a term for anaesthetic effect, they calculated the long-time limiting values for soma voltage, and showed that only certain stable steady-states were available to the anaesthetized macrocolumn. Also, by using an “adiabatic” approximation Steyn-Ross *et al.* (1999) were able to reduce the Liley equations from a set of eight partial differential equations, to a single pair of coupled ordinary differential equations in h_e and h_i . Stochastic subcortical terms were then included to model the fluctuations seen in an EEG. The stability analysis of the steady-states indicates that, as anaesthetic concentration is increased, there must occur an abrupt change of state at the point of transition into unconsciousness. The steady-states

also show a hysteresis effect: A person will regain consciousness at a *lower* level of anaesthetic than that at which they fell unconscious.

With these simplifying approximations, all information about the time evolution of the post-synaptic potentials and the spatial changes in the long-range (cortico-cortical) activity is discarded. As consciousness is a bulk property (it is the most grossly measurable property of the cerebral cortex) these assumptions were not thought to effect the prediction of a change in state of consciousness.

The Steyn-Ross alterations to the Liley equations are as follows:

- Anaesthetic effect is included by altering the rate-“constant” of the inhibitory post-synaptic potential,

$$\overline{\gamma}_i = \frac{\gamma_i}{\lambda_{\text{GABA}}} \quad (3.28)$$

where λ_{GABA} is a dimensionless multiplicative scaling factor assumed proportional to GABA anaesthetic effect. By increasing λ_{GABA} we are effectively increasing the amount of inhibitory synaptic input. The effect of increasing λ_{GABA} is shown in Fig. 3.9.

- Spatial homogeneity is assumed. This removes the $\frac{\partial^2}{\partial x^2}$ diffusion term in Eq. (3.26–3.27) resulting in,

$$\left(\frac{d}{dt} + \bar{v}\Lambda_{ee}\right)^2 \phi_e(h_e) = \bar{v}\Lambda_{ee}N_{ee}^\alpha \left(\frac{d}{dt} + \bar{v}\Lambda_{ee}\right) \mathcal{S}_e(h_e) \quad (3.29)$$

$$\left(\frac{d}{dt} + \bar{v}\Lambda_{ei}\right)^2 \phi_i(h_e) = \bar{v}\Lambda_{ei}N_{ei}^\alpha \left(\frac{d}{dt} + \bar{v}\Lambda_{ei}\right) \mathcal{S}_e(h_e) \quad (3.30)$$

- The Liley equations are transformed into a set of stochastic equations by including noise which drives the system. Noise is assumed to arise from the sub-cortical inputs to the macrocolumn. This assumption is modelled by replacing each of the four subcortical inputs p_{jk} with a random variation $\widetilde{p}_{jk}(t)$ about its mean $\langle p_{jk} \rangle$,

$$p_{jk} = \langle p_{jk} \rangle + \alpha_{jk} \sqrt{\langle p_{jk} \rangle} \xi_n(t) \quad (3.31)$$

where α_{jk} are dimensionless scale factors to ensure that the fluctuations are always small, and $\xi_n(t)$ are independent Gaussian-distributed white-noise sources.

The Gaussian-distributed white-noise sources are defined to have zero mean,

$$\langle \xi_n(t) \rangle = 0 \quad (3.32)$$

and delta-function covariances,

$$\langle \xi_n(t) \xi_m(t') \rangle = \delta_{nm} \delta(t - t'). \quad (3.33)$$

A common identity involving the delta function is,

$$\int_{t'-\epsilon}^{t'+\epsilon} \delta(t - t') dt = 1 \quad (3.34)$$

where ϵ is any positive number. This identity tells us that the total area under a delta function is a dimensionless unity. Hence $\delta(t - t')$ must have units of inverse-time, and hence, from the covariance property of Eq. 3.33, the random noise $\xi(t)$ has units of $1/\sqrt{\text{time}} = \text{s}^{-1/2}$ (Steyn-Ross (2002)). It is reasonable to assume that if the mean of subcortical activity increases (increase in $\langle p_{jk} \rangle$), then the size of the subcortical *fluctuations* about the mean will also increase. This is achieved by multiplying the noise-terms ξ by the (square-root of) the mean $\langle p_{jk} \rangle$ term. This scaling by $\sqrt{\langle p_{jk} \rangle}$ ensures dimensional consistency.

Scale factors α_{jk} are introduced in order to keep cortico-cortical inputs physiologically meaningful. By modelling the sub-cortical fluctuations as Gaussian-distributed white-noise, there comes the possibility that if the fluctuations are large enough, the p_{jk} subcortical input fluxes could become negative. However, in the present context, a negative flux is meaningless, so should be suppressed. By multiplying the noise-term with a correctly chosen scale-factor, the probability of negative subcortical inputs can be greatly diminished. (White-noise is defined to have infinite variance and hence there will always be some possibility that a negative input will occur). This safety scale factor is chosen to be,

$$\alpha_{jk} = 0.01 \quad (3.35)$$

The derivation of this value is discussed in Sec. 6.3.

The above alterations to the Liley equations lead to the following set of stochastic differential equations

$$\tau_e \frac{dh_e}{dt} = (h_e^{\text{rest}} - h_e) + \psi_{ee}(h_e)I_{ee}(h_e) + \psi_{ie}(h_e)I_{ie}(h_i) \quad (3.36)$$

$$\tau_i \frac{dh_i}{dt} = (h_i^{\text{rest}} - h_i) + \psi_{ei}(h_i)I_{ei}(h_e) + \psi_{ii}(h_i)I_{ii}(h_i) \quad (3.37)$$

$$\left(\frac{d}{dt} + \gamma_e\right)^2 I_{ee}(h_e) = [N_{ee}^\beta \mathcal{S}_e(h_e) + \phi_e(h_e) + \langle p_{ee} \rangle] G_e \gamma_e e + \Gamma_1(t) \quad (3.38)$$

$$\left(\frac{d}{dt} + \gamma_e\right)^2 I_{ei}(h_e) = [N_{ei}^\beta \mathcal{S}_e(h_e) + \phi_i(h_e) + \langle p_{ei} \rangle] G_e \gamma_e e + \Gamma_2(t) \quad (3.39)$$

$$\left(\frac{d}{dt} + \frac{\gamma_i}{\lambda_{\text{GABA}}}\right)^2 I_{ie}(h_i) = [N_{ie}^\beta \mathcal{S}_i(h_i) + \langle p_{ie} \rangle] G_i e \frac{\gamma_i}{\lambda_{\text{GABA}}} + \Gamma_3(t) \quad (3.40)$$

$$\left(\frac{d}{dt} + \frac{\gamma_i}{\lambda_{\text{GABA}}}\right)^2 I_{ii}(h_i) = [N_{ii}^\beta \mathcal{S}_i(h_i) + \langle p_{ii} \rangle] G_i e \frac{\gamma_i}{\lambda_{\text{GABA}}} + \Gamma_4(t) \quad (3.41)$$

$$\left(\frac{d}{dt} + \bar{\nu} \Lambda_{ee}\right)^2 \phi_e(h_e) = \bar{\nu} \Lambda_{ee} N_{ee}^\alpha \left(\frac{d}{dt} + \bar{\nu} \Lambda_{ee}\right) \mathcal{S}_e(h_e) \quad (3.42)$$

$$\left(\frac{d}{dt} + \bar{\nu} \Lambda_{ei}\right)^2 \phi_i(h_e) = \bar{\nu} \Lambda_{ei} N_{ei}^\alpha \left(\frac{d}{dt} + \bar{\nu} \Lambda_{ei}\right) \mathcal{S}_e(h_e) \quad (3.43)$$

where the $\Gamma_m (m = 1 \dots 4)$ are the stochastic driving terms,

$$\Gamma_1(t) = \alpha_{ee} \sqrt{\langle p_{ee} \rangle} \xi_1(t) G_e \gamma_e e \quad \Gamma_2(t) = \alpha_{ei} \sqrt{\langle p_{ei} \rangle} \xi_2(t) G_e \gamma_e e \quad (3.44)$$

$$\Gamma_3(t) = \frac{\alpha_{ie} \sqrt{\langle p_{ie} \rangle} \xi_3(t) G_i \gamma_i e}{\lambda_{\text{GABA}}} \quad \Gamma_4(t) = \frac{\alpha_{ii} \sqrt{\langle p_{ii} \rangle} \xi_4(t) G_i \gamma_i e}{\lambda_{\text{GABA}}} \quad (3.45)$$

3.6 Stationary States

In order to find the stationary states of the cortex, Eqs. (3.36–3.43) are solved in the long-time limit, $\frac{d}{dt} \rightarrow 0$, with the noise sources turned off. Using this simplification and manipulating the resulting equations, a pair of coupled nonlinear equations for the equilibrium spike-rates can be

derived (Steyn-Ross (2002))

$$\hat{S}_i(h_i) = - \left[\frac{\tilde{\gamma}_i}{G_i e \psi_{ie}(h_e)} [h_e^{\text{rest}} - h_e + \psi_{ee}(h_e) I_{ee}(h_e)] + p_{ie} \right] / N_{ie}^\beta, \quad (3.46)$$

$$\hat{S}_e(h_e) = - \left[\frac{\gamma_e}{G_e \psi_{ei}(h_i)} [h_i^{\text{rest}} - h_i + \psi_{ii}(h_i) I_{ii}(h_i)] + p_{ei} \right] / (N_{ei}^\alpha + N_{ei}^\beta). \quad (3.47)$$

Inverting the sigmoids of Eq. (3.23), we can obtain corresponding steady-state membrane voltages for $\mathcal{S}_e(h_e)$, $\mathcal{S}_i(h_i)$,

$$\hat{h}_i(h_e) = \theta_i - \frac{1}{g_i} \ln(\mathcal{S}_i^{\text{max}} / \hat{S}_i(h_e) - 1), \quad (3.48)$$

$$\hat{h}_e(h_i) = \theta_e - \frac{1}{g_e} \ln(\mathcal{S}_e^{\text{max}} / \hat{S}_e(h_i) - 1). \quad (3.49)$$

The above equations cannot be solved analytically. In order to find equilibrium values (or stationary states) for h_e, h_i a numerical scheme has to be implemented (Steyn-Ross (2002) uses an iterative method). To show that stationary values exist (values for which Eq. (3.48) and (3.49) are simultaneously satisfied), isoclines can be plotted. Using Eq. (3.49) and (3.47) in isolation, we can vary h_i and obtain a graph of $\hat{h}_e(h_i)$. Likewise using Eq. (3.48) and (3.46), in isolation, we can obtain a graph of $\hat{h}_i(h_e)$. Plotting these graphs on a single pair of axes, shows that the two functions intersect (Fig. 3.10), with the intersection points giving the equilibrium values (h_e^0, h_i^0) for a given anaesthetic value (Eq. 3.28). The numerical scheme used by Steyn-Ross *et al.* (2003) makes an initial guess and then “zooms” in on each of the isocline intersections in turn.

As the anaesthetic effect is varied, different steady-state values are obtained. Plotting the steady-states as a function of anaesthetic “amount” λ_{GABA} , the structure shown in Fig. 3.11 is obtained. For a majority of the values shown, there are three solutions, but those lying on only the top and bottom branches are stable. The top branch is called “active”, while the bottom branch is labelled “quiescent” (Steyn-Ross *et al.* (1999)). The reason for this distinction is that the values of (h_e^0, h_i^0) on the “active” branch lie above the sigmoid inflection point, and hence have a high average firing rate. In contrast, the values on the “quiescent” branch lie below the sigmoid inflection point, and therefore have a comparatively lower average firing rate.

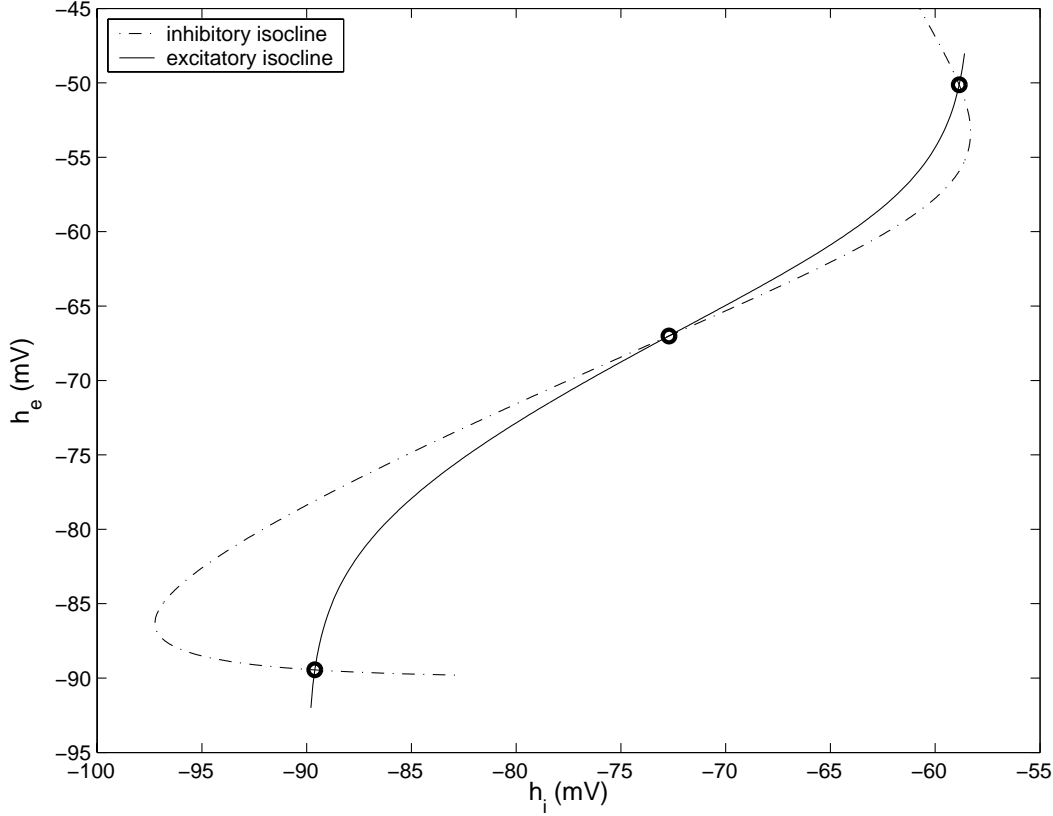


Figure 3.10: Example of isocline intersections, $\lambda_{\text{GABA}} = 1$. These intersection points locate the steady-state soma voltages.

3.7 Adiabatic Elimination of Fast Variables

On closer inspection of Eqs. (3.36) and Table 3.1, it becomes obvious that the “input” terms $(I_{jk}, \phi_{e,i})$ vary on time-scales that are quite different from the time-scales of the soma potentials h_e and h_i . The relaxation times of the input terms (computed from the numerical values listed in Table 3.1) are:

$$\text{relaxation time for } I_{ee}(h_e), I_{ei}(h_e) = (\gamma_e)^{-1} \approx 3.3 \text{ ms}$$

$$\text{relaxation time for } I_{ie}(h_i), I_{ii}(h_i) = (\gamma_i)^{-1} \approx 15.4 \text{ ms}$$

$$\text{relaxation time for } \phi_e(h_e) = (\bar{v}\Lambda_{ee})^{-1} \approx 3.6 \text{ ms}$$

$$\text{relaxation time for } \phi_i(h_e) = (\bar{v}\Lambda_{ei})^{-1} \approx 2.2 \text{ ms}$$

while the relaxation times of the $h_{e,i}$ soma potentials, are set at $\tau_e = \tau_i = 40$ ms. Note, the relaxation times of the $h_{e,i}$ can actually be as large as 100 ms (Koch *et al.* (1996)).

Using this difference in time-scales we can assert that the neural inputs $(I_{jk}, \phi_{e,i})$ are “fast” variables that equilibrate to their steady-states much faster than the soma potentials h_e, h_i . This assertion can be incorporated into the equations by setting $\frac{d}{dt} \rightarrow 0$ in the synaptic-input Eqs. 3.38–3.43. This simplification is referred to as the *adiabatic elimination of the fast variables*.

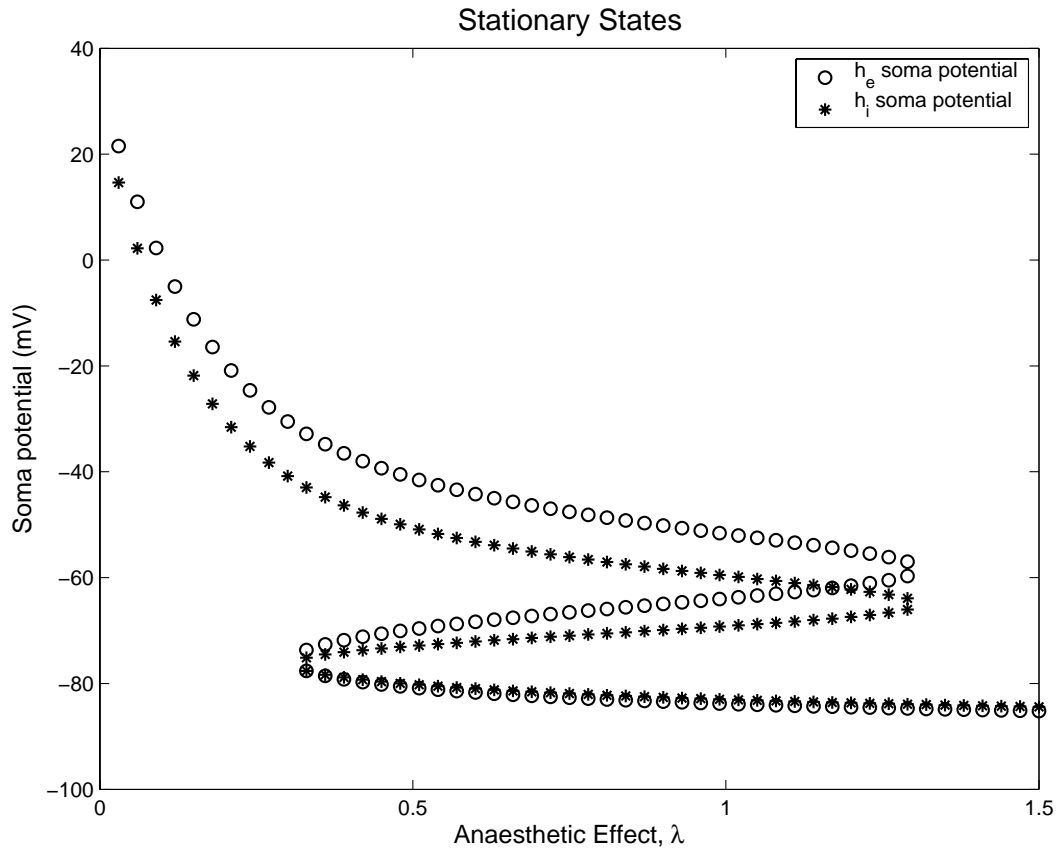


Figure 3.11: Model prediction for stationary states as a function of anaesthetic effect λ_{GABA} .

Note that the noise terms *are* not set to zero in the adiabatic elimination. This is to allow fluctuations from the fast variables to be incorporated into the $h_{e,i}$ equations. By setting the time-derivatives of the fast variables to zero we have transformed the synaptic input response functions (Eq. 3.25) into delta-function spikes. Interestingly, the anaesthetic effect was included in the model by altering the relaxation time of the post-synaptic potentials due to inhibitory neurons. But by replacing the post-synaptic potentials as delta-function spikes, this relaxation time no longer exists! Nevertheless, anaesthetic effect is still incorporated in the model, as the *area* of the time-evolving post-synaptic potential (PSP) function is the same as the *area* of the spike PSP function. The impulse responses of the two PSPs are shown in Fig. 3.12.

Conservation of area is easily demonstrated. Expanding on Wilcocks (2001), the impulse response $\zeta(t)$ of the PSPs of the Liley equations,

$$\zeta(t) = G\gamma te^{1-\gamma t} \quad t \geq 0 \quad (3.50)$$

$$\zeta(t) = 0 \quad t < 0 \quad (3.51)$$

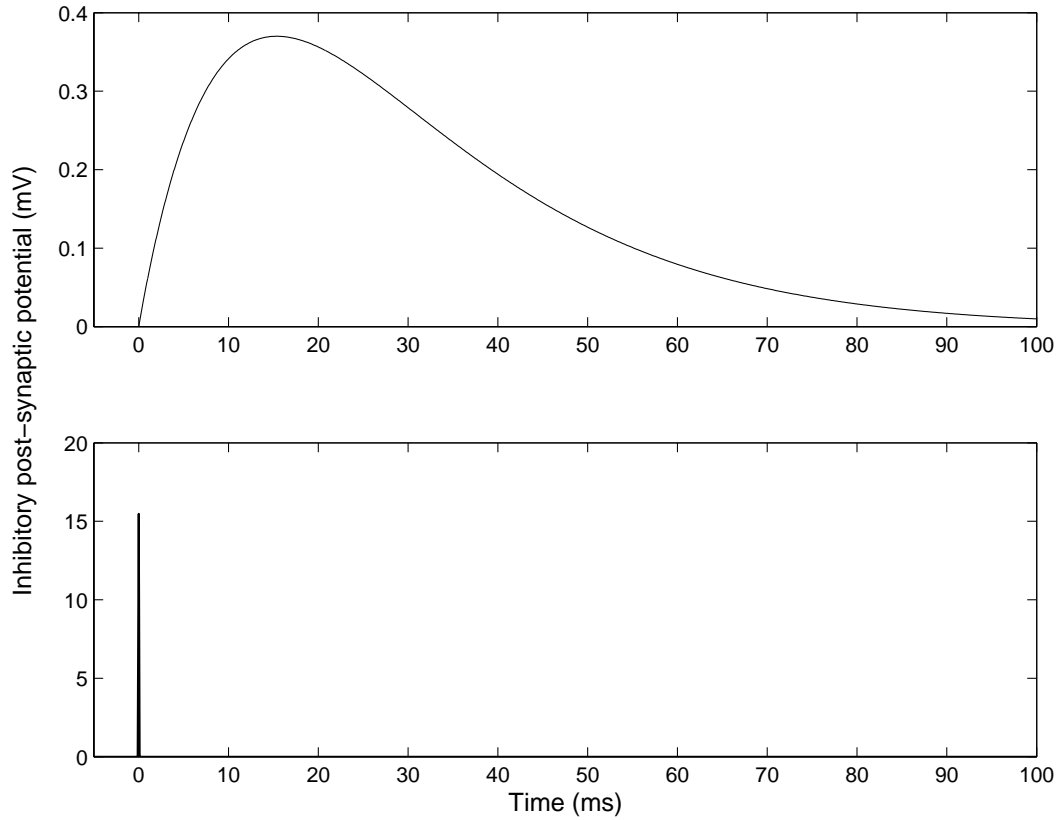


Figure 3.12: Post-synaptic potentials for the *full Liley* equations (top) and the *adiabatic* equations (bottom). The full equations represent the postsynaptic potential as a smooth rise- and decay-curve, while the adiabatic equations replace this time course with a delta-function whose *area* matches that of the smooth curve.

has area given by

$$\int_{-\infty}^{+\infty} \varsigma(t) dt = \int_0^{+\infty} G\gamma t e^{1-\gamma t} dt \quad (3.52)$$

which can be evaluated by making use of the identity

$$\int_0^{\infty} x^{n-1} e^{-x} dx = (n-1)! \quad (3.53)$$

Making the substitutions $x = \gamma t$, $n = 2$ gives area

$$\int_{-\infty}^{+\infty} \varsigma(t) dt = \frac{Ge}{\gamma} \int_0^{+\infty} x e^{-x} dx \quad (3.54)$$

$$= \frac{Ge}{\gamma} \quad \textcircled{*} \quad (3.55)$$

The *adiabatic* post-synaptic potential is a scaled delta-function,

$$\varsigma'(t) = \frac{Ge\delta(t)}{\gamma} \quad (3.56)$$

with area

$$\begin{aligned} \int_{-\infty}^{+\infty} \varsigma'(t)dt &= \frac{Ge}{\gamma} \int_{-\infty}^{+\infty} \delta(t)dt \\ &= \frac{Ge}{\gamma} \end{aligned} \quad (3.57)$$

which matches $\textcircled{*}$, verifying that both the full and the adiabatic forms of the PSP have equal area.

Once the adiabatic simplifications have been made, the following equations are obtained,

$$\frac{dh_e}{dt} = F_1(h_e, h_i) + \Gamma_e(t) \quad (3.58)$$

$$\frac{dh_i}{dt} = F_2(h_e, h_i) + \Gamma_i(t) \quad (3.59)$$

where the *drift* terms are,

$$\begin{aligned} F_1(h_e, h_i) &= [(h_e^{\text{rest}} - h_e) + \psi_{ee}(h_e)][(N_{ee}^\alpha + N_{ee}^\beta)\mathcal{S}_e(h_e) + \langle p_{ee} \rangle]G_e e / \gamma_e \\ &\quad + \lambda_{\text{GABA}}\psi_{ie}(h_e)[N_{ie}^\beta\mathcal{S}_i(h_i) + \langle p_{ie} \rangle]G_i e / \gamma_i / \tau_e \end{aligned} \quad (3.60)$$

$$\begin{aligned} F_2(h_e, h_i) &= [(h_i^{\text{rest}} - h_i) + \psi_{ei}(h_i)][(N_{ei}^\alpha + N_{ei}^\beta)\mathcal{S}_e(h_e) + \langle p_{ei} \rangle]G_e e / \gamma_e \\ &\quad + \lambda_{\text{GABA}}\psi_{ii}(h_i)[N_{ii}^\beta\mathcal{S}_i(h_i) + \langle p_{ii} \rangle]G_i e / \gamma_i / \tau_i \end{aligned} \quad (3.61)$$

and the corresponding noise terms are,

$$\Gamma_e(t) = \psi_{ee}(h_e)\alpha_{ee}\sqrt{\langle p_{ee} \rangle}G_e e \xi_1(t) / \gamma_e \tau_e + \lambda_{\text{GABA}}\psi_{ie}(h_e)\alpha_{ie}\sqrt{\langle p_{ie} \rangle}G_i e \xi_3(t) / \gamma_i \tau_e \quad (3.62)$$

$$\Gamma_i(t) = \psi_{ei}(h_i)\alpha_{ei}\sqrt{\langle p_{ei} \rangle}G_e e \xi_2(t) / \gamma_e \tau_e + \lambda_{\text{GABA}}\psi_{ii}(h_i)\alpha_{ii}\sqrt{\langle p_{ii} \rangle}G_i e \xi_4(t) / \gamma_i \tau_i \quad (3.63)$$

Eqs. (3.60–3.63) will be referred to as the *adiabatic equations* throughout this thesis.

3.8 Linearizing and Stability Analysis

The adiabatic simplifications only alter the time-evolution of the post-synaptic potentials. Hence the stationary states for the adiabatic equations are the same as those discussed in Sec. 3.6. Stability analysis involves linearizing about the steady-state solutions and analyzing the resulting eigenvalues (linear stability analysis is discussed in Sec. 4.3). The resulting linearized equations model small fluctuations $(\delta h_e, \delta h_i)$ about the steady-states (h_e^0, h_i^0) . Steyn-Ross *et al.* (1999) linearize the adiabatic equations about (h_e^0, h_i^0) , to form a pair of linear, constant-matrix equations for $(\delta h_e, \delta h_i)$,

$$\frac{d}{dt} \begin{bmatrix} \delta h_e \\ \delta h_i \end{bmatrix} = -\mathbf{A} \begin{bmatrix} \delta h_e \\ \delta h_i \end{bmatrix} + \sqrt{\mathbf{D}} \begin{bmatrix} \xi_e(t) \\ \xi_i(t) \end{bmatrix} \quad (3.64)$$

where \mathbf{A} is the 2×2 drift matrix, \mathbf{D} is the 2×2 diffusion matrix and $\xi_e(t), \xi_i(t)$ are noise terms. Eigenvalue stability analysis shows that the *active* and *quiescent* branch are *stable* while the middle branch is *unstable*. This result can be visualized as two valleys separated by a hill. The two valleys are the *active* and *quiescent* branches while the hill is the middle branch. Consider a ball sitting in one of the valleys, and compare its motion with that of a ball perched atop the hill. Small movement perturbations to the “valley” ball cause the ball to oscillate to and fro about the bottom of the valley, while small perturbations to the “hill” ball will knock the ball off its unstable equilibrium position and into one of the neighbouring valleys. Similarly, the potential energy landscape of the cortex only allows voltage fluctuations about the stable equilibrium values corresponding to points on the upper and lower branches.

Following Steyn-Ross *et al.* (1999) the stationary states of the cortex can be partitioned into three regions, Fig 3.13. Region III is labelled “seizure” as this is a very high-firing portion of the inverted S-bend. Region I is labelled “coma” as only a very-low firing portion of the inverted S-bend is available. In region II multiple states are available, currently thought to represent a dissociated (dream-like) state. Normal consciousness is probably located near A_1 on Fig 3.13

Due to the inverted S-bend distribution of steady-state solutions, it is impossible for the macrocolumn to traverse continuously between the upper and lower branches — there must be jump transitions at both the A_3 and the Q_1 turning points.

Consider a person undergoing anaesthesia. As anaesthetic concentration is increased, the patient will progress down along the top branch of the inverted S-bend until the A_3 end of the

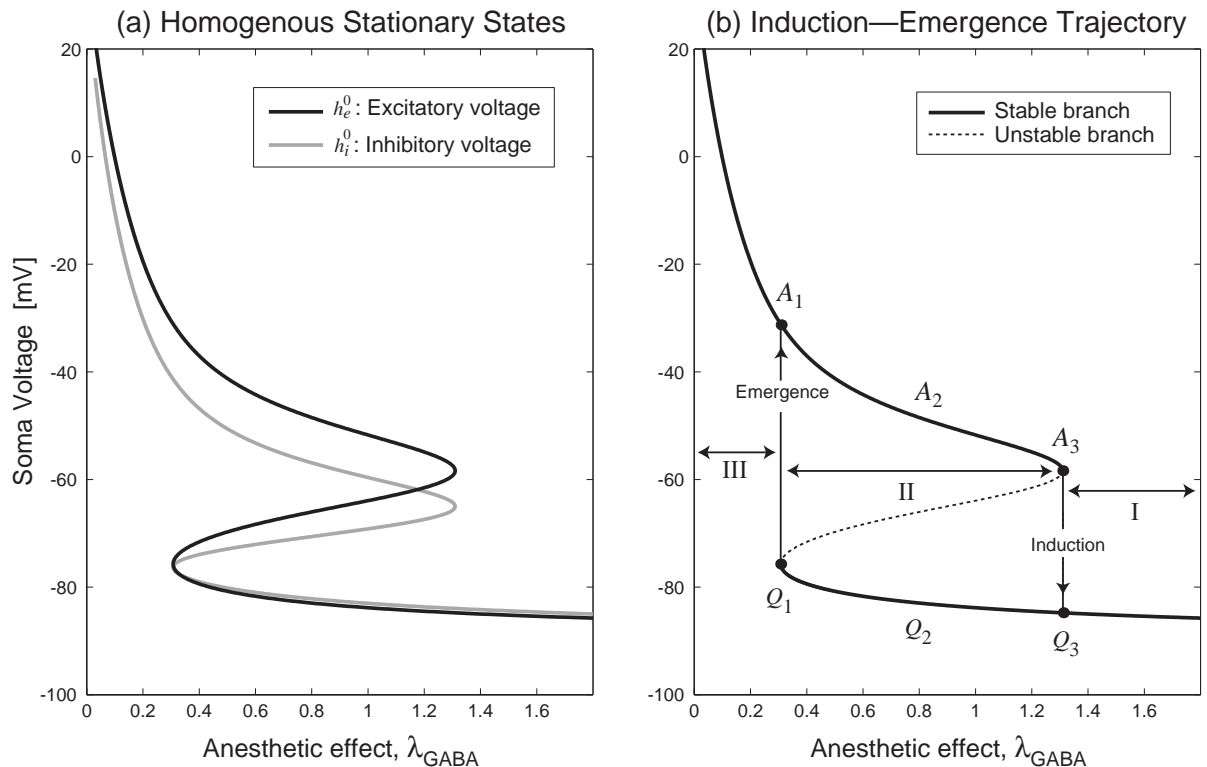


Figure 3.13: The stationary states of the macrocolumn, separated into three regions [Steyn-Ross *et al.* (2003)].

branch is reached. At this point, as the middle branch is unstable, the cortex must make a sudden discontinuous “state” change to the lower branch (Q_3). The patient is now deemed to be unconscious and if anaesthetic is increased further, will progress towards the coma limit.

In order to bring a patient back to consciousness anaesthetic concentration has to be reduced. Moving along the bottom branch until Q_1 is reached, here another sudden change of states has to occur in order to regain consciousness. In general, the model predicts that at a critical anaesthetic concentration a rapid active→quiescent (or vice versa) change of “phase” will signal a change in the state of consciousness. The next chapter looks at extending the homogeneous model to include space. With the inclusion of spatial variability the possibility of *nonequilibrium* phase transitions arises. General properties of nonequilibrium phase transitions are discussed using the Brusselator a well known chemical example that displays some similarities to our 1-D cortex model.

Spatial Variation

4.1 Nonequilibrium Phase Transitions

Particular systems are known to undergo a phase transition such that they are no longer in absolute thermodynamic equilibrium (Reichl (1998)). Systems which exhibit this effect are initially at an isotropic steady state (thermodynamic equilibrium). A certain parameter is then forced such that this state is no longer stable. A nonequilibrium phase transition then occurs, and the system moves to a *new stable* configuration which is not described by the thermal equilibrium condition.

A system in thermodynamic equilibrium can be treated by linear theory, assuming the system is never far from this stable state. If this state becomes unstable, the system will move away from the linear regime, so nonlinear effects must be included in the governing equations. Nonlinear equations allow for the possibility of multiple solutions, each with different regions of stability. Thus, as we change the parameters of a nonlinear system, it can exhibit phase transitions from one state to another.

When a system in thermodynamic equilibrium undergoes a nonequilibrium phase transition, the new state that appears in the nonlinear regime can oscillate in space and/or time. The spatial or temporal symmetry of such systems is broken at the phase transition. The new stable nonequilibrium state is typically much more ordered (in space or time) than the disordered equilibrium state from which it evolved. So are referred to as *dissipative* or *self-organized structures* (Reichl (1998)). They are named dissipative as a constant flow of energy and sometimes matter (hence production of entropy) is required.

To better explain symmetry breaking, the well known water-freezing-to-ice equilibrium phase transition can be used. Liquid water is rotationally symmetric, that is, it looks the same from every point. In contrast, ice has preferential lattice directions along which water molecules align. Thus when water freezes, the original symmetry of the liquid water phase is broken.

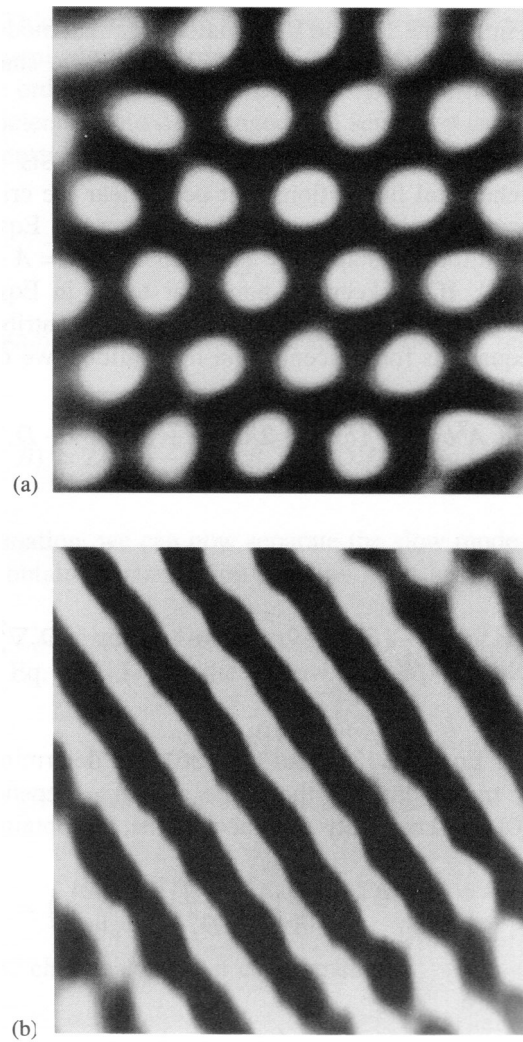


Figure 4.1: Two-dimensional stationary Turing structures produced with the chlorite–iodide–malonic acid–starch (CIMA) chemical reaction in a two-dimensional gel. (a) Hexagons, (b) stripes. [Source: figure from Reichl (1998)]

The spontaneous formation of self-organized structures has been observed in chemical experiments, hydrodynamic systems and biological systems. The chemical reaction–diffusion system, polyacrylamide–methyleneblue–sulfide–oxygen, forms stationary spatial patterns. Comparable phenomena have been observed in bacteria colonies and in cardiac muscle (Münster (2002)). Jung *et al.* (1998) has also demonstrated a system of cultured rat brain cells that produce spiral-shaped chemical waves.

In 1952, Alan Turing predicted that stationary patterns could arise in nonlinear systems via the coupling between reaction and diffusion processes. In order for these stationary patterns (or *Turing patterns*) to occur, a system must contain an activatory species that stimulates self-production, and an inhibitory species that limits the growth of the activatory species. Furthermore, the diffusion coefficients of the activatory species must be significantly *smaller than* the

diffusion coefficient of the inhibitory species (Andrésen *et al.* (1999)). Due to the requirement of differing diffusion coefficients, experimental verification of Turing patterns has been difficult to achieve. The laboratory verification of Turing patterns was finally achieved in 1990 (Reichl (1998)). Two Turing patterns are shown in Fig. 4.1.

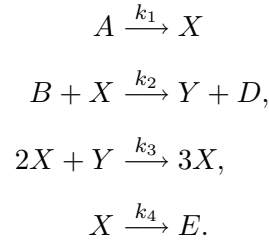
We will find that the spatially variable 1-D model of the cortex can also form Turing patterns. A famous reaction–diffusion system that also leads to the possibility of Turing patterns is the *Brusselator*. Following similar analytical techniques as those developed to investigate the Brusselator, predictions about the behaviour of the 1-D cortex can be made. Thus it is wise to review the methods used to analyse the Brusselator system.

4.2 The Brusselator

The Brusselator is a reaction–diffusion system which can form long-lived spatially-organized patterns. First studied in Brussels (hence the name), it has proved very useful in understanding the basic principles of nonlinear chemical reactions. The Brusselator can be used to qualitatively model chemical oscillations that occur in the well known *Belousov–Zhabotinsky* reaction (the first evidence of a dissipative structure). Belousov discovered this reaction in the early 1950’s but no one believed him. Many scientists were strongly disinclined to believe there could exist a chemical such a solution that could, from the products of the initial reactants, reform the initial components again and again, in a repeating loop. It was considered a violation of the second law of thermodynamics: Entropy in a *closed* system can never decrease, where entropy is a measure of the disorder or randomness of a system. The reason that the second law is *not* violated is that a constant input of energy and matter are required to sustain the structures formed by the Belousov–Zhabotinsky reaction. In 1959 Belousov managed to publish his results in an obscure medical journal.

The Brusselator is one of the simplest models of a nonlinear chemical system for which the constituents can oscillate in time, or can exhibit nonlinear wave motion. Following Reichl (1998)

the four steps of the Brusselator model are,



A, B, D, E, X and Y are the six chemicals involved in the reaction. k_1, k_2, k_3 , and k_4 are the rate constants for the appropriate reaction. In practice, chemicals A and B are held at constant concentration by being continuously fed into the system, and D and E are held constant by being removed as soon as they appear. Placing these restrictions on the system forces the reactions to progress in only one direction and to be held far from thermodynamic equilibrium. As X and Y are both inputs and outputs their concentrations can vary in both space and time.

Chaturvedi *et al.* (1977) define the rate equations for the concentrations of X and Y as,

$$\partial\rho_X(r, t)/\partial t = D_X\nabla^2\rho_X(r, t) + \kappa_1 - \kappa_2\rho_X(r, t) + \kappa_3\rho_X^2(r, t)\rho_Y(r, t) - \kappa_4\rho_X(r, t) \quad (4.1)$$

$$\partial\rho_Y(r, t)/\partial t = D_Y\nabla^2\rho_Y(r, t) + \kappa_2\rho_X(r, t) - \kappa_3\rho_X^2(r, t)\rho_Y(r, t) \quad (4.2)$$

where ρ_X and ρ_Y are the concentrations of X and Y and they have taken into account the cell size dependence of k_1, k_2, k_3, k_4, A and B by defining

$$\kappa_1\Delta V = k_1A, \quad \kappa_2 = k_2B, \quad \kappa_3(\Delta V)^{-2} = k_3, \quad \kappa_4 = k_4 \quad (4.3)$$

The concentrations are allowed to vary in space by allowing for the possibility of diffusion (D_X and D_Y are the coefficients of diffusion). By setting the time and space derivatives to zero in equations (4.1) and (4.2), we can obtain the spatially uniform steady-state solution,

$$\rho_{X,0} = \frac{\kappa_1}{\kappa_4} \quad \rho_{Y,0} = \frac{\kappa_2\kappa_4}{\kappa_1\kappa_3} \quad (4.4)$$

The steady-state solution (Eq. (4.4)) lies on the thermodynamic branch of steady-state solutions for the Brusselator system (Reichl (1998)). If the thermodynamic steady-state becomes unstable a nonequilibrium phase transition (bifurcation) to a state which does not lie on the thermodynamic branch may occur. This new nonequilibrium state may oscillate in space and time.

In order to determine whether the thermodynamic branch is unstable to small perturbations, linear stability theory is invoked.

4.3 Linear Stability Analysis

In order to linearize a general system consisting of two first-order ordinary differential equations,

$$\dot{x} = f(x, y) \quad (4.5)$$

$$\dot{y} = g(x, y) \quad (4.6)$$

there must exist a fixed point (x_0, y_0) such that,

$$f(x_0, y_0) = 0 \quad (4.7)$$

$$g(x_0, y_0) = 0. \quad (4.8)$$

We then expand about $(x = x_0 + \delta_x, y = y_0 + \delta_y)$ using a Taylor series in two variables where f_x is understood to be the partial derivative of f with respect to x ,

$$\begin{aligned} f(x_0 + \delta_x, y_0 + \delta_y) &= f(x_0, y_0) + [f_x(x_0, y_0)\delta_x + f_y(x_0, y_0)\delta_y] \\ &+ \frac{1}{2!}[(\delta_x)^2 f_{xx}(x_0, y_0) + 2\delta_x\delta_y f_{xy}(x_0, y_0) + (\delta_y)^2 f_{yy}(x_0, y_0)] \dots \end{aligned} \quad (4.9)$$

$$\begin{aligned} g(x_0 + \delta_x, y_0 + \delta_y) &= g(x_0, y_0) + [g_x(x_0, y_0)\delta_x + g_y(x_0, y_0)\delta_y] \\ &+ \frac{1}{2!}[(\delta_x)^2 g_{xx}(x_0, y_0) + 2\delta_x\delta_y g_{xy}(x_0, y_0) + (\delta_y)^2 g_{yy}(x_0, y_0)] \dots \end{aligned} \quad (4.10)$$

Using Eqs. (4.5–4.6) and Eqs. (4.9–4.10) we write,

$$\dot{\delta}_x = f_x(x_0, y_0)\delta_x + f_y(x_0, y_0)\delta_y + f_{xy}(x_0, y_0)\delta_x\delta_y + \dots \quad (4.11)$$

$$\dot{\delta}_y = g_x(x_0, y_0)\delta_x + g_y(x_0, y_0)\delta_y + g_{xy}(x_0, y_0)\delta_x\delta_y + \dots \quad (4.12)$$

Making the assumption that δ_x and δ_y are always small, to first order we have,

$$\frac{d}{dt} \begin{bmatrix} \delta_x \\ \delta_y \end{bmatrix} = \begin{bmatrix} f_x(x_0, y_0) & f_y(x_0, y_0) \\ g_x(x_0, y_0) & g_y(x_0, y_0) \end{bmatrix} \begin{bmatrix} \delta_x \\ \delta_y \end{bmatrix}. \quad (4.13)$$

Using the process outlined above a general system consisting of two first-order ordinary differential equations can be transformed into two linear differential equations (Eq. (4.13)).

A linear homogeneous system, consisting of two first-order differential equations with constant coefficients, such as the one described by Eq. (4.13), has the form,

$$d\mathbf{x}/dt = \mathbf{A}\mathbf{x}, \quad (4.14)$$

where \mathbf{A} is a 2×2 constant matrix and \mathbf{x} is a 2×1 vector (Boyce and Diprima (1997)). \mathbf{A} is called the stability matrix because its eigenvalues determine whether the solution of the system will decay exponentially towards, or grow exponentially away from, its steady-state value. In the case $\det \mathbf{A} \neq 0$, the stability matrix is nonsingular and $\mathbf{x} = \mathbf{0}$ is the only steady-state point of the system. Following Boyce and Diprima (1997), if we seek solutions of the form $\mathbf{x} = \xi e^{rt}$, we find via substitution of \mathbf{x} into Eq. 4.14 that,

$$(\mathbf{A} - r\mathbf{I})\xi = \mathbf{0}. \quad (4.15)$$

Thus r must be a eigenvalue of the matrix \mathbf{A} and ξ the corresponding eigenvector. The eigenvalues are the roots of the polynomial equation

$$\det(\mathbf{A} - r\mathbf{I}) = 0 \quad (4.16)$$

and Eq. 4.15 can be used to determine the eigenvectors.

The general solution of Eq. (4.14) is,

$$\mathbf{x} = c_1 \xi^{(1)} e^{r_1 t} + c_2 \xi^{(2)} e^{r_2 t} \quad (4.17)$$

where c_1, c_2 are constants, r_1, r_2 are eigenvalues and $\xi^{(1)}, \xi^{(2)}$ are eigenvectors. The type (complex or real) and value (positive or negative) of the eigenvalues determine the stability of the system. Following Reichl (1998) we will consider several cases which can occur depending on values of the real and imaginary parts of r_1 and r_2 .

1. Both r_1 and r_2 are real and $r_1 < r_2 < 0$. This state is *completely stable*. A solution displaced from the steady-state will decay exponentially back to this state.

2. Both r_1 and r_2 are real and $0 < r_1 < r_2$. This state is *completely unstable*. A solution displaced from the steady-state will exponentially move away.
3. Both r_1 and r_2 are real and $r_1 < 0 < r_2$. This state is *unstable*. As long as c_2 is nonzero, the positive eigenvalue (c_2) will dominate as $t \rightarrow \infty$.
4. Both r_1 and r_2 are purely imaginary. In this case the nonlinear terms determine the stability of the state. In the linear regime the solution neither decays nor moves away from the steady-state, it *oscillates* around it.
5. Both r_1 and r_2 are complex with negative real part, so $r_1 = \alpha + i\beta$ and $r_2 = \alpha - i\beta$ where $\alpha < 0$. This state is *stable*. A solution displaced from the steady-state is exponentially damped towards the steady-state while oscillating around it.
6. Both r_1 and r_2 are complex with positive real part, so $r_1 = \alpha + i\beta$ and $r_2 = \alpha - i\beta$ where $\alpha > 0$. This state is *unstable*. A solution displaced from the steady-state will exponentially move away from the steady-state while oscillating around it.

Linear stability analysis provides a way to determine whether a steady-state of a nonlinear system is stable or not. If a steady-state is stable then nonlinear terms neglected in the analysis cannot alter this. Similarly, if a steady-state is unstable, nonlinear terms neglected in the analysis cannot make it stable. When a steady-state is unstable in a nonlinear system, a phase transition or bifurcation to a nonequilibrium steady-state occurs (Reichl (1998)). Linear stability analysis can tell us when this change of state will occur, but it cannot tell us the form of the new state.

4.3.1 Linear Stability Analysis for Diffusive Systems

The Brusselator and 1-D cortex systems also include a diffusion term. The **Brusselator** system has the form,

$$\dot{x} = f(x, y) + \kappa_1 \nabla^2 x \tag{4.18}$$

$$\dot{y} = g(x, y) + \kappa_2 \nabla^2 y \tag{4.19}$$

where $x = \rho_X(r, t)$, $y = \rho_Y(r, t)$ and κ_1, κ_2 are the diffusion coefficients. We can linearize the above system using the method outlined in Sec. 4.3, but we also need to consider the diffusion

term. Taking the Laplacian of $x = x_0 + \delta_x$ and $y = y_0 + \delta_y$ gives,

$$\nabla^2 x = \nabla^2 \delta_x \quad (4.20)$$

$$\nabla^2 y = \nabla^2 \delta_y \quad (4.21)$$

Hence, using the above result and Sec. 4.3, the linearized system for the Brusselator will take the form,

$$\frac{d}{dt} \begin{bmatrix} \delta_x \\ \delta_y \end{bmatrix} = \begin{bmatrix} f_x(x_0, y_0) + \kappa_1 \nabla^2 & f_y(x_0, y_0) \\ g_x(x_0, y_0) & g_y(x_0, y_0) + \kappa_1 \nabla^2 \end{bmatrix} \begin{bmatrix} \delta_x \\ \delta_y \end{bmatrix}. \quad (4.22)$$

For the **1-D model of the cortex** (detailed shortly) the system equations have the mathematical form,

$$\dot{x} = f(x, y) + \kappa_1 \frac{\partial^2 h(x)}{\partial x^2} \quad (4.23)$$

$$\dot{y} = g(x, y) + \kappa_2 \frac{\partial^2 k(x)}{\partial x^2}. \quad (4.24)$$

Expanding $h(x)$ and $k(x)$ about $(x = x_0 + \delta_x, y = y_0 + \delta_y)$ to first order gives,

$$h(x_0 + \delta_x) = h(x_0) + h_x(x_0) \delta_x \quad (4.25)$$

$$k(x_0 + \delta_x) = k(x_0) + k_x(x_0) \delta_x \quad (4.26)$$

and then operating on both sides with $\partial^2 / \partial x^2$ gives,

$$\frac{\partial^2 h(x_0 + \delta_x)}{\partial x^2} = h_x(x_0) \frac{\partial^2 \delta_x}{\partial x^2} \quad (4.27)$$

$$\frac{\partial^2 k(x_0 + \delta_x)}{\partial x^2} = k_x(x_0) \frac{\partial^2 \delta_x}{\partial x^2}. \quad (4.28)$$

Therefore the linearized system for the 1-D cortex will take the form,

$$\frac{d}{dt} \begin{bmatrix} \delta_x \\ \delta_y \end{bmatrix} = \begin{bmatrix} f_x(x_0, y_0) + \kappa_1 h_x(x_0) \frac{\partial^2}{\partial x^2} & f_y(x_0, y_0) \\ g_x(x_0, y_0) + \kappa_2 k_x(x_0) \frac{\partial^2}{\partial x^2} & g_y(x_0, y_0) \end{bmatrix} \begin{bmatrix} \delta_x \\ \delta_y \end{bmatrix}. \quad (4.29)$$

In order to perform stability analysis on linear systems containing a diffusion term, we Fourier transform the system to wavenumber space then investigate eigenvalue stability in Fourier space. This technique applied first to the linear Brusselator (Sec. 4.4) and later to the 1-D cortex (Secs 3.6–3.8).

4.4 Linear Stability Analysis of the Brusselator

In order to use linear stability analysis on the rate equations of the Brusselator (Eqs. (4.1-4.2)), we linearize the system about its steady-state (Eq. (4.4)). Writing $\rho_X(r, t)$ and $\rho_Y(r, t)$ as,

$$\rho_X(r, t) = \frac{\kappa_1}{\kappa_4} + \delta_x(r, t) \quad (4.30)$$

$$\rho_Y(r, t) = \frac{\kappa_2 \kappa_4}{\kappa_1 \kappa_3} + \delta_y(r, t), \quad (4.31)$$

where δ_x and δ_y are small space and time-dependent perturbations, linearizing gives,

$$\frac{d}{dt} \begin{bmatrix} \delta_x(r, t) \\ \delta_y(r, t) \end{bmatrix} = \begin{bmatrix} D_X \nabla^2 + \kappa_2 - 1 & -\kappa_1^2 \\ -\kappa_2 & D_Y \nabla^2 - \kappa_1^2 \end{bmatrix} \begin{bmatrix} \delta_x(r, t) \\ \delta_y(r, t) \end{bmatrix} \quad (4.32)$$

where, following Chaturvedi *et al.* (1977), $\kappa_3 = \kappa_4 = 1$ for simplicity. We will use the 2×2 matrix in the above equation for stability analysis but first will introduce the possibility of noise entering the system. Chaturvedi *et al.* apply stochastic analysis to the Brusselator system, in which chemical noise has been incorporated. The rate equation with noise included is given as,

$$\frac{d}{dt} \begin{bmatrix} \delta_x(\mathbf{r}, t) \\ \delta_y(\mathbf{r}, t) \end{bmatrix} = -\mathbf{A} \begin{bmatrix} \delta_x(\mathbf{r}, t) \\ \delta_y(\mathbf{r}, t) \end{bmatrix} + \mathbf{D} \begin{bmatrix} \xi_x(\mathbf{r}, t) \\ \xi_y(\mathbf{r}, t) \end{bmatrix} \quad (4.33)$$

where

$$\mathbf{A} = \begin{bmatrix} -D_X \nabla^2 - \kappa_2 + 1 & -\kappa_1^2 \\ \kappa_2 & -D_Y \nabla^2 + \kappa_1^2 \end{bmatrix} \quad (4.34)$$

$$\mathbf{D} = 2(\kappa_2 \kappa_1)^{1/2} \begin{bmatrix} 1 & -1/2 \\ -1/2 & 0 \end{bmatrix}^{1/2}. \quad (4.35)$$

The terms $\xi_x(\mathbf{r}, t), \xi_y(\mathbf{r}, t)$ are white-noise terms defined to satisfy the mean and correlation properties

$$\langle \xi_m(\mathbf{r}, t) \rangle = 0, \quad \langle \xi_m(\mathbf{r}, t) \xi_n(\mathbf{r}', t') \rangle = \delta_{nm} \delta(\mathbf{r} - \mathbf{r}') \delta(t - t') \quad (4.36)$$

Note that \mathbf{A} is equivalent to the matrix derived via linearization in Eq. (4.32) except it has been rearranged so that it carries an explicit negative sign. Chaturvedi *et.al* choose to do this in order that Eq. (4.33) takes the form of a two-variable Ornstein-Uhlenbeck (OU) process. There is well-defined stochastic calculus for OU systems that allows properties such as correlation length and correlation time to be calculated. The analysis that Chaturvedi *et al.* give for the Brusselator system is directly related to analysis that Steyn-Ross *et al.* (2003) perform for the one-dimensional cerebral cortex. Both systems exhibit analogous behaviour and hence the Brusselator serves as a well known reference example.

In order to analyse the stability of the steady-state branch for the Brusselator system, we have to take into account the diffusion term. We follow Chaturvedi *et al.*, and use Fourier transform theory for an *infinite* system in order to simplify the Fourier transform mathematics. Defining spatial Fourier transforms which map the three-dimensional position \mathbf{r} to the three-dimensional wavenumber \mathbf{q} as,

$$\tilde{\delta}_x(\mathbf{q}, t) \equiv \int \int \int_{-\infty}^{+\infty} e^{-i2\pi\mathbf{q}\cdot\mathbf{r}} \delta_x(\mathbf{r}, t) d\mathbf{r} \quad (4.37)$$

$$\tilde{\delta}_y(\mathbf{q}, t) \equiv \int \int \int_{-\infty}^{+\infty} e^{-i2\pi\mathbf{q}\cdot\mathbf{r}} \delta_y(\mathbf{r}, t) d\mathbf{r} \quad (4.38)$$

we obtain the Fourier transform of Eq. 4.32

$$\frac{d}{dt} \begin{bmatrix} \tilde{\delta}_x(\mathbf{q}, t) \\ \tilde{\delta}_y(\mathbf{q}, t) \end{bmatrix} = -\tilde{\mathbf{A}}(q^2) \begin{bmatrix} \tilde{\delta}_x(\mathbf{q}, t) \\ \tilde{\delta}_y(\mathbf{q}, t) \end{bmatrix} \quad (4.39)$$

where

$$\tilde{\mathbf{A}}(q^2) = \begin{bmatrix} D_x q^2 - \kappa_2 + 1 & -\kappa_1^2 \\ \kappa_2 & D_Y q^2 + \kappa_1^2 \end{bmatrix}. \quad (4.40)$$

We can now use linear stability theory on the $\tilde{\mathbf{A}}(q^2)$ matrix in Eq. (4.39) to determine the stability of the steady-state for values of $|q|$.

The stability analysis that follows is a summary of the analysis presented by Chaturvedi *et al.* The eigenvalues of $\tilde{\mathbf{A}}(q^2)$ are given by,

$$\begin{aligned}\lambda_1, \lambda_2 &= \frac{1}{2}[(D_X + D_Y)q^2 + 1 + \kappa_1^2 - \kappa_2 \\ &\quad \pm \{[(D_X + D_Y)q^2 + \kappa_1^2 + 1 - \kappa_2]^2 - 4[(D_X q^2 - \kappa_2 + 1)(D_Y q^2 + \kappa_1^2) + \kappa_1^2 \kappa_2]\}^{1/2}] \\ &= \frac{1}{2}\{(D_X + D_Y)q^2 + 1 + \kappa_1^2 - \kappa_2 \pm [(\delta - \kappa_2 + \kappa_1^2)^2 - 4\delta\kappa_1^2]^{1/2}\}\end{aligned}\tag{4.41}$$

where $\delta = 1 + (D_X - D_Y)q^2$. Due to the explicit negative sign in Eq. (4.39) the homogeneous steady-state will be stable provided that both eigenvalues are *positive*. There are two marginally stable situations: (a) λ_1, λ_2 real and positive with $\lambda_2 \rightarrow 0^+$ (the ‘‘soft mode’’ instability, i.e., spatial oscillations); (b) λ_1, λ_2 complex with $\text{Re}(\lambda_1, \lambda_2) \rightarrow 0^+$ (the ‘‘hard mode’’ instability, i.e., temporal oscillations). In order for the eigenvalues defined in Eq. (4.41) to be real, we require

$$(\delta - \kappa_2 + \kappa_1^2)^2 - 4\delta\kappa_1^2 > 0\tag{4.42}$$

For $\delta < 0$, λ_1 and λ_2 are always real. For $\delta > 0$, λ_1 and λ_2 are real if either

$$\kappa_2 > (\sqrt{\delta} + \kappa_1)^2 \quad \text{or} \quad \kappa_1 < (\sqrt{\delta} - \kappa_1)^2\tag{4.43}$$

λ_1 and λ_2 are real and positive if, in addition to Eq. (4.43), we have,

$$\kappa_2 < (D_X + D_Y)q^2 + 1 + \kappa_1^2\tag{4.44}$$

and

$$(D_X q^2 - \kappa^2 + 1)(D_Y q^2 + \kappa_1^2) + \kappa_1^2 \kappa_2 > 0\tag{4.45}$$

$$\Rightarrow \quad \kappa_2 < 1 + D_X q^2 + (\kappa_1^2/D_Y q^2) + (D_X \kappa_1^2/D_Y)\tag{4.46}$$

The soft mode instability is approached as $\lambda_2 \rightarrow 0^+$ along the real axis with λ_1 real and positive. This is the case if Eq. (4.43) and Eq. (4.44) are satisfied and

$$\kappa_2 \rightarrow \kappa_{2S}(q^2) \equiv 1 + D_X q^2 + (\kappa_1^2/D_Y q^2) + (D_X \kappa_1^2/D_Y)\tag{4.47}$$

from below. Fixing κ_1 , D_X , and D_Y , the minimum of $\kappa_{2S}(q^2)$ occurs at

$$|q| = \kappa_1 / (D_X D_Y)^{1/2} \quad (4.48)$$

giving a minimum value of

$$\kappa_{2S} = [1 + \kappa_1 (D_X / D_Y)^{1/2}]^2. \quad (4.49)$$

Equation (4.49) gives the threshold for the **soft mode** instability. As κ_2 is increased beyond κ_{2S} a bifurcation to a dissipative steady-state which exhibits **spatial oscillations** will occur. The *marginally stable* configuration is characterized by the wave vector given in Eq. (4.48). The steady-state is stable for any spatial mode with wavenumber $q < [1 + \kappa_1 (D_X / D_Y)^{1/2}]^2$, and unstable for any spatial mode with wavenumber $q > [1 + \kappa_1 (D_X / D_Y)^{1/2}]^2$.

In order for the eigenvalues defined in Eq. (4.41) to be complex, we require $(\delta - \kappa_2 + \kappa_1^2)^2 - 4\delta\kappa_1^2 < 0$, i.e.,

$$(\sqrt{\delta} - \kappa_1)^2 < \kappa_2 < (\sqrt{\delta} + \kappa_1)^2, \quad \delta > 0. \quad (4.50)$$

The eigenvalue's real parts are positive if

$$\kappa_2 < (D_X + D_Y)q^2 + 1 + \kappa_1^2. \quad (4.51)$$

The eigenvalues λ_1 and λ_2 become purely imaginary as

$$\kappa_2 \rightarrow \kappa_1^2 + (D_X + D_Y)q^2 \quad (4.52)$$

from below. The minimum of $\kappa_{2H}(q^2)$ occurs when $q = 0$ and hence the threshold for the **hard mode** instability is

$$\kappa_{2H} = 1 + \kappa_1^2 \quad (4.53)$$

As κ_2 is increased beyond κ_{2H} a bifurcation to a dissipative steady-state exhibiting **temporal oscillations** will occur. For the Brusselator system, which of the two instabilities occurs first

depends on the relative magnitudes of D_X and D_Y . The soft mode instability occurs first if

$$\kappa_{2S} < \kappa_{2H} \quad (4.54)$$

and vice versa. The prediction of the soft- and hard-mode instabilities allow us to predict when a bifurcation to a nonequilibrium state will occur.

4.5 Spatial Correlation Functions

For a two-variable OU system in the steady-state, such as the one defined by Eq. (4.33), the fluctuation covariance in Fourier space is defined as (Chaturvedi *et al.* (1977))

$$\tilde{\mathbf{G}}(\mathbf{q}, \mathbf{q}') \equiv 2\pi\delta(\mathbf{q} + \mathbf{q}')\tilde{\mathbf{G}}(\mathbf{q}) \quad (4.55)$$

where

$$\tilde{\mathbf{G}}(\mathbf{q}) = \frac{(\text{Det}\tilde{\mathbf{A}})\mathbf{D}^2 + [\tilde{\mathbf{A}} - (\text{Tr}\tilde{\mathbf{A}})\mathbf{I}]\mathbf{D}^2[\tilde{\mathbf{A}} - (\text{Tr}\tilde{\mathbf{A}})\mathbf{I}]^T}{2(\text{Det}\tilde{\mathbf{A}})(\text{Tr}\tilde{\mathbf{A}})}. \quad (4.56)$$

Once $\tilde{\mathbf{G}}(\mathbf{q}, \mathbf{q}')$ has been calculated, then, via Fourier inversion, the spatial covariance can be derived. Chaturvedi *et al.* calculate the spatial covariance for the Brusselator system. They find that the spatial covariance function is characterized by two correlation lengths and also a wave vector. As the soft-mode threshold is approached, the covariance function is dominated by an exponentially decreasing term and a purely oscillatory term. In contrast, near the point of hard-mode instability, the covariance function is characterized by a long-range $1/|\mathbf{r} - \mathbf{r}'|$ dependence.

I will now consider the cortical system to which similar analysis techniques will be applied.

4.6 Linearization of the 1-D Cortex

In order to generalize the “zero-dimensional” homogeneous cortex (Eqs. 3.60–3.63) to a 1-D line of cortical “mass”, Steyn-Ross *et al.* (2003) explicitly include weak spatial variation by retaining the $\partial^2/\partial x^2$ terms in the wave equations for the long-range macrocolumn contributions Eqs. (3.26–3.27). Allowing spatial variability to occur, and once again including noise terms via

the subcortical inputs, results in the following PDEs:

$$\tau_e \frac{dh_e}{dt} = (h_e^{\text{rest}} - h_e) + \psi_{ee}(h_e)I_{ee}(h_e) + \psi_{ie}(h_e)I_{ie}(h_i) \quad (4.57)$$

$$\tau_i \frac{dh_i}{dt} = (h_i^{\text{rest}} - h_i) + \psi_{ei}(h_i)I_{ei}(h_e) + \psi_{ii}(h_i)I_{ii}(h_i) \quad (4.58)$$

$$\left(\frac{d}{dt} + \gamma_e\right)^2 I_{ee}(h_e) = [N_{ee}^\beta \mathcal{S}_e(h_e) + \phi_e(h_e) + \langle p_{ee} \rangle] G_e \gamma_e e + \Gamma_1(x, t) \quad (4.59)$$

$$\left(\frac{d}{dt} + \gamma_e\right)^2 I_{ei}(h_e) = [N_{ei}^\beta \mathcal{S}_e(h_e) + \phi_i(h_e) + \langle p_{ei} \rangle] G_e \gamma_e e + \Gamma_2(x, t) \quad (4.60)$$

$$\left(\frac{d}{dt} + \frac{\gamma_i}{\lambda_{\text{GABA}}}\right)^2 I_{ie}(h_i) = [N_{ie}^\beta \mathcal{S}_i(h_i) + \langle p_{ie} \rangle] \frac{G_i \gamma_i e}{\lambda_{\text{GABA}}} + \Gamma_3(x, t) \quad (4.61)$$

$$\left(\frac{d}{dt} + \frac{\gamma_i}{\lambda_{\text{GABA}}}\right)^2 I_{ii}(h_i) = [N_{ii}^\beta \mathcal{S}_i(h_i) + \langle p_{ii} \rangle] \frac{G_i \gamma_i e}{\lambda_{\text{GABA}}} + \Gamma_4(x, t) \quad (4.62)$$

$$\left[\left(\frac{d}{dt} + \bar{v}\Lambda_{ee}\right)^2 - \bar{v}^2 \frac{\partial^2}{\partial x^2}\right] \phi_e(h_e) = \bar{v}\Lambda_{ee} N_{ee}^\alpha \left(\frac{d}{dt} + \bar{v}\Lambda_{ee}\right) \mathcal{S}_e(h_e) \quad (4.63)$$

$$\left[\left(\frac{d}{dt} + \bar{v}\Lambda_{ei}\right)^2 - \bar{v}^2 \frac{\partial^2}{\partial x^2}\right] \phi_i(h_e) = \bar{v}\Lambda_{ei} N_{ei}^\alpha \left(\frac{d}{dt} + \bar{v}\Lambda_{ei}\right) \mathcal{S}_e(h_e) \quad (4.64)$$

The only differences between the set of stochastic equations (3.36–3.38) and the set defined above are: (i) spatial variation via the Laplacian term in the $\phi_e(h_e), \phi_i(h_e)$ rate equations has been included, (ii) the noise terms are redefined such that they are now a function of time *and* space, and (iii) the derivatives have been mapped to partial derivatives to indicate that the variables x and t are independent. The four Γ_j noise terms in Eqs. (4.59–4.62) are redefined as,

$$\Gamma_1(x, t) = \alpha_{ee} \sqrt{\langle p_{ee} \rangle} \xi_1(x, t) G_e \gamma_e e \quad \Gamma_2(x, t) = \alpha_{ei} \sqrt{\langle p_{ei} \rangle} \xi_2(x, t) G_e \gamma_e e \quad (4.65)$$

$$\Gamma_3(x, t) = \frac{\alpha_{ie} \sqrt{\langle p_{ie} \rangle} \xi_3(x, t) G_i \gamma_i e}{\lambda_{\text{GABA}}} \quad \Gamma_4(x, t) = \frac{\alpha_{ii} \sqrt{\langle p_{ii} \rangle} \xi_4(x, t) G_i \gamma_i e}{\lambda_{\text{GABA}}} \quad (4.66)$$

where the four ξ_m terms are zero-mean Gaussian-distributed delta-correlated white-noise sources,

$$\langle \xi_m(x, t) \rangle = 0, \quad \langle \xi_m(x, t) \xi_m(x', t') \rangle = \delta_{mn} \delta(x - x') \delta(t - t'). \quad (4.67)$$

We emphasize that the stationary states of the 1-D cortex (Eqs. (4.57–4.64)) are *identical* to the stationary states of the spatially homogeneous cortex (derived in Section 3.6).

Following Section 3.7, the “adiabatic” simplification is adopted, but the $\frac{\partial^2}{\partial x^2}$ term is retained. In this “spatio-adiabatic” limit, the cortical inputs of Eqs. (4.59–4.62) reduce to,

$$I_{ee}(h_e) = [N_{ee}^\beta \mathcal{S}_e(h_e) + \phi_e(h_e) + \langle p_{ee} \rangle] G_e e / \gamma_e + \Gamma_1(x, t) / \gamma_e^2 \quad (4.68)$$

$$I_{ei}(h_e) = [N_{ei}^\beta \mathcal{S}_e(h_e) + \phi_i(h_e) + \langle p_{ei} \rangle] G_e e / \gamma_e + \Gamma_2(x, t) / \gamma_e^2 \quad (4.69)$$

$$I_{ie}(h_i) = \lambda_{\text{GABA}} [N_{ie}^\beta \mathcal{S}_i(h_i) + \langle p_{ie} \rangle] G_i e / \gamma_i + \lambda_{\text{GABA}}^2 \Gamma_3(x, t) / \gamma_i^2 \quad (4.70)$$

$$I_{ii}(h_i) = \lambda_{\text{GABA}} [N_{ii}^\beta \mathcal{S}_i(h_i) + \langle p_{ii} \rangle] G_i e / \gamma_i + \lambda_{\text{GABA}}^2 \Gamma_4(x, t) / \gamma_i^2 \quad (4.71)$$

while the long-range inputs (Eqs. (4.63)–(4.64)) become,

$$\phi_e(h_e) = \frac{1}{\Lambda_{ee}^2} \frac{\partial^2 \phi_e(h_e)}{\partial x^2} + N_{ee}^\alpha \mathcal{S}_e(h_e) \quad (4.72)$$

$$\phi_i(h_e) = \frac{1}{\Lambda_{ei}^2} \frac{\partial^2 \phi_i(h_e)}{\partial x^2} + N_{ei}^\alpha \mathcal{S}_e(h_e). \quad (4.73)$$

Substituting Eqs. (4.68)–(4.73) back into Eqs. (4.57)–(4.64) gives a new system of equations,

$$\frac{\partial h_e}{\partial t} = F_1(h_e, h_i) + \Gamma_e(x, t) \quad (4.74)$$

$$\frac{\partial h_i}{\partial t} = F_2(h_e, h_i) + \Gamma_i(x, t) \quad (4.75)$$

where the F_1, F_2 are *drift* terms defined by,

$$F_1(h_e, h_i) = \frac{1}{\tau_e} \left\{ (h_e^{\text{rest}} - h_e) + \psi_{ee}(h_e) [(N_{ee}^\alpha + N_{ee}^\beta) \mathcal{S}_e(h_e) + \frac{1}{\Lambda_{ee}^2} \frac{\partial^2 \phi_e(h_e)}{\partial x^2} + \langle p_{ee} \rangle] G_e e / \gamma_e \right. \\ \left. + \lambda_{\text{GABA}} \psi_{ie}(h_e) [N_{ie}^\beta \mathcal{S}_i(h_i) + \langle p_{ie} \rangle] G_i e / \gamma_i \right\} \quad (4.76)$$

$$F_2(h_e, h_i) = \frac{1}{\tau_i} \left\{ (h_i^{\text{rest}} - h_i) + \psi_{ei}(h_i) [(N_{ei}^\alpha + N_{ei}^\beta) \mathcal{S}_e(h_e) + \frac{1}{\Lambda_{ei}^2} \frac{\partial^2 \phi_i(h_e)}{\partial x^2} + \langle p_{ei} \rangle] G_e e / \gamma_e \right. \\ \left. + \lambda_{\text{GABA}} \psi_{ii}(h_i) [N_{ii}^\beta \mathcal{S}_i(h_i) + \langle p_{ii} \rangle] G_i e / \gamma_i \right\} \quad (4.77)$$

and Γ_e, Γ_i are *diffusive noise* terms,

$$\Gamma_e(x, t) = b_{ee}\xi_1(x, t) + b_{ie}\xi_3(x, t) \quad (4.78)$$

$$\Gamma_i(x, t) = b_{ei}\xi_2(x, t) + b_{ii}\xi_4(x, t) \quad (4.79)$$

where the b_{jk} coefficients are,

$$b_{ee} = \psi_{ee}(h_e)\alpha_{ee}\sqrt{\langle p_{ee} \rangle}G_e e / \gamma_e \tau_e \quad (4.80)$$

$$b_{ei} = \psi_{ie}(h_e)\alpha_{ie}\sqrt{\langle p_{ie} \rangle}G_i e / \gamma_i \tau_e \quad (4.81)$$

$$b_{ie} = \lambda_{\text{GABA}}\psi_{ei}(h_i)\alpha_{ei}\sqrt{\langle p_{ei} \rangle}G_e e / \gamma_e \tau_i \quad (4.82)$$

$$b_{ii} = \lambda_{\text{GABA}}\psi_{ii}(h_i)\alpha_{ii}\sqrt{\langle p_{ii} \rangle}G_i e / \gamma_e \tau_i \quad (4.83)$$

In order to make theoretical predictions concerning the behaviour of the ‘‘spatio adiabatic’’ system (Eqs. (4.74–4.75)) we need to be linearize it about its *homogeneous* ($\partial^2/\partial x^2 \rightarrow 0$) steady-state equilibrium.

Following the linearization method outlined in section (4.3), we allow a small time- and space-dependent voltage-deviation ($\hat{h}_e(x, t), \hat{h}_i(x, t)$) away from the homogeneous steady state coordinate (h_e^0, h_i^0). Then the excitatory and inhibitory soma voltages at position x and time t can be written,

$$h_e(x, t) = h_e^0 + \hat{h}_e(x, t) \quad (4.84)$$

$$h_i(x, t) = h_i^0 + \hat{h}_i(x, t). \quad (4.85)$$

We note that evaluated at the homogeneous equilibrium, Eqs. (4.72)–(4.73) predicts,

$$\left. \frac{\partial \phi_e}{\partial h_e} \right|_{\text{eq.}} = N_{ee}^\alpha \left. \frac{\partial \mathcal{S}_e(h_e)}{\partial h_e} \right|_{\text{eq.}} \quad (4.86)$$

$$\left. \frac{\partial \phi_i}{\partial h_e} \right|_{\text{eq.}} = N_{ei}^\alpha \left. \frac{\partial \mathcal{S}_e(h_e)}{\partial h_e} \right|_{\text{eq.}} \quad (4.87)$$

Making use of Eqs. (4.27-4.28),

$$\frac{\partial^2 \phi_e(h_e^0 + \hat{h}_e(x, t))}{\partial x^2} \approx \left. \frac{\partial \phi_e}{\partial h_e} \right|_{\text{eq.}} \frac{\partial^2 \hat{h}_e(x, t)}{\partial x^2} \quad (4.88)$$

$$\frac{\partial^2 \phi_i(h_e^0 + \hat{h}_e(x, t))}{\partial x^2} \approx \left. \frac{\partial \phi_i}{\partial h_e} \right|_{\text{eq.}} \frac{\partial^2 \hat{h}_e(x, t)}{\partial x^2} \quad (4.89)$$

giving

$$\frac{\partial^2 \phi_e(h_e^0 + \hat{h}_e(x, t))}{\partial x^2} \approx N_{ee}^\alpha \left. \frac{d\mathcal{S}_e}{dh_e} \right|_{\text{eq.}} \frac{\partial^2 \hat{h}_e(x, t)}{\partial x^2} \quad (4.90)$$

$$\frac{\partial^2 \phi_i(h_e^0 + \hat{h}_e(x, t))}{\partial x^2} \approx N_{ei}^\alpha \left. \frac{d\mathcal{S}_e}{dh_e} \right|_{\text{eq.}} \frac{\partial^2 \hat{h}_e(x, t)}{\partial x^2} \quad (4.91)$$

Making use of Eqs. (4.90–4.91) we linearize about the homogeneous steady-state to obtain a pair of Langevin equations,

$$\frac{\partial}{\partial t} \begin{bmatrix} \hat{h}_e(x, t) \\ \hat{h}_i(x, t) \end{bmatrix} = \begin{bmatrix} J_{11} + \kappa_e \frac{\partial^2}{\partial x^2} & J_{12} \\ J_{21} + \kappa_i \frac{\partial^2}{\partial x^2} & J_{22} \end{bmatrix} \begin{bmatrix} \hat{h}_e(x, t) \\ \hat{h}_i(x, t) \end{bmatrix} + \begin{bmatrix} \Gamma_e(x, t) \\ \Gamma_i(x, t) \end{bmatrix}_{\text{eq.}} \quad (4.92)$$

where κ_e, κ_i are Fick's-law spatial diffusion coefficients [units: cm²/s],

$$\kappa_e = \frac{\psi_{ee}(h_e^0) \mathcal{S}_e^{(1)} N_{ee}^\alpha G_e e}{\Lambda_{ee}^2 \gamma_e \tau_e} \quad \kappa_i = \frac{\psi_{ei}(h_i^0) \mathcal{S}_e^{(1)} N_{ei}^\alpha G_e e}{\Lambda_{ei}^2 \gamma_i \tau_i} \quad (4.93)$$

and the J_{mn} terms are,

$$\begin{aligned}
J_{11} = & \left\{ -1 + \psi_{ee}^{(1)} \left[(N_{ee}^\alpha + N_{ee}^\beta) \mathcal{S}_e(h_e^0) + p_{ee} \right] G_{ee} e / \gamma_e \right. \\
& + \psi_{ee}(h_e^0) \left[(N_{ee}^\alpha + N_{ee}^\beta) \mathcal{S}_e^{(1)} \right] G_{ee} e / \gamma_e \\
& \left. + \lambda_{\text{GABA}} \psi_{ie}^{(1)} \left[N_{ie}^\beta \mathcal{S}_i(h_i^0) + p_{ie} \right] G_{ie} e / \gamma_i \right\} \frac{1}{\tau_e}
\end{aligned} \tag{4.94}$$

$$J_{12} = \lambda_{\text{GABA}} \psi_{ie}(h_e^0) N_{ie}^\beta \mathcal{S}_i^{(2)} G_{ie} e / \gamma_i \tau_e \tag{4.95}$$

$$J_{21} = \psi_{ei}(h_i^0) (N_{ei}^\alpha + N_{ei}^\beta) \mathcal{S}_i^{(1)} G_{ei} e / \gamma_i \tau_e \tag{4.96}$$

$$\begin{aligned}
J_{22} = & \left\{ -1 + \psi_{ei}^{(2)} \left[(N_{ei}^\alpha + N_{ei}^\beta) \mathcal{S}_e(h_e^0) + p_{ei} \right] G_{ei} e / \gamma_e \right. \\
& + \lambda_{\text{GABA}} \psi_{ii}^{(2)} \left[(N_{ii}^\beta) \mathcal{S}_i(h_i^0) + p_{ii} \right] G_{ii} e / \gamma_i \\
& \left. + \lambda_{\text{GABA}} \psi_{ii}(h_e^0) N_{ii}^\beta \mathcal{S}_i^{(2)} G_{ii} e / \gamma_i \right\} \frac{1}{\tau_i}
\end{aligned} \tag{4.97}$$

with partial derivatives of the weighting and sigmoid functions also evaluated at equilibrium,

$$\psi_{je}^{(1)} = \frac{\partial \psi_{je}}{\partial h_e} = \frac{-1}{|h_j^{\text{rev}} - h_e^{\text{rest}}|}, \quad \psi_{ji}^{(2)} = \frac{\partial \psi_{ji}}{\partial h_i} = \frac{-1}{|h_j^{\text{rev}} - h_i^{\text{rest}}|} \tag{4.98}$$

and,

$$\mathcal{S}_e^{(1)} = \left. \frac{\partial \mathcal{S}_e}{\partial h_e} \right|_{\text{eq.}}, \quad \mathcal{S}_i^{(2)} = \left. \frac{\partial \mathcal{S}_i}{\partial h_i} \right|_{\text{eq.}}. \tag{4.99}$$

Now that we have linearized Eqs. (4.74–4.75), stability prediction are fore coming, but first the approximation of a “infinite” brain must be made.

4.7 Infinite Brain

In a one-dimensional sense, we can think of the brain as having a length of approximately 40 cm. The cross-sectional width of a macrocolumn is $\sim 0.3\text{--}1$ mm. Hence on a macrocolumn scale, the cortex can be thought to have an “infinite” length. Making use of this approximation allows us to ignore the boundary conditions that otherwise would have to be imposed on our 1-D length of cortical mass. As in Sec. 4.4, we introduce Fourier transforms of the \hat{h}_e excitatory and \hat{h}_i inhibitory soma-voltage fluctuations, and of the ξ white-noise sources respectively, as the

variables $\tilde{h}_e, \tilde{h}_i, \tilde{\xi}$,

$$\tilde{h}_e(q, t) = \int_{-\infty}^{+\infty} e^{-iqx} \hat{h}_e(x, t) dx \quad (4.100)$$

$$\tilde{h}_i(q, t) = \int_{-\infty}^{+\infty} e^{-iqx} \hat{h}_i(x, t) dx \quad (4.101)$$

$$\tilde{\xi}(q, t) = \int_{-\infty}^{+\infty} e^{-iqx} \xi(x, t) dx. \quad (4.102)$$

These relations map the spatial position x in 1-D space, to the spatial frequency or *wavenumber* q in Fourier space. The corresponding inverse mappings from $q \rightarrow x$ are,

$$\hat{h}_e(x, t) = \frac{1}{2\pi} \int_{-\infty}^{+\infty} e^{iqx} \tilde{h}_e(q, t) dq \quad (4.103)$$

$$\hat{h}_i(x, t) = \frac{1}{2\pi} \int_{-\infty}^{+\infty} e^{iqx} \tilde{h}_i(q, t) dq \quad (4.104)$$

$$\xi(x, t) = \frac{1}{2\pi} \int_{-\infty}^{+\infty} e^{iqx} \tilde{\xi}(q, t) dq \quad (4.105)$$

Fourier transforming the Langevin equations (Eqs. (4.92)), we obtain,

$$\frac{\partial}{\partial t} \begin{bmatrix} \tilde{h}_e(q, t) \\ \tilde{h}_i(q, t) \end{bmatrix} = \begin{bmatrix} J_{11} - \kappa_e q^2 & J_{12} \\ J_{21} - \kappa_i q^2 & J_{22} \end{bmatrix} \begin{bmatrix} \tilde{h}_e(q, t) \\ \tilde{h}_i(q, t) \end{bmatrix} + \begin{bmatrix} \tilde{\Gamma}_e(q, t) \\ \tilde{\Gamma}_i(q, t) \end{bmatrix}_{\text{eq.}} \quad (4.106)$$

where

$$\tilde{\Gamma}_e(q, t) = b_{ee}\tilde{\xi}_1(q, t) + b_{ie}\tilde{\xi}_3(q, t) \quad (4.107)$$

$$\tilde{\Gamma}_i(q, t) = b_{ie}\tilde{\xi}_1(q, t) + b_{ie}\tilde{\xi}_3(q, t) \quad (4.108)$$

and where the Fourier-transformed white-noise terms satisfy the correlation property

$$\langle \tilde{\xi}_m(q, t) \tilde{\xi}_n(q', t') \rangle = 2\pi \delta_{mn} \delta(q + q') \delta(t - t') \quad (4.109)$$

Proof of Eq. (4.109): Fourier transforming the expectation $\langle \xi_m(x, t) \xi_m(x', t') \rangle$ from x -space to q -space gives

$$\langle \tilde{\xi}_m(q, t) \tilde{\xi}_n(q', t') \rangle = \left\langle \int_{-\infty}^{+\infty} \int_{-\infty}^{+\infty} e^{iqx} e^{iq'x'} \xi_m(x, t) \xi_m(x', t') dx dx' \right\rangle \quad (4.110)$$

$$= \int_{-\infty}^{+\infty} \int_{-\infty}^{+\infty} e^{iqx} e^{iq'x'} \langle \xi_m(x, t) \xi_m(x', t') \rangle dx dx' \quad (4.111)$$

Using Eq. (4.67)

$$= \delta_{nm} \delta(t - t') \int_{-\infty}^{+\infty} \int_{-\infty}^{+\infty} e^{iqx} e^{iq'x'} \delta(x - x') dx dx' \quad (4.112)$$

and the integral over x' collapses to give,

$$\langle \tilde{\xi}_m(q, t) \tilde{\xi}_n(q', t') \rangle = \delta_{nm} \delta(t - t') \int_{-\infty}^{+\infty} e^{i(q+q')x} dx \quad (4.113)$$

$$= 2\pi \delta_{mm} \delta(q + q') \delta(t - t') \quad (4.114)$$

where the second equality follows from the Fourier transform of unity,

$$\int_{-\infty}^{+\infty} 1 e^{-iuv} dv = 2\pi \delta(u) \quad (4.115)$$

Steyn-Ross *et al.* (2003) proceed by transforming Eq. (4.106) into a two-variable OU system.

First, a diagonal 2×2 diffusion matrix \mathbf{D} is defined,

$$\mathbf{D} = \begin{bmatrix} D_1 & 0 \\ 0 & D_2 \end{bmatrix} \quad (4.116)$$

whose elements are obtained by using the correlation identity (Eq. (4.109)) to compute the expectation values of the $\tilde{\Gamma}_e, \tilde{\Gamma}_i$ noise terms, giving

$$\langle \tilde{\Gamma}_e(q, t) \tilde{\Gamma}_e(q', t') \rangle = 2\pi D_1 \delta(q + q') \delta(t - t') \quad (4.117)$$

$$\langle \tilde{\Gamma}_i(q, t) \tilde{\Gamma}_i(q', t') \rangle = 2\pi D_2 \delta(q + q') \delta(t - t') \quad (4.118)$$

where

$$D_1 = (b_{ee})_{\text{eq.}}^2 + (b_{ie})_{\text{eq.}}^2 \quad (4.119)$$

$$D_2 = (b_{ei})_{\text{eq.}}^2 + (b_{ii})_{\text{eq.}}^2 \quad (4.120)$$

and $(b_{jk})_{\text{eq.}}$ are the noise coefficients (Eq. (4.80)–(4.83)) evaluated at equilibrium. The drift matrix in Eq. (4.106) is redefined to carry an explicit negative sign. These two steps result in the following OU system,

$$\frac{\partial}{\partial t} \begin{bmatrix} \tilde{h}_e(q, t) \\ \tilde{h}_i(q, t) \end{bmatrix} = -\mathbf{A}(q) \begin{bmatrix} \tilde{h}_e(q, t) \\ \tilde{h}_i(q, t) \end{bmatrix} + \sqrt{\mathbf{D}} \begin{bmatrix} \tilde{\xi}_e(q, t) \\ \tilde{\xi}_i(q, t) \end{bmatrix} \quad (4.121)$$

where

$$\mathbf{A}(q) = \begin{bmatrix} -J_{11} + \kappa_e q^2 & -J_{12} \\ -J_{21} + \kappa_i q^2 & -J_{22} \end{bmatrix}_{\text{eq.}} \quad (4.122)$$

and the J_{mn} terms are defined earlier in Eqs.(4.94–4.97).

4.8 Stability of the Spatio-Adiabatic system

As discussed in Sec. 4.4 for the Brusselator, in order for the homogeneous steady-state of Eq. (4.74–4.75) to be stable, we require the eigenvalues of $\mathbf{A}(q)$ to have *positive* real parts. The eigenvalues λ_1, λ_2 of matrix $\mathbf{A}(q)$ are,

$$\lambda_1, \lambda_2 = -\frac{1}{2}(c_1 - \kappa_e q^2) \pm \frac{1}{2} \sqrt{(c_1 - \kappa_e q^2)^2 - 4(c_2 + c_3 q^2)} \quad (4.123)$$

where c_1, c_2, c_3 have been defined as,

$$c_1 = J_{11} + J_{22} \quad (4.124)$$

$$c_2 = J_{11} J_{22} - J_{12} J_{21} \quad (4.125)$$

$$c_3 = \kappa_i J_{12} - \kappa_e J_{22}. \quad (4.126)$$

From previous analysis done by Steyn-Ross *et al.* (1999) we know, for the top- and bottom-branch steady-state solutions, that $c_1 < 0$, $c_2 > 0$, and both J_{12} and J_{22} are negative with

$|J_{12}| < |J_{22}|$. Furthermore, the weighting function $\psi_{ee}(h_e)$ will always be positive provided the soma voltage never exceeds the excitatory reversal potential $h_e^{\text{rev}} = +45$ mV. Hence $\kappa_e > 0$ via Eq. (4.93). Using the default values listed in Table 3.1 we find $0 < \kappa_i < \kappa_e$ (i.e., the long-range cortico-cortical $e-i$ diffusivity is *weaker* than the long-range $e-e$ diffusivity) which gives $c_3 > 0$. Taking the signs of c_1 and κ_e into account, we rewrite Eq. (4.123) as,

$$\lambda_1, \lambda_2 = \frac{1}{2}(|c_1| + \kappa_e q^2) \pm \frac{1}{2} \sqrt{(|c_1| + \kappa_e q^2)^2 - 4(c_2 + c_3 q^2)} \quad (4.127)$$

If both eigenvalues are real then we require,

$$(|c_1| + \kappa_e q^2)^2 - 4(c_2 + c_3 q^2) > 0 \quad (4.128)$$

which if true,

$$(|c_1| + \kappa_e q^2) > \sqrt{(|c_1| + \kappa_e q^2)^2 - 4(c_2 + c_3 q^2)} > 0. \quad (4.129)$$

From Eq. (4.129) and Eq. (4.128) it is obvious that if both eigenvalues are real, they both will be positive.

If the discriminant of Eq. (4.129) is negative, then the eigenvalues will form a complex conjugate pair with real parts given by,

$$\text{Re}(\lambda_1, \lambda_2) = \frac{1}{2}(|c_1| + \kappa_e q^2) \quad (4.130)$$

which is always positive. Hence for the above parameters, as the real parts of λ_1 and λ_2 are always positive for the top and bottom branch of the inverted S-bend (see Fig. 3.13), these steady-states are stable.

If we allow for the possibility of the long-range cortico-cortical $e-i$ diffusivity *dominating* the long-range $e-e$ diffusivity, then the possibility exists for c_3 to become negative. This will be the case if

$$\kappa_i > \frac{|J_{22}|}{|J_{12}|} \kappa_e \quad \rightarrow \quad c_3 < 0. \quad (4.131)$$

For this case let us examine the possibility of the top and bottom branch becoming unstable. The stability thresholds are given by (a) λ_1, λ_2 complex and $\text{Re}(\lambda_1, \lambda_2) \rightarrow 0^+$ (the hard mode instability) and (b) λ_1, λ_2 real and positive with $\lambda_2 \rightarrow 0^+$ (the soft mode instability). We now

consider each threshold in turn:

(a) When the eigenvalues form a complex conjugate pair, c_3 has no effect on the real part given by Eq. (4.130). As the real part is always positive there is no possibility of the hard mode instability occurring. Therefore temporal oscillations will not occur.

(b) The eigenvalues will be real when the discriminant is positive,

$$(|c_1| + \kappa_e q^2)^2 > 4(c_2 + c_3 q^2). \quad (4.132)$$

They will be *real and positive* if, in addition to Eq. (4.132), we have

$$c_2 + c_3 q^2 > 0. \quad (4.133)$$

From Eq. (4.127) we see that λ_1 remains positive while $\lambda_2 \rightarrow 0^+$ if in addition to Eq. (4.132),

$$c_2 + c_3 q^2 = 0. \quad (4.134)$$

This marginally-stable configuration is characterized by the wave vector q_s ,

$$q_s = \sqrt{\frac{c_2}{|c_3|}} \quad (\text{soft-mode instability}). \quad (4.135)$$

For $c_2 > 0$ and $c_3 < 0$, then any wavenumber $q > q_s$ will guarantee a *negative* λ_2 eigenvalue, resulting in an unstable steady-state for that q value. A bifurcation to a new state must then occur. Of note here is that for a specific value of *anaesthetic concentration* λ_{GABA} , the q_s value occurs at different top and bottom branch steady-state values (Fig. 3.11). Hence for wavenumbers greater than q_s there are two possible outcomes: (i) If only one equilibrium steady-state is unstable then a bifurcation from the unstable steady-state to the stable equilibrium steady-state will occur. (ii) If both equilibrium steady-state solutions are *unstable*, then a bifurcation to a *non-equilibrium* steady-state (i.e., a state which does *not* lie on the S-bend) will occur.

4.9 Spatial Covariance of \hat{h}_e

In order to quantify the degree to which voltage fluctuations at separate points x and x' are correlated Steyn-Ross *et al.* (2003) define the steady-state spatial covariance $G(x, x')$,

$$G(x, x') = \lim_{t \rightarrow \infty} \langle \hat{h}_e(x, t) \hat{h}_e(x', t) \rangle \quad (4.136)$$

They then assume that the voltage covariance will depend only on the separation $|x - x'|$ rather than the absolute positions x and x' , so the spatial covariance can be collapsed to,

$$G(x, x') = G(|x - x'|). \quad (4.137)$$

In order to determine the spatial covariance $G(x, x')$, the covariance in Fourier space is determined,

$$\tilde{G}(q, q') = \langle \hat{h}_e(q, t) \hat{h}_e(q', t) \rangle \quad (4.138)$$

and then Fourier inverted to give $G(x, x')$,

$$\begin{aligned} G(x, x') &= \frac{1}{(2\pi)^2} \int \int_{-\infty}^{+\infty} e^{iqx} e^{iq'x'} \tilde{G}(q, q') dq dq' \\ &= \frac{1}{2\pi} \int_{-\infty}^{+\infty} e^{iq|x-x'|} \tilde{G}(q) dq \end{aligned} \quad (4.139)$$

The 2×2 steady-state covariance matrix is defined as

$$\tilde{\mathbf{G}}(q, q') = \lim_{t \rightarrow \infty} \begin{bmatrix} \langle \hat{h}_e(q, t) \hat{h}_e(q', t) \rangle & \langle \hat{h}_e(q, t) \hat{h}_i(q', t) \rangle \\ \langle \hat{h}_i(q, t) \hat{h}_e(q', t) \rangle & \langle \hat{h}_i(q, t) \hat{h}_i(q', t) \rangle \end{bmatrix} \quad (4.140)$$

$$= 2\pi \delta(q + q') \tilde{\mathbf{G}}(q) \quad (4.141)$$

where for an OU system $\tilde{\mathbf{G}}(q)$ is defined in Eq. (4.56). The goal of Steyn-Ross *et al.* (2003) is to predict the covariance of h_e fluctuations separated by a distance $|x - x'|$ (these fluctuations will be referred to as e - e from now on). To this end they investigate the \tilde{G}_{11} element of the $\tilde{\mathbf{G}}$ matrix. Expanding Eq. (4.56) in 1-D, using the $\mathbf{A} = \mathbf{A}(q)$ drift matrix of Eq. (4.122) and the

D diffusion matrix of Eq. (4.116), we obtain

$$\begin{aligned} \left[\tilde{\mathbf{G}}(\mathbf{q}) \right]_{11} &= \frac{D_1}{2(A_{11} + A_{22})} + \frac{A_{22}^2 D_1 + A_{12}^2 D_2}{2(A_{11} + A_{22})(A_{11} A_{22} - A_{12} A_{21})} \\ &= \frac{D_1 + \kappa_e c_4}{2(\kappa_e q^2 - c_1)} - \frac{c_3 c_4}{2(c_3 q^2 + c_2)} \end{aligned} \quad (4.142)$$

where c_1, c_2, c_3 were defined in Eqs. (4.124)–(4.126), and c_4 is given by,

$$c_4 = \frac{J_{12}^2 D_2 + J_{22}^2 D_1}{c_1 c_3 + \kappa_e c_2}. \quad (4.143)$$

Taking signs into account and the possibility of c_3 being positive or negative, we rewrite Eq. (4.142) as

$$\left[\tilde{\mathbf{G}}(\mathbf{q}) \right]_{11} = \frac{D_1/\kappa_e + c_4}{2(q^2 + |c_1/\kappa_e|)} - \frac{c_4}{2(q^2 \pm |c_2/c_3|)} \quad (4.144)$$

where, in the second denominator, the “ \pm ” operator follows the sign of c_3 (i.e., “+” if $c_3 > 0$; “−” if $c_3 < 0$).

In order to obtain the spatial covariance $G(|x - x'|)$, we Fourier invert Eq. (4.144). Depending on the sign of c_3 , two forms of the e – e spatial covariance are predicted. If c_3 is positive the e – e spatial covariance is the difference of *two exponential decays* whose respective $1/e$ decay-lengths are L_1 and L_2 (defined below),

$$\begin{aligned} G(|x - x'|) &= \frac{D_1/\kappa_e + c_4}{4} L_1 \exp(-|x - x'|/L_1) \\ &\quad - \frac{c_4}{4} L_2 \exp(-|x - x'|/L_2), \quad c_3 > 0 \end{aligned} \quad (4.145)$$

Alternatively, if c_3 is negative then the e – e spatial covariance consists of an L_1 -length *exponential decay plus a sinewave variation* of wavelength $2\pi L_2$,

$$\begin{aligned} G(|x - x'|) &= \frac{D_1/\kappa_e + c_4}{4} L_1 \exp(-|x - x'|/L_1) \\ &\quad - \frac{c_4}{4} L_2 \sin(|x - x'|/L_2), \quad c_3 < 0 \end{aligned} \quad (4.146)$$

where the quantities

$$L_1 \equiv \sqrt{|\kappa_e/c_1|} \quad (4.147)$$

$$L_2 \equiv \sqrt{|c_3/c_1|} \quad (4.148)$$

define the characteristic lengths (either a correlation length or a scaled wavelength) for the spatial covariance patterns.

4.10 Previous Models and Clinical Evidence

Analysis of the default theoretical correlation function (Eq. (4.145)) shows that as the transition from consciousness to unconsciousness, or vice versa, is approached the correlation length increases (Sec. 7.2.1). This suggests that just prior to the loss of consciousness (LOC) and return of consciousness (ROC) transition points, the electrical activity in the brain is more synchronized (i.e., voltage fluctuations separated by a distant $|x - x'|$ are more correlated) than normal.

Clinical confirmation of increased correlation lengths near transition points has recently been reported by John *et al.* (1999). They conducted experiments involving 176 patients undergoing general anaesthesia. For each patient, 19 EEG-recording electrodes were placed around the scalp at positions corresponding to the International 10/20 System.

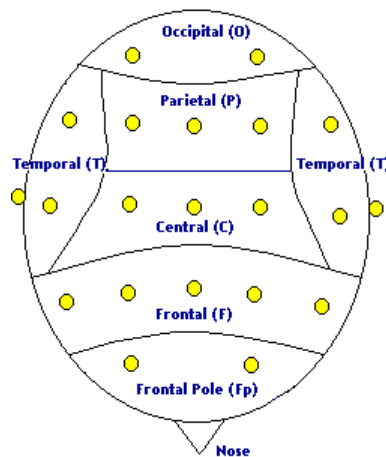


Figure 4.2: International 10/20 EEG electrode positioning system. The reference electrode is often placed on one of the positions indicated on either ear. [Source: <http://www.innernet.net/doco/sjo/neurofeedback.html>]

A range of different anaesthetic agents were used in order to determine EEG changes that are *common to all anesthetics*. Induction of anesthesia was accomplished using etomidate, propofol

or thiopental, while desflurane, isoflurane, sevoflurane, propofol or nitrous oxide/narcotic were used during surgery.

One of the main findings of John and coworkers was a general increase in EEG *coherence* just prior to LOC and ROC, particularly for the frontal (forehead) pair of electrodes. While the 1-D spatio-adiabatic model cannot tell us why the frontal electrodes are favoured, the reported increase in coherence is consistent with the theoretical prediction of increase in correlation length prior to the LOC and ROC transition points.

A more controversial piece of clinical evidence, involving sleep rather than general anaesthesia, was reported by Destexhe *et al.* (1999), who investigated the spatiotemporal patterns of oscillations in the cerebral cortex of cats during waking and natural sleep. They found that there is a marked increase in correlation length for slow-wave sleep (SWS) relative to that of rapid eye movement sleep (REM) and the awake state. When a person is in REM sleep the body is paralyzed (only the eye muscles and ear muscles twitch), yet the activity in the cerebral cortex is very similar to the awake state. In fact, REM sleep is when dreaming usually occurs. SWS sleep is considered deep sleep and is characterized by slow waves in the EEG signal. If we consider SWS sleep to be analogous to the anesthetized brain and REM sleep and awake to be analogous to the awake brain, then these cat experiments demonstrate qualitative agreement with the predicted difference in correlation length between the unconscious and conscious states (Sec. 7.2.1).

In the spatio-adiabatic model we have allowed for the possibility that the inhibitory diffusivity κ_i may dominate the excitatory diffusivity κ_e . This leads to the possibility of stationary large-amplitude voltage patterns occurring in space (Sec. 7.6). It is interesting to note that Ermentrout and Cowan (1979) identified the possibility of stationary periodic spatial patterns occurring in their idealized 1-D neural net models. Their paper shows that spatial standing waves can form via a bifurcation from the resting state of the system. Consistent with the present work they showed that strong inhibitory influences are necessary in order for a bifurcation from the resting state to a self-organized stable state exhibiting stationary spatial patterns.

Diffusion

5.1 The Diffusion Equation

As the cortical model includes a diffusion term, it is prudent to review the properties of the diffusion equation (Garcia (2000)). In particular, we wish to establish how to scale the noise inputs in space, and to determine the effects this scaling is likely to have.

The diffusion equation is one of the most common partial differential equations:

$$\frac{\partial}{\partial t}T(x, t) = \kappa \frac{\partial^2}{\partial x^2}T(x, t) \quad (5.1)$$

This equation describes many diffusive processes: For example if $T(x, t)$ is the temperature at position x , time t in a uniform rod, and κ is the thermal diffusion coefficient, then this equation describes the diffusion of heat along the rod. The diffusion equation is normally solved as an initial value problem. If we know the initial temperature distribution at $T(x, t = 0)$ and the boundary conditions, then we can solve the diffusion equation such that the temperature distribution can be found for all $t > 0$. Partial differential equations can be solved numerically to investigate the effect of changing both the initial conditions and the boundary conditions.

5.2 Numerical Approximation for Derivatives

The derivative of a function $f(x)$ with respect to the variable x is defined,

$$f'(x) \equiv \lim_{h \rightarrow 0} \frac{f(x+h) - f(x)}{h} \quad (5.2)$$

By choosing a suitably small value for increment h , we can write an approximation for Eq. (5.2) that allows us to solve the diffusion equation numerically. The value of h must be selected with some care. While an overly small value for h will lead to round-off error, a large value for h will give a poor estimate of the derivative.

Assuming for a finite h , negligible round-off error occurs, there will remain a truncation error arising from the difference between the analytical value $f'(x)$ and its numerical estimate $\frac{f(x+h)-f(x)}{h}$. This difference can be found via the Taylor expansion,

$$f(x+h) = f(x) + hf'(x) + \frac{h^2}{2}f''(x) + \dots \quad (5.3)$$

where \dots indicates higher-order terms. An equivalent form that has a finite number of terms is

$$f(x+h) = f(x) + hf'(x) + \frac{h^2}{2}f''(\zeta) \quad (5.4)$$

where ζ is a number lying between x and $x+h$; Taylor's theorem guarantees that there will always be some value ζ such that Eq. (5.4) is true; the catch is that we cannot analytically determine this value ζ . Rearranging Eq. (5.4) gives us

$$f'(x) = \frac{f(x+h) - f(x)}{h} - \frac{1}{2}hf''(\zeta) \quad (5.5)$$

where $x \leq \zeta \leq x+h$. This equation is known as the *forward derivative* formula. The last term is the truncation error that arises from truncating the infinite Taylor's series. Sometimes Eq. (5.5) is written as

$$f'(x) = \frac{f(x+h) - f(x)}{h} + O(h) \quad (5.6)$$

where $O(h)$ indicates that the truncation error is linear in increment h .

5.3 Numerical Solution of the Diffusion Equation

In order to solve the diffusion equation as an initial value problem we need: initial conditions, a way to calculate how these propagate forward in time, and boundary conditions. If we are looking at a diffusion process along a rod of length L , then we need to specify the conditions that apply at the left ($x = -L/2$) and the right ($x = L/2$) ends of the rod. Normally one of three different types of boundary conditions are considered: Dirichlet, von Neumann, or periodic. If

we set the ends of our rod to a constant temperature

$$T(x = -L/2, t) = T_a \quad (5.7)$$

$$T(x = L/2, t) = T_b \quad (5.8)$$

then we are imposing **Dirichlet** boundary conditions. Alternatively we can set the heat flux at the ends

$$-\kappa \frac{dT}{dx} \Big|_{x=-L/2} = F_a \quad (5.9)$$

$$-\kappa \frac{dT}{dx} \Big|_{x=L/2} = F_b \quad (5.10)$$

If we set $F_a = F_b = 0$ the ends of the rod are insulated. Setting the gradients at the endpoints imposes **von Neumann** boundary conditions. **Periodic** boundary conditions, are imposed by equating the function at the two ends. In one dimension this is equivalent to connecting the two ends of the rod to form a circle,

$$T(x = -L/2, t) = T(x = L/2, t) \quad (5.11)$$

$$\frac{dT}{dx} \Big|_{x=-L/2} = \frac{dT}{dx} \Big|_{x=L/2} \quad (5.12)$$

In order to solve the diffusion equation we need to discretize space and time. We discretize time via the formula $t_n = (n-1)\tau$ where τ is the time-step and $n = 1, 2, 3, \dots$. Space is discretized by setting up grid-points x_i between $x = -L/2$ and $x = L/2$ with $x_i = (i-1)h - L/2$; h is the grid spacing, and $i = 1, 2, 3, \dots$

The index i denotes the spatial location of a grid-point and the index n denotes the temporal step. Following Garcia (2000) we adopt the shorthand

$$T_i^n \equiv T(x_i, t_n) \quad (5.13)$$

to represent the temperature at position x_i and time t_n . Using the forward-derivative equation, the time derivative can be approximated numerically

$$\frac{\partial T(x, t)}{\partial t} \Rightarrow \frac{T(x_i, t_n + \tau) - T(x_i, t_n)}{\tau} \quad (5.14)$$

$$= \frac{T_i^{n+1} - T_i^n}{\tau} \quad (5.15)$$

Likewise the space derivative can be written using the *centered derivative* form,

$$\frac{\partial^2 T(x, t)}{\partial x^2} \Rightarrow \frac{T(x_i + h, t_n) + T(x_i - h, t_n) - 2T(x_i, t_n)}{h^2} \quad (5.16)$$

$$= \frac{T_{i+1}^n + T_{i-1}^n - 2T_i^n}{h^2} \quad (5.17)$$

This method of iteration takes the name *forward-time centered-space* (FTCS). Applying FTCS discretization to the diffusion equation Eq. (5.1) yields,

$$\frac{T_i^{n+1} - T_i^n}{\tau} = \kappa \frac{T_{i+1}^n + T_{i-1}^n - 2T_i^n}{h^2} \quad (5.18)$$

which can be rearranged to give an update formula for T_i^{n+1} ,

$$T_i^{n+1} = T_i^n + \frac{\kappa\tau}{h^2} (T_{i+1}^n + T_{i-1}^n - 2T_i^n) \quad (5.19)$$

If we know all the spatial information at a temporal step n (RHS of Eq. 5.19), then we can determine all spatial values at the next step in time $n + 1$. We can apply this iteration formula to an initial temperature profile to numerically determine $T(x, t)$ for $t > 0$.

5.4 Simulations of the Diffusion Equation

Once the diffusion equation has been coded we can investigate various initial conditions. Let us suppose we would like to see how a small impulse of heat in the middle of the rod diffuses through space at each successive time-step. To achieve this, a delta spike at $x = 0, t = 0$ is used as an initial condition. A delta spike represented in 1-D, is shown in Fig. 5.1.

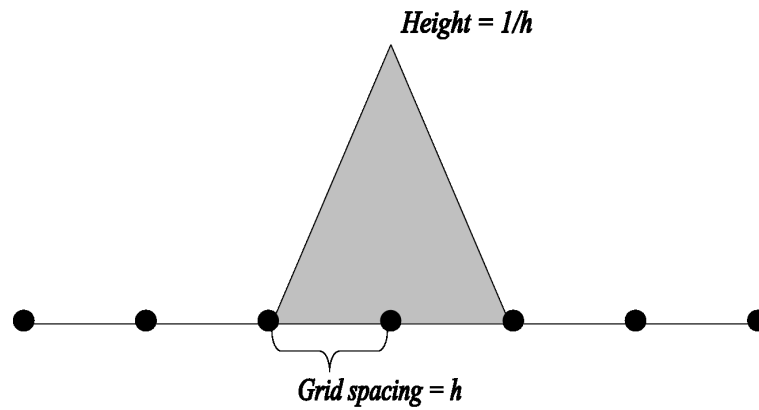


Figure 5.1: Discretized representation of a delta spike

With just an initial impulse of heat at the centre of the rod, we expect the heat to diffuse out along the rod. As energy must be conserved, the temperature at the centre will decay as the thermal energy diffuses out along the rod. A typical simulation is shown in Fig. 5.2. As the numerical scheme progresses forward in time, the delta spike decays in height and broadens symmetrically along the rod. To represent the delta spike numerically we use,

$$\Delta(x) = \begin{cases} (x+h)/h^2 & \text{for } -h < x \leq 0 \\ (h-x)/h^2 & \text{for } 0 \leq x < h \\ 0 & \text{otherwise} \end{cases} \quad (5.20)$$

such that

$$\lim_{h \rightarrow 0} \Delta(x) = \delta(x) \quad (5.21)$$

The function $\Delta(x)$ is a triangular distribution with unit area (Fig. 5.1). Discretizing $\Delta(x)$ gives

$$\Delta_i = \begin{cases} 1/h & \text{for } i = N/2 \\ 0 & \text{otherwise} \end{cases} \quad (5.22)$$

Note that integrating gives

$$\int_{-L/2}^{L/2} \Delta(x) dx \rightarrow \sum_{i=1}^N \Delta_i h = 1 \quad (5.23)$$

so Δ_i also has unit area.

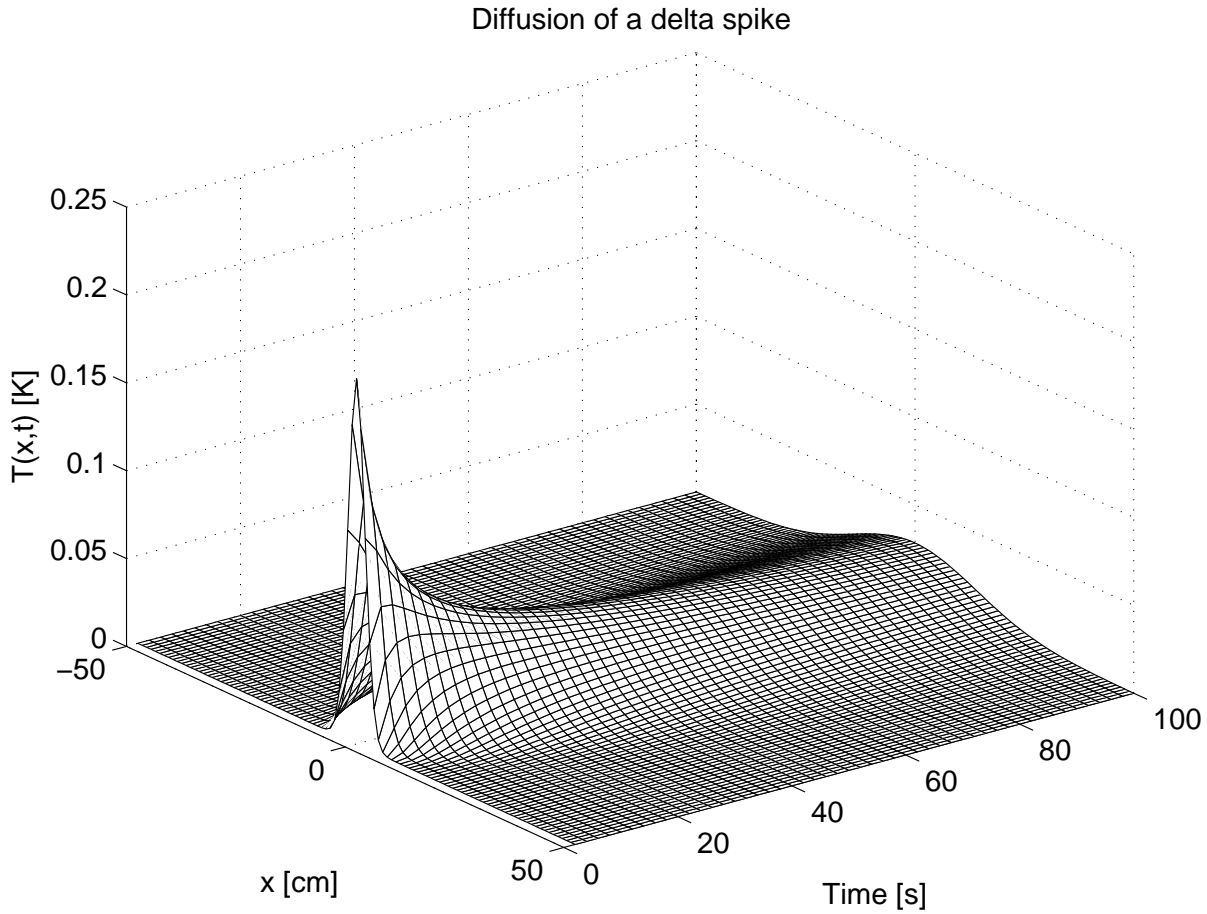


Figure 5.2: Mesh plot from simulation of a temperature spike diffusing along a 1 m rod. In order to emphasize the diffusion of the spike, the initial temperature $T(x = 0, t = 0) = 1$ K is not shown. Grid spacing $h = 1$ cm, timestep $\tau = 0.1$ s, and $\kappa = 1$ cm²/s.

Scaling the height of the delta spike by $1/h$ ensures that the triangle always has unit area. The physical significance of this is that the amount of heat inputted as a delta spike is *independent of the grid spacing*. If we keep the length of the rod the same but change the grid spacing, and hence the number of grid-points, the $T(x, t)$ solution should remain the same. For example, if we have a rod discretized into 1-cm spacings, a delta spike should diffuse outwards at the same speed as does a delta spike in a rod divided into 2-cm spacings. However, if we run simulations of these two situations, it becomes apparent that the two solutions take a certain amount of time to converge. This is illustrated in Figs. 5.3 and 5.4.

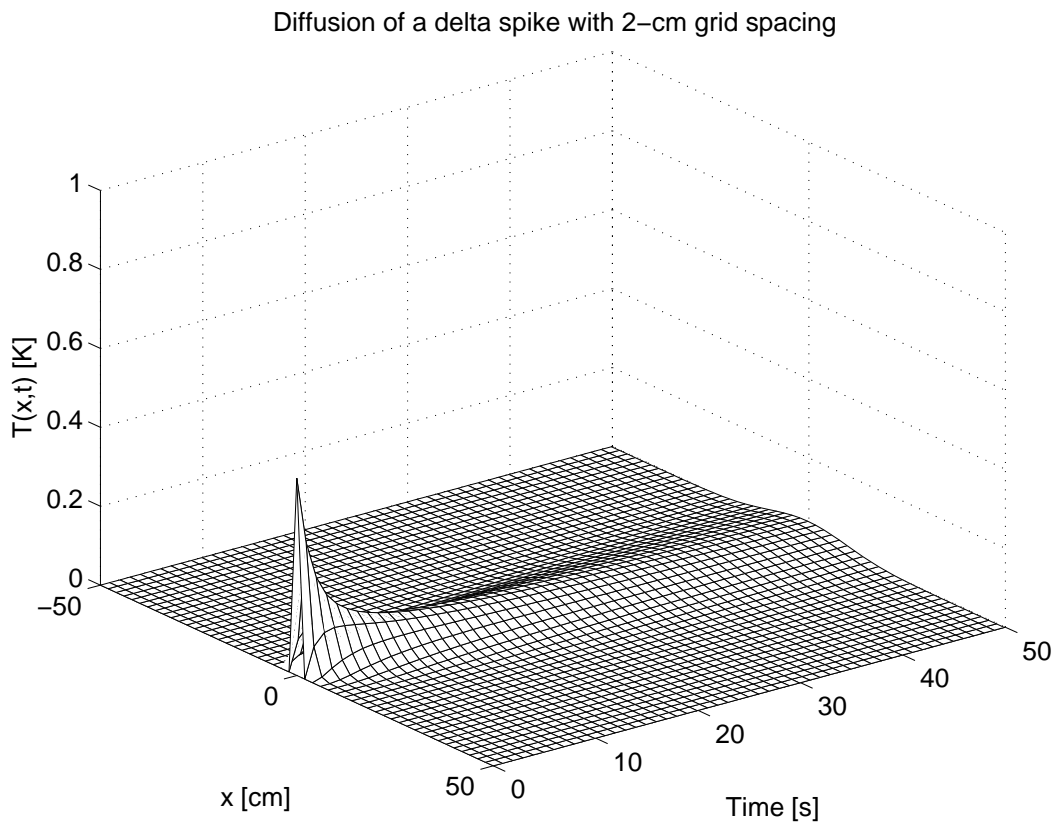
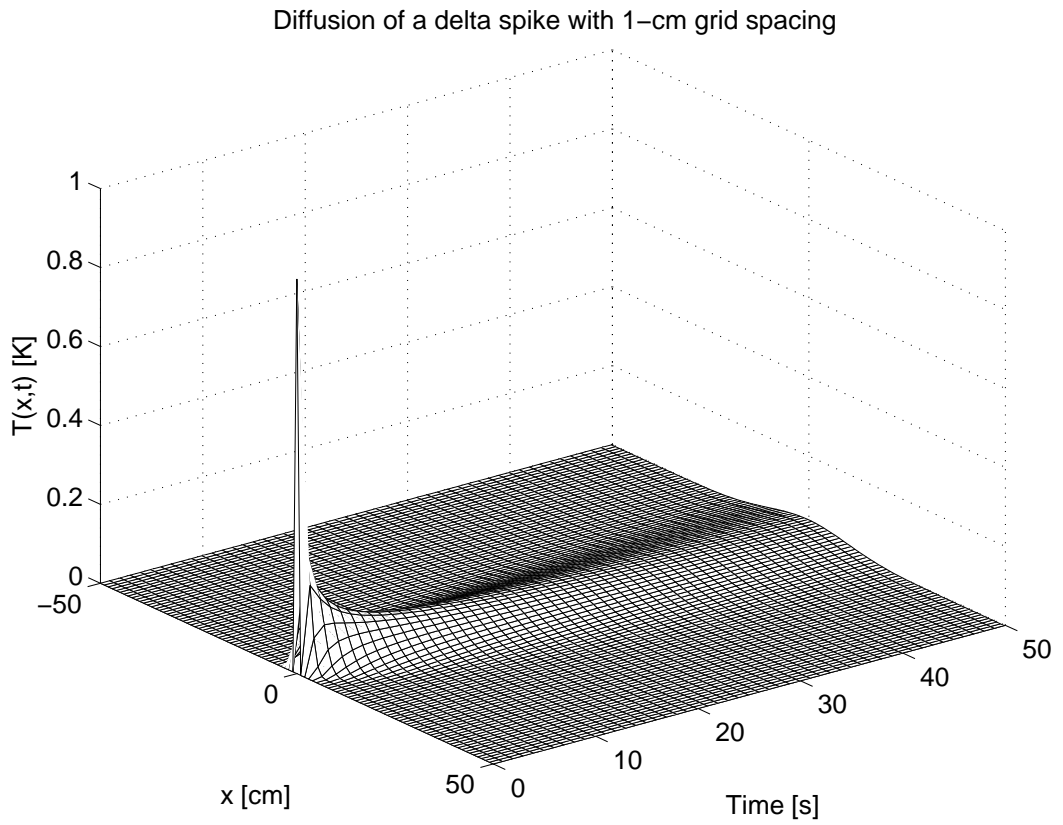


Figure 5.3: Diffusion of a delta spike for different grid spacings

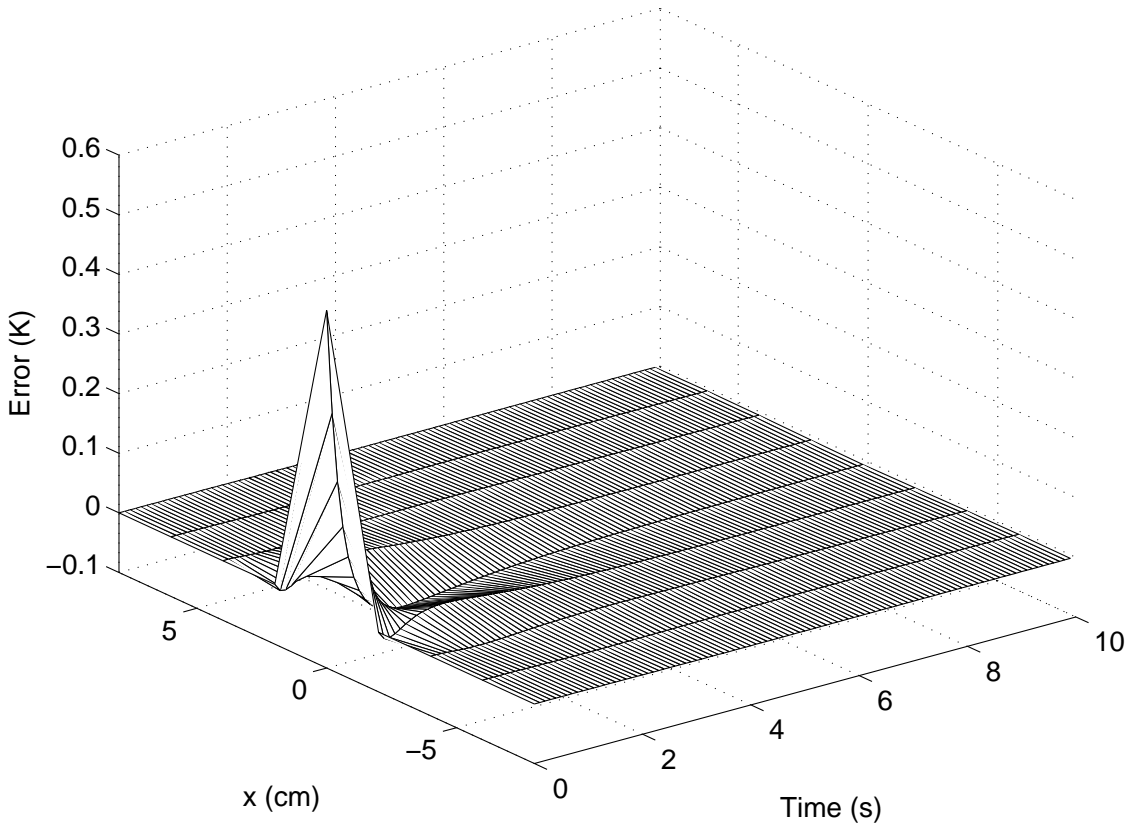
3D error profile for $T(x,t)$ illustrating truncation error

Figure 5.4: Temperature error profile showing the difference between time evolution of spike diffusion on grid spacings 1 and 2 cm. Calculated as $T_{h_1}(x, t) - T_{h_2}(x, t)$ where $h_1 = 1$ cm and $h_2 = 2$ cm

There is an obvious and expected disagreement at $t = 0$ s because by changing the grid spacing we have changed the initial height of the spike. But by changing the grid spacing we have also changed the truncation error. After one time step the two solutions should agree within the difference of their relative truncation errors. An error profile, calculated using the differences between the two simulations is shown in Fig. 5.4. Using the FTCS we can derive the truncation error ϵ . The FTCS scheme of Eq. (5.18) reads,

$$\frac{T_i^{n+1} - T_i^n}{\tau} = \kappa \frac{T_{i+1}^n + T_{i-1}^n - 2T_i^n}{h^2} \quad (5.24)$$

In section (5.2) we noted that there are truncation errors associated with the forward- and centered-derivative formulas. Hence we aim to write the FTCS including its associated truncation error ϵ . Following the analysis similar to Tannehill *et al.* (1997), we write a Taylor series expansion in time for $T(x, t + \tau)$,

$$T(x, t + \tau) = T(x, t) + \tau \frac{\partial T(x, t)}{\partial t} + \frac{\tau^2}{2!} \frac{\partial^2 T(x, t)}{\partial t^2} + \frac{\tau^3}{3!} \frac{\partial^3 T(x, t)}{\partial t^3} + \dots \quad (5.25)$$

and a pair of Taylor expansions in space for $T(x+h, t)$ and $T(x-h, t)$,

$$T(x+h, t) = T(x, t) + h \frac{\partial T(x, t)}{\partial x} + \frac{h^2}{2!} \frac{\partial^2 T(x, t)}{\partial x^2} + \frac{h^3}{3!} \frac{\partial^3 T(x, t)}{\partial x^3} + \dots \quad (5.26)$$

$$T(x-h, t) = T(x, t) - h \frac{\partial T(x, t)}{\partial x} + \frac{h^2}{2!} \frac{\partial^2 T(x, t)}{\partial x^2} - \frac{h^3}{3!} \frac{\partial^3 T(x, t)}{\partial x^3} + \dots \quad (5.27)$$

Making use of Eqs. (5.25–5.27) we write,

$$\begin{aligned} \frac{\partial T(x, t)}{\partial t} - \kappa \frac{\partial^2 T}{\partial x^2} &= \left(\frac{T(x, t+\tau) - T(x, t)}{\tau} - \kappa \frac{T(x+h, t) + T(x-h, t) - 2T(x, t)}{h^2} \right) \\ &\quad - \frac{\tau}{2!} \frac{\partial^2 T(x, t)}{\partial t^2} + \kappa \frac{2h^2}{4!} \frac{\partial^4 T(x, t)}{\partial x^4} + \dots \end{aligned} \quad (5.28)$$

In discrete form, the LHS of Eq.(1.28) becomes

$$\frac{\partial T(x, t)}{\partial t} - \kappa \frac{\partial^2 T}{\partial x^2} \Rightarrow \left(\frac{T_i^{n+1} - T_i^n}{\tau} - \kappa \frac{T_{i+1}^n + T_{i-1}^n - 2T_i^n}{h^2} \right) + \epsilon \quad (5.29)$$

where ϵ , the truncation error, is given by

$$\epsilon = -\frac{\tau}{2} \frac{\partial^2 T}{\partial t^2} + \kappa \frac{h^2}{12} \frac{\partial^4 T}{\partial x^4} + \dots \quad (5.30)$$

Taking the time derivative of Eq. (5.1), we find

$$\frac{\partial^2 T}{\partial t^2} = \kappa \frac{\partial}{\partial t} \frac{\partial^2 T}{\partial x^2} \quad (5.31)$$

$$= \kappa \frac{\partial^2}{\partial x^2} \frac{\partial T}{\partial t} \quad (5.32)$$

$$= \kappa \frac{\partial^2}{\partial x^2} \left(\kappa \frac{\partial^2 T}{\partial x^2} \right) \quad (5.33)$$

$$= \kappa^2 \frac{\partial^4 T}{\partial x^4} \quad (5.34)$$

and thus rearrange the truncation error to give,

$$\epsilon = \left(-\frac{\kappa^2 \tau}{2} + \frac{\kappa h^2}{12} \right) \frac{\partial^4 T}{\partial x^4} + O(t^2 + h^4) \quad (5.35)$$

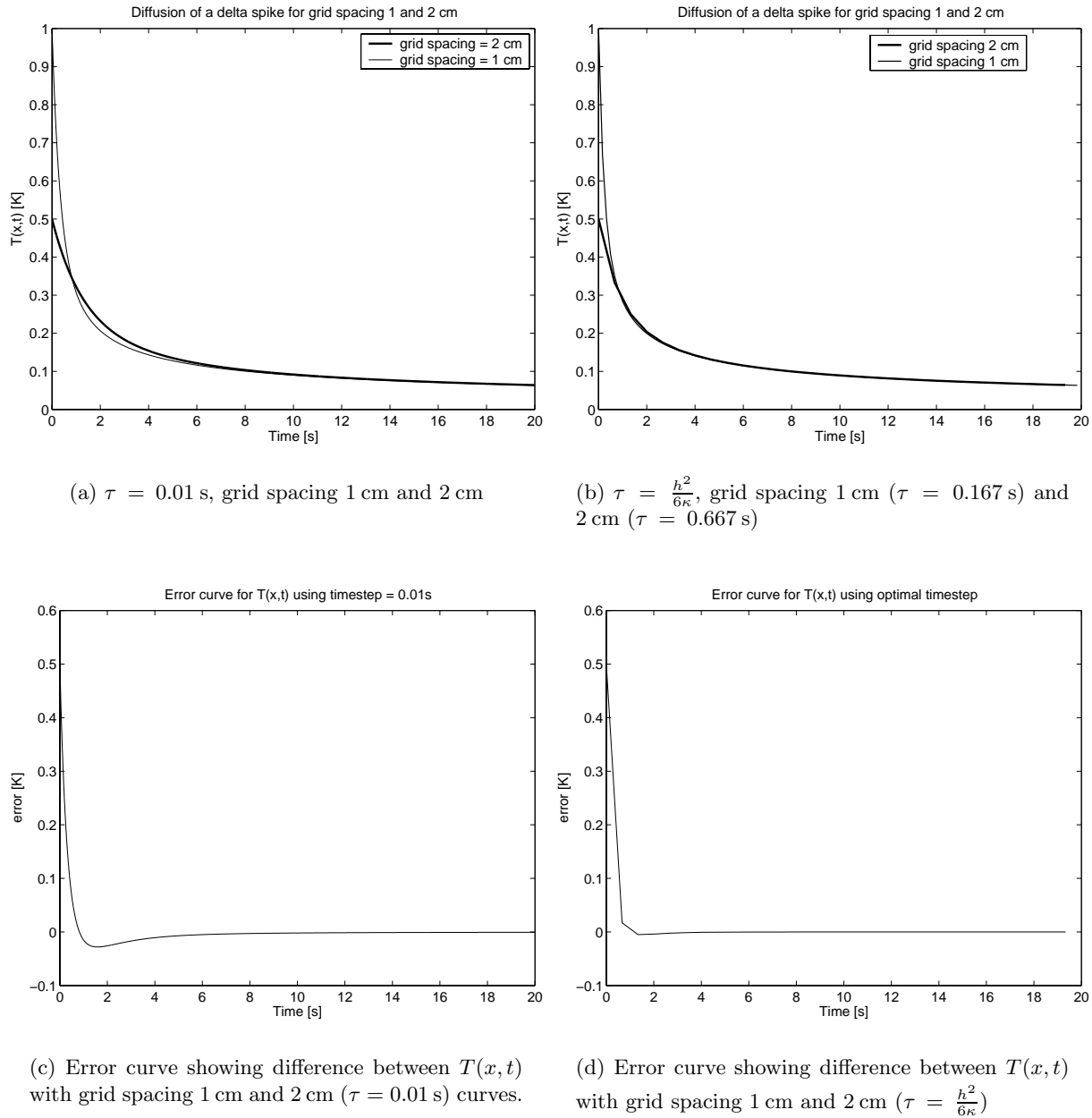


Figure 5.5: Decay of peak of delta spikes illustrating effect of truncation error

This suggests that we can minimize the truncation error for a given grid spacing by arranging that the coefficient of $\partial^4 T / \partial x^4$ be zero. Thus we should set the timestep τ to,

$$\tau = \frac{h^2}{6\kappa} \quad (5.36)$$

Close observation of the numerical processes in Fig. 5.3, shows the effect of truncation error. When the grid spacing is increased from 1 cm to 2 cm, the two numerical solutions should converge after a number of iterations. Looking at the agreement of the rate of decay for each delta spike, the effect of minimising the truncation error can be seen. Figure 5.5 illustrates that

by minimizing the truncation error, the simulations with differing grid spacings converge more rapidly. The effect of the truncation error is important when numerical simulations of a system are being compared with analytical prediction. In the cortical simulations, noise is added in at every timestep. After a single iteration the noise has not had sufficient time to fully diffuse along the rod, hence we need to be especially watchful for truncation error in the cortical simulations.

5.5 Noise and the Diffusion Equation

Simulating stochastic processes requires a lot of care, especially how one is to go about discretizing continuous white-noise. As a step towards accurately discretizing spatial white-noise we consider the diffusion equation “driven” white noise. When inputting a single delta spike into the diffusion equation, we have to ensure that the area of the triangle representing the spike is always constant and independent of grid spacing. Using this principle, we proceed to investigate how noise inputs should be scaled in space. One should ask: How do we scale the noise in space in order to ensure that the cortical rod is being driven with the same amount of noise energy per unit length, independent of the grid-spacing? Let us consider the implied area of the delta spike Fig. 5.1 in the diffusion equation,

$$\begin{aligned} \text{area} &= \frac{1}{2} \text{base} \times \text{height} \\ &= \frac{1}{2} 2h \times \frac{1}{h} = 1 \end{aligned} \tag{5.37}$$

The cortical model is driven by continuous spatial white-noise. Consider the discretized version where we assume an oppositely-signed delta spike at every grid point (Fig. 5.6)). In this case

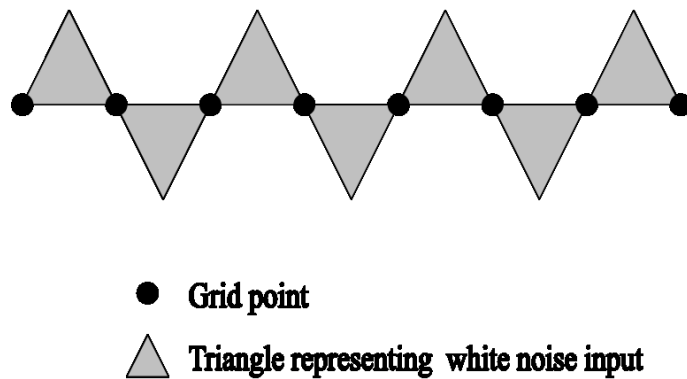


Figure 5.6: Discretized (triangle) representation of spatial white noise

the absolute area for the noise impulses input into an N -point rod is,

$$\begin{aligned} \text{total area} &= \sum_{i=1}^N |\text{area of each triangle}| & (5.38) \\ &= N \times \frac{1}{2}h \times |\text{mean height of each triangle}| \end{aligned}$$

Using this formula it becomes obvious that if we do not scale the noise with the grid spacing the total absolute area will in fact still be conserved. This is because if we halve the grid spacing (i.e., improve the spatial resolution: $h \rightarrow h/2$) then in order to keep the length of the cortical rod the same we will need to double the number of grid points ($N \rightarrow 2N$). Hence impulse “area” will be conserved.

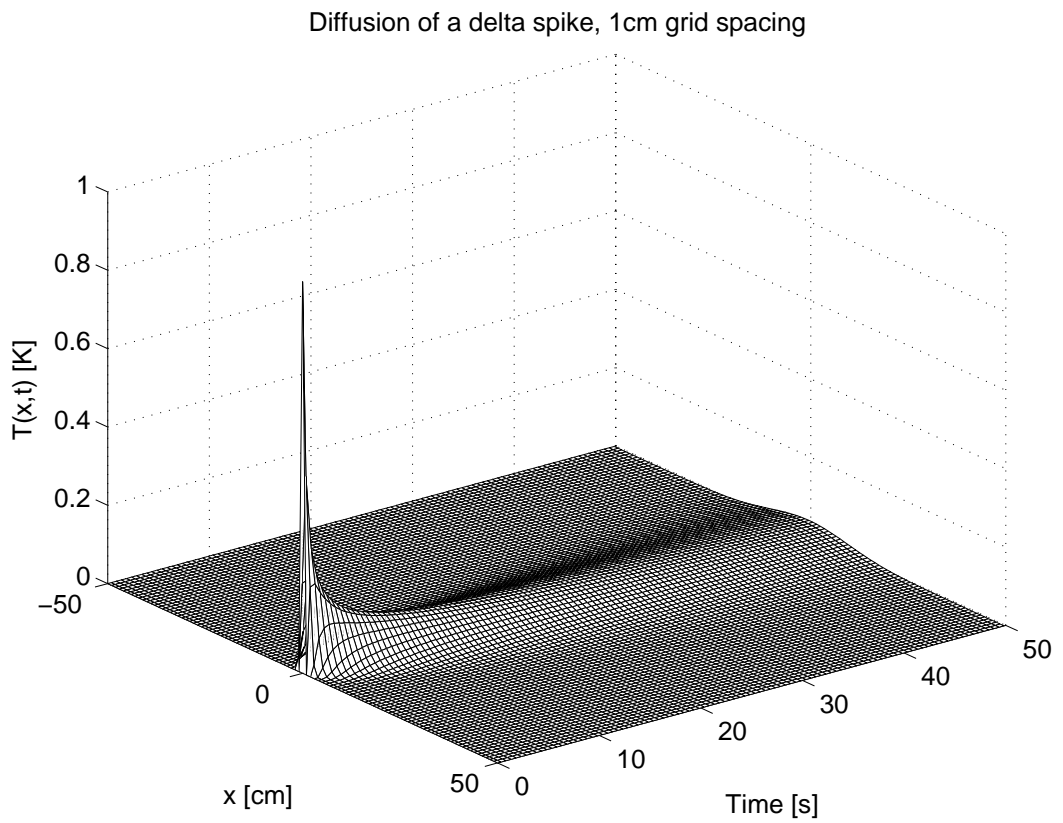
What about the case of varying the length of the rod? If we double the length we will need to either double the number of grid points or double the grid spacing. Doing either will mean the absolute total impulse area would double which is desirable because then the noise *per unit length* is conserved. *Not* scaling the noise with the inverse grid spacing in order to conserve impulse area stands in stark contrast to the case of a single delta spike used as an initial condition for the diffusion equation. Hence it is a good idea to investigate the effect of *fixing the height* of the delta spike in the diffusion equation.

We will apply a single spike as an initial condition, but keep the *height* fixed, independent of grid spacing. In order to minimize the change in truncation error due to changes in grid spacing, the time-step is set as described in Eq. (5.36). We find that the larger the grid spacing, the longer it takes, in absolute time, for the height of the delta spike to decay to the same value $T(x, t)$. Two simulations were run using grid spacings $h_1 = 1$ cm and $h_2 = 2$ cm (Fig. 5.7). As the rod with grid spacing 2 cm has twice (or h_2/h_1) as much heat applied as the initial condition, at any time-step $t > 0$ s, the bar will be twice as hot at a given position x as the rod with 1 cm grid spacing (within numerical error). This is illustrated in Fig. 5.7.

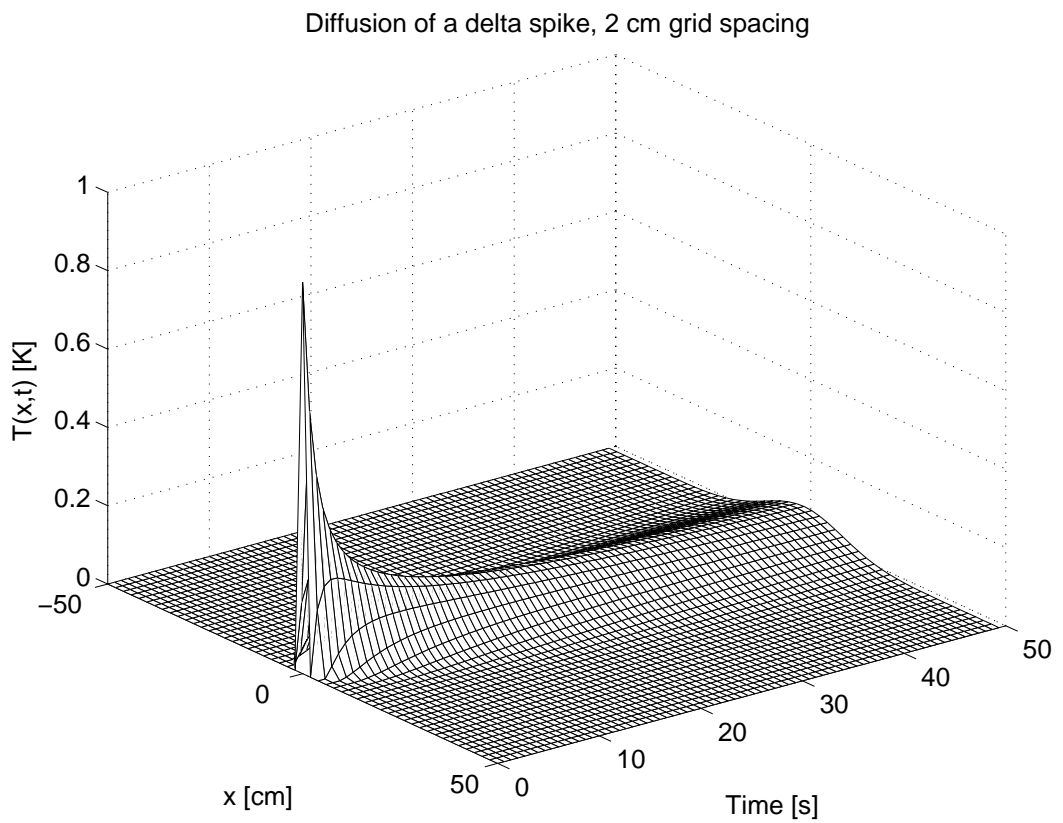
Using this reasoning, two temperature distributions $T(x, t)$ obtained by simulating a rod of fixed length Nh , with different grid-spacings h_1 and h_2 , with a *fixed height* delta spike as an initial condition, can be equated by dividing by the appropriate gridspacing,

$$\frac{T_{h_1}(x, t)}{h_1} = \frac{T_{h_2}(x, t)}{h_2} \quad \forall t > 0 \quad (5.39)$$

where h_1 and h_2 are two different grid spacings for the same length of rod.



(a) Grid spacing 1 cm, height of spike 1



(b) Grid spacing 2 cm, height of spike 1

Figure 5.7: The effect of changing the grid spacing while keeping the height of the initial-condition spike constant

5.6 Correlations and the Diffusion Equation

When looking at the cortical model, one of the main objectives is to investigate spatial correlations. If the length of the cortical rod is kept constant, the correlations should remain the same irrespective of changes to grid spacing or number of grid points. This point can be investigated using the diffusion equation with noise added at every time step. Let us examine the case of noise being added continuously at the centre point of the rod. Two runs with the same time step and using the same random numbers are shown in Fig. 5.8. (Note, when adding noise in at every time-step, it is well established that the noise amplitude should be pre-scaled by $\frac{1}{\sqrt{\tau}}$ in order to preserve input energy per unit time (Wilcocks (2001))).

In Fig. 5.8 simulations using grid spacings of 1 cm and 4 cm are shown. Inspection of these two graphs shows they obey Eq 5.39 (within numerical error). Notice that along the $x = 0$ cm axis the agreement with Eq. (5.39) is not exact. This is due to the difference in truncation error between the two simulations.

In order to measure the correlations in a single series, the autocorrelation function is used. Applying the (unnormalized) autocorrelation function to a spatial sequence returns values,

$$r(m) = \sum_{n=-N+1}^{N-1} x(n)x(n-m) \quad (5.40)$$

where $x(n)$ is a N element sequence (zero-padded to map to a $2N - 1$ element sequence) and $m = 0, 1, 2 \dots$ is the lag. The correlations as a function of space, in cm, is then,

$$r(m) \Rightarrow r(m h) = r(|x - x'|) \quad (5.41)$$

where h is the grid spacing and $|x - x'|$ is the distance of point x from reference point x' (in the following examples $x' = 0$ cm).

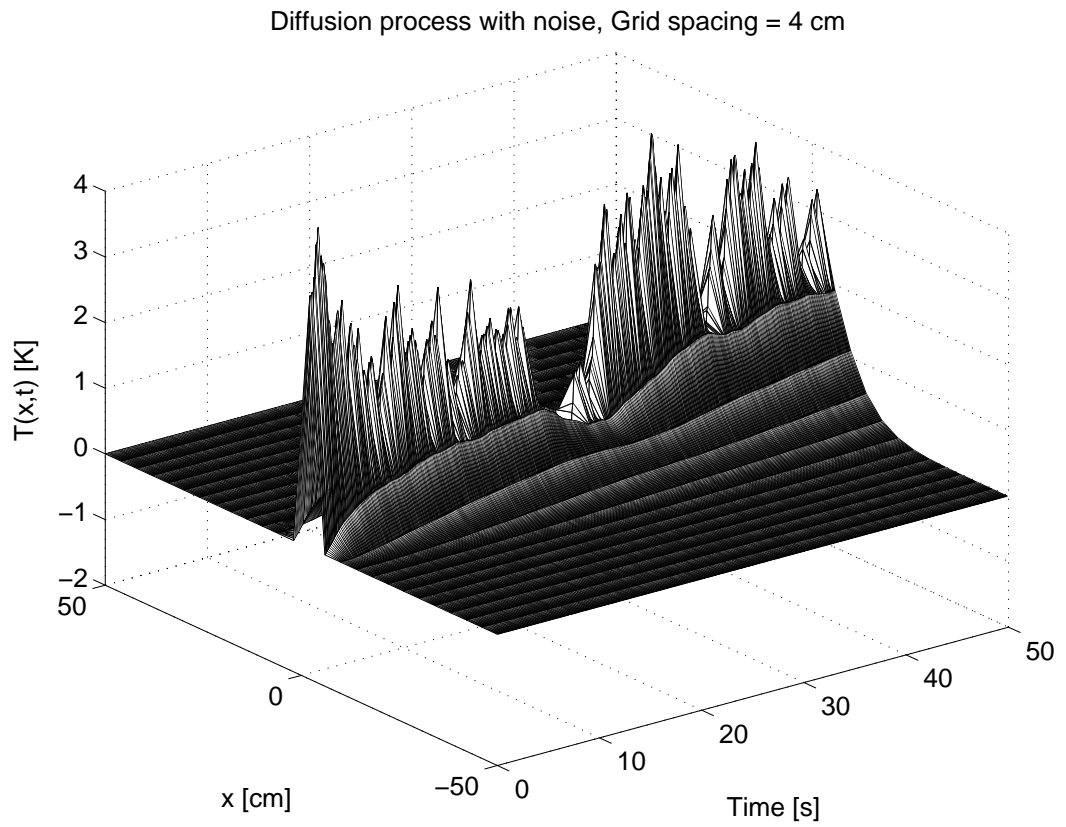
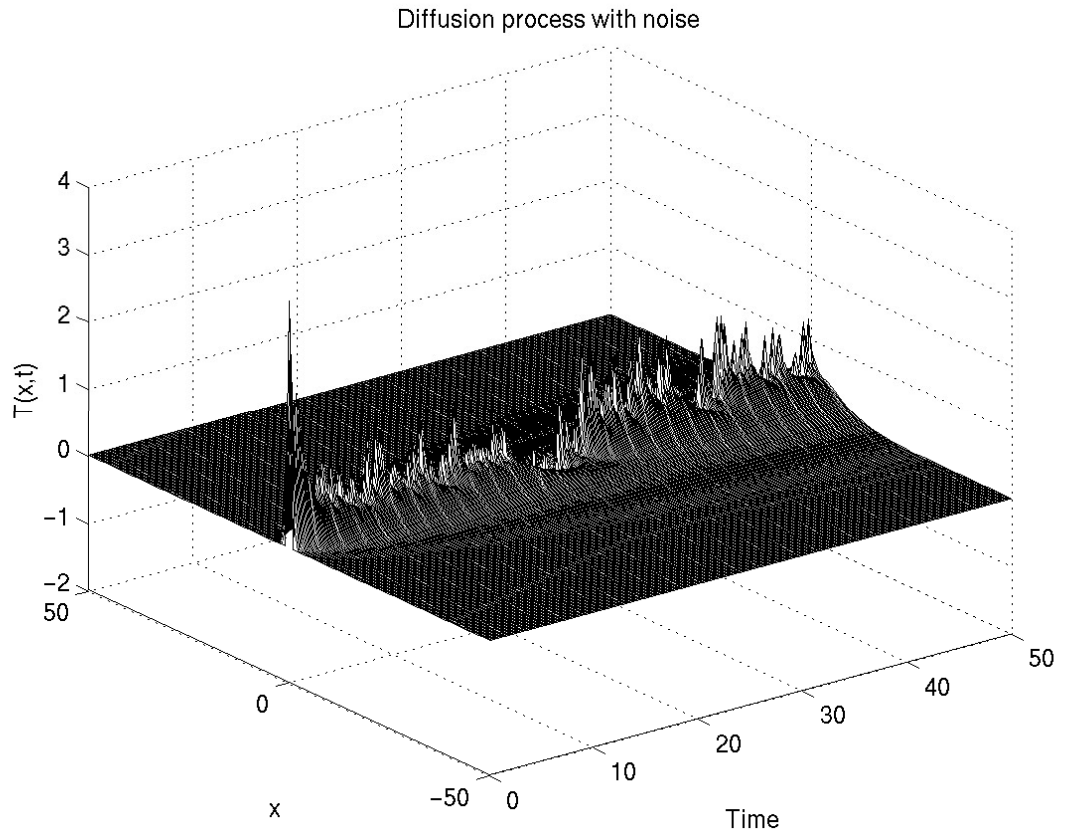


Figure 5.8: Diffusion process with noise for grid spacings of 1 cm and 4 cm

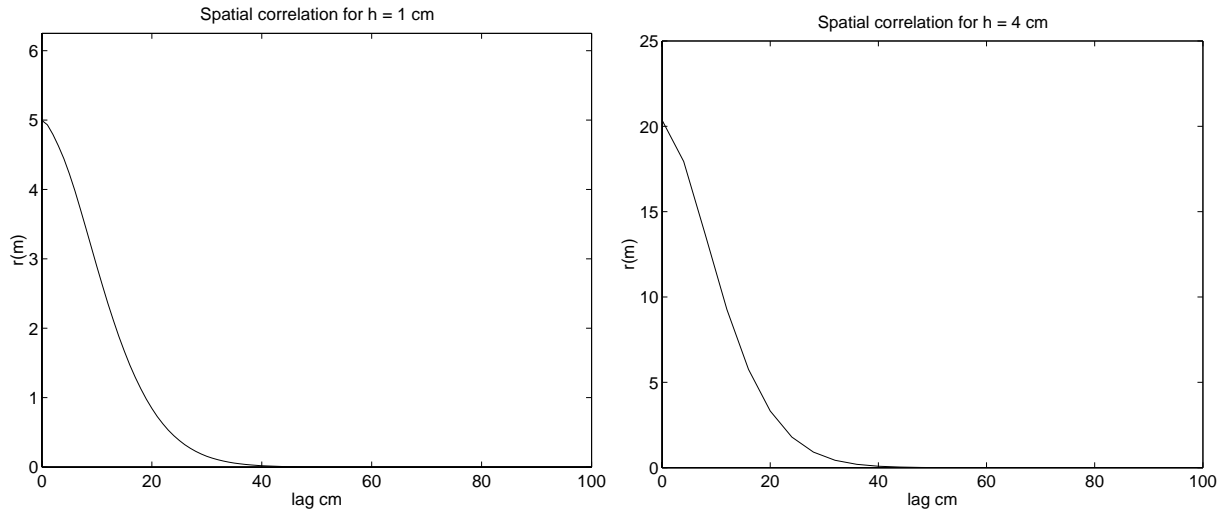


Figure 5.9: Spatial correlations for grid spacings 1 cm and 4 cm. These graphs were computed from the average autocorrelation, obtained by taking the autocorrelation of space series of Fig. 5.9 at each time-step. Note that the spatial lag is in cm and not gridpoints

Taking the autocorrelation of the two simulations (Fig. 5.9), we determine that they are related by a factor of 4 or h_2/h_1 ($h_1 = 1$ cm and $h_2 = 4$ cm). This is because although $T_{h_2}(x, t) = 4T_{h_1}(x, t)$ (approximately), we have kept the length of the rod the same, hence there are *four times* as many grid points ($N \rightarrow 4N$) in the rod with $h = 1$ cm compared to the rod where $h = 4$ cm. Thus in order to normalize correlations between constant length rods we need to divide through by the grid spacing h . If $r_{h_1}(|x - x'|)$ is the correlation for each series as defined in Eq. (5.40), then

$$\frac{r_{h_1}(|x - x'|)}{h_1} = \frac{r_{h_2}(|x - x'|)}{h_2} \quad (5.42)$$

where $|x - x'| = mh_1 = m'h_2$ are the lags in cm.

When adding noise in at every grid point rather than just one, similar logic should follow. In this case by changing the number of grid points in a rod of length L we also change the number of noise inputs. Hence to normalize we need to divide by the number of grid-points as well.

$$\frac{r_{h_1}}{N_1 h_1} = \frac{r_{h_2}}{N_2 h_2} \quad (5.43)$$

By doing this we are effectively dividing by the length of the cortical bar $L = N\Delta x$. Using Eq. 5.43 to normalize all correlations in the cortical model allows different length rods to be investigated as it normalizes to give correlation energy per unit length.

5.7 Disagreement with Stochastic Theory

For a time-stochastic system such as Ornstein–Uhlenbeck process, the theoretical correlation is known to agree exactly with numerical simulation when the (normalised) time-autocorrelation function at lag l is calculated via,

$$r(l) = \frac{1}{N} \sum_{k=-N+1}^{N-1} x(k)x(k-l). \quad (5.44)$$

provided that the stochastic inputs that drive the time-sequence $x(k)$ have been prescaled by $1/\sqrt{\tau}$.

For our spatial experiment with the diffusion process in which noise (prescaled by $1/\sqrt{\tau}$) drives every gridpoint, we determined experimentally that the spatial-autocorrelation function required a scaling by $1/Nh$ giving,

$$r(m) = \frac{1}{Nh} \sum_{n=-N+1}^{N-1} x(n)x(n-m). \quad (5.45)$$

This scale factor ensures that the correlations are independent of the grid spacing used to simulate a rod of fixed length. In deriving this factor we have ignored the fact that the input noise for the continuous 1-D cortical model is delta-correlated in time *and* space. To ensure that the “amount” of delta-correlated noise (impulses of noise rather than a continuous input) is constant per unit length we *have* to prescale the noise appropriately both in time *and* space. Comparing the correct autocorrelation formula Eq. (5.44) with the derived formula Eq. (5.45) indicates we should prescale the noise by $1/\sqrt{h}$.

The reason for the scaling discrepancy between my derived formula Eq. (5.45) and the expected form of Eq. (5.44) arises from my implicit assumption in Fig. 5.6 that one can “connect up the dots”. This improperly implies a nonzero spatial correlation exists between grid points, contradicting the delta-correlation property required of spatial white noise.

In Sec. 6.1 I will prove that when simulating a stochastic process driven by spatio-temporal white noise, the computer-generated (i.e., finite-variance) noise must be prescaled by both $1/\sqrt{\tau}$ and $1/\sqrt{h}$ in order that in the limit $\tau \rightarrow 0$, $h \rightarrow 0$, the discrete simulation approaches its white-noise continuous limit.

Numerical Simulations

This chapter discusses the numerical simulations of both the spatio-adiabatic equations Eqs. (4.74–4.75) and the linearized spatio-adiabatic equations Eq. (4.92). The purpose of the simulations is to provide confirmation of the formation of *nonequilibrium steady-states* (stationary Turing structures), and to confirm the theoretical correlation predictions described by Eqs. (4.145–4.146).

6.1 Numerical Method for Discretizing White-Noise

In order to solve the spatio-adiabatic and linearized spatio-adiabatic equations numerically we need to discretize time and space. The time- and space-derivatives in the equations are simulated using the *forward time derivative* and the *space-centred derivative*. In Section 5.3 we introduced the shorthand

$$(h_e)_j^n \equiv h_e(x_j, t_n) \quad (6.1)$$

where the n subscript indicates “value at time-increment n ”,

$$t_n = t_0 + \Delta t n \quad (6.2)$$

and where t_0 is the initial time (set to zero for these simulations) and Δt is the time-step. Similarly, j subscript reads “value at gridpoint j ”,

$$x_j = x_0 + jh \quad (6.3)$$

where x_0 is set to zero, and h is the gridspacing. The updating methods used have the generic form

$$(h_e)_j^{n+1} = (h_e)_j^n + \left[\frac{\partial h_e}{\partial t} \right]_j^n \Delta t \quad (6.4)$$

where $\left[\frac{\partial h_e}{\partial t} \right]_j^n$ denotes the forward derivative in time and includes a diffusion term modelled using the space-centred derivative.

The theoretical equations are based on an *infinite* 1-D cortex. While an infinite 1-D cortex is impossible to simulate, provided the cortex is long enough, meaningful comparisons between experiment and theory can be made. The minimum length of cortex depends on a number of factors, including exactly what fluctuation property is being measured (this will be discussed when we investigate different properties of the space-time series).

When simulating the 1-D cortex we also have to be rather careful about how noise is input in both *space and in time*. We need to determine how to correctly map the continuous spatial and temporal white-noise to its discretized approximation. Murthy (1983) presents a treatment for discretizing continuous *temporal* white-noise. Here I adapt the ideas presented by Murthy to include continuous *spatial* white-noise.

The *continuous* random function $\xi(x, t)$ is modelled as white noise which has zero mean and is delta-correlated in both space and time:

$$\langle \xi(x, t) \rangle = 0, \quad \langle \xi(x, t) \xi(x', t') \rangle = \delta(x - x') \delta(t - t'). \quad (6.5)$$

The second result implies that white-noise is defined to have *infinite* variance. In order to simulate white-noise we need a discretized approximation. We define a discrete random variable $\{\eta_j^n\}$ of mean zero and variance σ^2 :

$$\langle \eta_j^n \rangle = 0, \quad \langle \eta_j^n, \eta_j^m \rangle = \sigma^2 \delta_{j,k} \delta_{n,m} \quad (6.6)$$

where $\delta_{n,m}$ (and $\delta_{j,k}$) is the Kronecker delta,

$$\delta_{n,m} = \begin{cases} 1 & \text{when } m = n \\ 0 & \text{when } m \neq n \end{cases} \quad (6.7)$$

For a time-step Δt and space-step h sufficiently small,

$$\int_0^L \int_0^T \xi(x, t) dx dt \approx \sum_{j=1}^J \sum_{n=1}^N \eta_j^n h \Delta t \quad \text{where } T = N\Delta t \text{ and } L = Jh \quad (6.8)$$

with both sides going to zero as $L, T \rightarrow 0$ since both $\xi(x, t)$ and $\{\xi_j^n\}$ have zero mean.

For the product $\xi(x, t)\xi(x', t')$, the expected value of the integral over all space and time is

$$\left\langle \lim_{L \rightarrow \infty} \lim_{T \rightarrow \infty} \int_{-L}^L \int_{-T}^T \xi(x, t)\xi(x', t') dx dt \right\rangle = \int_{-\infty}^{\infty} \int_{-\infty}^{\infty} \langle \xi(x, t)\xi(x', t') \rangle dx dt = 1 \quad (6.9)$$

which must match the corresponding expectation value for the summation of the discrete product $\{\eta_j^n \eta_j^m\}$,

$$\left\langle \lim_{J \rightarrow \infty} \lim_{N \rightarrow \infty} \sum_{j=1}^J \sum_{n=1}^N \eta_j^n \eta_k^m h \Delta t \right\rangle = \lim_{J \rightarrow \infty} \lim_{N \rightarrow \infty} \sum_{j=1}^J \sum_{n=1}^N \langle \eta_j^n \eta_k^m \rangle h \Delta t = \sigma^2 h \Delta t \quad (6.10)$$

Equating Eqs (6.9) and (6.10), we see that the standard deviation of the discrete variable must be

$$\sigma = \frac{1}{\sqrt{h \Delta t}}. \quad (6.11)$$

For the stochastic simulations throughout this thesis, we use MATLAB's `randn` function to generate Gaussian-distributed random numbers $\{R_j^n\}$ of zero mean, unit variance:

$$\langle R_j^n \rangle = 0, \quad \langle R_j^n, R_k^m \rangle = \delta_{n,m} \delta_{j,k}. \quad (6.12)$$

Hence to map from continuous spatial and temporal noise $\xi(x, t)$, to its discrete-time approximation η_j^n we set,

$$\xi(x, t) \longrightarrow \{\eta_j^n\} = \frac{1}{\sqrt{h \Delta t}} \{R_j^n\}, \quad x = jh \text{ and } t = n\Delta t. \quad (6.13)$$

In the limit $\Delta t \rightarrow 0$, $h \rightarrow 0$, the variance of $\{\eta_j^n\}$ tends to infinity, and better approximates white-noise. Therefore as we reduce Δt and h the stochastic simulation should become increasing accurate.

6.2 Difference Equations

The difference equations used in the numerical simulations are derived in the following subsections. $[R_k]_j^n$ are random independent Gaussian-distributed variables as in Eq. (6.13), and the random variables driving each grid-point j are independent.

6.2.1 Linearized ‘‘Spatio-Adiabatic’’ Equations

The difference equations used to simulate the linearized ‘‘spatio-adiabatic’’ equations derived in Chapter 3 (i.e., Eq. (4.92)) are as follows,

$$\begin{aligned}
[\widehat{h}_e]_j^{n+1} &= [\widehat{h}_e]_j^n + [\Gamma_e]_j^n \Delta t + \kappa_e \Delta t \left\{ \frac{[\widehat{h}_e]_{j+1}^n + [\widehat{h}_e]_{j-1}^n - 2[\widehat{h}_e]_j^n}{h^2} \right\} \\
&+ \frac{\Delta t}{\tau_e} \left\{ -1 + \psi_{ee}^{(1)} \left[(N_{ee}^\alpha + N_{ee}^\beta) \mathcal{S}_e(h_e^0) + \langle p_{ee} \rangle \right] G_{ee} e / \gamma_e \right. \\
&+ \psi_{ee}(h_e^0) \left. \left[(N_{ee}^\alpha + N_{ee}^\beta) \mathcal{S}_e^{(1)} \right] G_{ee} e / \gamma_e \right. \\
&+ \lambda_{\text{GABA}} \psi_{ie}^{(1)} \left. \left[N_{ie}^\beta \mathcal{S}_i(h_i^0) + \langle p_{ie} \rangle \right] G_{ie} e / \gamma_i \right\} [\widehat{h}_e]_j^n \\
&+ \Delta t \left\{ \lambda_{\text{GABA}} \psi_{ie}(h_e^0) N_{ie}^\beta \mathcal{S}_i^{(2)} G_{ie} e / \gamma_i \tau_e \right\} [\widehat{h}_e]_j^n
\end{aligned} \tag{6.14}$$

$$\begin{aligned}
[\widehat{h}_i]_j^{n+1} &= [\widehat{h}_i]_j^n + [\Gamma_i]_j^n \Delta t + \kappa_i \Delta t \left\{ \frac{[\widehat{h}_e]_{j+1}^n + [\widehat{h}_e]_{j-1}^n - 2[\widehat{h}_e]_j^n}{h^2} \right\} \\
&+ \Delta t \left\{ \psi_{ei}(h_e^0) (N_{ei}^\alpha + N_{ei}^\beta) \mathcal{S}_e^{(1)} G_{ee} e / \gamma_e \tau_i \right\} [\widehat{h}_e]_j^n \\
&+ \frac{\Delta t}{\tau_i} \left\{ -1 + \psi_{ei}^{(2)} \left[(N_{ei}^\alpha + N_{ei}^\beta) \mathcal{S}_e(h_e^0) + \langle p_{ei} \rangle \right] G_{ee} e / \gamma_e \right. \\
&+ \lambda_{\text{GABA}} \psi_{ii}^{(2)} \left. \left[N_{ii}^\beta \mathcal{S}_i(h_i^0) + \langle p_{ii} \rangle \right] G_{ii} e / \gamma_i \right. \\
&+ \lambda_{\text{GABA}} \psi_{ii}(h_i^0) N_{ii}^\beta \mathcal{S}_i^{(2)} G_{ii} e / \gamma_i \left. \right\} [\widehat{h}_i]_j^n
\end{aligned} \tag{6.15}$$

where the continuous noise functions in Eqs. (4.78–4.79) become the following discrete noise time-series,

$$[\Gamma_e]_j^n = \frac{[R_1]_j^n \psi_{ee}([h_e]_j^n) \alpha_{ee} \sqrt{\langle p_{ee} \rangle} G_e e}{\sqrt{h\Delta t} \gamma_e \tau_e} + \frac{[R_3]_j^n \lambda_{\text{GABA}} \psi_{ie}([h_e]_j^n) \alpha_{ie} \sqrt{\langle p_{ie} \rangle} G_i e}{\sqrt{h\Delta t} \gamma_i \tau_e} \quad (6.16)$$

$$[\Gamma_i]_j^n = \frac{[R_2]_j^n \psi_{ei}([h_i]_j^n) \alpha_{ei} \sqrt{\langle p_{ei} \rangle} G_e e}{\sqrt{h\Delta t} \gamma_e \tau_i} + \frac{[R_4]_j^n \lambda_{\text{GABA}} \psi_{ii}([h_i]_j^n) \alpha_{ii} \sqrt{\langle p_{ii} \rangle} G_i e}{\sqrt{h\Delta t} \gamma_i \tau_i} \quad (6.17)$$

and the partial derivatives of the weighting and sigmoid functions are evaluated at equilibrium and defined by Eqs. (4.98–4.99).

6.2.2 “Spatio-Adiabatic” Equations

Simulating the nonlinearized “spatio-adiabatic” differential equations Eqs. (4.74–4.75) requires considerable care and thought. Naively writing the difference equations of Eqs. (4.74–4.75) straight out gives,

$$\begin{aligned} [h_e]_j^{n+1} &= [h_e]_j^n + [\Gamma_e]_j^n \Delta t + \frac{\Delta t}{\tau_e} \left\{ (h_e^{\text{rest}} - [h_e]_j^n) \right. \\ &\quad \left. + \psi_{ee}([h_e]_j^n) \left[(N_{ee}^\alpha + N_{ee}^\beta) \mathcal{S}_e([h_e]_j^n) + \frac{1}{\Lambda_{ee}^2} \left(\left[\frac{\partial^2 \phi_e}{\partial x^2} \right]_j^n \right) + \langle p_{ee} \rangle \right] G_e e / \gamma_e \right. \\ &\quad \left. + \lambda_{\text{GABA}} \psi_{ie}([h_e]_j^n) \left[N_{ie}^\beta \mathcal{S}_i([h_i]_j^n) + \langle p_{ie} \rangle \right] G_i e / \gamma_i \right\} \end{aligned} \quad (6.18)$$

$$\begin{aligned} [h_i]_j^{n+1} &= [h_i]_j^n + [\Gamma_i]_j^n \Delta t + \frac{\Delta t}{\tau_i} \left\{ (h_i^{\text{rest}} - [h_i]_j^n) \right. \\ &\quad \left. + \psi_{ei}([h_i]_j^n) \left[(N_{ei}^\alpha + N_{ei}^\beta) \mathcal{S}_e([h_e]_j^n) + \frac{1}{\Lambda_{ei}^2} \left(\left[\frac{\partial^2 \phi_i}{\partial x^2} \right]_j^n \right) + \langle p_{ee} \rangle \right] G_e e / \gamma_i \right. \\ &\quad \left. + \lambda_{\text{GABA}} \psi_{ii}([h_i]_j^n) \left[N_{ii}^\beta \mathcal{S}_i([h_i]_j^n) + \langle p_{ii} \rangle \right] G_i e / \gamma_i \right\} \end{aligned} \quad (6.19)$$

and the discrete Laplacian terms obey,

$$\frac{1}{\Lambda_{ee}^2} \left[\frac{\partial^2 \phi_e}{\partial x^2} \right]_j^n = [\phi_e]_j^n - N_{ee}^\alpha \mathcal{S}_e([h_e]_j^n) \quad (6.20)$$

$$\frac{1}{\Lambda_{ei}^2} \left[\frac{\partial^2 \phi_i}{\partial x^2} \right]_j^n = [\phi_i]_j^n - N_{ei}^\alpha \mathcal{S}_e([h_e]_j^n) \quad (6.21)$$

Unfortunately the above difference equations are impossible to simulate. This is because as the $\phi_{e,i}$ terms in Eqs. (4.74–4.75) have *no* time-dependence, the $\phi_{e,i}$ terms in the difference equations Eqs. (6.20–6.21) cannot be marched forward in time. As we cannot determine $\phi_{e,i}$ at $n + 1$ we cannot march h_e and h_i forward in time.

“Spatio-Adiabatic” Equations Near Homogeneous Equilibrium

In order to simulate the h_e fluctuations about the steady-state for the nonlinear spatio-adiabatic equations, we need to be able to march the difference equations forward in time. If we make the assumption that the system is never far from equilibrium, we can make use of the approximation,

$$\frac{\partial^2 \phi_e}{\partial x^2} \approx N_{ee}^\alpha \frac{dS_e}{dh_e} \Big|_{\text{eq.}} \frac{\partial^2 h_e}{\partial x^2} \quad (6.22)$$

$$\frac{\partial^2 \phi_i}{\partial x^2} \approx N_{ei}^\alpha \frac{dS_e}{dh_e} \Big|_{\text{eq.}} \frac{\partial^2 h_e}{\partial x^2} \quad (6.23)$$

derived in Chapter 3 (i.e., Eq. (4.90)). Discretizing gives,

$$\left[\frac{\partial^2 \phi_e}{\partial x^2} \right]_j^n \approx N_{ee}^\alpha \frac{dS_e}{dh_e} \Big|_{\text{eq.}} \left[\frac{\partial^2 h_e}{\partial x^2} \right]_j^n \quad (6.24)$$

$$\left[\frac{\partial^2 \phi_i}{\partial x^2} \right]_j^n \approx N_{ei}^\alpha \frac{dS_e}{dh_e} \Big|_{\text{eq.}} \left[\frac{\partial^2 h_e}{\partial x^2} \right]_j^n \quad (6.25)$$

and using the centred derivative form,

$$\left[\frac{\partial^2 h_e}{\partial x^2} \right]_j^n = \frac{[h_e]_{j+1}^n + [h_e]_{j-1}^n - 2[h_e]_j^n}{h^2} \quad (6.26)$$

Substituting the above approximation into Eqs. (6.18–6.19) gives a pair of difference equations for h_e and h_i that *can* be marched forward in time and hence simulated. The difference

equations become,

$$\begin{aligned}
[h_e]_j^{n+1} &= [h_e]_j^n + [\Gamma_e]_j^n \Delta t + \frac{\Delta t}{\tau_e} \left\{ (h_e^{\text{rest}} - [h_e]_j^n) \right. \\
&\quad + \psi_{ee}([h_e]_j^n) \left[(N_{ee}^\alpha + N_{ee}^\beta) \mathcal{S}_e([h_e]_j^n) + \frac{1}{\Lambda_{ee}^2} \left(N_{ee}^\alpha \frac{d\mathcal{S}_e}{dh_e} \Big|_{\text{eq.}} \left[\frac{\partial^2 h_e}{\partial x^2} \right]_j^n \right) + \langle p_{ee} \rangle \right] G_{ee} e / \gamma_e \\
&\quad \left. + \lambda_{\text{GABA}} \psi_{ie}([h_e]_j^n) \left[N_{ie}^\beta \mathcal{S}_i([h_i]_j^n) + \langle p_{ie} \rangle \right] G_{ie} e / \gamma_i \right\}
\end{aligned} \tag{6.27}$$

$$\begin{aligned}
[h_i]_j^{n+1} &= [h_i]_j^n + [\Gamma_i]_j^n \Delta t + \frac{\Delta t}{\tau_i} \left\{ (h_i^{\text{rest}} - [h_i]_j^n) \right. \\
&\quad + \psi_{ei}([h_i]_j^n) \left[(N_{ei}^\alpha + N_{ei}^\beta) \mathcal{S}_e([h_e]_j^n) + \frac{1}{\Lambda_{ei}^2} \left(N_{ei}^\alpha \frac{d\mathcal{S}_e}{dh_e} \Big|_{\text{eq.}} \left[\frac{\partial^2 h_e}{\partial x^2} \right]_j^n \right) + \langle p_{ee} \rangle \right] G_{ee} e / \gamma_i \\
&\quad \left. + \lambda_{\text{GABA}} \psi_{ii}([h_i]_j^n) \left[N_{ii}^\beta \mathcal{S}_i([h_i]_j^n) + \langle p_{ii} \rangle \right] G_{ii} e / \gamma_i \right\}
\end{aligned} \tag{6.28}$$

“Spatio-Adiabatic” Equations Far from Homogeneous Equilibrium

As discussed in Section 4.8 for the 1-D cortex, if we alter the long-range cortico-cortical $e-i$ diffusivity relative to the long-range $e-e$ diffusivity, the possibility exists for c_3 to become negative causing the top and/or bottom branch of the homogeneous steady-state solutions to become unstable for all wavenumbers $q > q_s$. Therefore, when driven by white noise, the homogeneous steady-state will be unstable as spatial white noise consists of *all* wavenumbers including $q > q_s$ (discussed in detail in Sec. 7.5). If for a certain λ_{GABA} the two stable *homogeneous* steady-state become unstable with respect to white noise, the system must bifurcate to a new stable *nonequilibrium* state, which we call $h_{e,i}(x)|_s$. As discussed in Sec. 4.8 there only exists the possibility of a bifurcation to a nonequilibrium state that oscillates in space but *not* time. Thus, if we give the system an initial perturbation away from the unstable state it will bifurcate to a new state,

$$\lim_{t \rightarrow \infty} h_e(x, t) = h_e(x)|_s \tag{6.29}$$

$$\lim_{t \rightarrow \infty} h_i(x, t) = h_i(x)|_s. \tag{6.30}$$

For a nonequilibrium state that is stationary in time, $\partial h_{e,i}(x)|_s/\partial t = 0$. Hence from Eqs. (4.74–4.75), and ignoring noise terms as we are only interested in the new steady-state, the $h_{e,i}|_s$ obey

$$0 = \frac{1}{\tau_e} \left\{ (h_e^{\text{rest}} - h_e|_s) + \psi_{ee}(h_e|_s) \left[(N_{ee}^\alpha + N_{ee}^\beta) \mathcal{S}_e(h_e|_s) + \frac{1}{\Lambda_{ee}^2} \frac{\partial^2 \phi_e|_s}{\partial x^2} + \langle p_{ee} \rangle \right] G_e e / \gamma_e \right. \\ \left. + \lambda_{\text{GABA}} \psi_{ie}(h_e|_s) \left[N_{ie}^\beta \mathcal{S}_i(h_i|_s) + \langle p_{ie} \rangle \right] G_i e / \gamma_i \right\} \quad (6.31)$$

$$0 = \frac{1}{\tau_i} \left\{ (h_i^{\text{rest}} - h_i|_s) + \psi_{ei}(h_i|_s) \left[(N_{ei}^\alpha + N_{ei}^\beta) \mathcal{S}_e(h_e|_s) + \frac{1}{\Lambda_{ei}^2} \frac{\partial^2 \phi_i|_s}{\partial x^2} + \langle p_{ee} \rangle \right] G_e e / \gamma_i \right. \\ \left. + \lambda_{\text{GABA}} \psi_{ii}(h_i|_s) \left[N_{ii}^\beta \mathcal{S}_i(h_i|_s) + \langle p_{ii} \rangle \right] G_i e / \gamma_i \right\} \quad (6.32)$$

where $\phi_e|_s$ and $\phi_i|_s$ are stable nonequilibrium solutions,

$$\lim_{t \rightarrow \infty} \phi_e(x, t) = \phi_e(x)|_s \quad (6.33)$$

$$\lim_{t \rightarrow \infty} \phi_i(x, t) = \phi_i(x)|_s \quad (6.34)$$

such that $\partial \phi_{e,i}|_s/\partial t = 0$ when $\partial h_{e,i}|_s/\partial t = 0$.

The idea of a relaxation method is that the solution of Eqs. (6.31–6.32) are just the solution of

$$\frac{\partial h_e}{\partial t} = \frac{1}{\tau_e} \left\{ (h_e^{\text{rest}} - h_e + \psi_{ee}(h_e)) \left[(N_{ee}^\alpha + N_{ee}^\beta) \mathcal{S}_e(h_e) + \frac{1}{\Lambda_{ee}^2} \frac{\partial^2 \phi_e}{\partial x^2} + \langle p_{ee} \rangle \right] G_e e / \gamma_e \right. \\ \left. + \lambda_{\text{GABA}} \psi_{ie}(h_e) \left[N_{ie}^\beta \mathcal{S}_i(h_i) + \langle p_{ie} \rangle \right] G_i e / \gamma_i \right\} \quad (6.35)$$

$$\frac{\partial h_i}{\partial t} = \frac{1}{\tau_i} \left\{ (h_i^{\text{rest}} - h_i) + \psi_{ei}(h_i) \left[(N_{ei}^\alpha + N_{ei}^\beta) \mathcal{S}_e(h_e) + \frac{1}{\Lambda_{ei}^2} \frac{\partial^2 \phi_i}{\partial x^2} + \langle p_{ee} \rangle \right] G_e e / \gamma_i \right. \\ \left. + \lambda_{\text{GABA}} \psi_{ii}(h_i) \left[N_{ii}^\beta \mathcal{S}_i(h_i) + \langle p_{ii} \rangle \right] G_i e / \gamma_i \right\} \quad (6.36)$$

in the limit $t \rightarrow \infty$. Using a FTCS scheme we cast Eqs. (6.35–6.36) into a pair of difference equations,

$$\begin{aligned}
[h_e]_j^{n+1} &= [h_e]_j^n + \frac{\Delta t}{\tau_e} \left\{ (h_e^{\text{rest}} - [h_e]_j^n) \right. \\
&\quad \left. + \psi_{ee}([h_e]_j^n) \left[(N_{ee}^\alpha + N_{ee}^\beta) \mathcal{S}_e([h_e]_j^n) + \frac{1}{\Lambda_{ee}^2} \left(\left[\frac{\partial^2 \phi_e}{\partial x^2} \right]_j^n \right) + \langle p_{ee} \rangle \right] G_{ee} e / \gamma_e \right. \\
&\quad \left. + \lambda_{\text{GABA}} \psi_{ie}([h_e]_j^n) \left[N_{ie}^\beta \mathcal{S}_i([h_i]_j^n) + \langle p_{ie} \rangle \right] G_{ie} e / \gamma_i \right\}
\end{aligned} \tag{6.37}$$

$$\begin{aligned}
[h_i]_j^{n+1} &= [h_i]_j^n + \frac{\Delta t}{\tau_i} \left\{ (h_i^{\text{rest}} - [h_i]_j^n) \right. \\
&\quad \left. + \psi_{ei}([h_i]_j^n) \left[(N_{ei}^\alpha + N_{ei}^\beta) \mathcal{S}_e([h_e]_j^n) + \frac{1}{\Lambda_{ei}^2} \left(\left[\frac{\partial^2 \phi_i}{\partial x^2} \right]_j^n \right) + \langle p_{ee} \rangle \right] G_{ee} e / \gamma_i \right. \\
&\quad \left. + \lambda_{\text{GABA}} \psi_{ii}([h_i]_j^n) \left[N_{ii}^\beta \mathcal{S}_i([h_i]_j^n) + \langle p_{ii} \rangle \right] G_{ii} e / \gamma_i \right\}
\end{aligned} \tag{6.38}$$

In order to simulate the $[\partial^2 \phi_{e,i} / \partial x^2]_j^n$ terms we also use the relaxation technique. From Eq. (4.72–4.73), we have

$$0 = \frac{1}{\Lambda_{ee}^2} \frac{\partial^2 \phi_e|_s}{\partial x^2} + N_{ee}^\alpha \mathcal{S}_e(h_e) - \phi_e|_s \tag{6.39}$$

$$0 = \frac{1}{\Lambda_{ei}^2} \frac{\partial^2 \phi_i|_s}{\partial x^2} + N_{ei}^\alpha \mathcal{S}_e(h_e) - \phi_i|_s \tag{6.40}$$

which is the stationary solution of

$$\frac{\partial \phi_e}{\partial t} = \mu \left(\frac{1}{\Lambda_{ee}^2} \frac{\partial^2 \phi_e}{\partial x^2} + N_{ee}^\alpha \mathcal{S}_e(h_e) - \phi_e \right) \tag{6.41}$$

$$\frac{\partial \phi_i}{\partial t} = \mu \left(\frac{1}{\Lambda_{ei}^2} \frac{\partial^2 \phi_i}{\partial x^2} + N_{ei}^\alpha \mathcal{S}_e(h_e) - \phi_i \right) \tag{6.42}$$

in the limit $t \rightarrow \infty$. The value of the constant μ does not alter the stationary value, but is used to ensure the scheme is stable. A new time increment m is introduced to determine the stationary value for each $[\phi]_j$ at time-increment n . The m increment can be thought of as a “fast” time increment, while the n increment can be thought of as a “slow” time increment. Using a FTCS

scheme we update over the new time-increment m for a given $[h_e]_j$ at time-increment n ,

$$[\phi_e]_j^m = [\phi_e]_j^{m-1} + \frac{\mu\Delta t}{\Lambda_{ee}^2} \frac{[\phi_e]_{j-1}^{m-1} + [\phi_e]_{j+1}^{m-1} - 2[\phi_e]_j^{m-1}}{h^2} + \mu\Delta t N_{ee}^\alpha \mathcal{S}_e([h_e]_j^n) - \mu\Delta t [\phi_e]_j^{m-1} \quad (6.43)$$

$$[\phi_i]_j^m = [\phi_i]_j^{m-1} + \frac{\mu\Delta t}{\Lambda_{ei}^2} \frac{[\phi_e]_{j-1}^{m-1} + [\phi_e]_{j+1}^{m-1} - 2[\phi_e]_j^{m-1}}{h^2} + \mu\Delta t N_{ei}^\alpha \mathcal{S}_e([h_e]_j^n) - \mu\Delta t [\phi_i]_j^{m-1}. \quad (6.44)$$

When $\phi_{e,i}$ has reached its stationary solution, we use Eqs. (6.39–6.40), giving

$$\frac{1}{\Lambda_{ee}^2} \left(\left[\frac{\partial^2 \phi_e}{\partial x^2} \right]_j^n \right) = -N_{ee}^\alpha \mathcal{S}_e([h_e]_j^n) + [\phi_e]_j^m \quad (6.45)$$

$$\frac{1}{\Lambda_{ei}^2} \left(\left[\frac{\partial^2 \phi_i}{\partial x^2} \right]_j^n \right) = -N_{ei}^\alpha \mathcal{S}_e([h_e]_j^n) + [\phi_i]_j^m \quad (6.46)$$

and substitute Eqs. (6.45–6.46) back into Eqs. (6.37–6.38) resulting in,

$$\begin{aligned} [h_e]_j^{n+1} = [h_e]_j^n + \frac{\Delta t}{\tau_e} \left\{ (h_e^{\text{rest}} - [h_e]_j^n) + \psi_{ee}([h_e]_j^n) \left[N_{ee}^\beta \mathcal{S}_e([h_e]_j^n) + [\phi_e]_j^m + \langle p_{ee} \rangle \right] G_{ee} e / \gamma_e \right. \\ \left. + \lambda_{\text{GABA}} \psi_{ie}([h_e]_j^n) \left[N_{ie}^\beta \mathcal{S}_i([h_i]_j^n) + \langle p_{ie} \rangle \right] G_{ie} e / \gamma_i \right\} \end{aligned} \quad (6.47)$$

$$\begin{aligned} [h_i]_j^{n+1} = [h_i]_j^n + \frac{\Delta t}{\tau_i} \left\{ (h_i^{\text{rest}} - [h_i]_j^n) + \psi_{ei}([h_i]_j^n) \left[N_{ei}^\beta \mathcal{S}_e([h_e]_j^n) + [\phi_e]_j^m + \langle p_{ee} \rangle \right] G_{ee} e / \gamma_e \right. \\ \left. + \lambda_{\text{GABA}} \psi_{ii}([h_i]_j^n) \left[N_{ii}^\beta \mathcal{S}_i([h_i]_j^n) + \langle p_{ii} \rangle \right] G_{ii} e / \gamma_i \right\} \end{aligned} \quad (6.48)$$

Eqs. (6.47–6.48) and Eqs. (6.43–6.44) are the difference equations used to stimulate the formation of the nonequilibrium states. The overall scheme progresses forward such that for each h_e at time-step n we find the stationary solutions of Eqs. (6.43–6.44) by updating $\phi_{e,i}$ over the separate time-increment m , until $\phi_{e,i}$ is stationary and then update $h_{e,i}$ via Eqs. (6.47–6.48) and repeat the process. In order to perturb the system, noise via Eqs. (6.16–6.17) are included for the first time-increment, and then turned off for subsequent time steps.

6.3 Avoiding Negative Subcortical Inputs

In Section 3.5 the scale factors α_{jk} were introduced to keep the cortico-cortical inputs physiologically meaningful. Modelling the sub-cortical fluctuations as Gaussian-distributed noise leads to the possibility of negative sub-cortical firing rates. This can occur mathematically because the Gaussian-distributed random variables η do not have upper and lower bounds. However, there is no *physiological* meaning for negative firing rates, so we are motivated to suppress such unphysical events.

In Section 3.5 the four sub-cortical inputs p_{jk} were transformed into Gaussian-distributed random numbers,

$$p_{jk}(x, t) = \langle p_{jk} \rangle + \alpha_{jk} \sqrt{\langle p_{jk} \rangle} \xi_n(x, t) \quad (6.49)$$

In order to simulate the $\xi(x, t)$ noise sources, they are replaced by their discrete-time approximation $R_j^n / \sqrt{h\Delta t}$. Hence

$$p_{jk}(x, t) \rightarrow [p_{jk}]_j^n = \langle p_{jk} \rangle + \alpha_{jk} \sqrt{\langle p_{jk} \rangle} \frac{[R]_j^n}{\sqrt{h\Delta t}}, \quad x = jh \text{ and } t = n\Delta t \quad (6.50)$$

which is Gaussian-distributed with mean $\langle p_{jk} \rangle$ and standard deviation

$$\text{sdev}\{p_{jk}\} = \alpha_{jk} \sqrt{\langle p_{jk} \rangle / h\Delta t}. \quad (6.51)$$

The dimensionless “safety factors” α_{jk} are used to ensure that the probability of negative sub-cortical firing rates is vanishingly small. It was decided to use a safety factor of,

$$\alpha = 0.01 \quad (6.52)$$

which applies to *all four* subcortical noise inputs. From Table 3.1 the values for p_{jk} are $p_{ee}, p_{ii} = 1100 \text{ s}^{-1}$ and $p_{ie}, p_{ei} = 1600 \text{ s}^{-1}$. If a time-step of $\Delta t = 10^{-5}$ and a spacing of 0.05 cm is used in

the numerical simulations, then constraining p_{jk} to one standard deviation bounds gives,

$$p_{ee} = 1100 \pm 469 \text{ s}^{-1} \quad (6.53)$$

$$p_{ii} = 1100 \pm 469 \text{ s}^{-1} \quad (6.54)$$

$$p_{ie} = 1600 \pm 566 \text{ s}^{-1} \quad (6.55)$$

$$p_{ei} = 1600 \pm 566 \text{ s}^{-1}. \quad (6.56)$$

This is the worst case scenario: Negative firing rates occurring 2 percent of the time for p_{ee}, p_{ii} and 0.5 percent of the time for p_{ie}, p_{ei} . For all the simulations used throughout this thesis a time-step of 10^{-5} s was used, as it provides stable simulations for a range of grid-spacings (discussed in the next section). The spacing was never reduced below 0.05 cm except on one occasion when investigating the power spectrum at $\lambda_{\text{GABA}} = 0.1$. The spacing had to be reduced to 0.001 cm to give an accurate simulation, giving rise to a 74 percent chance of negative firing for the p_{ie}, p_{ei} . Even though the physiology has been compromised the simulation still gives good agreement with the theoretical prediction.

6.4 von Neumann Stability Analysis

The stability of the difference equations used to simulate the spatial cortex is dependent on the time-step Δt and the grid-spacing h . If for a certain grid-spacing the time-step Δt is too big, the numerical scheme will be numerically unstable. The stability of the scheme is determined by the rate at which information propagates out in space. For the numerical schemes described above, in an amount of time Δt , the information from a grid-point $[h_e]_j$ at time n can only be passed onto the grid-points $[h_e]_{j-1}, [h_e]_j$ and $[h_e]_{j+1}$ at time $n + 1$. If according to the partial differential equation governing the difference equation, the spatial information should have propagated further than *twice* the grid-spacing (the distance between $[h_e]_{j-1}$ and $[h_e]_{j+1}$) in a time-step Δt , then information required to march forward in time accurately has been lost. This lack of information gives rise to numerical instability. Using *von Neumann stability analysis* we can determine what combinations of time-step and grid-spacing are numerically stable.

von Neumann stability analysis only works for constant-coefficient, linear difference equations solved as initial value problems. For a nonlinear system, we apply the von Neumann stability analysis to the *linearized* system. Stability conditions obtained using this technique are not necessary valid for the nonlinear problem. Nevertheless, it usually gives a good estimate of the

true stability condition. Since a general theory of stability for nonlinear problems does not exist, linearization is the only practical approach.

Following Press *et al.* (1988) for a single non-coupled constant-coefficient linear difference equation, the independent solutions, or *eigenmodes*, of the difference equation are all of the form

$$u_j^n = \xi^n e^{iqjh} \quad (6.57)$$

where u_j^n is the variable being updated in time and space, h is the grid-spacing, q is a real spatial wave number (which can have any value) and $\xi = \xi(q)$ is a complex number that depends on q . Advancing Eq. (6.57) by one time-step gives

$$u_j^{n+1} = \xi^{n+1} e^{iqjh} \quad (6.58)$$

This equation implies that the time dependence of a single eigenmode is nothing more than successive integer powers of the complex number ξ . Hence the difference equation will be unstable (have exponentially growing modes) if $|\xi(q)| > 1$ for *some* q . The number ξ is called the *amplification factor* at a given wave number q .

The linearized spatio-adiabatic equations read,

$$\frac{\partial}{\partial t} \begin{bmatrix} \hat{h}_e(x, t) \\ \hat{h}_i(x, t) \end{bmatrix} = \begin{bmatrix} J_{11} + \kappa_e \frac{\partial^2}{\partial x^2} & J_{12} \\ J_{21} + \kappa_i \frac{\partial^2}{\partial x^2} & J_{22} \end{bmatrix} \begin{bmatrix} \hat{h}_e(x, t) \\ \hat{h}_i(x, t) \end{bmatrix} + \begin{bmatrix} \Gamma_e(x, t) \\ \Gamma_i(x, t) \end{bmatrix}_{\text{eq.}} \quad (6.59)$$

Ignoring the noise terms, these are equivalent to a pair of coupled constant-coefficient linear difference equations,

$$[\hat{h}_e]_j^{n+1} = [\hat{h}_e]_j^n + \Delta t J_{11} [\hat{h}_e]_j^n + \kappa_e \Delta t \left\{ \frac{[\hat{h}_e]_{j+1}^n + [\hat{h}_e]_{j-1}^n - 2[\hat{h}_e]_j^n}{h^2} \right\} + \Delta t J_{12} [\hat{h}_i]_j^n \quad (6.60)$$

$$[\hat{h}_i]_j^{n+1} = [\hat{h}_i]_j^n + \Delta t J_{21} [\hat{h}_e]_j^n + \kappa_i \Delta t \left\{ \frac{[\hat{h}_e]_{j+1}^n + [\hat{h}_e]_{j-1}^n - 2[\hat{h}_e]_j^n}{h^2} \right\} + \Delta t J_{22} [\hat{h}_i]_j^n . \quad (6.61)$$

(We can ignore the noise terms as they do not directly contribute to the numerical scheme's stability.)

Following Press *et al.* (1988), we proceed by assuming that the eigenmodes are of the following form,

$$\begin{bmatrix} [h_e]_j^n \\ [h_i]_j^n \end{bmatrix} = \xi^n e^{iqjh} \begin{bmatrix} h_e^0 \\ h_i^0 \end{bmatrix} \quad (6.62)$$

where h_e^0, h_i^0 are the steady-state solutions. The vector on the right-hand side is a constant eigenvector, and ξ is a complex number as before. Substituting Eq. (6.62) into Eqs. (6.60–6.61) gives,

$$\begin{aligned} \xi^{n+1} e^{iqjh} h_e^0 &= \xi^n e^{iqjh} h_e^0 + \Delta t J_{11} \xi^n e^{iqjh} h_e^0 + \Delta t J_{12} \xi^n e^{iqjh} h_i^0 \\ &+ \frac{\kappa_e \Delta t}{h^2} \left(\xi^n e^{iq(j+1)h} h_e^0 + \xi^n e^{iq(j-1)h} h_e^0 - 2\xi^n e^{iqjh} h_e^0 \right) \end{aligned} \quad (6.63)$$

and

$$\begin{aligned} \xi^{n+1} e^{iqjh} h_i^0 &= \xi^n e^{iqjh} h_i^0 + \Delta t J_{21} \xi^n e^{iqjh} h_e^0 + \Delta t J_{22} \xi^n e^{iqjh} h_i^0 \\ &+ \frac{\kappa_i \Delta t}{h^2} \left(\xi^n e^{iq(j+1)h} h_e^0 + \xi^n e^{iq(j-1)h} h_e^0 - 2\xi^n e^{iqjh} h_e^0 \right) \end{aligned} \quad (6.64)$$

Dividing both sides of Eqs. (6.63–6.64) by $\xi^n e^{iqjh}$ gives,

$$\xi h_e^0 = h_e^0 + \Delta t J_{11} h_e^0 + \Delta t J_{12} h_i^0 + \frac{\kappa_e \Delta t}{h^2} (e^{iqh} h_e^0 + e^{-iqh} h_e^0 - 2h_e^0) \quad (6.65)$$

$$\Rightarrow h_e^0 + \Delta t J_{11} h_e^0 + \Delta t J_{12} h_i^0 + \frac{\kappa_e \Delta t}{h^2} h_e^0 (2 \cos(qh) - 2) - \xi h_e^0 = 0 \quad (6.66)$$

and

$$\xi h_i^0 = h_i^0 + \Delta t J_{21} h_e^0 + \Delta t J_{22} h_i^0 + \frac{\kappa_i \Delta t}{h^2} (e^{iqh} h_e^0 + e^{-iqh} h_e^0 - 2h_e^0) \quad (6.67)$$

$$\Rightarrow h_i^0 + \Delta t J_{21} h_e^0 + \Delta t J_{22} h_i^0 + \frac{\kappa_i \Delta t}{h^2} h_e^0 (2 \cos(qh) - 2) - \xi h_i^0 = 0 \quad (6.68)$$

We can write Eqs. (6.66) and (6.68) as a vector equation

$$\begin{bmatrix} 1 + \Delta t J_{11} + \frac{\kappa_e \Delta t}{h^2} (2 \cos(qh) - 2) - \xi & \Delta t J_{12} \\ \Delta t J_{21} + \frac{\kappa_i \Delta t}{h^2} (2 \cos(qh) - 2) & 1 + \Delta t J_{22} - \xi \end{bmatrix} \cdot \begin{bmatrix} h_e^0 \\ h_i^0 \end{bmatrix} = \begin{bmatrix} 0 \\ 0 \end{bmatrix} \quad (6.69)$$

This admits a solution only if the determinant of the matrix on the left vanishes, a condition that requires,

$$\xi^2 + b\xi + c = 0 \quad (6.70)$$

where b and c are defined as

$$b = -1 - \Delta t J_{11} - \frac{\kappa_e \Delta t}{h^2} (2 \cos(qh) - 2) - 1 - \Delta t J_{22} \quad (6.71)$$

$$c = (1 + \Delta t J_{11} + \frac{\kappa_e \Delta t}{h^2} (2 \cos(qh) - 2))(1 + \Delta t J_{22}) - (\Delta t J_{12})(\Delta t J_{21} + \frac{\kappa_i \Delta t}{h^2} (2 \cos(qh) - 2)) \quad (6.72)$$

The two roots of Eq. (6.70) are given by,

$$\xi = \frac{-b \pm \sqrt{b^2 - 4c}}{2} \quad (6.73)$$

In order to calculate for which time-steps and grid-spacing the stability condition is satisfied the MATLAB code `stability.m` was written. Numerical stability requires $|\xi| \leq 1$ for *all* wavenumbers q (i.e. $q = 0 \rightarrow \infty$). But in Eq. (6.73) q only appears in the cosine function. As the cosine function is symmetric and repeats its range of values every π it is sufficient to consider q over the range $0 \rightarrow \pi$. For a given time-step and grid-spacing the code ramps q through 0 to π and calculates the associated roots for ξ . These roots are then checked against the stability condition $|\xi| \leq 1$.

Figure 6.1 shows the maximum value for each $|\xi(k)|$ associated with a time-step and grid-spacing, for a simulation on the top branch at $\lambda_{\text{GABA}} = 0.3$. The process is also repeated in Fig. 6.2 for the top branch at $\lambda_{\text{GABA}} = 1.3$. The figures show that we have to be careful when choosing a grid-spacing for a given time-step. Notice that for the top-branch at $\lambda_{\text{GABA}} = 1.3$, for a given time-step a larger grid-spacing has to be used than at $\lambda_{\text{GABA}} = 0.3$. In general for a given time-step the closer we are to the transition points on the top and bottom branch, the *larger* the grid-spacing required for numerical stability. This increase in required grid-spacing is consistent with the increase in correlation lengths as the transition points are approached i.e., near transition, information for a given time-step propagates further in space.

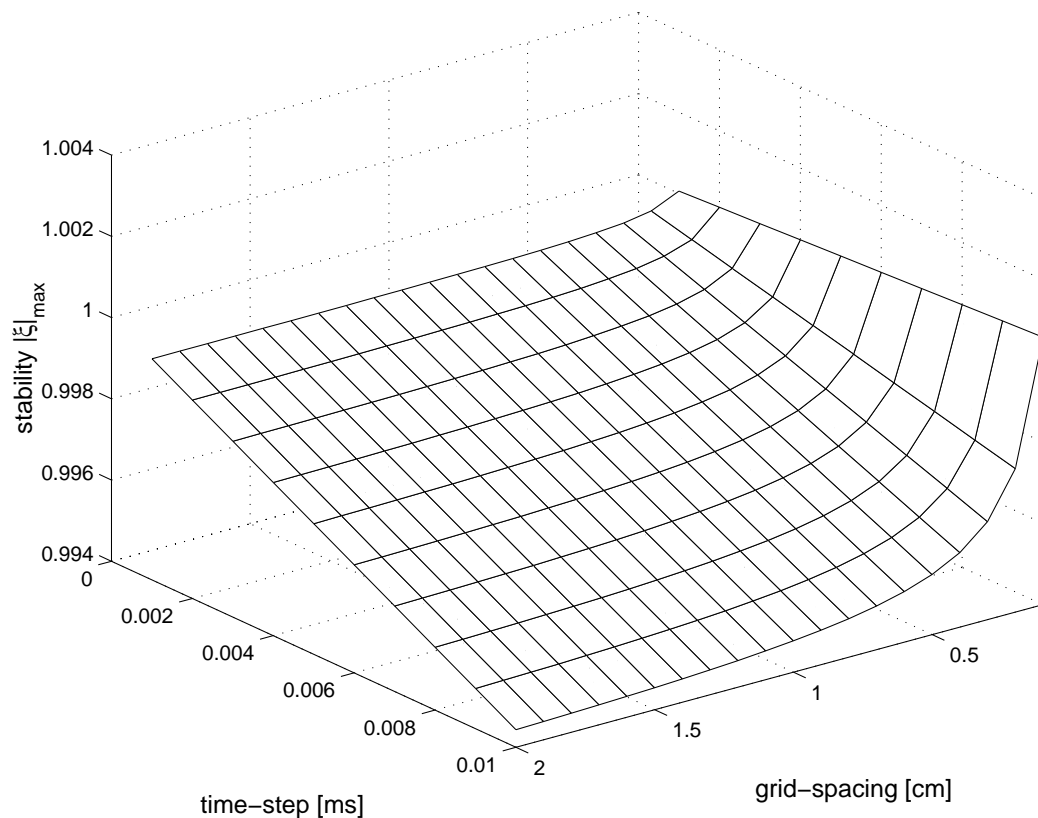


Figure 6.1: Stability as a function of time-step and grid-spacing for $\lambda_{\text{GABA}} = 0.3$ on the top branch

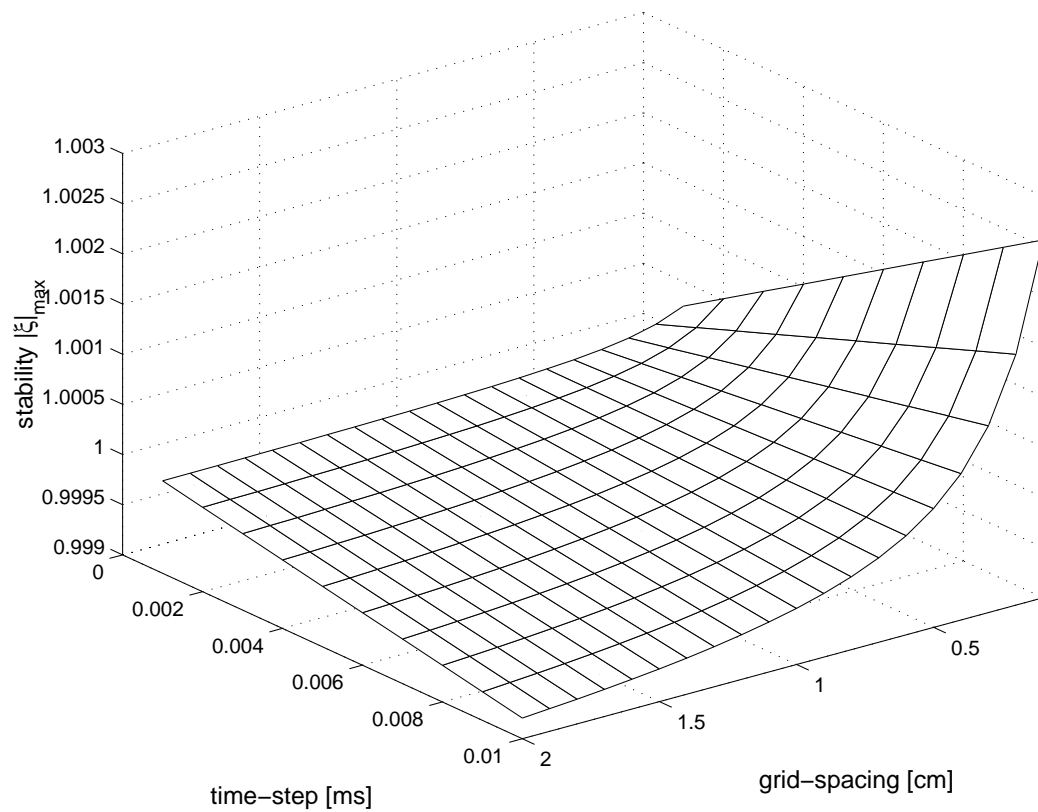


Figure 6.2: Stability as a function of time-step and grid-spacing for $\lambda_{\text{GABA}} = 1.3$ on the top branch

6.5 Boundary Conditions

The theory assumes an infinitely long 1-D cortical rod and therefore there are no boundary conditions. For our numerical simulations we *have* to include boundary conditions as it is impossible to simulate a truly infinite rod. However, provided the rod is “long enough” we should still obtain good comparisons between theory and numerical experiment.

I investigated two types of boundary conditions: *periodic* and *zero flux*. With **periodic boundary conditions** the cortex is effectively connected at the ends, transforming the coordinates from a 1-D line to a circle. Thus, if spatial information reaches the end of the rod, this information is immediately transmitted to the beginning of the rod. When determining the spatial covariance curve of the cortical fluctuations, we do not want any spatial information to travel further than the numerical “length” of the rod. A clear indication that the length is “too short”, is when, instead of the expected bi-exponential decay in spatial covariance, we obtain an exponential decay followed by a “hump” (Fig. 7.10). This hump indicates that information has propagated around the entire length of the rod, suggesting that a longer rod is required for more accurate comparisons.

Zero flux boundary conditions are simulated by fixing the flux at both ends of the 1-D rod. For the cortical simulations this was achieved by setting the value of the grid-points at the ends of the rods to their equilibrium value and *not* driving those grid-points with noise.

We discovered that as long as the cortical rod was of sufficient length, the type of boundary condition imposed made little difference to the properties of the h_e fluctuations about equilibrium. However when simulating the formation of *nonequilibrium* states, the imposition of zero flux boundary conditions by holding ends of the cortical rod at the homogeneous steady-state is not appropriate because the homogeneous steady-state is no longer stable. Therefore periodic boundary conditions are the better choice for this case. The only constraint periodic boundary conditions place on the nonequilibrium states is they must form on a 1-D circle, rather than along an infinite 1-D rod.

For simplicity, periodic boundary conditions were used for all simulations presented throughout this thesis.

6.6 Examples of h_e time-series

Fig. 6.3 shows four time-series of the simulated spatio-adiabatic equations near equilibrium. The difference equations Eqs. (6.27–6.28) were used, with a timestep of 0.01 ms and the grid-spacing adjusted for numerical stability.

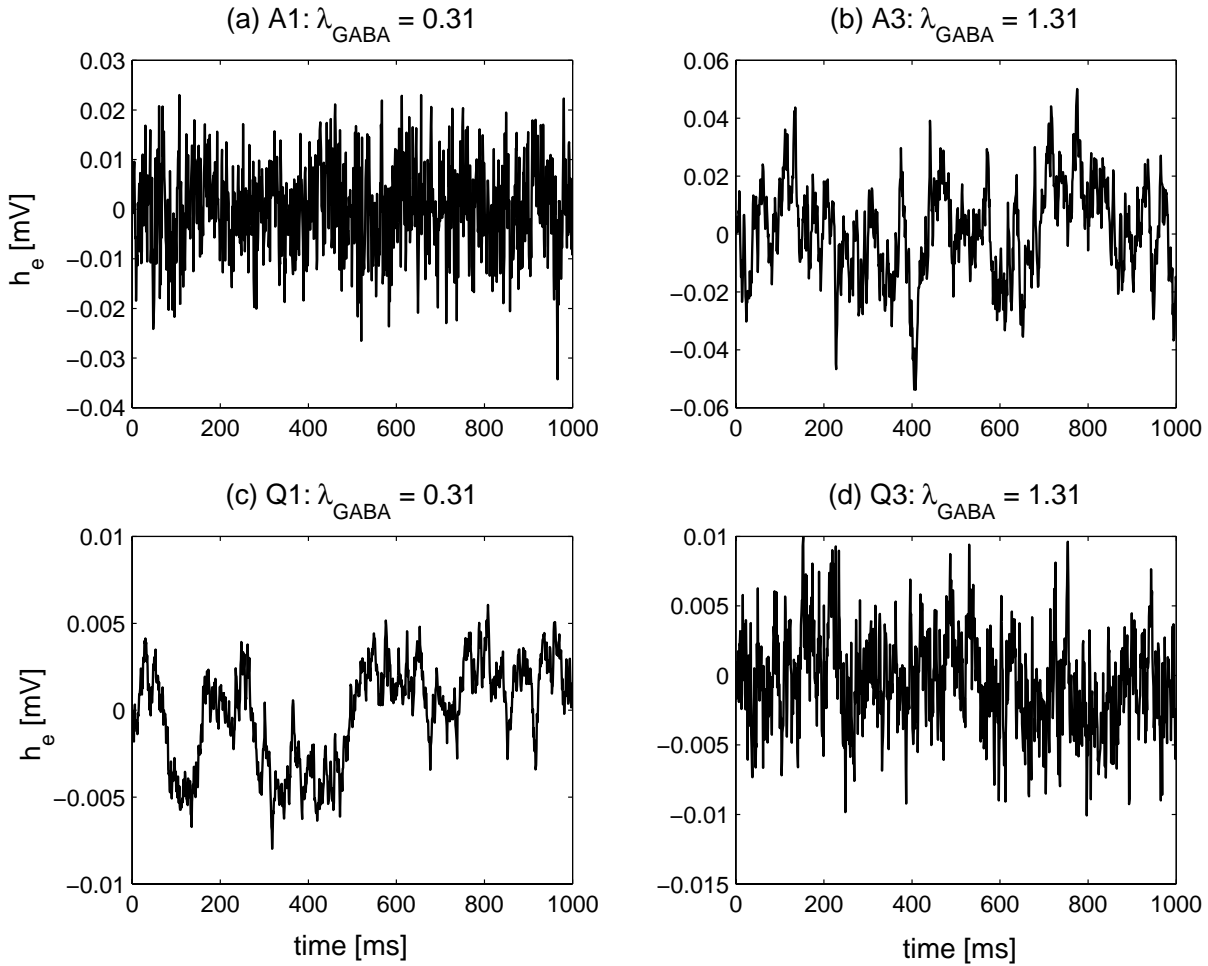


Figure 6.3: Time series for $\lambda_{\text{GABA}} = 0.31$ and $\lambda_{\text{GABA}} = 1.31$ on the top and bottom branches. A time-step of 0.01 ms, and 100 grid points were used for all simulations. The grid spacing used for each plot is (a) 0.05 cm (b) 2 cm (c) 1 cm (d) 0.1 cm.

Properties of the “Spatio-Adiabatic”

Macrocolumn

7.1 Altering the Strength of the e - e Diffusivity Relative to the e - i Diffusivity

Following Steyn-Ross *et al.* (2003), in order to increase the strength of the e - i diffusivity relative to the e - e diffusivity (allowing for the possibility of c_3 going negative), a dimensionless factor $f \geq 1$ is introduced to scale the inverse-length connectivity constants Λ_{ee} and Λ_{ei} in opposite directions:

$$\Lambda'_{ee} = f\Lambda_{ee}, \quad \Lambda'_{ei} = \Lambda_{ei}/f. \quad (7.1)$$

We define a dendritic “wiring” ratio

$$R = \frac{\Lambda'_{ee}}{\Lambda'_{ei}}. \quad (7.2)$$

(We note that changing Λ_{ee} or Λ_{ei} has no effect on the values for (h_e^0, h_i^0) , the stationary solutions of the spatially homogeneous cortex.)

From Eq. (4.93), $\kappa_{e,i} \propto 1/\Lambda_{ee,ei}^2$, so the respective e - and i -diffusivities will scale as:

$$\kappa'_e = \kappa_e/f^2, \quad \kappa'_i = f^2\kappa_i. \quad (7.3)$$

Hence an increase in f will simultaneously strengthen κ_i while weakening κ_e . Setting $f = 1$ gives the default values for diffusivities κ_e, κ_i and corresponds to a default wiring ratio of $R = 0.615$. Setting $f = 1.58$ ($R = 1.536$) is sufficient to cause c_3 to become negative in the immediate

vicinity of the loss of consciousness transition point, $\lambda_{\text{GABA}} = 1.31$. Raising the factor f above 1.58 results in a larger region of the top-branch exhibiting a negative c_3 .

7.2 Correlation Length

Generally the *correlation length* L is defined as the length required for the covariance function $G(|x - x'|)$ to decay to $1/e$ of its zero-lag value. This definition makes the assumption that the covariance function is a simple, single-exponential decaying function of space of the form,

$$G(\tau) = G(0)e^{-k\tau}, \quad \tau \geq 0 \quad (7.4)$$

for which $L = 1/k$. We can extract the correlation length by plotting a semilog graph of $\ln G(\tau)$ vs τ , giving

$$\ln G(\tau) = \ln G(0) - k|\tau| \quad (7.5)$$

The slope of this graph retrieves k , the inverse of the correlation length.

The spatial covariance for the cortex, derived in Sec. 4.9, has two forms depending on the sign of c_3 . If $c_3 > 0$, the spatial covariance has the form,

$$G(|x - x'|) = \alpha_1 e^{-|x-x'|/L_1} + \alpha_2 e^{-|x-x'|/L_2} \quad (7.6)$$

where

$$\alpha_1 = \frac{D_1/\kappa_e + c_4}{4} L_1, \quad \alpha_2 = -\frac{c_4}{4} L_2. \quad (7.7)$$

As Eq. (7.6) consists of two exponentially-decaying functions, L_1 and L_2 are labelled correlation lengths for both exponential functions. (It is possible to calculate a generalized correlation length for the above process, as outlined by Gardiner (1985), but it does not help in seeking comparisons between theory and experiment.) However it is very difficult to determine the two correlation lengths accurately from stochastic simulations. Curve-fitting methods were tried but yielded poor results. For these reasons, agreement between theory and stochastic experiment was established by comparing the theoretical covariance curve with the smoothed experimental covariance measurement, obtained after averaging over a large number of stochastic runs.

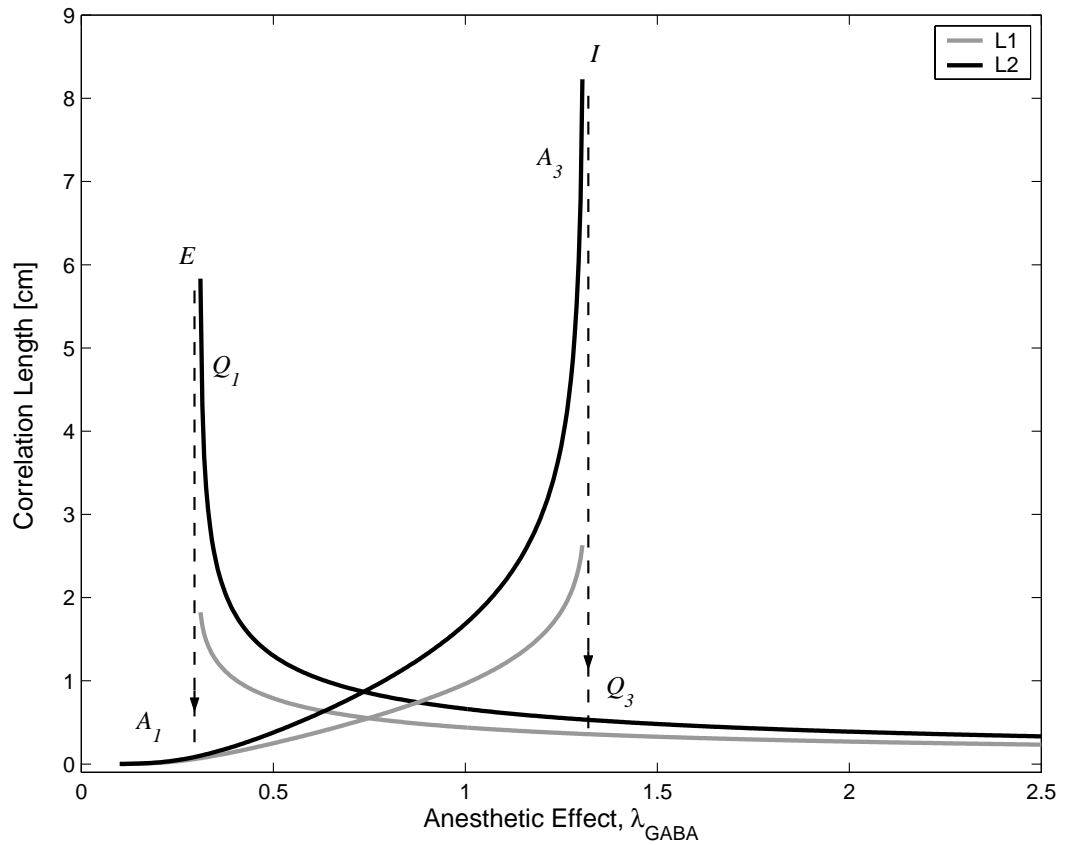


Figure 7.1: Theoretical predictions for L_1 and L_2 correlation lengths as a function of anaesthetic effect λ_{GABA} for the spatio-adiabatic 1-D cortex with default cortico-cortical wiring ratio $R = 0.615$ ($f = 1$).

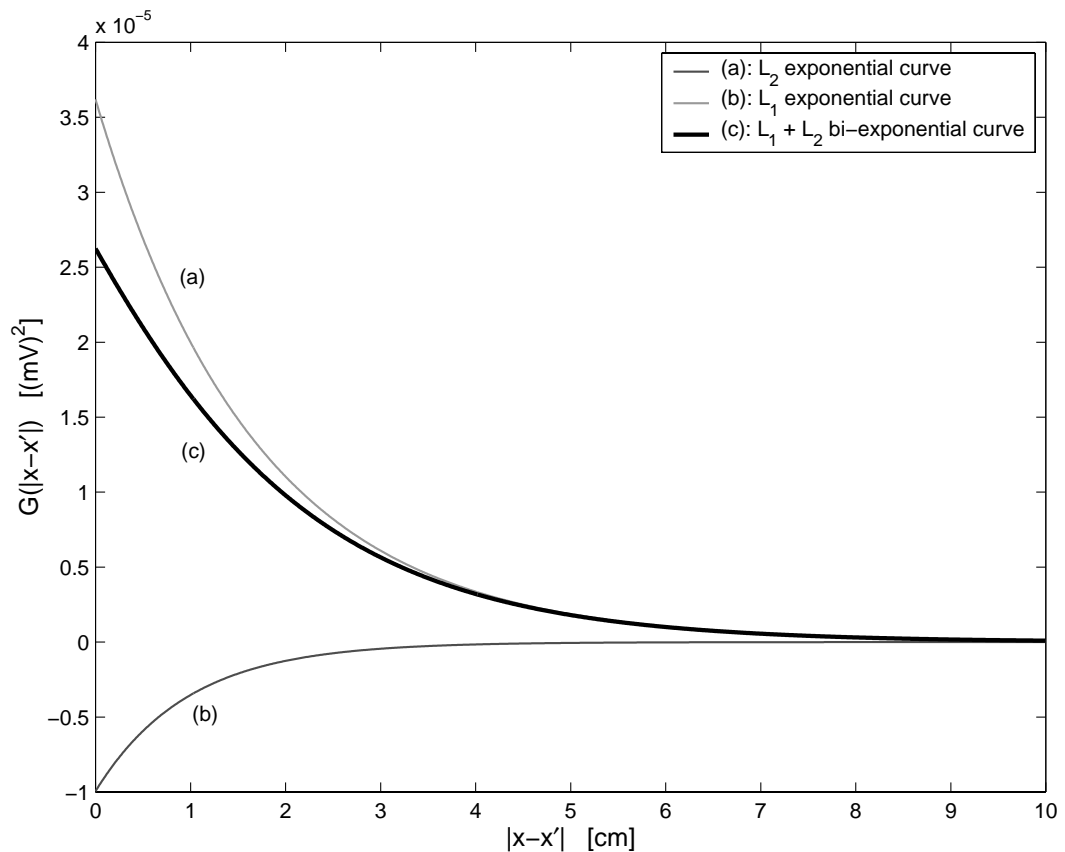


Figure 7.2: Theoretical predictions for L_1 , L_2 and $L_1 + L_2$ covariance curves at an anaesthetic effect of $\lambda_{\text{GABA}} = 1$, for the spatio-adiabatic 1-D cortex with default cortico-cortical wiring ratio $R = 0.615$ ($f = 1$).

The second form of the covariance function occurs when $c_3 < 0$, and has the form

$$G(|x - x'|) = \alpha_1 e^{-|x-x'|/L_1} - \alpha_2 \sin(|x - x'|/L_2). \quad (7.8)$$

This function consists of an exponential with correlation length L_1 added to a *sinewave variation* of wavelength $2\pi L_2$.

7.2.1 Theoretical Predictions of Correlation Length for $c_3 > 0$

Figure 7.1 plots the theoretical predictions for the correlation lengths L_1 and L_2 as anaesthetic concentration is varied for the default value of the dendritic ‘‘wiring’’ ratio $R = 0.615$ (corresponding to $f = 1$). As the transition points of loss of consciousness (A_3) and return to

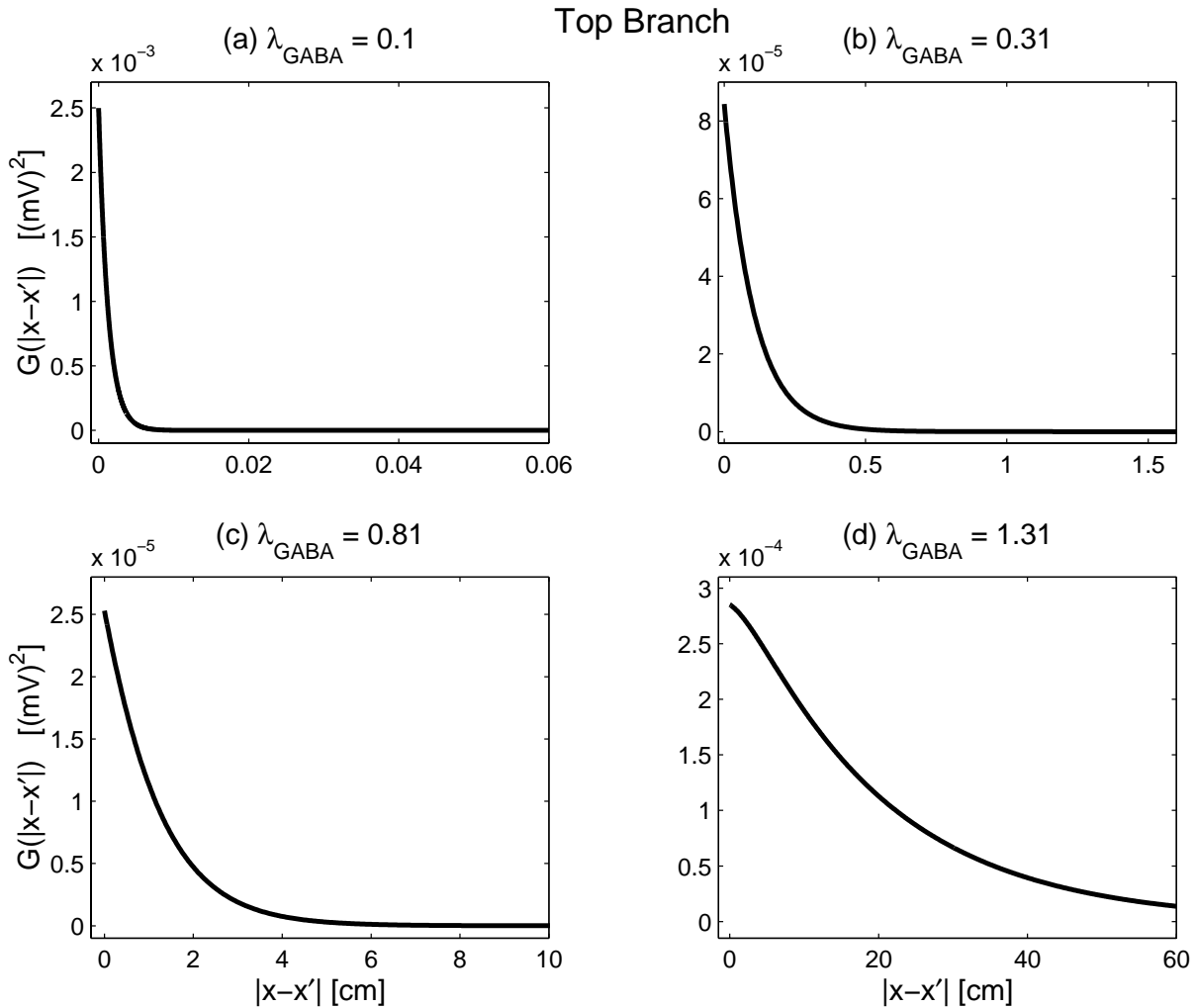


Figure 7.3: Theoretical covariance predictions for separations of $|x - x'|$ cm along the cortical rod. The four panels (a, b, c, d) show the difference in the spatial width of the covariance curve at four anaesthetic concentrations, along the top branch (active branch) of Fig. 3.11. The four panels illustrate that as the point of loss-of-consciousness is approached the spatial width of the covariance curve strongly increases. These predictions are for the default of the $\kappa_{e,i}$ diffusivities.

consciousness (Q_1) are approached, the correlation lengths L_1 and L_2 dramatically increase. Also note that the correlation lengths are larger at Q_3 compared to A_1 . This indicates the unconscious brain is predicted to have greater spatial coherence compared to the conscious brain.

As the spatial covariance curves consist of two exponentially-decaying curves it is wise to check the sum of the two exponentials. A typical summation of the two exponential curves is illustrated in Fig. 7.2. Noting that L_1 and L_2 are always positive, and the coefficients of the two exponential functions in Eq. (7.6) maintain the same sign for all stable steady-state solutions, Fig. 7.2 illustrates the general form each exponential term will take and the resulting covariance function.

Figure 7.3 shows the theoretical spatial covariance curves for a range of values of λ_{GABA} along the top-branch. Similarly, for a range of values of λ_{GABA} along the bottom-branch, the theoretical spatial covariance curves are shown in Fig. 7.4. Figures 7.3 and 7.4 demonstrate that the overall spatial correlation increases strongly as the LOC and ROC transition points are approached. This increase in correlation *length* for the 1-D spatio-adiabatic cortex is consistent with a phase transition picture for the change of state of the cortex.

7.2.2 Zero-lag Covariance

Of note is that the zero-lag value of $G(|x - x'|)$ changes as anaesthetic concentration is altered. It is easily shown that the zero-lag value $G(0)$ is proportional to the net spatial power in the 1-D cortex at any one point in time. The covariance function in space, for a continuous stochastic system is given by:

$$G(l) = \lim_{L \rightarrow \infty} \frac{1}{L} \int_0^L y(x+l)y(x)dx, \quad (7.9)$$

where $G(l)$ is defined for all lags $-\infty < l < \infty$, and is an even function. Parseval's theorem states: The total energy computed in the space domain must be identical to the total energy in the spatial-frequency (wavenumber q) domain. In order to apply Parseval's theorem to a signal of infinite extent, we use the theorem in terms of spatial power conservation, i.e., the energy *per unit length* must be identical in the space and wavenumber domains:

$$\lim_{L \rightarrow \infty} \frac{1}{L} \int_0^L |y(x)|^2 dx = \int_{-\infty}^{+\infty} S(q) dq. \quad (7.10)$$

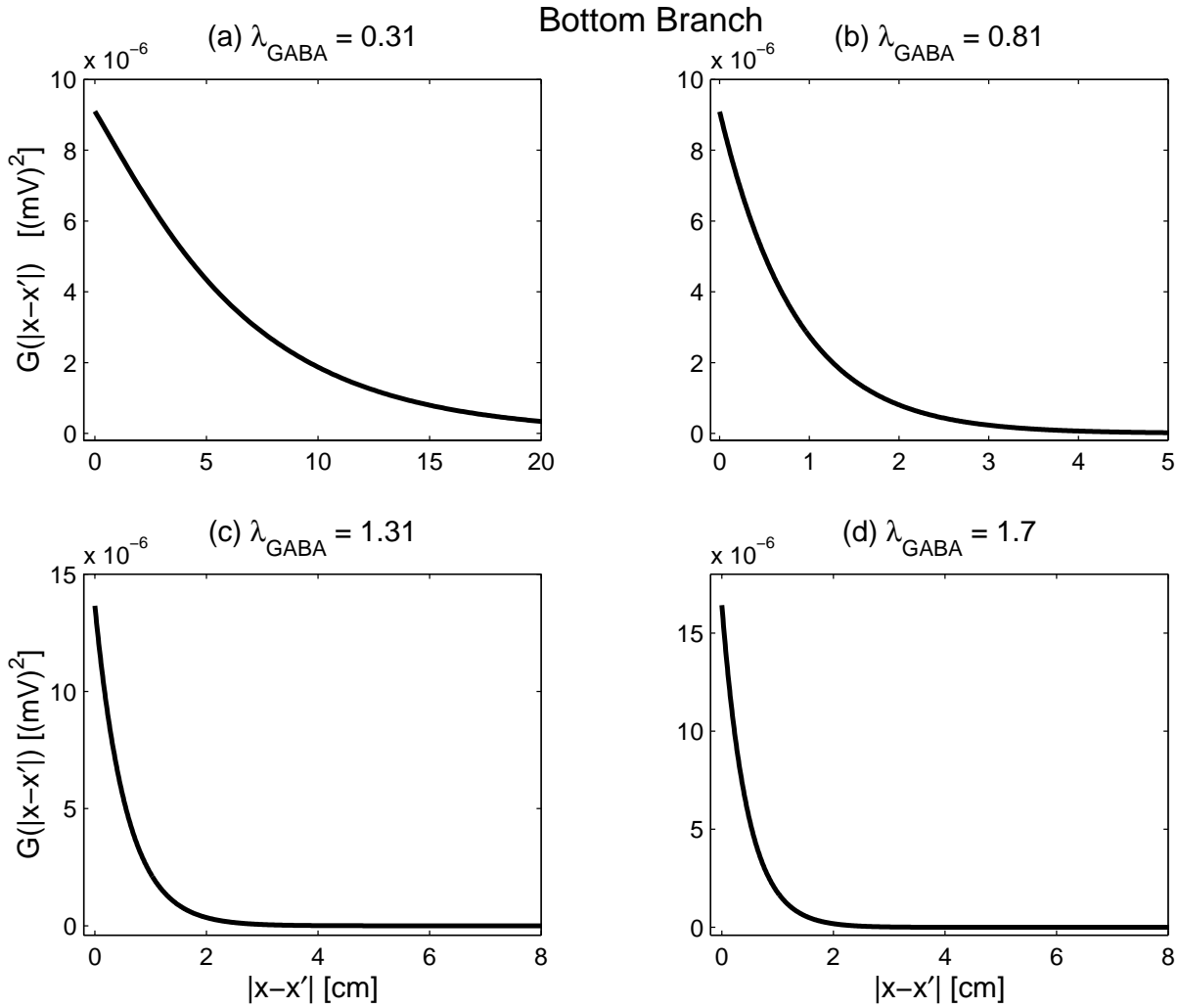


Figure 7.4: Theoretical covariance predictions for separations of $|x - x'|$ cm along the cortical rod. The four panels (a, b, c, d) show the difference in the spatial width of the covariance curve at four anaesthetic concentrations, along the bottom branch (quiescent branch) of Fig. 3.11. The four panels illustrate that similar to the approach to the loss-of-consciousness point, the approach to the return-of-consciousness point is characterized by a strong increase in the spatial width of the covariance curves. These predictions are for the default of the $\kappa_{e,i}$ diffusivities.

Hence, via Eqs. (7.9–7.10) it is obvious the zero-lag covariance $G(0)$ gives us the net spatial power over all spatial frequencies.

Plotting $G(0)$ (Eq. (7.6)) as a function of anaesthetic concentration reveals that the net spatial-power at any one point in time increases as the consciousness \rightarrow unconsciousness transition point is approached (see Fig. 7.5).

This figure also shows that the net spatial power increases as we move ‘‘back’’ along the top-branch towards $\lambda_{GABA} = 0$. In Fig. 7.6 we consider the immediate neighbourhood of $\lambda_{GABA} = 0$, and note that the net spatial-power initially increases significantly, then at $\lambda_{GABA} \sim 0.027$ rapidly drops to its $\lambda = 0$ value. The MATLAB code used to calculate the equilibrium values (h_e^0, h_i^0) fails for $\lambda_{GABA} < 0.015$ (and for $\lambda_{GABA} > 20$), hence in order to calculate the zero-lag covariance

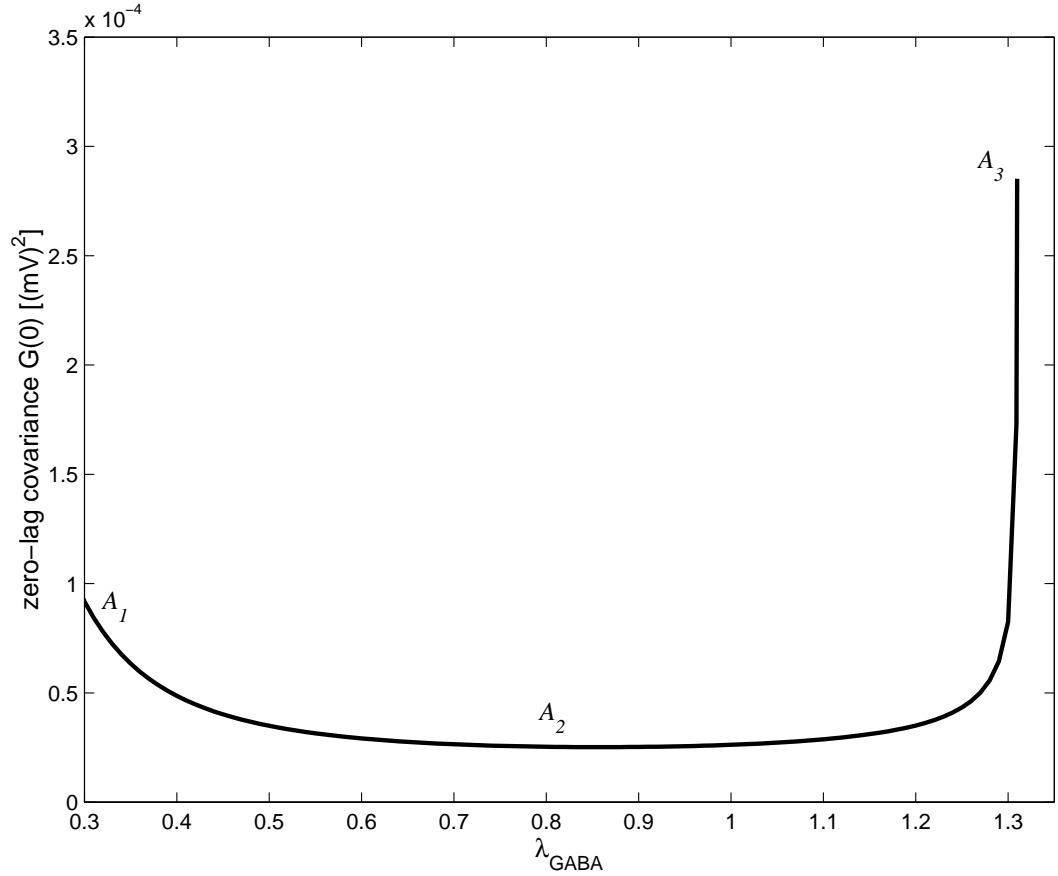


Figure 7.5: *Top-branch* theoretical zero-lag covariance as a function of anaesthetic concentration. As the consciousness \rightarrow unconsciousness transition point is approached there is an increase in zero-lag covariance (equivalent to an increase in net spatial power).

aa $\lambda_{\text{GABA}} \rightarrow 0$ (and for $\lambda_{\text{GABA}} \rightarrow \infty$), we need to determine the two asymptotic limits for h_e^0, h_i^0 analytically.

Zero Inhibition: Seizure

To calculate the steady-states of the homogeneous cortex, Eqs. (3.36–3.43) are used with the noise turned off and in the long-time limit, $\frac{d}{dt} \rightarrow 0$. The inhibitory contributions to the cortex Eqs. (3.40–3.41) then become,

$$I_{ie}(h_i) = \lambda_{\text{GABA}} \left[N_{ie}^\beta \mathcal{S}_i(h_i) + \langle p_{ie} \rangle \right] G_i e / \gamma_i \quad (7.11)$$

$$I_{ii}(h_i) = \lambda_{\text{GABA}} \left[N_{ii}^\beta \mathcal{S}_i(h_i) + \langle p_{ii} \rangle \right] G_i e / \gamma_i \quad (7.12)$$

For $\lambda \rightarrow 0$ the inhibitory restraint $(I_{ie}(h_i), I_{ii}(h_i))$ of the macrocolumn equates to zero, and both inhibitory and excitatory sigmoids are at their $\mathcal{S}_e^{\text{max}}$ asymptotic limit corresponding to

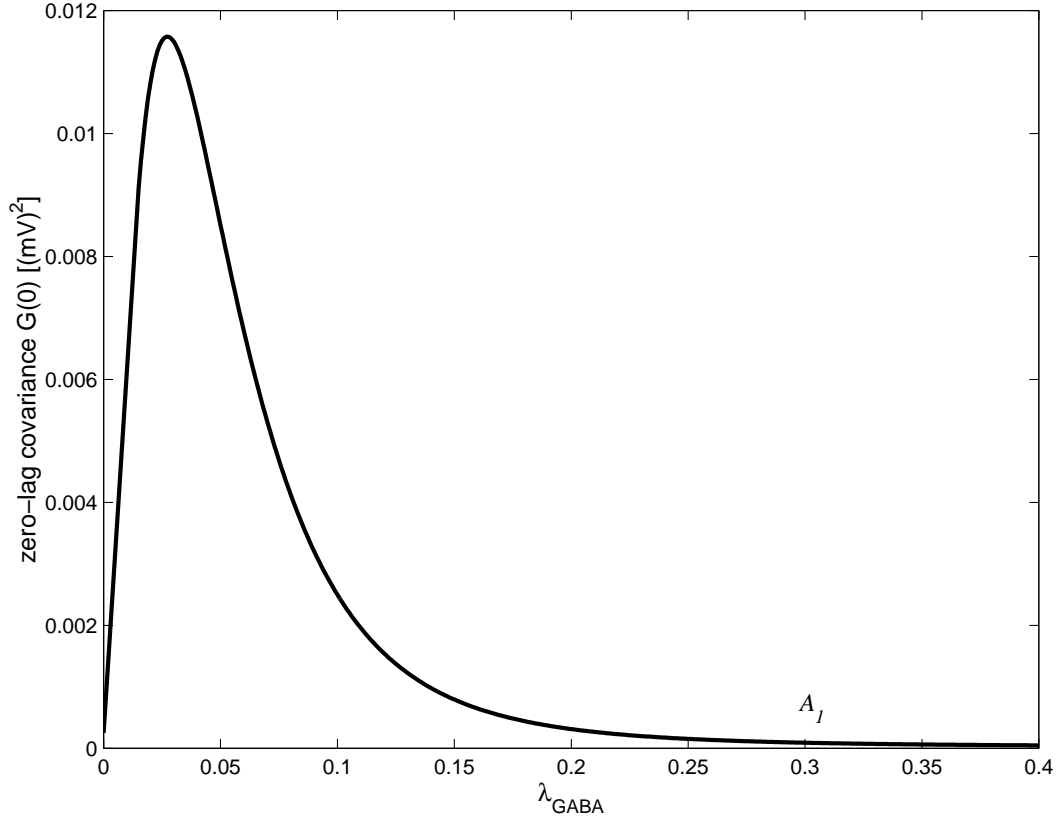


Figure 7.6: $\lambda_{\text{GABA}} \rightarrow 0$ region of *top-branch* theoretical zero-lag covariance. As the we move ‘‘back’’ towards $\lambda_{\text{GABA}} = 0$ the net spatial-power increases significantly, then at $\lambda_{\text{GABA}} \sim 0.027$ rapidly drops to its $\lambda = 0$ value.

maximum neural firing. Steyn-Ross (2002) derives the $\lambda_{\text{GABA}} \rightarrow 0$ steady-state voltages as,

$$h_e^{\text{seiz}} = \frac{|h_e^{\text{rev}} - h_e^{\text{rest}}| h_e^{\text{rest}} + h_e^{\text{rev}} I_{ee}^{\text{seiz}}}{|h_e^{\text{rev}} - h_e^{\text{rest}}| + I_{ee}^{\text{seiz}}} \quad (7.13)$$

$$h_i^{\text{seiz}} = \frac{|h_e^{\text{rev}} - h_i^{\text{rest}}| h_i^{\text{rest}} + h_i^{\text{rev}} I_{ei}^{\text{seiz}}}{|h_e^{\text{rev}} - h_i^{\text{rest}}| + I_{ei}^{\text{seiz}}} \quad (7.14)$$

where

$$I_{ee}^{\text{seiz}} \equiv \left[(N_{ee}^{\alpha} + N_{ee}^{\beta}) \mathcal{S}_e^{\text{max}} + p_{ee} \right] G_e e / \gamma_e \quad (7.15)$$

$$I_{ei}^{\text{seiz}} \equiv \left[(N_{ei}^{\alpha} + N_{ei}^{\beta}) \mathcal{S}_e^{\text{max}} + p_{ei} \right] G_e e / \gamma_e. \quad (7.16)$$

Substituting the constant values from Table 3.1 gives,

$$h_e^{\text{seiz}} = +34.5 \text{ mV}, \quad h_i^{\text{seiz}} = +30.91 \text{ mV}. \quad (7.17)$$

To obtain the limiting $\lambda_{\text{GABA}} = 0$ zero-lag covariance, we substitute $h_e^{\text{seiz}}, h_i^{\text{seiz}}, |x - x'| = 0$ and $\lambda_{\text{GABA}} = 0$ into Eq. (7.6) and obtain $G(0) = 2.51 \times 10^{-4} \text{ mV}^2$. This seems consistent with a $\lambda_{\text{GABA}} \rightarrow 0$ extrapolation on Fig. 7.6.

Infinite Inhibition: Coma

For the $\lambda \rightarrow \infty$ limit the inhibitory restraint on the macrocolumn will become infinite, leading to both the inhibitory and excitatory sigmoids approaching their zero-firing asymptotic limit; this is *deep coma*. For the limit $\lambda \rightarrow \infty$, Steyn-Ross (2002) obtains the steady-state voltages,

$$h_e^{\text{coma}} = h_i^{\text{coma}} = -90 \text{ mV}. \quad (7.18)$$

Unfortunately for $\lambda \rightarrow \infty$ limit we cannot analytically determine the zero-lag covariance, because for this limit it is not clear whether the covariance function converges analytically. If we plot the zero-lag covariance on the bottom branch out to $\lambda_{\text{GABA}} = 20$, we obtain the graph shown in Fig. 7.8. The behaviour shown in Fig. 7.8 for large λ_{GABA} is strange, and the physiological

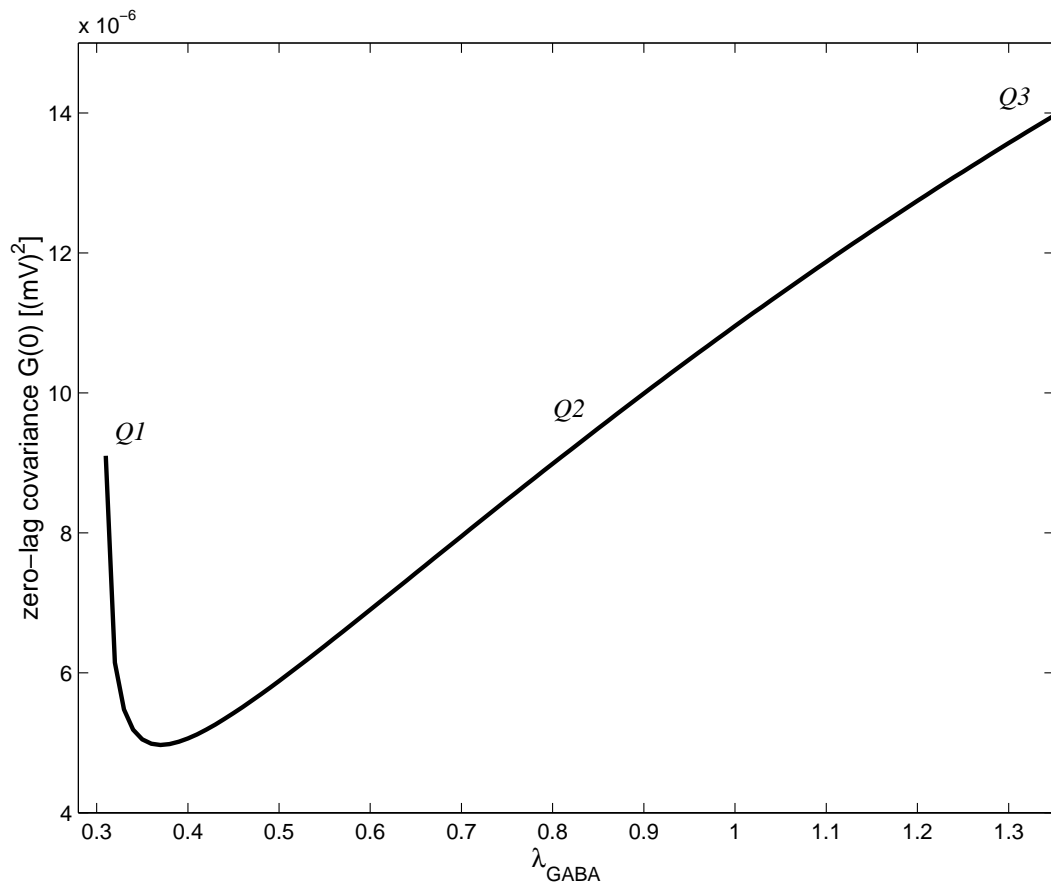


Figure 7.7: *Bottom-branch* theoretical zero-lag covariance as a function of anaesthetic effect. Prior to the unconsciousness \rightarrow consciousness transition point there is a decrease in zero-lag covariance (or net spatial-power) followed by a sharp increase at the Q_1 transition point.

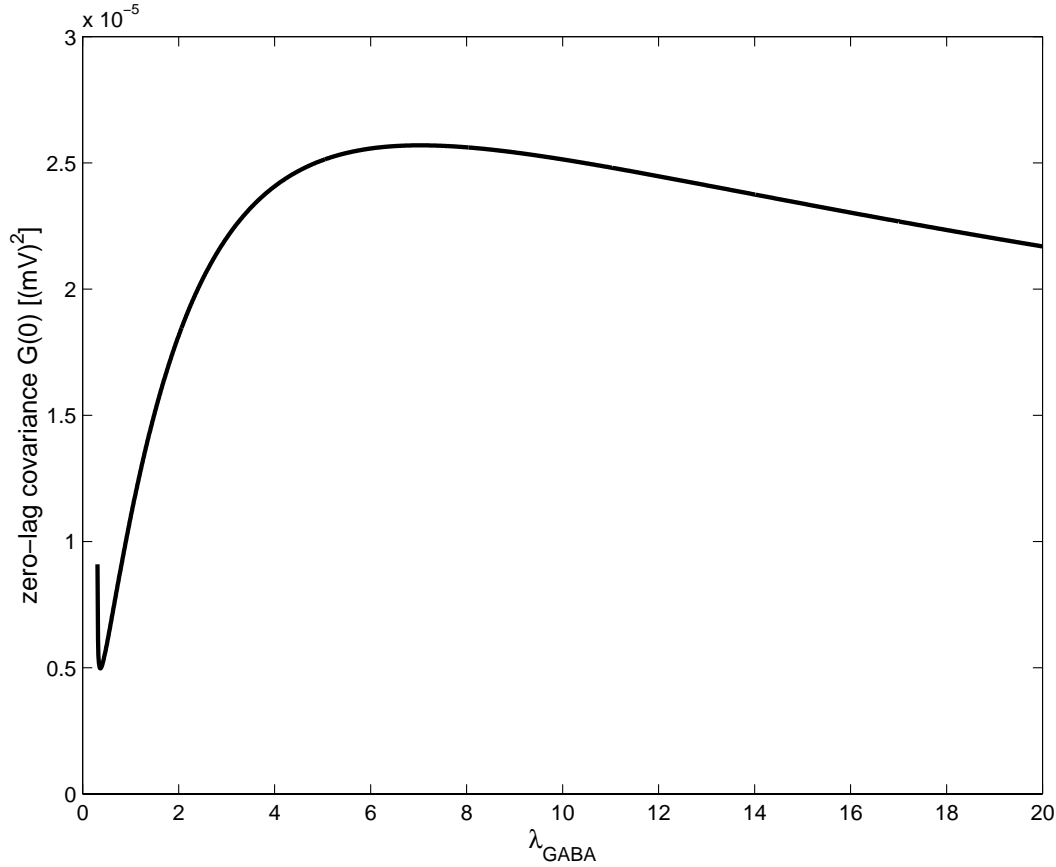


Figure 7.8: $\lambda_{\text{GABA}} \rightarrow 20$ region of the *bottom-branch* theoretical zero-lag covariance. As we move towards deep coma the net spatial-power increases and then begins to decrease. The physiological interpretation of this trend is unclear.

meaning is unclear. Note that similar to the top-branch there is a decrease in the zero-lag covariance followed by an increase prior to the transition at $\lambda_{\text{GABA}} \rightarrow 0.31$ from unconsciousness to consciousness. Figure 7.7 shows a close-up view of this change in zero-lag covariance for the region $\lambda_{\text{GABA}} = 0.31 \rightarrow 1.31$.

On the top- and bottom-branch the zero-lag covariance (equivalent to net spatial-power) as a function of anaesthetic effect shows unusual behaviour at the two extremes $\lambda_{\text{GABA}} \rightarrow 0$ and $\lambda_{\text{GABA}} \rightarrow \infty$. Near the two transition points (Q_1 and A_3) the net spatial-power shows the expected increase (power surges just prior to transition are evident in clinical recordings and are referred to as a ‘‘biphasic’’ peak). The effect of the peculiarities near the $\lambda_{\text{GABA}} \rightarrow 0$ and $\lambda_{\text{GABA}} \rightarrow \infty$ limits on the predicted theoretical power spectrum in time is investigated in the next chapter.

7.3 Covariance Agreement with Numerical Simulations

To test the theoretical covariance prediction for the $c_3 > 0$ case, we simulated both the nonlinear system and the linearized system, allowing them to evolve for a number of steps before computing the covariance. For the linearized system, the soma voltages were initialized to zero deviation from their homogeneous steady-state value (i.e., $\widehat{h}_e(x, 0) = \widehat{h}_i(x, 0) = 0$). For the nonlinear spatio-adiabatic system the soma-voltages were initialized to their homogeneous steady-state values (i.e. $h_e(x, 0) = h_e^0$ and $h_i(x, 0) = h_i^0$), and the long-range cortico-cortical inputs (ϕ_e and ϕ_i) were initialized to their homogeneous steady-state values,

$$\phi_e(x, 0) = N_{ee}^\alpha \mathcal{S}_e(h_e^0) \quad \phi_i(x, 0) = N_{ei}^\alpha \mathcal{S}_e(h_e^0). \quad (7.19)$$

7.3.1 Nonlinear Spatio-Adiabatic Simulations Near Equilibrium

Figure 7.9 shows the agreement between theory and the nonlinear spatio-adiabatic simulations, close to homogeneous equilibrium. A time-step of 0.01 ms was used for all runs and the grid-spacing h was adjusted to maintain numerical stability, while remaining fine enough to obtain adequate spatial resolution. The number of grid-points was set to $N = 100$ which ensured the cortical rod was of sufficient length. The system was allowed to evolve for 10000 time-steps and then the spatial covariance was calculated using the MATLAB `xcorr` cross-correlation function,

$$G_{\text{sim}}(|x - x'|) = \frac{\text{xcorr}(\mathbf{h}_e)}{N} \quad (7.20)$$

where \mathbf{h}_e is the 100-element vector of $h_e - h_e^0$ values along the rod. (The mean h_e^0 is subtracted from \mathbf{h}_e as the theoretical correlations are based on the *fluctuations* about the homogeneous steady-state.) The average of ten such runs was calculated (thin black line) and compared with theoretical predictions (thick grey line). The covariance of each individual run is represented by the dots, which shows nicely the stochastic nature of the simulations. Increasing the number of runs (and hence decreasing the average covariance error) gives simulation covariance that converges to the theoretical prediction.

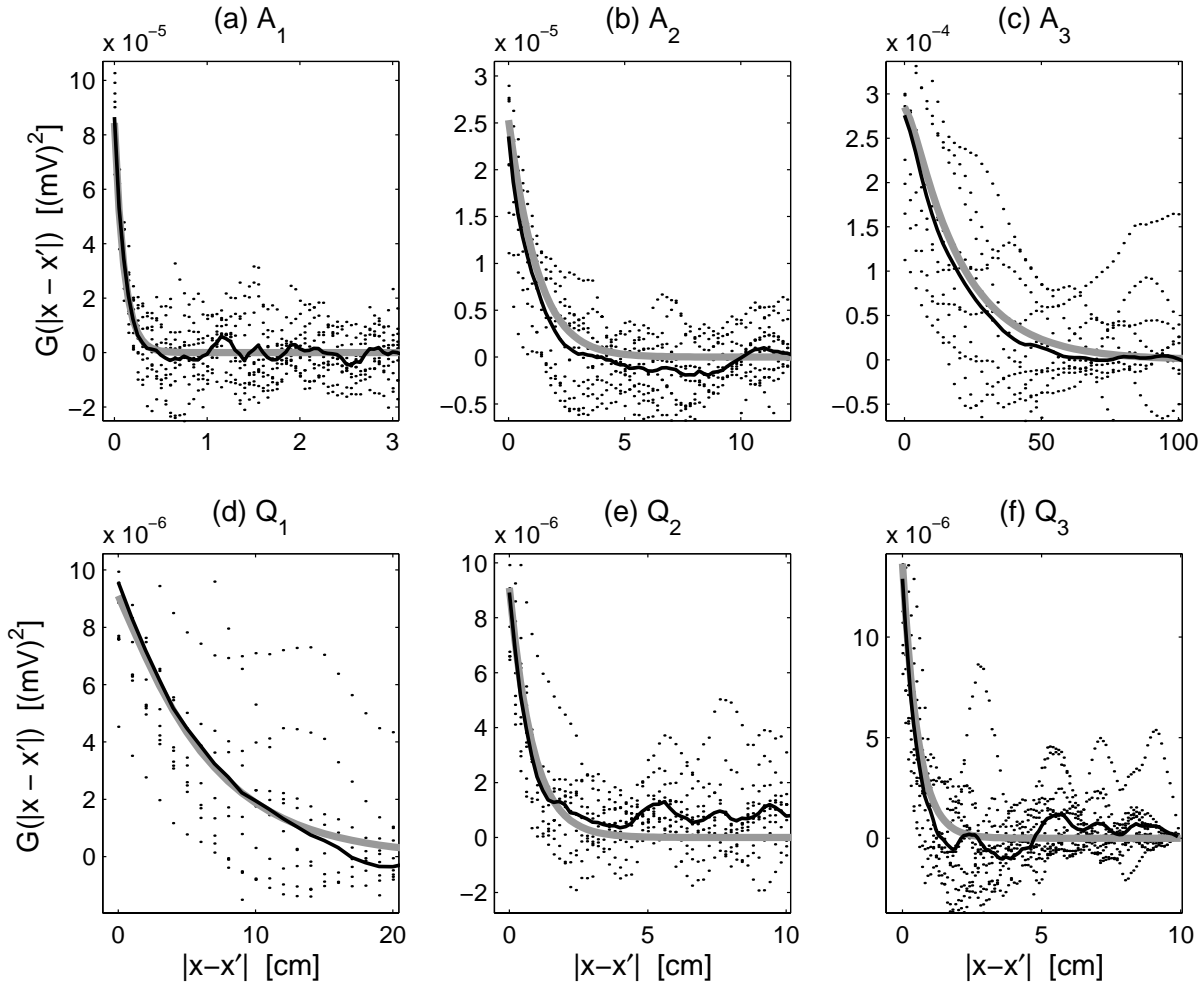


Figure 7.9: Comparison of the theoretical covariance predictions (thick-grey curves) and stochastic results (black dots) using the *nonlinear difference equations* (Eqs. (6.27–6.28)) at discrete points along the cortical rod. The thin-black curves show the average simulation covariance of ten runs. The top three panels (a),(b),(c) show the increase in correlation length as the anaesthetic effect is increased from $\lambda_{\text{GABA}} = 0.31 \rightarrow 0.81 \rightarrow 1.31$. This increase in anaesthetic effect corresponds to the induction towards unconsciousness along the top branch. Likewise the bottom three panels (f),(d),(e) show the increase in correlation length as the anaesthetic effect is *reduced* $\lambda_{\text{GABA}} = 1.31 \rightarrow 0.81 \rightarrow 0.31$, corresponding to the emergence trajectory along the bottom branch. For all runs the time-step was set to $\Delta t = 0.01$ ms, the number of grid-points were set to $N = 100$, but the grid-point spacing was altered to maintain numerical stability while simultaneously being fine enough to obtain adequate spatial resolution. These grid-point spacing settings and corresponding rod-length Nh (in cm) are: (a) $h = 0.05$, $L = 5$; (b) $h = 0.2$, $L = 20$; (c) $h = 2$, $L = 100$; (d) $h = 1$, $L = 100$; (e) $h = 0.2$, $L = 20$; (f) $h = 0.1$, $L = 10$;

If the simulation length of the cortical rod is too short, a “hump” appears at the end of the covariance curve. To illustrate this hump, the covariance of a simulated 100 cm cortical rod at $\lambda_{\text{GABA}} = 1.31$ on the top-branch was computed (Fig. 7.10). The time-step used was 0.01 ms, the grid-point spacing used was 1 cm, and 100 averages were taken instead of the previous 10. As in this case the length of the rod is not sufficiently longer than the predicted correlation length, information from a grid-point is propagated around the entire length of the 1-D circle (periodic boundary conditions are used) resulting in the hump like tail of the covariance curve.

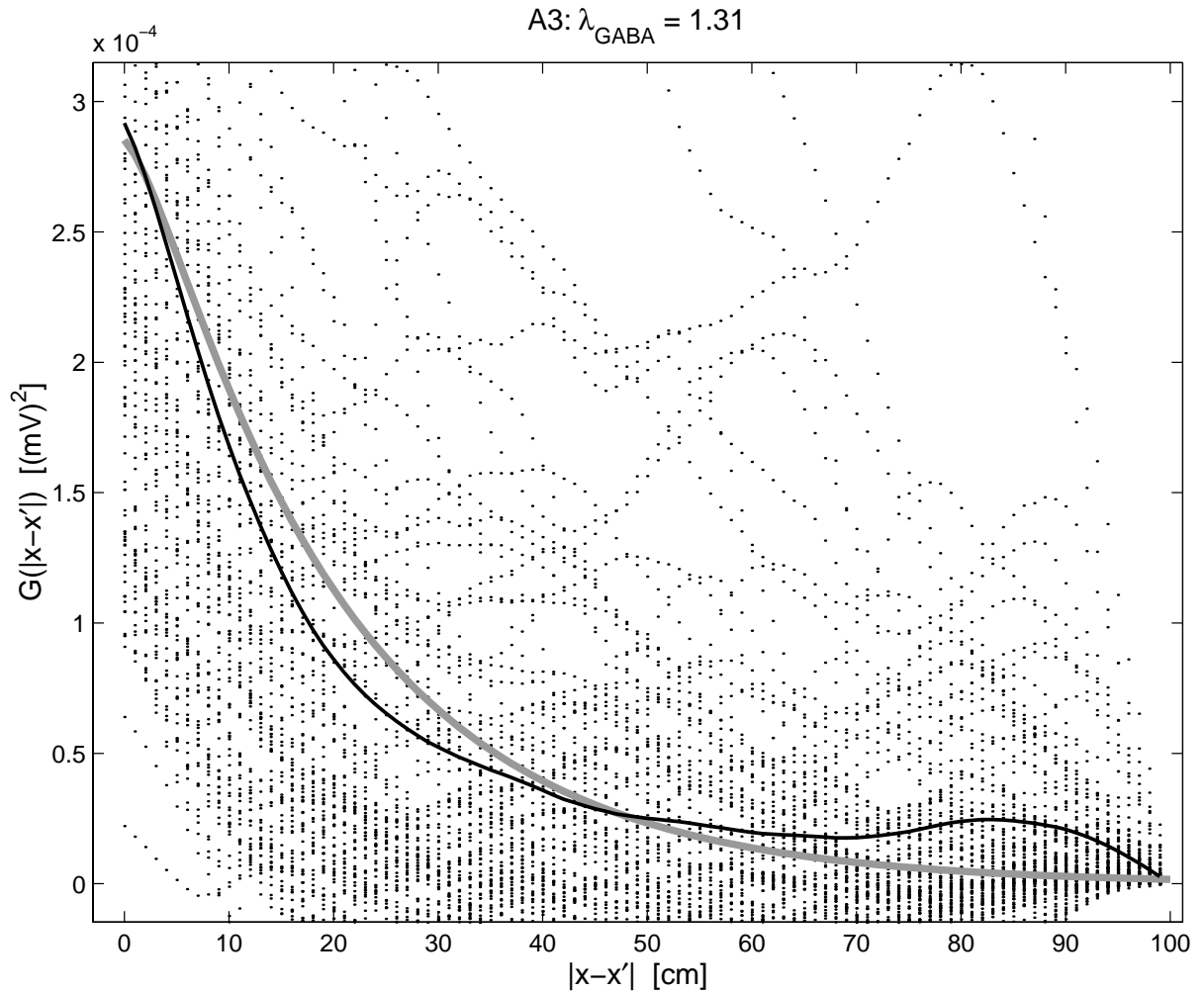


Figure 7.10: Covariance curve showing the “hump” that occurs when the cortical-rod is not of sufficient length. The rod was simulated about the steady-state at $\lambda_{\text{GABA}} = 1.31$ on the top branch and the covariance was computed from 100 averages. The settings used were: $\Delta t = 0.01$ ms; $h = 1$ cm; $N = 100$.

7.3.2 Linearized Spatio-Adiabatic Simulations Near Equilibrium

Figure 7.11 shows the agreement between theory and the simulations of the *linearized* spatio-adiabatic equations. As the theoretical predictions arise from the linearized theory, it is not surprising that the spatial-covariance of the simulated linear system shows good agreement with the predicted spatial-covariance. This good agreement suggests that as long as we are close to the homogeneous steady-state, the linearized system is a good approximation to the nonlinear system. The theoretical predictions do not appear to favour either the non-linear or linear system in particular, which is evident from the similarity of Fig. 7.11 and Fig. 7.9.

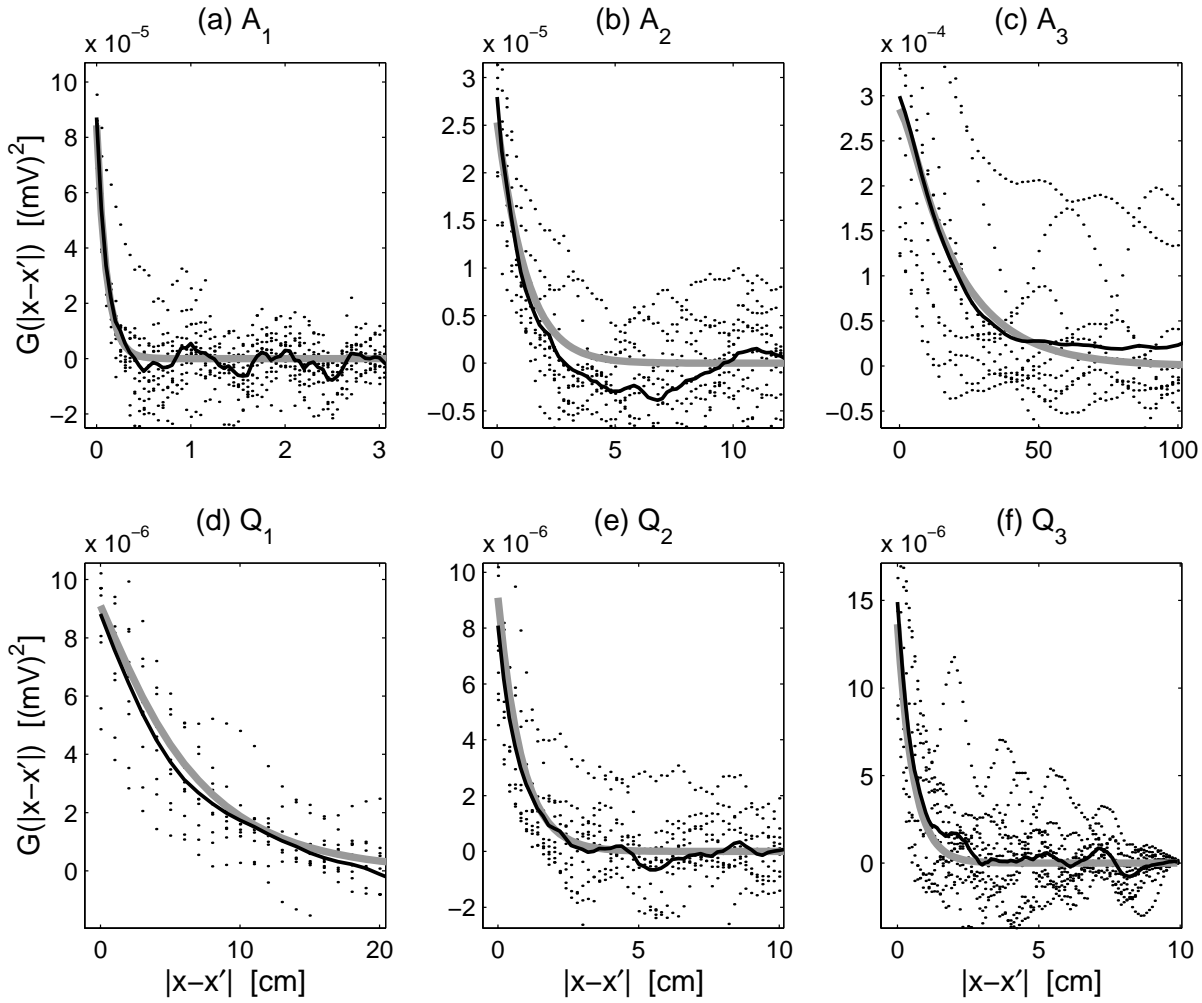


Figure 7.11: Comparison of the theoretical covariance predictions (thick-grey curves) and stochastic simulation results (black dots) using the *linear difference equations* (Eqs. (6.14–6.15)) at discrete points along the cortical rod. The thin-black curves shows the average simulation covariance of ten runs. The top three panels (a),(b),(c) show the increase in correlation length as the anaesthetic effect is increased from $\lambda_{\text{GABA}} = 0.31 \rightarrow 0.81 \rightarrow 1.31$. Likewise the bottom three panels (f),(d),(e) show the increase in correlation length as the anaesthetic effect is reduced $\lambda_{\text{GABA}} = 1.31 \rightarrow 0.81 \rightarrow 0.31$ along the bottom branch. The settings used were identical to those used to generate the plots of Fig. 7.9.

7.4 Theoretical Predictions of Covariance and Numerical Agreement for $c_3 < 0$

If the dendritic ‘‘wiring’’ ratio R is altered such that $c_3 < 0$ then the spatial covariance is predicted by Eq. (7.8). The theory used to derive Eq. (7.8) makes use of Taylor series expansions, which assume the cortex is always close to the homogeneous steady-state solution. When c_3 becomes negative, eigenvalue stability analysis shows the homogeneous steady-state solutions are no longer stable for the spatio-adiabatic equations (discussed shortly in Sec. 7.5); the predictions of Eq. (7.8) cannot be expected to be accurate.

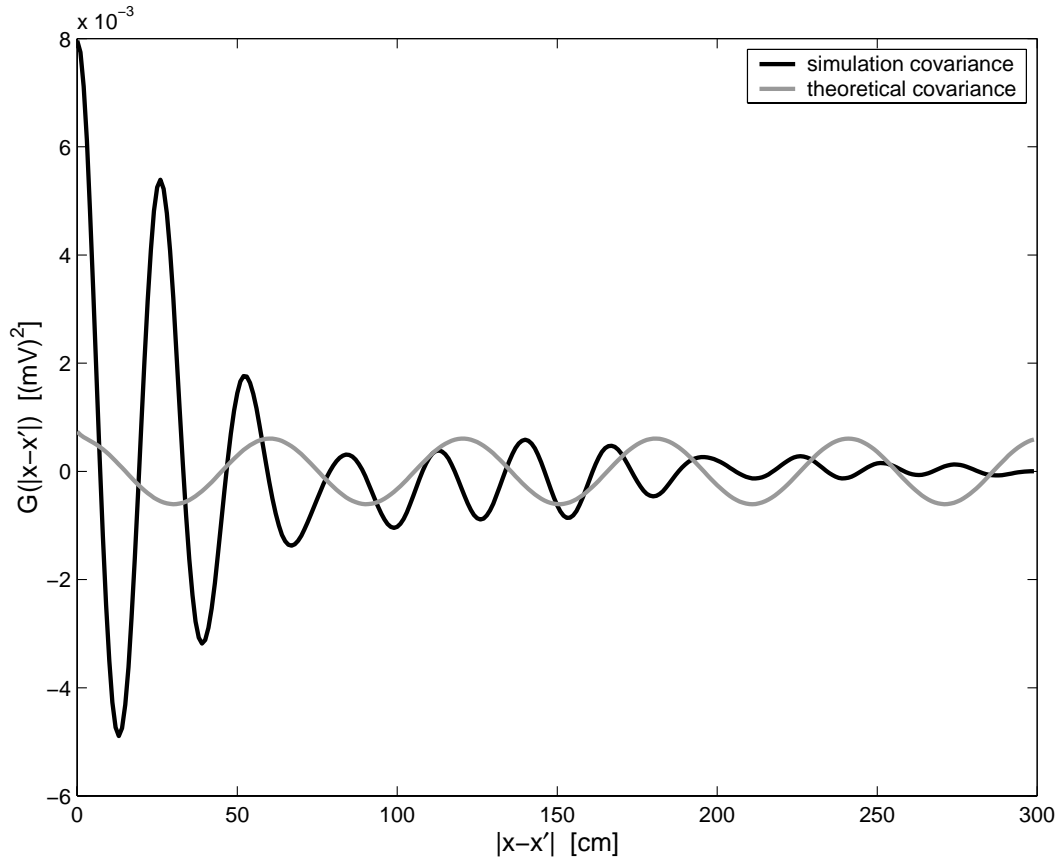


Figure 7.12: Covariance curve for the theoretical covariance function Eq. (7.6), and the “unstable” covariance curve of the *formation* of steady-states. A factor of $f = 1.8$ was used, and the simulation was initialized about the $\lambda_{\text{GABA}} = 1.31$ homogeneous steady-state. The experimental covariance curve is labelled “unstable” as the simulation was stopped before *further* formation of the nonequilibrium state led to a huge experimental curve. Settings used: $h = 1$ cm, $N = 300$, and $\Delta t = 0.01$ ms.

For the linearized set of equations this instability leads to the numerical scheme “blowing up”. This occurs because the state about which the system is linearized about is unstable. Nevertheless, the nonlinear difference equations used to simulate the formation of nonequilibrium states, show increasing-amplitude periodic correlations in the covariance (unfortunately not of wavelength $2\pi L_2$) about the unstable state, as the system bifurcates to its new state. One example is shown in Fig. 7.12. A factor of $f = 1.8$ was used, and the simulation was initialized about the $\lambda_{\text{GABA}} = 1.31$ top-branch homogeneous steady-state. The length of the cortical-rod was set to 300 cm consisting of 300 grid-points separated by 1 cm and with a time-step of 0.01 ms used. The system was allowed to evolve until the covariance shown in Fig. 7.12 was obtained. The covariance was calculated numerically using Eq. (7.20).

7.5 Stability of the Homogeneous Steady-State

In Sec. 4.8 we investigated the criteria required for stability of the spatio-adiabatic equations. It was found that for $c_3 < 0$, the neutrally-stable point was characterized by wave number q_s (Eq. (4.135)). For any wavenumber greater than q_s , the eigenvalue of the matrix $\mathbf{A}(q)$ (refer to Eq. (4.122), and note the negative sign) will be *negative*, resulting in the amplitude of the eigenmode growing exponentially. Shown in Fig. 7.13 is the eigenvalue distribution for $\lambda_{\text{GABA}} = 1.25$ on the top-branch with the connectivity factor $f = 1.8$, giving $c_3 < 0$.

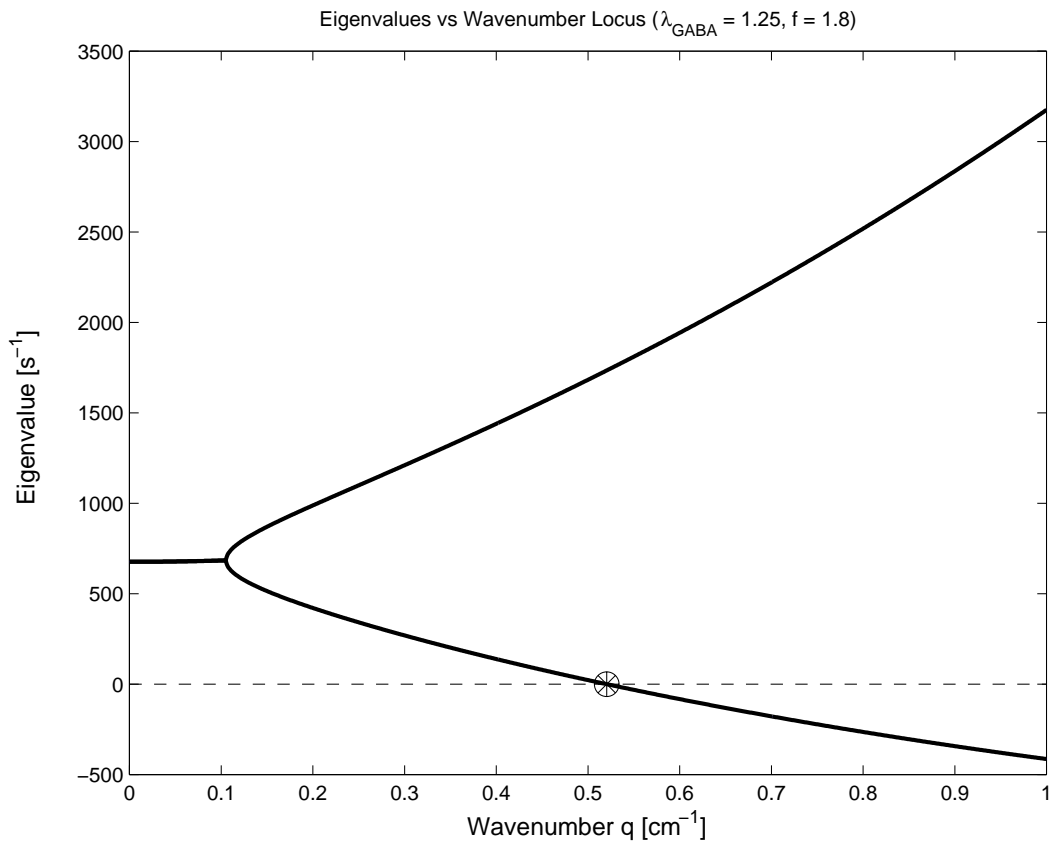


Figure 7.13: Eigenvalues as a function of wavenumber q for $f = 1.8$ at $\lambda_{\text{GABA}} = 1.25$. The eigenvalue pair is complex with positive real part for $0 \leq q \leq 0.101 \text{ cm}^{-1}$, then becomes purely real for $q > 0.101 \text{ cm}^{-1}$. The smaller wavenumber crosses the x -axis at $q = q_s = 0.5205 \text{ cm}^{-1}$.

The zero-crossing of Fig. 7.13 occurs at wavenumber q_s , indicating a marginally-stable eigenmode of wavelength $2\pi/q_s = 12.1 \text{ cm}$. All wavenumbers larger than 0.52 cm^{-1} will render a negative eigenvalue resulting in an unstable state. The greater the eigenvalue magnitude the greater the rate of exponential growth of the eigenmode. Conversely, wavenumbers less than 0.52 cm^{-1} will give an exponentially-decaying eigenmode resulting in a stable state, with smaller wavenumbers decaying more rapidly. If an eigenmode has a wavenumber equal to q_s , then that mode will neither decay nor grow, so will be long-lived. To illustrate this long-lived mode (Fig. 7.14), we

gave the linearized spatio-adiabatic system (with no noise contributions) an initial excitatory voltage perturbation away from the steady-state defined by,

$$\widehat{h}_e(x, t = 0) = \sum_{k=1}^8 \frac{(-1)^{k+1}}{k} \sin(kq_s x/8) \quad (7.21)$$

and left the inhibitory voltage unperturbed,

$$\widehat{h}_i(x, t = 0) = 0. \quad (7.22)$$

The summation in Eq. (7.21) represents the first eight terms of a harmonic expansion of a sawtooth waveform, where the final term is the long-lived eigenmode of wavelength $2\pi/q_s$. The $k = 1$ sawtooth waveform has a wavelength of $8 \times 2\pi/q_s$. To ensure the $k = 1$ wavelength is exactly periodic on the cortical rod, the spacing is set to $h = \frac{8 \times 2\pi/q_s}{N}$ for N grid-points (100 gridpoints were used to generate Fig. 7.14).

The initial sawtooth perturbation is shown in panel (a) of Fig. 7.14. Panel (b) shows a “snap-shot” in time, in which the seven eigenmodes with $q < q_s$ are decaying to the homogeneous steady-state. The final panel (c) shows the decaying eigenmodes have almost completely settled to the steady-state, leaving only the long-lived eigen mode of wavelength $q_s/2\pi$. The reason the completely relaxed state is not shown is because the scheme becomes unstable due to accumulation of round-off error that acts like exponentially-growing high-wavenumber eigenmodes.

In Fig. 7.14 the evolution of the long-lived mode cause \widehat{h}_e and \widehat{h}_i to become in phase. Interestingly this is not always the case. Figure 7.15 shows the same sawtooth experiment repeated, but for $\lambda_{\text{GABA}} = 1, f = 2$. The final panel in Fig. 7.15 shows that for these parameters \widehat{h}_e and \widehat{h}_i are out of phase. A stable mode that has an inhibitory voltage with opposite sign to the excitatory voltage, effectively *exciting* rather than inhibiting, seems counterintuitive. We have actually made the inhibitory diffusivity so large that the excitatory voltage is now required to *inhibit* the inhibitory voltage to form a stable state (hence being out of phase). Further investigation showed that for the long-lived modes, \widehat{h}_e and \widehat{h}_i are either in phase or out of phase depending on λ_{GABA} and f . If for a certain λ_{GABA} and f combination the stable modes are in phase, we find that increasing f decreases the magnitude of the \widehat{h}_i mode while retaining the phase, until, for some value of f the inhibitory voltage is zero. Increasing f further results in the stable modes of \widehat{h}_e and \widehat{h}_i becoming out of phase.

For our cortical simulations we drive the system with white noise in space and time. Spatial white noise contains *all* wavenumbers $0 < q < \infty$. Hence, if $c_3 < 0$ the *homogeneous steady-state will no longer be stable*.

7.6 Formation of Nonequilibrium Steady-States

If we adjust f such that $c_3 < 0$ for some λ_{GABA} on the top-branch, then perturb the system with spatial white-noise, it must move away from the now unstable state. If for a value of f such that $c_3 < 0$ for λ_{GABA} on the top-branch, but $c_3 > 0$ on the bottom branch, the system will bifurcate to the stable bottom-branch homogeneous solution. For example, for factor $f = 1.58$ at $\lambda_{\text{GABA}} = 1.31$ the top-branch is unstable while the bottom-branch is stable. Figure 7.16 shows the change of states from the unstable top-branch to the stable bottom-branch.

If for a value of f , c_3 is negative for a specific λ_{GABA} on the top- *and* bottom-branch, the system will bifurcate to a nonequilibrium steady-state (a nonequilibrium state stationary in time). Starting on the top-branch, simulation of the formation of these nonequilibrium steady-states shows that when we perturb the homogeneous steady-state via spatial noise, the system evolves by forming strongly growing diffusive “fingers”. These fingers proceed towards, and then overshoot, the second homogeneous stable state. The system continues to arrange itself until a diffusion finger-pattern persists indefinitely. The above criteria is satisfied for a large range of λ_{GABA} and factor $f > 1.58$. Figure 7.17 shows a typical simulation of the formation of one such nonequilibrium “finger” state for $\lambda_{\text{GABA}} = 1.31$, $f = 3$. Another formation is illustrated in Fig. 7.18. In general we find that for a certain λ_{GABA} the greater the factor f , the narrower the diffusive finger patterns. For a set factor, we also find different patterns occur for different values of λ_{GABA} .

The formation of the nonequilibrium “finger” states is also very sensitive to initial perturbations. Although each finger has a very similar chain-like curvature, the location on the rod at which the fingers form is random, depending sensitively on the noise pattern used to perturb the initial state. Figure 7.19 shows a distribution of nonequilibrium states for $f = 4$ at $\lambda_{\text{GABA}} = 1.2$.

With respect to anaesthesia, the biological significance of nonequilibrium steady-states, also known as dissipative structures, is unclear. It seems unlikely that any neural process could be associated with these structures that show a large variation in DC voltage offsets over space. The development of a frozen pattern of brain activity would severely constrain dynamic communication attempts from non-participating neuronal assemblies. One suggestion is that if we were

to relax the adiabatic requirement, the structures might “unfreeze” into temporal oscillations (hard-mode instabilities) or travelling wave patterns.

The next chapter moves away from the development of spatial-structures and instead focuses on the effect that incorporating space has on the power spectrum of the cortex. We look at the energy distribution of the stochastic fluctuations about the homogeneous steady-state in space and time.

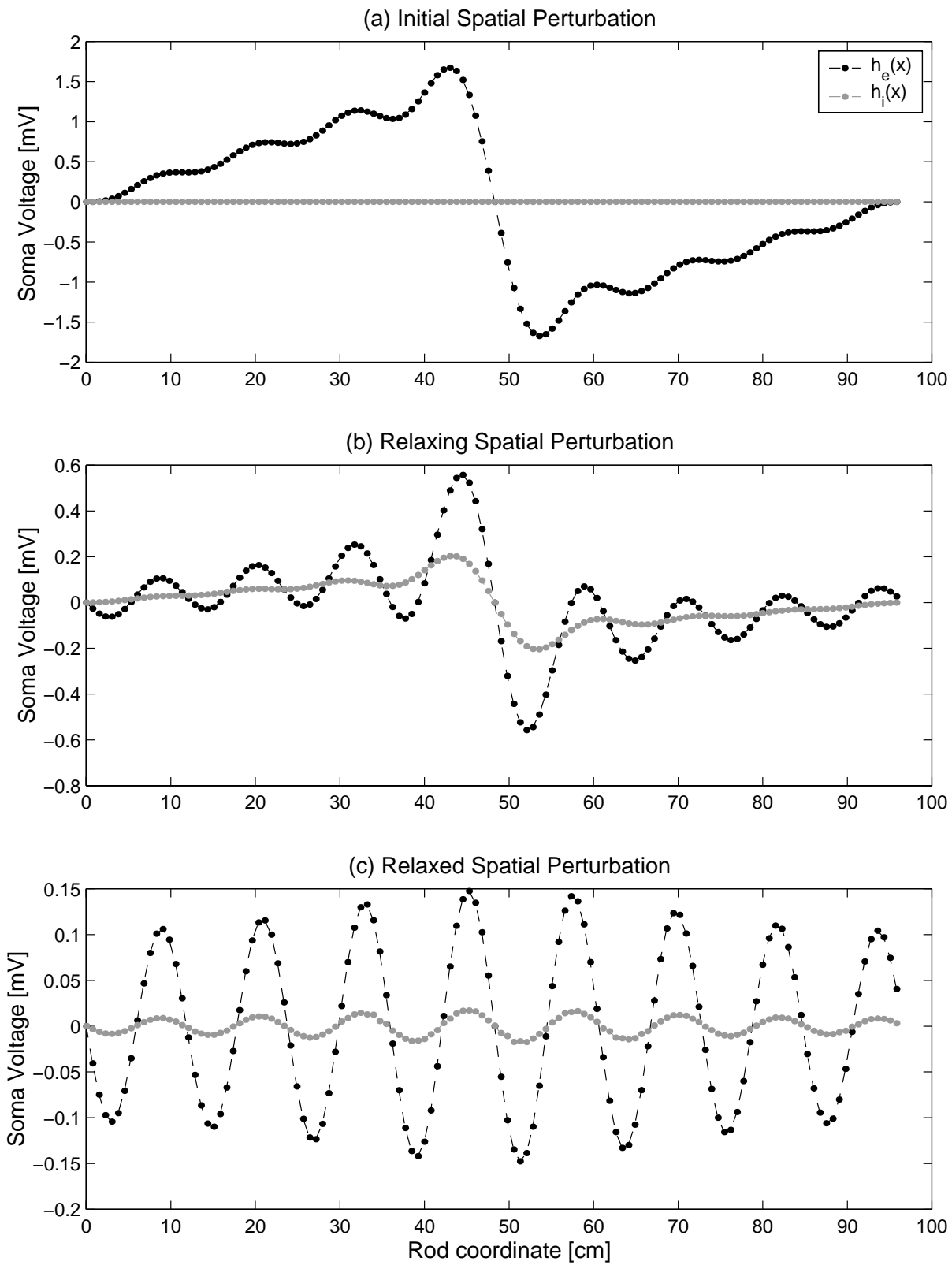


Figure 7.14: (a) Initial voltage perturbation at 100 points along the cortical-rod. (b) “Snap-shot” in time showing the decay of eigenmodes with $q < q_s$. (c) Near-relaxed voltage distribution after 30 000 iterations ($\Delta t = 1 \mu s$), leaving the marginally-stable q_s eigenmode. $\lambda_{GABA} = 1.25$, $f = 1.8$

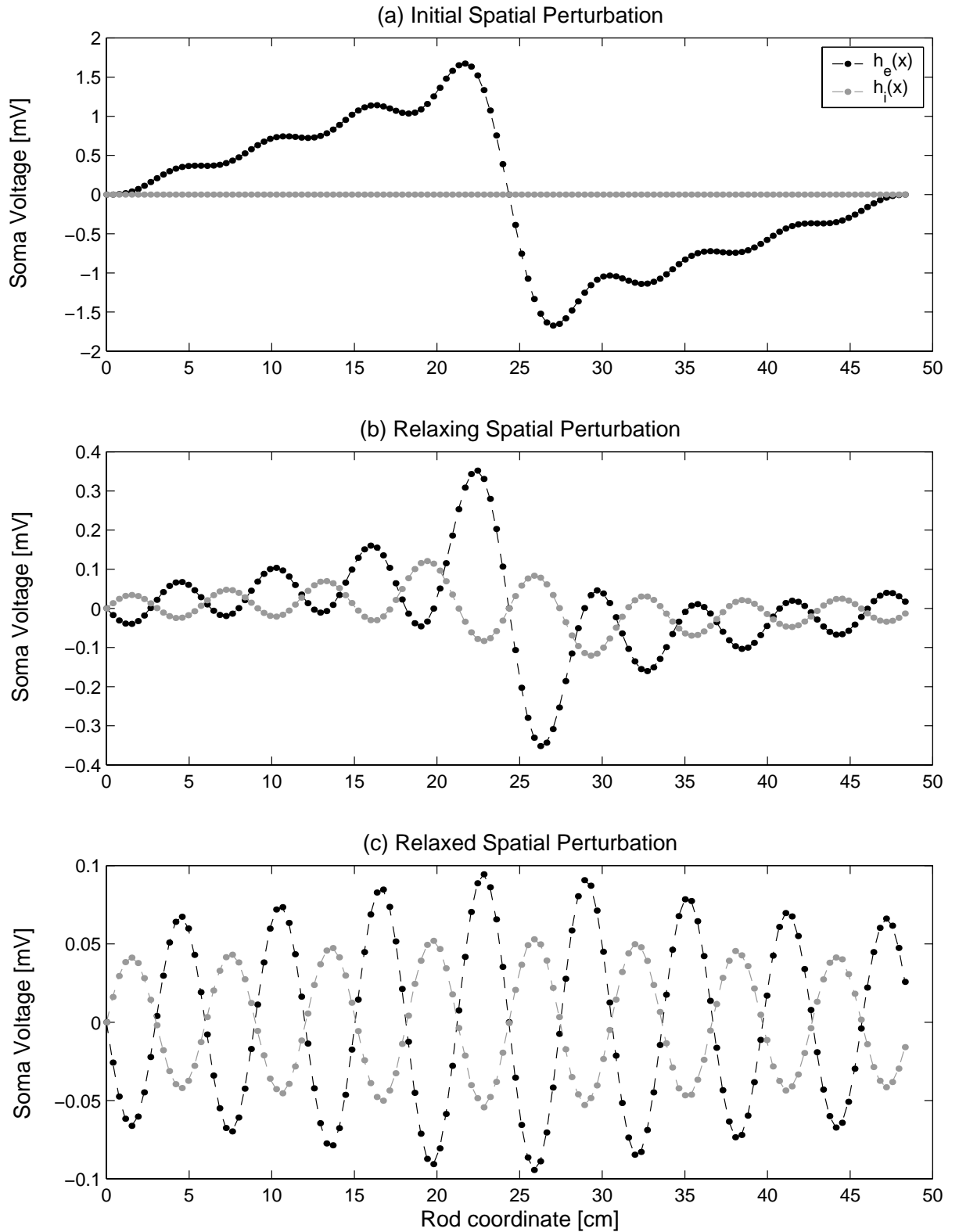


Figure 7.15: Decay of a sawtooth waveform towards the q_s eigenmode for $f = 2$ at $\lambda_{\text{GABA}} = 1$ on the top-branch. Except for the slight spacing adjustment required to ensure that the new $k = 1$ fundamental remains exactly periodic on the length Nh , the simulation settings are identical to those used for Fig. 7.14. Notice that in contrast to Fig. 7.14, in panel (c) \hat{h}_e and \hat{h}_i are out of phase.

Relaxation from Unstable Top-Branch to Stable Bottom-Branch

$$(\lambda_{\text{GABA}} = 1.31, f = 1.58)$$

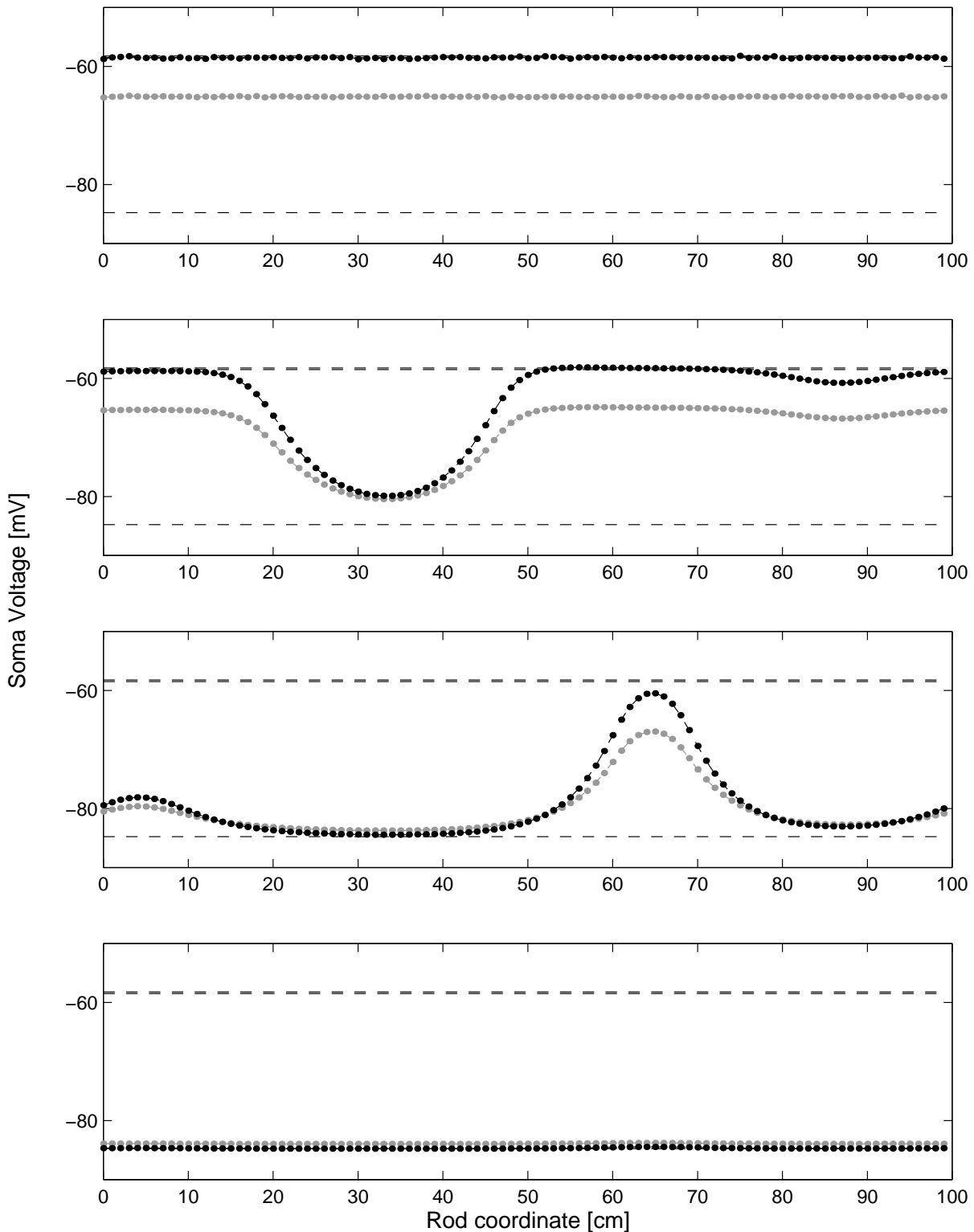


Figure 7.16: Simulation showing the system moving from the unstable top-branch to the stable bottom-branch. Black dots represent h_e and gray dots represent h_i at each gridpoint. The dashed lines represent the homogeneous steady-states. Simulation parameters: $N = 100$ points, $h = 1$ cm, $\Delta t = 0.01$ ms, $\lambda_{\text{GABA}} = 1.31$, connectivity scalefactor $f = 1.58$. (a) System is perturbed away from the homogeneous state via an impulse of spatial noise. (b) Each point "slides" off the unstable state. (c) Each point moves towards the stable bottom-branch and (d) settles.

Relaxation from Unstable Top-Branch to Stable

Nonequilibrium State ($\lambda_{\text{GABA}} = 1.31, f = 3$)

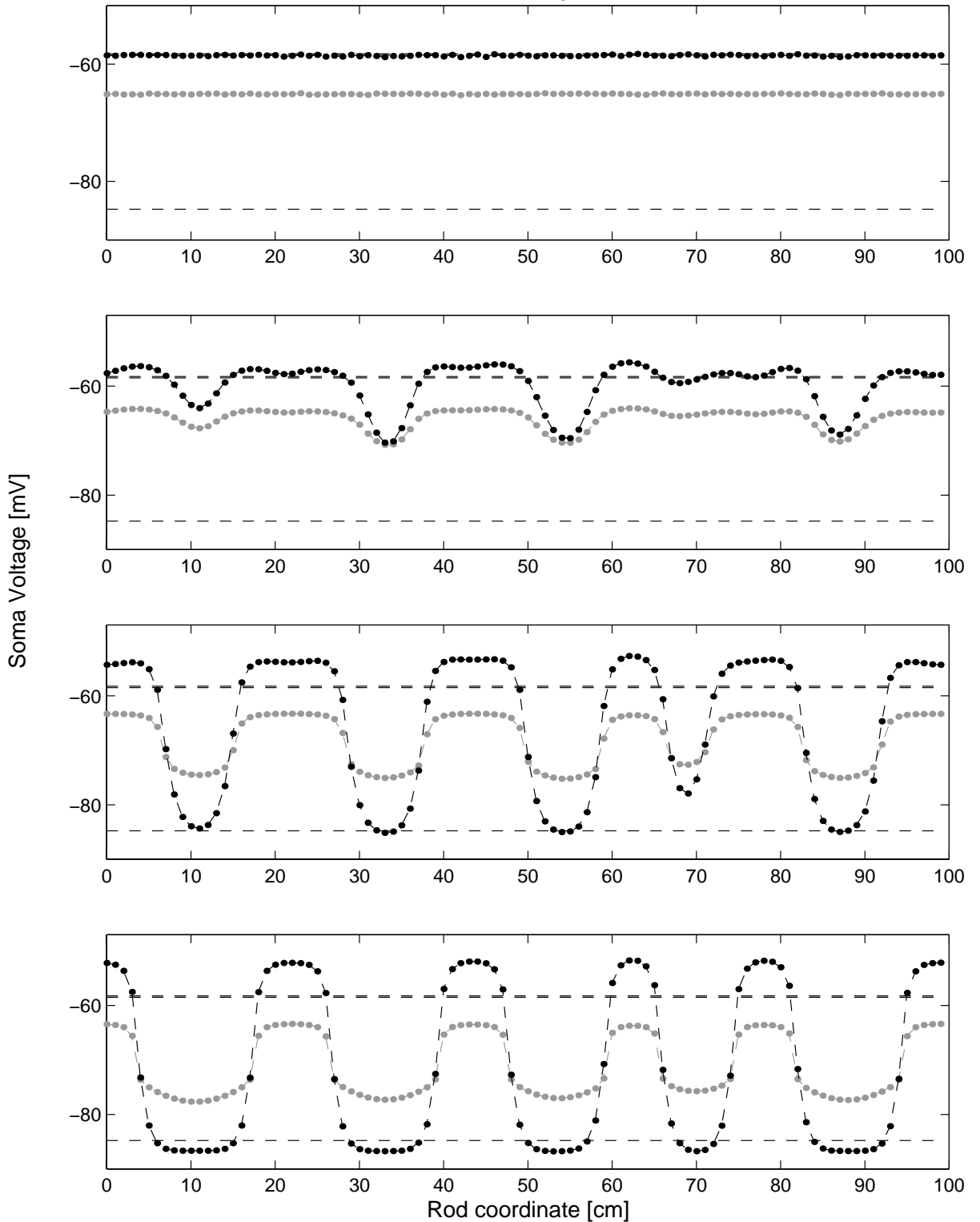


Figure 7.17: Simulation showing the emergence of nonequilibrium steady-states. Black dots represent h_e and gray dots represent h_i at each gridpoint. The dashed lines show the homogeneous steady-states of the cortex. Simulation parameters: $N = 100$ points, $h = 1$ cm, $\Delta t = 0.01$ ms, $\lambda_{\text{GABA}} = 1.31$, connectivity scalefactor $f = 3$. (a) System is perturbed away from the homogeneous state via an impulse of spatial noise. (b) Each point “slides” off the unstable state and (c) “falls” towards one or the other of the potential valleys near the top- or bottom-branch. (d) Fully developed spatial pattern.

Relaxation from Unstable Mid-Branch to Stable

Nonequilibrium State ($\lambda_{\text{GABA}} = 1.2, f = 4$)

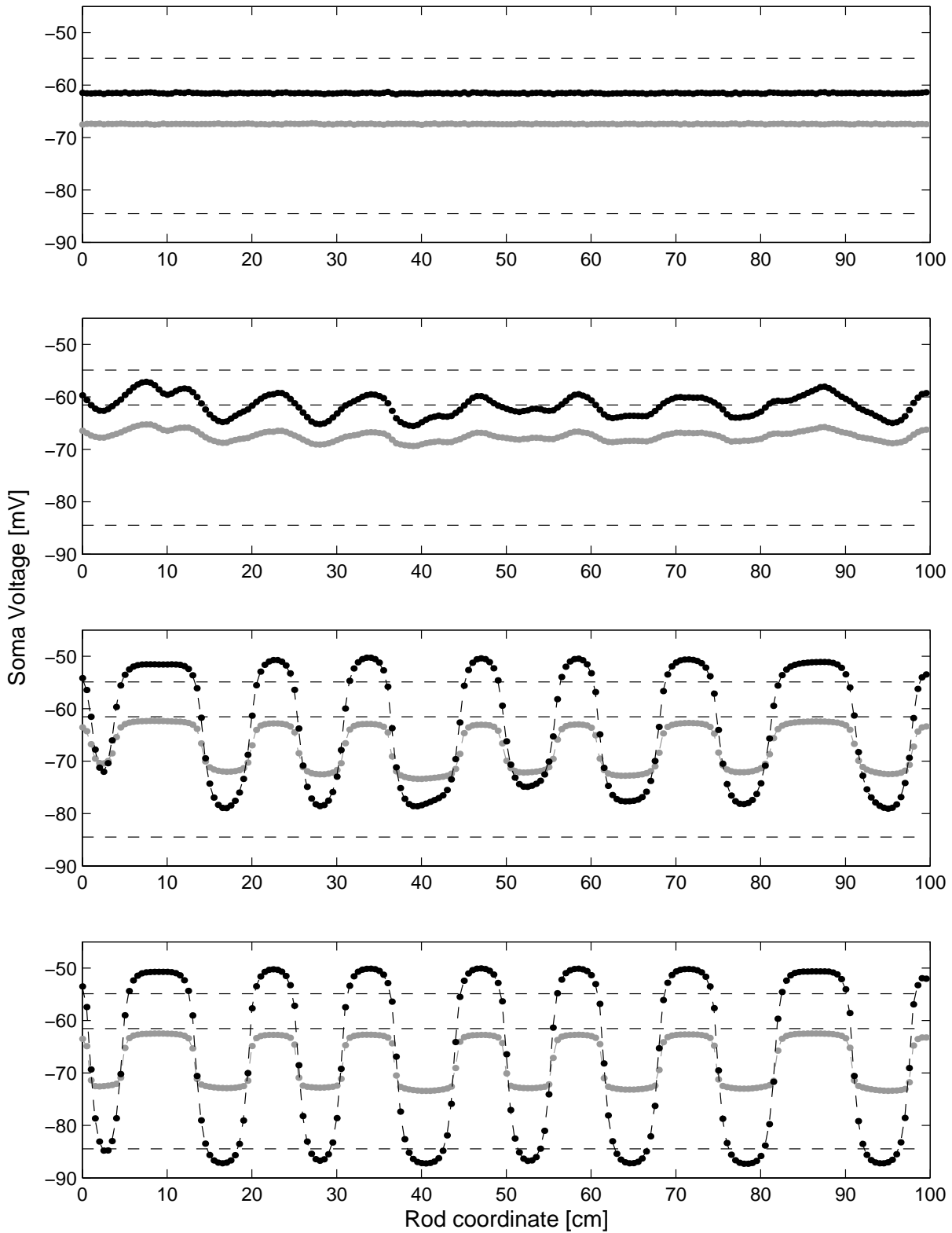


Figure 7.18: Simulation showing the emergence of nonequilibrium steady-states for factor $f = 1.2$ at $\lambda_{\text{GABA}} = 4$. Black dots represent h_e and gray dots represent h_i at each gridpoint. Simulation parameters are identical to those used in Fig. 7.17.

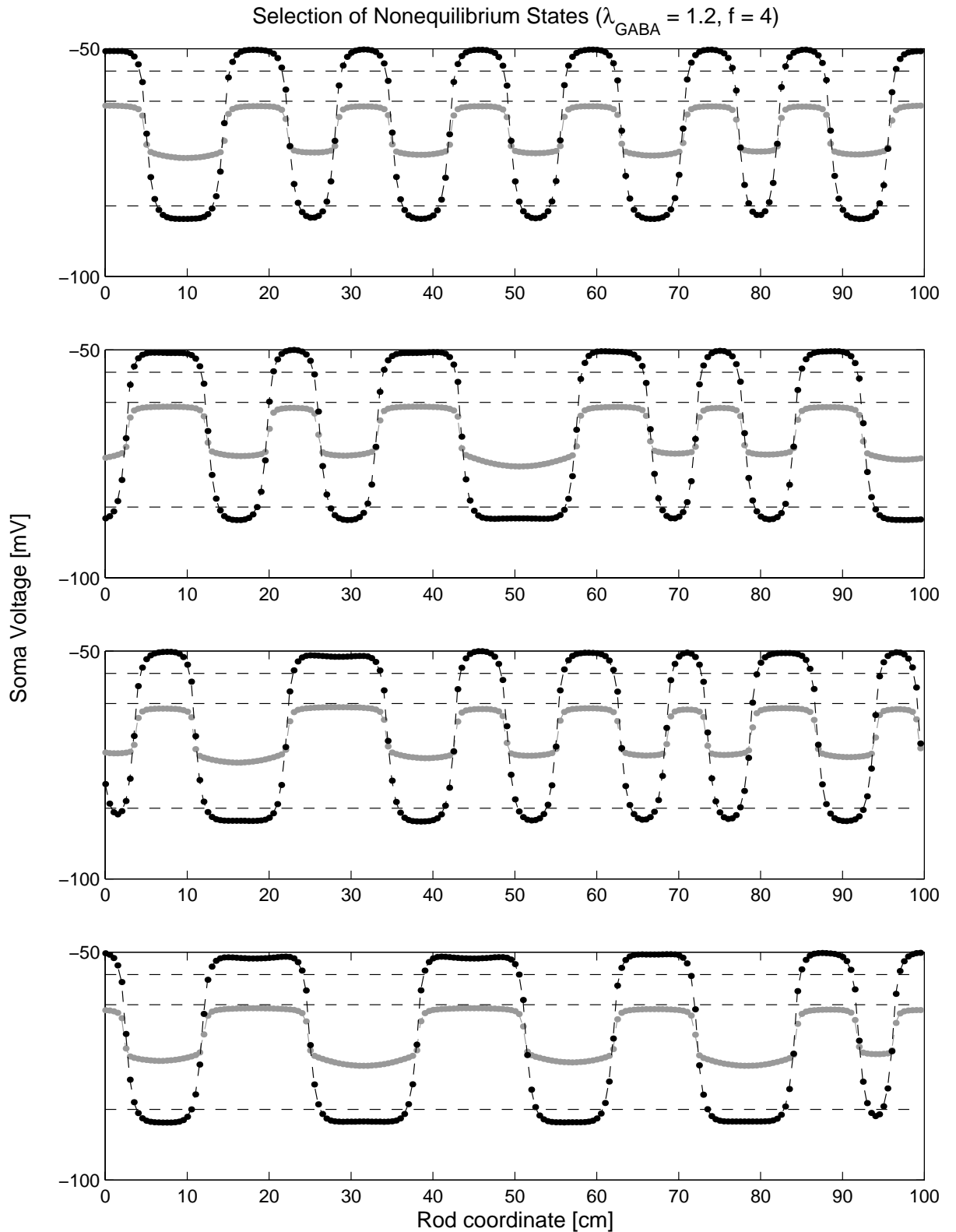


Figure 7.19: Distribution of nonequilibrium steady-states for factor $f = 1.2$ at $\lambda_{\text{GABA}} = 4$ formed on the spatio-adiabatic 1-D cortical rod. Black dots represent h_e and gray dots represent h_i at each gridpoint. Simulation parameters are identical to those used in Fig. 7.18. In each case the simulation was run until the new state (spatial pattern) was fully stabilized.

Power Spectra of Linearized Spatio-Adiabatic Equations

In this chapter I derive the theoretical power spectrum of the excitatory \widehat{h}_e soma voltage fluctuations for the linearized spatio-adiabatic equations.

8.1 Theoretical Power Spectrum of Stationary Stochastic Processes

For a stationary process the **ensemble average**, in which we repeat the same measurement many times and compute the average $\langle \ \rangle$, is equal to the **time average**. For such stochastic processes, Gardiner (1985) derives a relationship between the fluctuating quantity $x(t)$ and its power spectrum $S(\omega)$. Gardiner proceeds by defining the Fourier transform of the stochastic quantity $x(t)$ as,

$$c(\omega) = \frac{1}{2\pi} \int_{-\infty}^{+\infty} dt x(t) e^{-i\omega t} \quad (8.1)$$

and derives the power spectrum as,

$$\langle c(\omega)c(\omega')^* \rangle = \delta(\omega - \omega')S(\omega) \quad (8.2)$$

where $*$ denotes the complex conjugate. Likewise, the two-variable power spectrum $S(q, \omega)$ is given by,

$$\langle c(q, \omega)c(q', \omega')^* \rangle = \delta(q - q')\delta(\omega - \omega')S(q, \omega). \quad (8.3)$$

Gardiner's definition of a Fourier transform Eq. (8.1) differs by a factor of $1/2\pi$ from the form used so far throughout this thesis. Our definition of the one-variable Fourier transform reads,

$$c(\omega) = \int_{-\infty}^{+\infty} dt x(t) e^{-i\omega t} \quad (8.4)$$

and hence Eq. (8.2) will become,

$$\frac{1}{(2\pi)^2} \langle c(\omega)c(\omega')^* \rangle = \delta(\omega - \omega')S(\omega). \quad (8.5)$$

Likewise, our two-variable Fourier transform requires a factor of $1/(2\pi)^2$ giving,

$$\frac{1}{(2\pi)^4} \langle c(q, \omega)c(q', \omega')^* \rangle = \delta(q - q')\delta(\omega - \omega')S(q, \omega). \quad (8.6)$$

8.2 General Power Spectrum $S(q, \omega)$

In order to calculate the power spectrum $S(q, \omega)$, we calculate $\tilde{h}_e(q, \omega)$ and use Eq. (8.6),

$$\delta(q - q')\delta(\omega - \omega')S(q, \omega) = \frac{1}{(2\pi)^4} \langle \tilde{h}_e(q, \omega)\tilde{h}_e(q', \omega')^* \rangle. \quad (8.7)$$

If the wavenumber q is set to zero, it should be possible to collapse the ‘‘spatio-adiabatic’’ power spectrum down to the ‘‘adiabatic’’ power spectrum. The *adiabatic* power spectrum derived by Steyn-Ross *et al.* (1999) does *not* include spatial variation, so all of its power will be situated at the $q = 0$ wavenumber. In contrast, the power spectrum $S(q, \omega)$ for the spatio-adiabatic equations gives the average power distributed over spatial and temporal frequencies for an infinite cortex.

For an infinite 1-D cortex, we define two-variable Fourier transforms of the \hat{h}_e excitatory and \hat{h}_i inhibitory soma-voltage fluctuations, and of the ξ white-noise sources of Eq. (4.92) as,

$$\tilde{h}_e(q, \omega) = \int_{-\infty}^{+\infty} \int_{-\infty}^{+\infty} e^{-i(qx+\omega t)} \hat{h}_e(x, t) dx dt \quad (8.8)$$

$$\tilde{h}_i(q, \omega) = \int_{-\infty}^{+\infty} \int_{-\infty}^{+\infty} e^{-i(qx+\omega t)} \hat{h}_i(x, t) dx dt \quad (8.9)$$

$$\tilde{\xi}(q, \omega) = \int_{-\infty}^{+\infty} \int_{-\infty}^{+\infty} e^{-i(qx+\omega t)} \xi(x, t) dx dt. \quad (8.10)$$

Fourier transforming Eq. (4.92) results in,

$$i\omega\tilde{h}_e(q, \omega) = (J_{11} - \kappa_e q^2)\tilde{h}_e(q, \omega) + J_{12}\tilde{h}_i(q, \omega) + b_{ee}\tilde{\xi}_1(q, \omega) + b_{ie}\tilde{\xi}_3(q, \omega) \quad (8.11)$$

$$i\omega\tilde{h}_i(q, \omega) = (J_{21} - \kappa_i q^2)\tilde{h}_e(q, \omega) + J_{22}\tilde{h}_i(q, \omega) + b_{ei}\tilde{\xi}_2(q, \omega) + b_{ii}\tilde{\xi}_4(q, \omega). \quad (8.12)$$

Rearranging Eq. (8.12) to make $\tilde{h}_i(q, \omega)$ the subject gives,

$$\tilde{h}_i(q, \omega) = \frac{(J_{21} - \kappa_i q^2)\tilde{h}_e(q, \omega) + b_{ei}\tilde{\xi}_2(q, \omega) + b_{ii}\tilde{\xi}_4(q, \omega)}{i\omega - J_{22}} \quad (8.13)$$

Substituting Eq. (8.13) into Eq. (8.11),

$$\begin{aligned} i\omega\tilde{h}_e(q, \omega) &= (J_{11} - \kappa_e q^2)\tilde{h}_e(q, \omega) + b_{ee}\tilde{\xi}_1(q, \omega) + b_{ie}\tilde{\xi}_3(q, \omega) \\ &+ J_{12} \left(\frac{J_{21}\tilde{h}_e(q, \omega) - \kappa_i q^2\tilde{h}_e(q, \omega) + b_{ei}\tilde{\xi}_2(q, \omega) + b_{ii}\tilde{\xi}_4(q, \omega)}{i\omega - J_{22}} \right), \end{aligned} \quad (8.14)$$

and rearranging to make $\tilde{h}_e(q, \omega)$ the subject

$$\begin{aligned} \tilde{h}_e(q, \omega) &= \frac{(i\omega - J_{22})(b_{ee}\tilde{\xi}_1(q, \omega) + b_{ie}\tilde{\xi}_3(q, \omega)) + J_{12}(b_{ei}\tilde{\xi}_2(q, \omega) + b_{ii}\tilde{\xi}_4(q, \omega))}{(i\omega - J_{22})(i\omega - J_{11} + \kappa_e q^2) - J_{12}J_{21} + J_{12}\kappa_i q^2} \\ &= \frac{(i\omega - J_{22})(b_{ee}\tilde{\xi}_1(q, \omega) + b_{ie}\tilde{\xi}_3(q, \omega)) + J_{12}(b_{ei}\tilde{\xi}_2(q, \omega) + b_{ii}\tilde{\xi}_4(q, \omega))}{q^2(i\omega\kappa_e - J_{22}\kappa_e + J_{12}\kappa_i) - \omega^2 - i\omega J_{11} - J_{22}i\omega + J_{22}J_{11} - J_{12}J_{21}} \end{aligned} \quad (8.15)$$

Multiplying the numerator and denominator of Eq. (8.15) by $1/(i\omega\kappa_e - J_{22}\kappa_e + J_{12}\kappa_i)$ we obtain

$$\tilde{h}_e(q, \omega) = \frac{n}{d} \quad (8.16)$$

where

$$n = \frac{(i\omega - J_{22})(b_{ee}\tilde{\xi}_1(q, \omega) + b_{ie}\tilde{\xi}_3(q, \omega)) + J_{12}(b_{ei}\tilde{\xi}_2(q, \omega) + b_{ii}\tilde{\xi}_4(q, \omega))}{(i\omega\kappa_e - J_{22}\kappa_e + J_{12}\kappa_i)} \quad (8.17)$$

$$d = q^2 + \frac{-\omega^2 - i\omega J_{11} - J_{22}i\omega + J_{22}J_{11} - J_{12}J_{21}}{(i\omega\kappa_e - J_{22}\kappa_e + J_{12}\kappa_i)} \quad (8.18)$$

Now that we have $\tilde{h}_e(q, \omega)$ as a function of q and ω we can calculate $S(q, \omega)$. First we determine $\langle \tilde{\xi}_m(q, \omega) \tilde{\xi}_n(q', \omega')^* \rangle$. Starting from Eq. (4.67), we have

$$\langle \xi_m(x, t) \xi_n(x', t') \rangle = \delta_{mn} \delta(x - x') \delta(t - t') \quad (8.19)$$

which, via Fourier transforming gives

$$\begin{aligned} \langle \tilde{\xi}_m(q, \omega) \tilde{\xi}_n(q', \omega')^* \rangle &= \left\langle \int \dots \int_{-\infty}^{+\infty} e^{-(qx+\omega t)} e^{+(q'x'+\omega't')} \xi_m(x, t) \xi_n(x', t') dx dt dx' dt' \right\rangle \\ &= \int \dots \int_{-\infty}^{+\infty} e^{-(qx+\omega t)} e^{+(q'x'+\omega't')} \langle \xi_m(x, t) \xi_n(x', t') \rangle dx dt dx' dt' \\ &= \int \dots \int_{-\infty}^{+\infty} e^{-(qx+\omega t)} e^{+(q'x'+\omega't')} \delta_{mn} \delta(x - x') \delta(t - t') dx dt dx' dt' \end{aligned}$$

and the integrals over x' and t' collapse to give

$$\begin{aligned} \langle \tilde{\xi}_m(q, \omega) \tilde{\xi}_n(q', \omega')^* \rangle &= \delta_{nm} \int_{-\infty}^{+\infty} \int_{-\infty}^{+\infty} e^{-i(q-q')x} e^{-(\omega-\omega')t} dx dt \\ &= (2\pi)^2 \delta_{nm} \delta(q - q') \delta(\omega - \omega') \end{aligned} \quad (8.20)$$

where the second equality follows from the definition of the Fourier transform of unity (Eq. 4.115).

Using equations (8.7), (8.16) and (8.20) we can calculate $S(q, \omega)$. When calculating the term $\langle \tilde{h}_e(q, \omega) \tilde{h}_e(q', \omega')^* \rangle$ all of the parameters besides the noise terms can be pulled out the front of the operator $\langle \rangle$. The $\langle \rangle$ operator then only acts on the noise terms, which obey Eq. (8.20).

The resulting $S(q, \omega)$ is given by,

$$S(q, \omega) = \frac{1}{4\pi^2} \frac{a_1}{(q^2 + a_2)(q^2 + a_2^*)} \quad (8.21)$$

where a_1, a_2 are defined as,

$$a_1 = \frac{J_{12}^2 b_{ei}^2 + J_{12}^2 b_{ii}^2 + \omega^2 b_{ee}^2 + \omega^2 b_{ie}^2 + J_{22}^2 b_{ee}^2 + J_{22}^2 b_{ie}^2}{\omega^2 + J_{22}^2 - J_{22} \kappa_e J_{12} \kappa_i + J_{12}^2 \kappa_i^2} \quad (8.22)$$

$$a_2 = \frac{-\omega^2 - i\omega J_{11} - J_{22} i\omega + J_{22} J_{11} - J_{12} J_{21}}{i\omega \kappa_e - J_{22} \kappa_e + J_{12} \kappa_i} \quad (8.23)$$

8.3 Power spectrum for $q = 0$

Steyn-Ross *et al.* (1999) derives the theoretical stationary power spectrum for the spatially homogeneous cortex. Making appropriate substitutions we obtain the homogeneous power spectrum as,

$$S[h_e(\omega)] = \frac{1}{2\pi} \frac{J_{12}^2 b_{ei}^2 + J_{12} b_{ii}^2 + J_{22}^2 b_{ee}^2 + J_{22}^2 b_{ie}^2 + \omega^2 b_{ee}^2 + \omega^2 b_{ie}^2}{J_{11}^2 J_{22}^2 - 2J_{11} J_{22} J_{21} J_{12} + J_{21}^2 J_{12}^2 + 2\omega^2 J_{12} J_{21} + \omega^4 J_{11}^2 \omega^2 J_{22}^2 \omega^2} \quad (8.24)$$

As a check we should be able to collapse Eq. (8.21) down to the stationary power spectrum Eq. (8.24) of the spatial homogeneous cortex. To do so we set $q = 0$ in Eq. (8.21) and note that the $\frac{1}{4\pi^2}$ maps to $\frac{1}{2\pi}$ as for no spatial variation the noise terms are constant in space and delta-correlated in time giving,

$$\langle \xi_m(t) \xi_n(t') \rangle = \delta_{mn} \delta(t - t') \quad (8.25)$$

therefore

$$\begin{aligned} \langle \tilde{\xi}_m(\omega) \tilde{\xi}_n(\omega)^* \rangle &= \delta_{mn} \int_{-\infty}^{+\infty} \int_{-\infty}^{+\infty} e^{-i\omega t} e^{-i\omega' t'} \delta(t - t') dt dt' \\ &= 2\pi \delta_{mn} \delta(\omega - \omega') \end{aligned} \quad (8.26)$$

Setting $q = 0$ and mapping $\frac{1}{4\pi^2} \rightarrow \frac{1}{2\pi}$ in Eq. (8.21) gives,

$$S(\omega) = \frac{a_1}{|a_2|^2} \quad (8.27)$$

Applying a bit of algebra, if we expand Eq. (8.27) using Eqs. (8.22–8.23) and simplify, then the two power spectra can be shown to agree exactly.

8.4 Power Spectrum including Spatial Variation

From our expression $S(q, \omega)$ for the infinite 1-D cortex, we want to be able to predict $S(\omega)$. The power spectra $S(q, \omega)$ from Eq. (8.21) gives an expression describing how power is distributed over spatial and temporal frequencies. To obtain $S(\omega)$, we add up the contributions from all q

for each ω . This is achieved by integrating over all wavenumbers q from $-\infty$ to $+\infty$,

$$S(\omega) = \int_{-\infty}^{+\infty} S(q, \omega) dq. \quad (8.28)$$

Substituting Eq. (8.21) into Eq. (8.28) gives

$$\begin{aligned} S(\omega) &= \int_{-\infty}^{+\infty} \frac{1}{4\pi^2} \frac{a_1}{(q^2 + a_2)(q^2 + a_2^*)} dq \\ &= \int_{-\infty}^{+\infty} \frac{1}{4\pi^2} \frac{a_1}{q^4 + (a_2 + a_2^*)q^2 + |a_2|^2} dq \end{aligned} \quad (8.29)$$

In order to calculate Eq. (8.29), contour integration in the complex plane is used. To do this we perform some complex calculus and then make use of the Residue theorem. First, following Spiegel (1974) we note that in the complex plane ($z = x + iy$), if the function $f(z)$ is bounded such that

$$|f(z)| \leq \frac{M}{R^k} \quad \text{for } z = Re^{i\theta} \quad (8.30)$$

where $k > 1$, and M and k are constants, then

$$\lim_{R \rightarrow \infty} \int_{\Gamma} f(z) dz = 0 \quad (8.31)$$

where Γ is the semi-circular arc of radius R shown in Fig. 8.1. Applying this identity to the problem in hand, we consider the complex function,

$$f(z) = \frac{1}{z^4 + b_1 z^2 + b_2} \quad (8.32)$$

in which we have defined

$$b_1 = (a_2 + a_2^*), \quad b_2 = |a_2|^2, \quad z = Re^{i\theta} \quad (8.33)$$

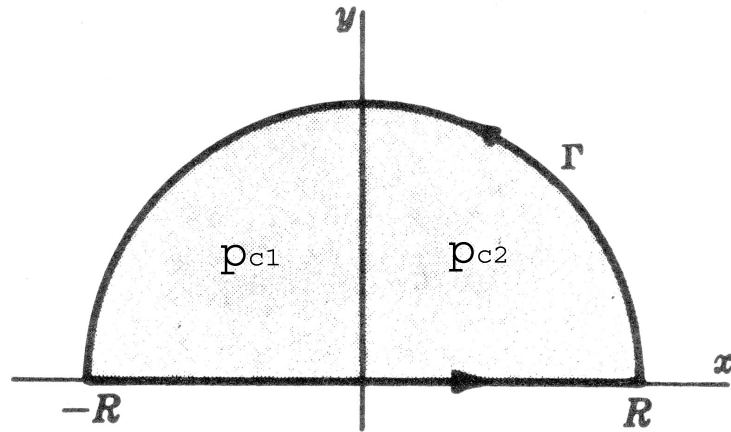


Figure 8.1: Contour of integration (circling the two poles p_{c1} and p_{c2}) in the complex plane. Adapted from Spiegel (1974)

then

$$\begin{aligned}
 |f(z)| &= \left| \frac{1}{R^4 e^{4i\theta} + b_1 R^2 e^{2i\theta} + b_2} \right| \\
 &\leq \frac{1}{|R^4 e^{4i\theta}| - |b_1 R^2 e^{2i\theta}| - |b_2|} \\
 &= \frac{1}{R^4 - (R^2 |b_1| + |b_2|)}
 \end{aligned} \tag{8.34}$$

using the inequality $|z_1 + z_2 + z_3| \geq |z_1| - |z_2| - |z_3|$. Continuing,

$$\begin{aligned}
 |f(z)| &\leq \frac{1}{R^4 - (R^2 |b_1| + |b_2|)} \\
 &\leq \frac{M}{R^4}
 \end{aligned} \tag{8.35}$$

if $R^4 \gg (R^2 |b_1| + |b_2|)$ and $M > 1$. Hence using Eqs. (8.30–8.31)

$$\lim_{R \rightarrow \infty} \int_{\Gamma} \frac{dz}{z^4 + (a_2 + a_2^*)z^2 + |a_2|^2} = 0. \tag{8.36}$$

We can now proceed to evaluate the power spectrum of Eq. (8.29). Consider the closed contour integral,

$$\oint_C \frac{dz}{z^4 + (a_2 + a_2^*)z^2 + |a_2|^2}, \tag{8.37}$$

where C is the closed path consisting of the line from $-R$ to R and the semi-circle Γ (see Fig. 8.1), traversed in the positive (counterclockwise) direction. The four poles of

$$\frac{1}{z^4 + (a_2 + a_2^*)z^2 + |a_2|^2} \quad (8.38)$$

are given by

$$p_1 = i\sqrt{a_2}, \quad p_2 = -i\sqrt{a_2} \quad (8.39)$$

$$p_3 = i\sqrt{a_2^*}, \quad p_4 = -i\sqrt{a_2^*} \quad (8.40)$$

Only two of these poles lie within C . Labelling the two poles that lie within C as p_{c1} and p_{c2} , then using the residue theorem we have

$$\oint_C \frac{dz}{z^4 + (a_2 + a_2^*)z^2 + |a_2|^2} = 2\pi i(r_{c1} + r_{c2}), \quad (8.41)$$

where r_{c1}, r_{c2} are the residues at the poles p_{c1}, p_{c2} . For a simple pole a the residue a_{-1} is

$$a_{-1} = \lim_{z \rightarrow a} (z - a)f(z). \quad (8.42)$$

Shortly we will also use L'Hôpital's rule, which states,

$$\lim_{x \rightarrow x_0} \frac{f(x)}{g(x)} = \lim_{x \rightarrow x_0} \frac{f'(x)}{g'(x)} \quad (8.43)$$

Calculating the residues r_{c1}, r_{c2} using Eq. (8.42) then Eq. (8.43) gives,

$$\begin{aligned} r_{c1} &= \lim_{z \rightarrow p_{c1}} \left\{ (z - p_{c1}) \frac{1}{z^4 + (a_2 + a_2^*)z^2 + |a_2|^2} \right\} \\ &= \lim_{z \rightarrow p_{c1}} \frac{1}{4z^3 + 2(a_2 + a_2^*)z} \\ &= \frac{1}{4p_{c1}^3 + 2(a_2 + a_2^*)p_{c1}}. \end{aligned} \quad (8.44)$$

Likewise,

$$r_{c2} = \frac{1}{4p_{c2}^3 + 2(a_2 + a_2^*)p_{c2}}. \quad (8.45)$$

Thus via Eq. (8.41)

$$\oint_C \frac{dz}{z^4 + (a_2 + a_2^*)z^2 + |a_2|^2} = 2\pi i \left(\frac{1}{4p_{c1}^3 + 2(a_2 + a_2^*)p_{c1}} + \frac{1}{4p_{c2}^3 + 2(a_2 + a_2^*)p_{c2}} \right) \quad (8.46)$$

and therefore

$$\begin{aligned} \int_{-R}^R \frac{dx}{x^4 + (a_2 + a_2^*)x^2 + |a_2|^2} + \int_{\Gamma} \frac{dz}{z^4 + (a_2 + a_2^*)z^2 + |a_2|^2} \\ = 2\pi i \left(\frac{1}{4p_{c1}^3 + 2(a_2 + a_2^*)p_{c1}} + \frac{1}{4p_{c2}^3 + 2(a_2 + a_2^*)p_{c2}} \right) \end{aligned} \quad (8.47)$$

where x is the real part of the complex variable $z = x + iy$. Taking the limit of both sides of Eq. (8.47) as $R \rightarrow \infty$ and using the result of Eq. (8.36), we have

$$\begin{aligned} \lim_{R \rightarrow \infty} \int_{-R}^R \frac{dx}{x^4 + (a_2 + a_2^*)x^2 + |a_2|^2} &= \int_{-\infty}^{\infty} \frac{dx}{x^4 + (a_2 + a_2^*)x^2 + |a_2|^2} \\ &= 2\pi i \left(\frac{1}{4p_{c1}^3 + 2(a_2 + a_2^*)p_{c1}} + \frac{1}{4p_{c2}^3 + 2(a_2 + a_2^*)p_{c2}} \right) \end{aligned} \quad (8.48)$$

Using the above equation the power spectrum can easily be derived as,

$$\begin{aligned} S(\omega) &= \int_{-\infty}^{+\infty} \frac{1}{4\pi^2} \frac{a_1}{q^4 + (a_2 + a_2^*)q^2 + |a_2|^2} dq \\ &= i \frac{a_1}{2\pi} \left(\frac{1}{4p_{c1}^3 + 2(a_2 + a_2^*)p_{c1}} + \frac{1}{4p_{c2}^3 + 2(a_2 + a_2^*)p_{c2}} \right). \end{aligned} \quad (8.49)$$

We can now use MATLAB to calculate $S(\omega)$ for the desired range of ω . The MATLAB program `theoryspec.m` first calculates a_1 and a_2 , then checks to see which two of the four poles p_1, p_2, p_3, p_4 has a positive imaginary component and hence is contained within the contour C . Once this has been established Eq. (8.49) is utilized to calculate $S(\omega)$. The program accepts a range of ω and ramps through them, calculating $S(\omega)$ for each.

Often $S(f)$ is desired rather than $S(\omega)$ where $\omega = 2\pi f$. To map from $S(\omega)$ to $S(f)$ we note that the total power in $S(\omega)$ must equal the total power in $S(f)$. Hence we require

$$\int_0^{\infty} S(\omega) d\omega = \int_0^{\infty} S(f) df. \quad (8.50)$$

Making the substitution $\omega = 2\pi f$ gives,

$$\int_0^\infty 2\pi S(2\pi f) df = \int_0^\infty S(f) df \quad (8.51)$$

hence

$$S(f) = 2\pi S(\omega). \quad (8.52)$$

8.5 Power Spectrum Predictions and Numerical Agreement

The theoretical power spectra $S(f)$ and the spectra determined from simulations of the non-linear spatio-adiabatic equations near homogeneous equilibrium are shown in Fig. 8.2. Each cortical rod simulation consisted of 100 grid-points separated by grid-spacings that were large enough for numerical stability, yet small enough to give accurate space-series as determined by comparison between numerical and theoretical spatial covariance at zero-lag. To calculate the power spectrum for each simulation, the power spectrum was calculated for each time-series at each grid point along the rod. The 100 power spectra obtained for each simulation were then averaged.

The power spectrum for each simulation was calculated using MATLAB's `fft.m` function with a Hanning window employed to reduce spectral leakage. Following Steyn-Ross (2002), each power spectrum was normalized according to,

$$S(k\Delta f) = \frac{\Delta t}{\|\mathbf{W}\|^2} |\text{DFT}\{\mathbf{x}\mathbf{W}\}_k|^2, \quad k = 0, 1, \dots, N-1 \quad (8.53)$$

where the $\mathbf{x}\mathbf{W}$ represents the element-by-element product of the times-series \mathbf{x} with window \mathbf{W} ,

$$\mathbf{x}\mathbf{W} = [x_0W_0, x_1W_1, \dots, x_{N-1}W_{N-1}] \quad (8.54)$$

and $\|\mathbf{W}\|$ is the norm or "rms height" of the \mathbf{W} window,

$$\|\mathbf{W}\| \equiv \sqrt{\sum_{j=0}^{N-1} W_j^2} \quad (8.55)$$

The experimental spectra and the theoretical spectra show good agreement at the lower frequencies, but tend to diverge at the higher frequencies. It is believed that this disagreement

at higher frequencies is due to the fact that the stochastic simulations have white noise entering at *every* time- and space-step, and are therefore vulnerable to aliasing contamination (spectral errors) entering from the high-frequency end of the spectrum. Steyn-Ross (2002) demonstrates that for a well-behaved stochastic process (though admittedly, his analysis does not include spatial variation) the theoretical and experimental power spectra are expected to show improved agreement for smaller time-steps.

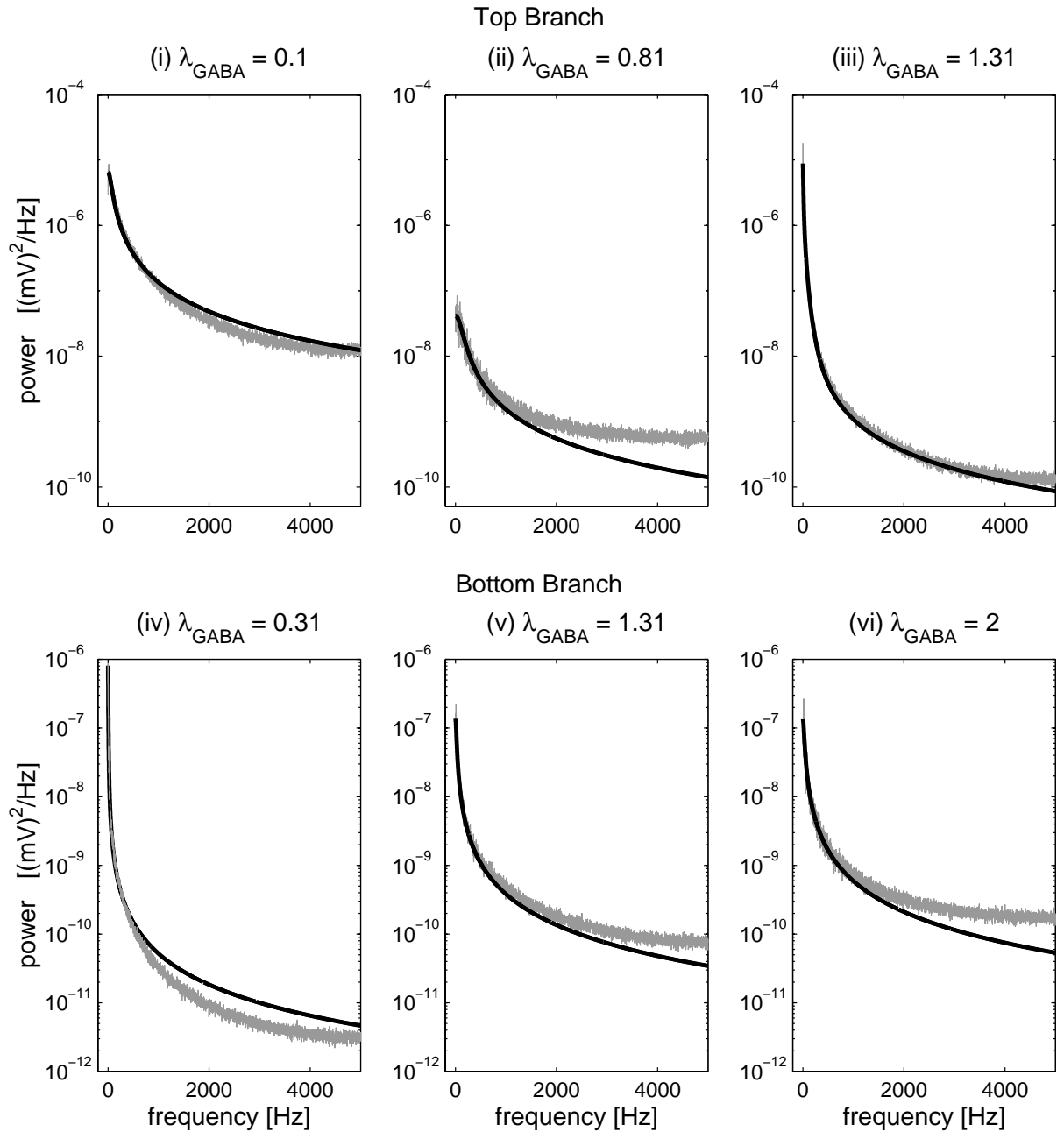


Figure 8.2: Comparison of theoretically predicted power spectra (Eq. 8.49) and spectra calculated from numerical experiments. The top three panels show the power spectra on the top-branch at (i) $\lambda_{\text{GABA}} = 0.1$, (ii) $\lambda_{\text{GABA}} = 0.81$, and (iii) $\lambda_{\text{GABA}} = 1.31$. The bottom three panels show the power spectra on the bottom-branch for (iv) $\lambda_{\text{GABA}} = 0.31$, (v) $\lambda_{\text{GABA}} = 1.31$, and (vi) $\lambda_{\text{GABA}} = 2$. All simulations were run using a time-step of 0.01 ms, $N = 100$ grid-points and grid spacings (in cm) (i) $h = 0.001$ (ii) $h = 0.2$ (iii) $h = 2$ (iv) $h = 1$ (v) $h = 0.1$ (vi) $h = 0.05$.

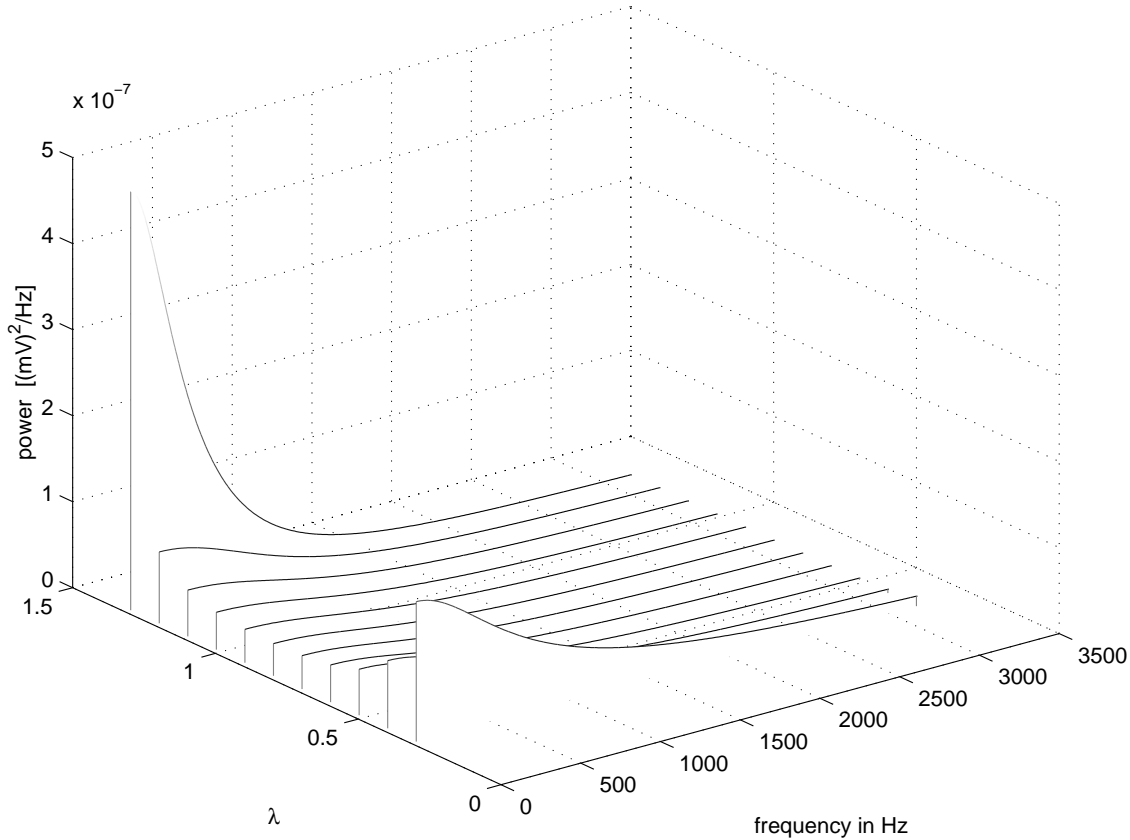


Figure 8.3: Analytic spectra for the linearized “spatio-adiabatic” equations, for fluctuations about the λ_{GABA} dependent *top-branch* steady-states. Spatial variability has been included, by integrating over all possible spatial frequencies. Noise scale-factor $\alpha = 0.01$ has been used, and all other constants are as defined in Table 3.1.

We have shown that the theoretical spectrum agrees well with numerical experiment and hence can investigate the spectrum in detail. In Fig. 8.3 we have plotted the stationary power spectrum $S(f)$ given by Eq. (8.49) and Eq. (8.52), for a range of top-branch equilibrium states. As λ_{GABA} is increased from 0.31 to 1.31 we see the spectra initially flattens out before evolving and into a low-frequency power surge on approach to the $\lambda_{\text{GABA}} = 1.31$ transition point (the “biphasic effect” at induction). In Fig. 8.4 the process is repeated for bottom-branch equilibrium states and similarly there is a surge in power at the $\lambda_{\text{GABA}} = 0.31$ transition point (emergence).

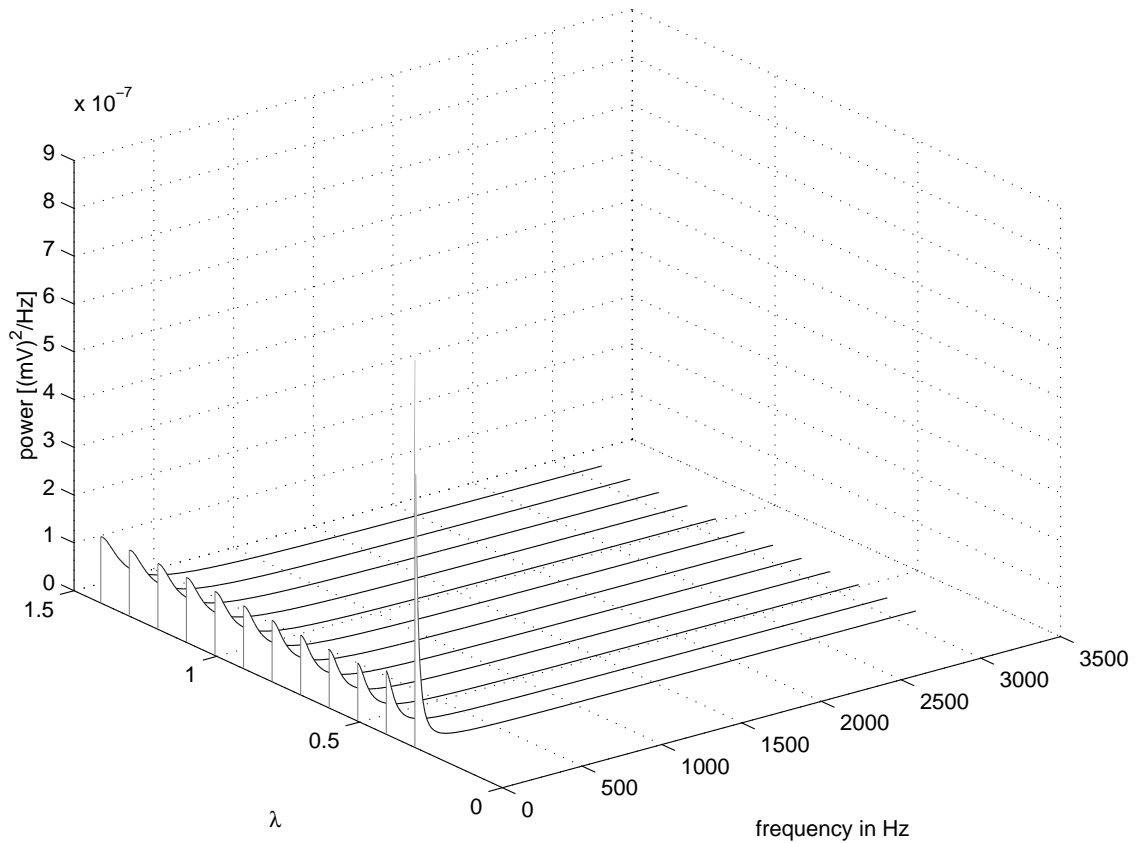


Figure 8.4: Analytic spectra of the linearized “spatio-adiabatic” equations, for fluctuations about the λ_{GABA} dependent *bottom-branch* steady-states. Spatial variability has been included, by integrating over all possible spatial frequencies. Noise scale $\alpha = 0.01$ has been used, and all other constants are as defined in Table 3.1.

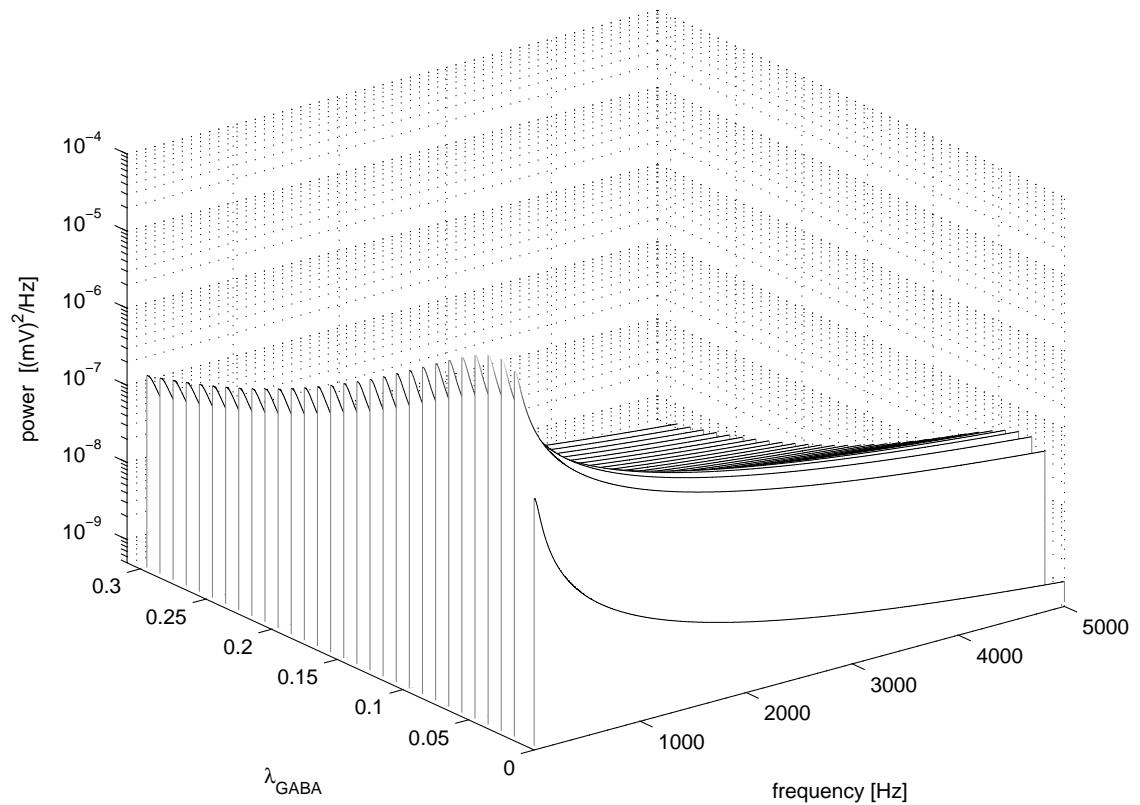


Figure 8.5: Analytical spectra of the linearized “spatio-adiabatic” equations, for fluctuations about the λ dependent *top-branch* steady-states in the region $\lambda_{\text{GABA}} = 0.3 \rightarrow 0$. Note a *log* scale has been used on the *z*-axis for clarity.

The zero-lag spatial covariance graph of Fig. 7.6 predicts a rapid surge in spatial power as $\lambda_{\text{GABA}} \rightarrow 0$, followed by a drop to the $\lambda_{\text{GABA}} = 0$ value. A power surge in $S(f)$ as $\lambda_{\text{GABA}} \rightarrow 0$ is also evident in Fig. 8.3. If we “zoom” in on the $\lambda_{\text{GABA}} = 0$ region we obtain Fig. 8.5. We

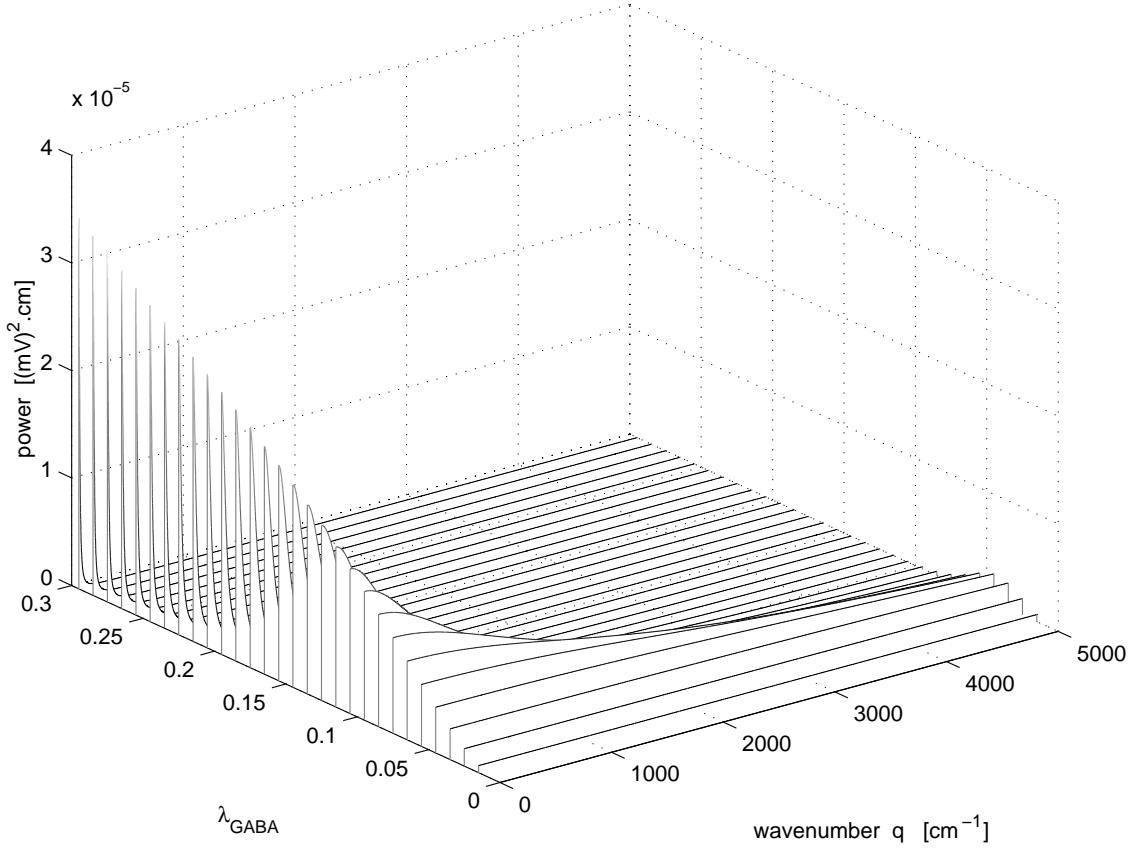


Figure 8.6: Analytical spatial spectra $S(q)$ of the linearized “spatio-adiabatic” equations, for fluctuations in space about steady-states, in the region $0 < \lambda < 0.3$.

can also plot the power distribution in space, by making use of the covariance function $\tilde{G}(q)$ (Eq. 4.144) and the *Wiener-Khinchin theorem*. The Wiener-Khinchin theorem in time states that the power spectrum and covariance function are related by,

$$S(\omega) = \frac{1}{2\pi} \int_{-\infty}^{\infty} e^{-i\omega\tau} G(\tau) d\tau. \quad (8.56)$$

Mapping this theorem to space we obtain,

$$S(q) = \frac{1}{2\pi} \int_{-\infty}^{\infty} e^{-iql} G(l) dl \quad (8.57)$$

where, for our function, $l = |x - x'|$. Referring to the $G(|x - x'|)$ definition of Eq. 4.139, we see that the spatial power spectrum $S(q)$ is actually equivalent to $\tilde{G}(q)$,

$$S(q) \equiv \tilde{G}(q) = \frac{D_1/\kappa_e + c_4}{2(q^2 + |c_1/\kappa_e|)} - \frac{c_4}{2(q^2 \pm |c_2/c_3|)}. \quad (8.58)$$

Plotting the power spectrum $S(q)$ in the $\lambda_{\text{GABA}} \rightarrow 0$ region reveals how power is distributed over the spatial wavenumbers as we approach $\lambda_{\text{GABA}} = 0$ (Fig. 8.6). Figure 8.6 shows that the power decrease for low wavenumbers while the power increases in the higher wavenumbers as $\lambda \rightarrow 0$. This change in power spatial power distribution is effecting the spectral power in time, but the two graphs do not appear to be simply related. As we do *not* get an increase in power as $\lambda \rightarrow 0$ for the spatial *homogeneous* (Steyn-Ross *et al.* (1999)), this peculiarity must arise from extending the generalization of the model from a homogeneous to a heterogeneous cortex.

Investigating the structure of power spectrum $S(f)$ as $\lambda_{\text{GABA}} \rightarrow 20$ reveals that the power decays away in the *low frequencies* as $\lambda_{\text{GABA}} \rightarrow 20$, analogous to the change in power spectrum for the homogeneous cortex (Fig. 8.8). But plotting the power using a log scale reveals that the power in the *higher frequencies* is in fact increasing (Fig. 8.7). The spectrum is effectively flattening out, but it appears the total power is slightly increasing. The spatial power spectra are shown in Fig. 8.9.

The physiological meaning of the increase and then sudden drop in power spectrum $S(f)$ as $\lambda_{\text{GABA}} \rightarrow 0$ is unclear. In this region the average neurons are firing very close to their maximum rate, so perhaps this surge in power could be related to epileptic fits. The physiological meaning of the increase in power in the high frequencies as $\lambda_{\text{GABA}} \rightarrow 20$ (approaching deep coma) is also unclear.

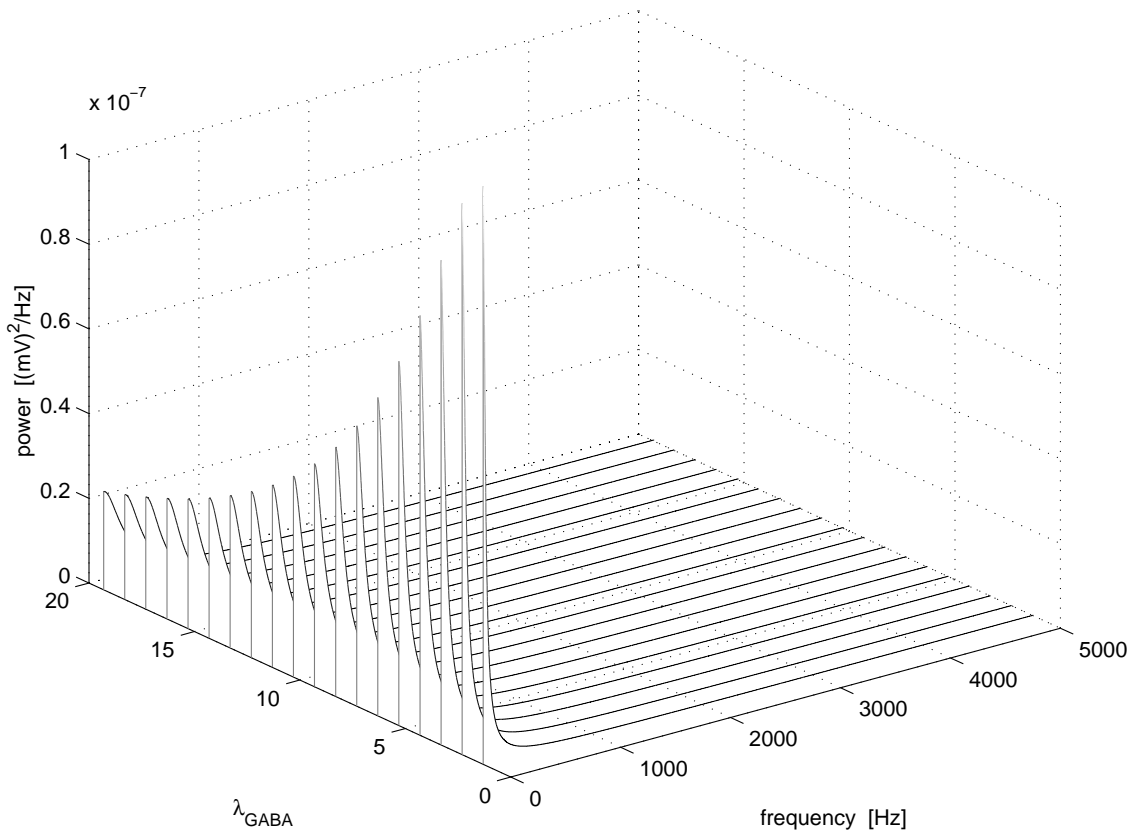


Figure 8.7: Analytical spectra $S(\omega)$ of the linearized “spatio-adiabatic” equations, for fluctuations about the λ dependent *bottom-branch* steady-states in the region $\lambda_{\text{GABA}} \rightarrow 20$

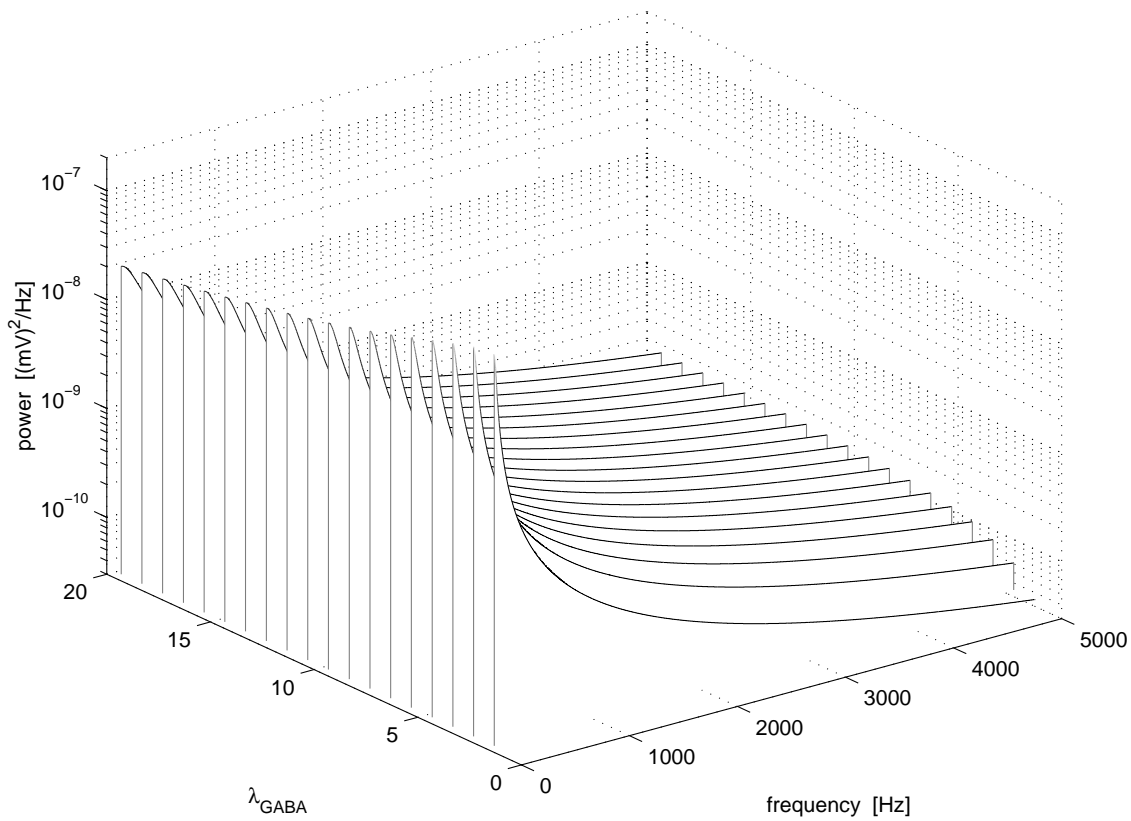


Figure 8.8: This figure is identical to Fig. 8.7 except a *log* scale has been used on the *z*-axis.

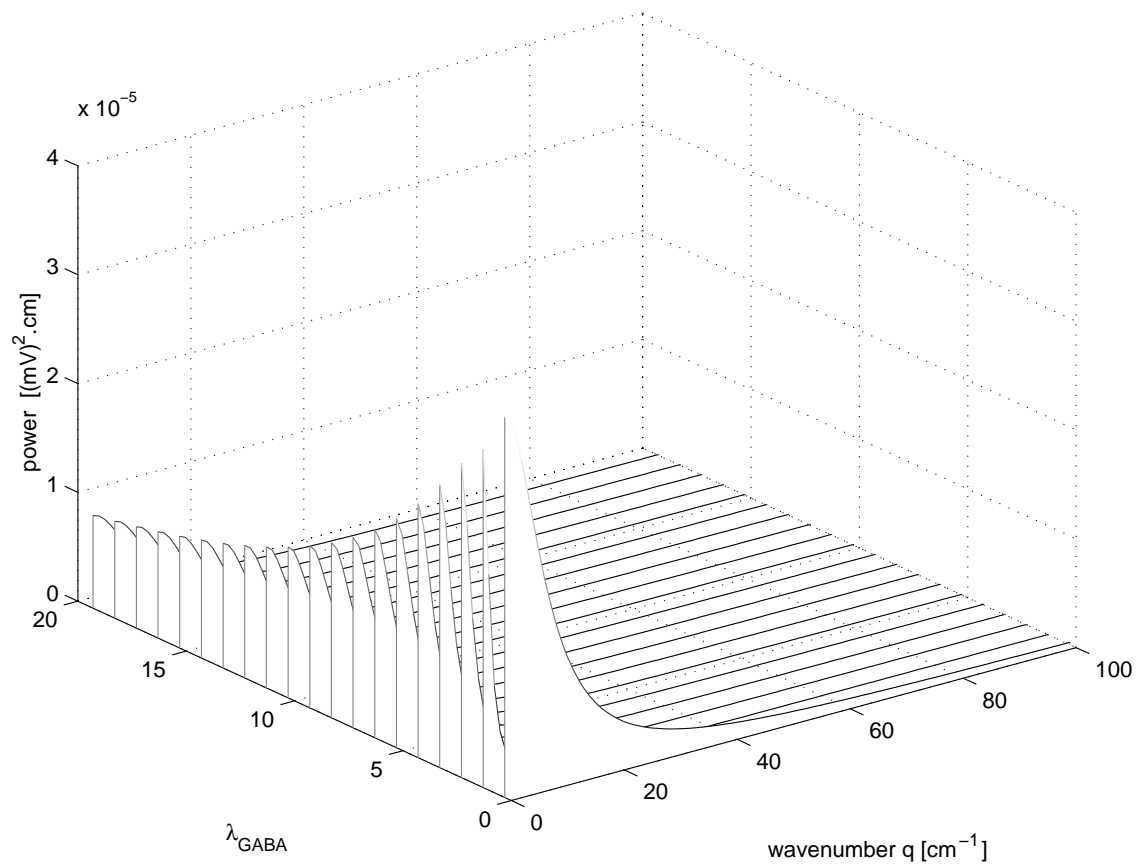


Figure 8.9: Analytical spatial spectra $S(q)$ of the linearized “spatio-adiabatic” equations, for fluctuations in space about the *bottom-branch* steady-states, for the region $0 < \lambda < 20$. Relative to Fig. 8.6 this graph has been rotated 180 degrees for clarity.

Conclusions and Future Work

9.1 Overview

In this thesis I have investigated the properties of the one-dimensional model of the spatio-adiabatic cerebral cortex developed by Steyn-Ross *et al.* (2003). The model aims to predict the changes in EEG activity as a person is rendered unconscious via anaesthetic induction. A set of theoretical functions were derived, namely the spatial-covariance and, the temporal- and spatial-power spectra. Numerical simulations for both the nonlinear and the linearized systems of equations were run, and both showed excellent agreement with the theoretical predictions. The theoretical covariance function and power spectrum were analyzed in detail, revealing some unexpected behaviours in the limits $\lambda_{\text{GABA}} \rightarrow 0$ and $\lambda_{\text{GABA}} \rightarrow \infty$. The stability of the spatio-adiabatic equations was also investigated and showed the possibility of dissipative stationary spatial patterns forming (nonequilibrium steady-states).

9.1.1 Diffusion Equation

In chapter 4 I investigated the classic diffusion equation for heat conduction along a rod. I looked at how to accurately model heat entering the cortical rod via a noise source. The effect of truncation error was briefly examined, and a scheme to minimize the error for the diffusion problem was derived. I determined the scaling required to allow matching up of fluctuation covariance curves (calculated from the space-series) for different combinations of grid-spacing h and number of grid-points N . It was then determined that to simulate the stochastic 1-D model, the spatial noise needed to be scaled by a factor of $1/\sqrt{h}$. An analytical confirmation of this scale factor was derived in Sec. 6.1.

9.1.2 Numerical Simulation of the “Spatio-Adiabatic” Equations

Three sets of difference equations were used to thoroughly investigate the spatio-adiabatic system. A mathematical derivation was done showing for a spatial-temporal stochastic system, that to accurately stimulate continuous white-noise we must introduce the scale factor $1/\sqrt{h\Delta t}$. I simulated the linearized spatio-adiabatic equations, the near-homogeneous equilibrium nonlinear spatio-adiabatic equations, and the far-from-homogeneous equilibrium nonlinear spatio-adiabatic equations. A von Neumann stability analysis was carried out on the linearized equations in order to determine the range of numerically stable time-steps and grid-spacings.

The time- and space-series close to homogeneous equilibrium, obtained by numerical simulation, were used to confirm the analytically-derived spatial covariance and power spectrum. The numerical data obtained from both the near-equilibrium nonlinear system and from the linearized system, showed excellent agreement with the analytically-derived functions. This agreement indicates that the linear system of equations, used to determine the theoretical functions, is an excellent approximation to the nonlinear equations (provided the system is close to homogeneous equilibrium).

I then proceeded to analyze the theoretical functions thoroughly.

9.1.3 Theoretical Predictions

It was shown that, for the 1-D spatio-adiabatic cortex, there is a predicted increase in correlation lengths (or spatial covariance) of EEG signals separated in space, just prior to the critical concentration at which a person is anaesthetically rendered unconscious. Similarly, an increase in correlation length is predicted just prior to a patient regaining consciousness. These increases in correlation length could be used as a clinical indication for a patient’s transition from consciousness to unconsciousness, and vice versa.

The power spectra showed the expected “biphasic” surges in spectral power, just prior to loss of consciousness and just prior to return to consciousness. This surge in power near transition has been extensively documented in clinical recordings.

The theoretical power spectra showed some unexpected behaviours in the limits $\lambda_{\text{GABA}} \rightarrow 0$ and $\lambda_{\text{GABA}} \rightarrow \infty$. The limit $\lambda_{\text{GABA}} \rightarrow 0$ corresponds to the brain being in a completely uninhibited and therefore highly active state (seizure), while the limit $\lambda_{\text{GABA}} \rightarrow \infty$ corresponds to brain activity being strongly suppressed (deep coma). The power spectra for the seizure state showed

a dramatic power increase followed by a sudden drop at $\lambda_{\text{GABA}} = 0$ across all spatial and temporal frequencies. The increase in power as λ_{GABA} approaches zero could possibly correspond to an epileptic fit. For the coma state, the theoretical spectra predicted the expected decrease in power across the low frequencies, but showed an increase in spectral power for the higher frequencies. As $\lambda_{\text{GABA}} \rightarrow 20$ this change in power distribution corresponds to the spectrum flattening out, but contradictory to the physiological intuition the net spatial power was predicted to increase, then gradually decline.

9.1.4 Formation of Nonequilibrium States

The implications of allowing the long-range inhibitory diffusion coefficient to dominate the excitatory diffusion coefficient were investigated. This led to the homogeneous steady-state of the cortex becoming unstable, with a bifurcation to a stable *nonequilibrium* steady-state being predicted. Linear stability theory was used to predict when the formation of the new state would occur, but could not tell us the form the new state will take. Linear theory predicts the new states will be stationary in time, displaying spatial oscillations (referred to in the literature as Turing patterns).

Numerical simulations were run to determine the form of these nonequilibrium states. It was shown that different states form for different values of anaesthetic effect and diffusivities. All the states displayed “finger”-like structure that were pseudo-periodic with the frequency of structures determined by the combination of anaesthetic effect and relative diffusivity. The nonequilibrium states were found to be very sensitive to the initial condition used to perturb the system, so different states form for different spatial-temporal noise patterns.

Whether such nonequilibrium states form in the human cortex is not yet determined. It seems physiologically unlikely that the brain could become “frozen” in such a state. One possibility is that these states could represent some sort of pathological condition similar to an epileptic fit.

9.2 Further Work

When investigating the 1-D cortex we found as λ_{GABA} approaches zero there is a surge followed by a drop at $\lambda_{\text{GABA}} = 0$ in power. What part of the model causes this increase then sudden decrease in power needs to be further investigated. Likewise, why the model predicts anomalies in the power spectra as $\lambda_{\text{GABA}} \rightarrow 20$ should be investigated further.

It would be worthwhile extending the model into a two-dimensional spatial system, since this would be a better physiological representation of the cortex than the present 1-D model. One could look at developing a theory for a *finite* length brain—specifically one of size similar to the cortex. Of interest would be the effect a finite model would have on the spatial covariance curves, especially for long correlation lengths. An important aspect of modelling a finite brain, would be to investigate what boundary conditions to use to best represent the physiology.

In the current model we could relax the spatio-adiabatic condition. This may allow the stationary 1-D dissipative structures to “unfreeze” and oscillate in time. It would be prudent to determine whether the mathematical requirement used to form these structures is physiologically realistic. If this is the case, one would investigate what is the physiological meaning of such structures forming in the cortex.

Summary of Matlab Code Used

Where applicable the code of Steyn-Ross (2002) has been used to calculate the homogeneous steady-state voltage for a value of λ_{GABA} on a specific branch of the inverted S-bend.

`Adiabaticwithspatial_linearised.m`: Simulates the linearized difference equations and produces a time-space series.

`Adiabaticwithspatial_nonequ.m`: Simulates the near-equilibrium nonlinear difference equations and produces a time-space series.

`Adiabaticwithspatial_nonequ_he.m`: Simulates the formation of nonequilibrium dissipative structures and produces a time-space series.

`dftcs.m`: This code simulates the diffusion equation using a forward-time centred-space scheme.

`eigenstability.m`: This code returns the eigenvalues for an input range of wavenumbers.

`OUprocess.m`: This code produces a time-series of the OU process.

`power_spec.m`: This code takes an input space-time series and calculates the average power spectrum.

`sbends.m`: This code reproduces the inverted S-bend of the homogeneous steady-states as a function of anaesthetic effect.

`stability.m`: This code uses the von Neumann stability analysis to determine whether a given time- and space-step is stable for the linearized spatio-adiabatic equations.

`theorycol.m`: This piece of code calculates the analytic spatial covariance function.

`theorypower.m`: This code calculates the analytic temporal power spectrum for a range of input parameters.

References

- Andrésen, P., M. Bache, and E. Mosekilde. Stationary space-periodic structures with equal diffusion coefficients. *Physical Review E*, **60**, pp. 297–301 (1999).
- Beurle, R. L. Properties of a mass of cells capable of regenerating pulses. *Transactions of the Royal Society (London)*, **240**, pp. 55–94 (1956).
- Boyce, W. E. and R. C. Dippima. *Elementary Differential Equations and Boundary Value Problems*. John Wiley and Sons, Inc., New York (1997).
- Braitenberg, V. and A. Schüz. *Anatomy of a Cortex: Statistics and Geometry*. Springer-Verlag, Berlin (1991).
- Chaturvedi, S., C. W. Gardiner, I. S. Matheson, and D. Walls. Stochastic analysis of a chemical reaction with spatial and temporal structures. *Statistical Physics*, **17**, pp. 469–489 (1977).
- Destexhe, A., D. Contreras, and M. Steriade. Spatiotemporal analysis of local field potentials and unit discharges in cat cerebral cortex natural wake and sleep states. *Neuroscience*, **19(11)**, pp. 4595–4608 (1999).
- Ermentrout, G. and J. Cowan. Temporal oscillations in neuronal nets. *Mathematical Biology*, **7**, pp. 265–280 (1979).
- Franks, N. P. and W. R. Lieb. Anaesthetics set their sites on ion channels. *Nature*, **389**, pp. 334–335 (1997).
- Freeman, W. J. *Mass Action in the Nervous System*. Academic Press, New York (1975).
- Garcia, A. L. *Numerical Methods for Physics*. Prentice Hall, New Jersey, second edition (2000).
- Gardiner, C. W. *Handbook of Stochastic Methods for Physics, Chemistry, and the Natural Sciences*, volume 13 of *Springer Series in Synergetics*. Springer-Verlag, Berlin (1985).
- Hodgkin, A. L. and A. F. Huxley. A quantitative description of membrane current and its application to conduction and excitation in nerve. *Journal of Physiology*, **117**, pp. 500–544 (1952).

- Jirsa, V. K. and H. Haken. A field theory of electromagnetic brain activity. *Physical Review Letters*, **77**, pp. 960–963 (1996).
- Jirsa, V. K. and H. Haken. A derivation of a macroscopic field theory of the brain from the quasi-microscopic neural dynamics. *Physica D*, **99**, pp. 503–526 (1997).
- John, E. R., L. S. Prichep, W. Kox, P. Valdés-Sosa, J. Bosch-Bayard, E. Aubert, M. Tom, F. diMichele, and L. D. Gugino. Consciousness and cognition. *Journal of Neurophysiology*, **70**, pp. 1339–1349 (1999).
- Jung, P., A. Cornell-Bell, K. S. Madden, and F. Moss. Noise-induced spiral waves in Astrocyte Syncytia show evidence of self-organised criticality. *The Journal of Neurophysiology*, **79**, pp. 1098–1101 (1998).
- Koch, C., M. Rapp, and I. Segev. A brief history of time (constants). *Cerebral Cortex*, **6**, pp. 93–101 (1996).
- Liley, D. T. J., P. J. Cadusch, and M. P. Dafilis. A spatially continuous mean field theory of electro-cortical activity. *Network: Computation in Neural Systems* (2002). In press.
- Liley, D. T. J., P. J. Cadusch, and J. J. Wright. A continuum theory of electro-cortical activity. California Institute of Technology, Santa Barabara, CA (1998).
- Liley, D. T. J., P. J. Cadusch, and J. J. Wright. A continuum theory of electro-cortical activity. *Neurocomputing*, **26–27**, pp. 795–800 (1999).
- Münster, A. F. Simulation of stationary chemical patterns and waves in ionic reactions. *Discrete and Continuous Dynamical Systems-Series B*, **2**, pp. 35–46 (2002).
- Murthy, K. P. N. Monte Carlo methods: An introduction. In: *Stochastic Processes Formalism and Applications*, edited by G. S. Agarwal and S. Dattagupta, Lecture Notes in Physics, no. 184, pp. 116–121. Springer-Verlag, Berlin (1983).
- Nunez, P. L. The brain wave function: A model for the EEG. *Mathematical Biosciences*, **21**, pp. 279–297 (1974).
- Nunez, P. L. *Electric Fields of the Brain: The Neurophysics of EEG*. Oxford University Press, New York (1981).
- Press, W. H., S. A. Teukolsky, W. T. Vetterling, and B. P. Flannery. *Numerical Recipes in C*. Cambridge University Press, Cambridge (1988).
- Reichl, L. E. *A Modern Course in Statistical Physics*. John Wiley and Sons, Inc, New York (1998).

- Robinson, P. A., C. J. Rennie, and J. J. Wright. Propagation and stability of waves of electrical activity in the cerebral cortex. *Physical Review E*, **56**, pp. 826–840 (1997).
- Robinson, P. A., C. J. Rennie, J. J. Wright, and P. D. Bourke. Steady states and global dynamics of electrical activity in the cerebral cortex. *Physical Review E*, **58**, pp. 3557–3571 (1998).
- Rotterdam, A., F. H. L. da Silva, J. van der Ende, M. A. Viergever, and A. J. Hermans. A model of the spatio-temporal characteristics of the alpha rhythm. *Bull. Math. Biol.*, **44**, pp. 283–305 (1982).
- Spiegel, M. R. *Theory and Problems of Advanced Calculus*. Schaum's Outline Series. McGraw-Hill, New York (1974).
- Steyn-Ross, D. A. *Modelling the Anaestheto-Dynamic Phase Transition of the Cerebral Cortex*. Ph.D. thesis, The University of Waikato (2002).
- Steyn-Ross, M. L., D. A. Steyn-Ross, J. W. Sleigh, and D. T. J. Liley. Theoretical electroencephalogram stationary spectrum for a white-noise-driven cortex: Evidence for a general anesthetic-induced phase transition. *Physical Review E*, **60**, pp. 7299–7311 (1999).
- Steyn-Ross, M. L., D. A. Steyn-Ross, J. W. Sleigh, and D. R. Whiting. Theoretical predictions for spatial covariance of the EEG signal during the anesthetic-induced phase transition: Increased correlation length and emergence of spatial self-organization. *submitted to Physical Review E* (2003).
- Steyn-Ross, M. L., D. A. Steyn-Ross, J. W. Sleigh, and L. C. Wilcocks. Toward a theory of the general anesthetic-induced phase transition of the cerebral cortex: I. A statistical mechanics analogy. *Physical Review E*, **64**, p. 011917 (2001).
- Tannehill, J. C., D. A. Anderson, and R. H. Pletcher. *Computational Fluid Mechanics and Heat Transfer*. Taylor and Francis, Washington, second edition (1997).
- Tortora, G. J. and S. R. Grabowski. *Principles of Anatomy and Physiology*. HarperCollins (1996).
- Tuckwell, H. C. *Introduction to Theoretical Neurobiology: Linear Cable Theory and Dendritic Structure*, volume 1. Cambridge University Press, Cambridge (1988a).
- Tuckwell, H. C. *Introduction to Theoretical Neurobiology: Nonlinear and Stochastic Theories*, volume 2. Cambridge University Press, Cambridge (1988b).
- Wilcocks, L. C. *Investigation of a Stochastic Model of the Electrical Behaviour of the Cerebral Cortex*. Master's thesis, University of Waikato, Hamilton, New Zealand (2001).

- Wilson, H. R. and J. D. Cowan. Excitatory and inhibitory interactions in localized populations of model neurons. *Biophysical Journal*, **12**, pp. 1–24 (1972).
- Wilson, H. R. and J. D. Cowan. A mathematical theory of the functional dynamics of cortical and thalamic nervous tissue. *Kybernetik*, **13**, pp. 55–80 (1973).
- Wright, J. J. and D. T. J. Liley. Dynamics of the brain at global and microscopic scales: Neural networks and the EEG. *Behavioral and Brain Science*, **19**, pp. 285–316 (1996).